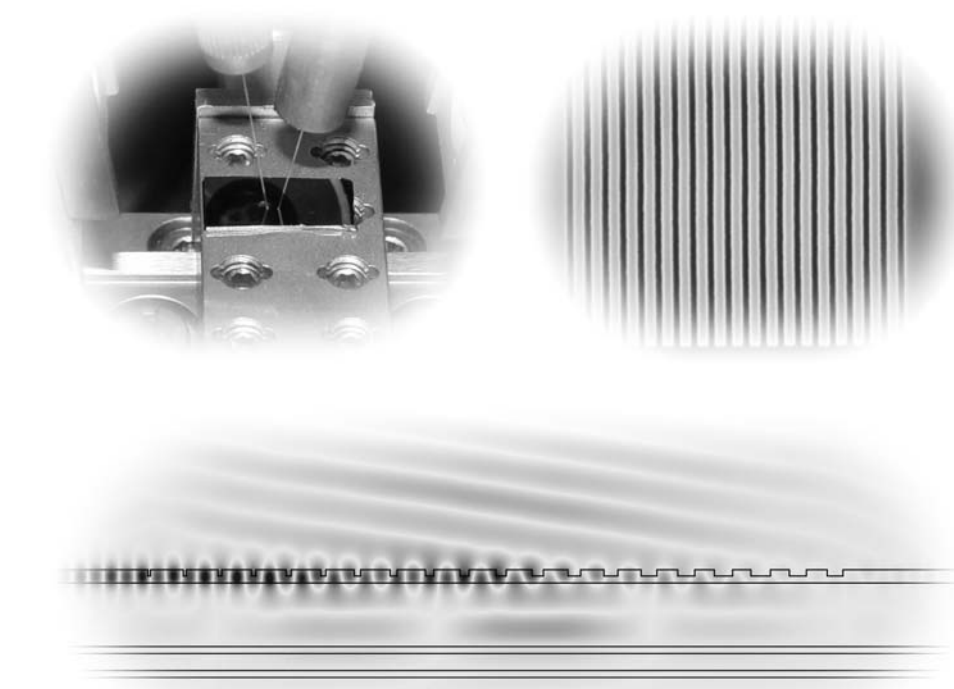


Roosterkoppelaars voor Koppeling tussen Optische Vezels en Nanofotonische Golfleiders

Grating couplers as Interface between
Optical Fibres and Nanophotonic Waveguides

Dirk Taillaert



Proefschrift tot het verkrijgen van de graad van
Doctor in de Toegepaste Wetenschappen:
Elektrotechniek
Academiejaar 2004-2005

Promotor:

Prof. dr. ir. R. Baets

Universiteit Gent, INTEC

Examencommissie:

Prof. dr. ir. J. Van Campenhout, voorzitter	Universiteit Gent, ELIS
Prof. dr. ir. R. De La Rue	University of Glasgow
Dr. P. Lalanne	Institut d'Optique, Orsay
Prof. dr. ir. K. Neyts	Universiteit Gent, ELIS
Prof. dr. ir. D. De Zutter	Universiteit Gent, INTEC
Prof. dr. ir. D. Van Thourhout	Universiteit Gent, INTEC
Prof. dr. ir. P. Bienstman, secretaris	Universiteit Gent, INTEC
Dr. ir. D. Delbeke	Universiteit Gent, INTEC

Universiteit Gent
Faculteit Toegepaste Wetenschappen

Vakgroep Informatietechnologie (INTEC)
Sint-Pietersnieuwstraat 41
9000 Gent
België

Tel.: +32-9-264.33.19
Fax: +32-9-264.35.93
<http://www.intec.ugent.be>

Preface - Voorwoord

Dit werk is tot stand gekomen door de inspanningen en creativiteit van heel wat mensen. Ik wil dit voorwoord dan ook gebruiken om hen te bedanken. In de eerste plaats wil ik mijn promotor, Prof. Roel Baets, bedanken om mij de mogelijkheid te bieden om dit onderzoek uit te voeren. Ook zijn suggesties en uitgebreide vakkennis waren zeer nuttig om dit werk tot een goed einde te brengen.

Bedankt, Ronny en Bart, mee dankzij jullie ben ik in de fotonica onderzoeksgroep (toen nog opto-elektronische componenten en systemen genoemd) terechtgekomen en vijf jaar gebleven.

Bedankt, Peter, voor je CAMFR-project. Het heeft mij enorm geholpen en het was een groot genoegen om CAMFR te kunnen loslaten op de roosterkoppelaars. Op de eerste versies heb ik soms gevloekt, maar de huidige CAMFR versie is topklasse.

Bedankt, Wim, voor de L^AT_EX introductie en het vele werk dat je verricht hebt in het kader van het PICCO onderzoeksproject. PICCO speelde een heel belangrijke rol in mijn werk. Bedankt, Bert en Pieter, om "mijn" roosterkoppelaars nuttig te gebruiken. Bedankt, Danaë, voor de hulp bij het holografie proces en het SEMmen.

Bedankt, Lieven, voor het scheppen van wat extra ambiance op de bureau. Bedankt, Kris, om Lieven af en toe eens af te koelen. Een goede sfeer was ook aanwezig in de ganse onderzoeksgroep, maar het is onmogelijk om hier iedereen bij naam te noemen, daarom bedankt aan alle fotoniekers.

Bedankt aan alle "bewoners" van de 39 voor de aangename werkseer, de koffiepauzes en andere ontspannende activiteiten, binnen en buiten de werkuren. Eigenlijk verdient ook de directie gebouwen van

de universiteit een pluim voor het nog niet afbreken van het beruchte huis nummer 39. Hierdoor hebben we ieder jaar een afbraak-barbecue georganiseerd en zijn we niet moeten verhuizen naar een of ander standaard kantoorgebouw. Bedankt ook aan die andere legende, die heeft bewezen dat deadlines niet zo strikt hoeven te zijn. Nog even volhouden, Thierry!

Onontbeerlijk waren ook de ondersteuning van het technisch en het administratief team. Ik zal hier niet iedereen bij naam noemen, omdat ik dan zeker iemand zou vergeten. Maar in het bijzonder wil ik Hendrik, Steven en Liesbet bedanken voor het operationeel houden van de meetruimte en de clean room.

I would also like to thank the PICCO project partners from Glasgow, St.-Andrews and Copenhagen. Special thanks to Harold for fabricating the best grating couplers.

And last but not least, thanks to all the people who have read my manuscript.

Dirk Taillaert
Gent, 13 juni 2004

Contents

Preface - Voorwoord	i
Contents	iii
Dutch summary - Nederlandstalige samenvatting	ix
1 Introduction	1
1.1 Research context	1
1.2 Waveguides and photonic integrated circuits	2
1.2.1 Nanophotonics	4
1.2.2 The coupling problem	4
1.2.3 Grating coupler	4
1.3 Purpose and outline of this work	5
1.4 Publications	6
2 Coupling light from fibres to nanophotonic waveguides	9
2.1 Nanophotonic waveguides in SOI	9
2.1.1 Silicon-on-insulator	9
2.1.2 Nanophotonics	10
2.2 Coupling to fibre	11
2.2.1 The problem	11
2.2.2 Tapered spot-size converters	12
2.2.3 Grating-assisted directional couplers	15
2.2.4 Waveguide grating couplers	16
2.3 Polarization	18
2.3.1 Polarization in fibre optics	18
2.3.2 Issues in nanophotonics	19
2.3.3 Polarization diversity approach	19
2.3.4 Integrated polarization diversity	20

3 Grating coupler theory and numerical methods	23
3.1 Introduction	23
3.1.1 Periodic structures	23
3.1.2 The Bragg condition	24
3.1.3 Definitions	27
3.1.4 Symmetry arguments	28
3.2 Perturbation analysis	29
3.2.1 Basic theory	29
3.2.2 Improved perturbation theory	30
3.3 Theory of periodic structures	31
3.3.1 The Floquet-Bloch theorem	31
3.3.2 Waveguide grating resonances	32
3.3.3 Coupled mode theory	35
3.4 Eigenmode expansion	38
3.4.1 Introduction	38
3.4.2 Boundary conditions	39
3.4.3 CAMFR	40
3.5 FDTD	41
3.6 Comparison of simulation results	42
3.7 Coupling to fibre	45
3.7.1 Introduction	45
3.7.2 Gaussian beams	45
3.7.3 Equations and approximations	46
3.7.4 Reciprocity	51
4 Design of a 1-D grating coupler	53
4.1 Introduction	53
4.2 Uniform rectangular grating	55
4.2.1 Vertical coupling	55
4.2.2 Almost vertical coupling	56
4.2.3 Layer thickness	60
4.2.4 Sensitivity to fabrication errors	61
4.2.5 TE versus TM	63
4.2.6 Oblique coupling	64
4.2.7 Very deep grating	65
4.2.8 Other index contrast waveguides	66
4.3 Coupler with rear reflector	69
4.3.1 Introduction	69
4.3.2 Coupler with deep reflector grating	72
4.3.3 Coupler with shallow reflector grating	73

4.4	Bottom mirror	76
4.5	Top mirror	77
4.6	Gaussian beam	81
4.6.1	Introduction	81
4.6.2	Optimization	83
4.6.3	Sensitivity to fabrication errors	86
4.6.4	Remarks and perspectives	86
4.7	Blazed grating	88
4.8	Summary	89
4.8.1	Vertical coupling	89
4.8.2	Almost vertical coupling	90
5	Fabrication technology	93
5.1	Introduction	93
5.2	Substrate	94
5.2.1	SOI	94
5.2.2	GaAs	94
5.3	Pattern definition	95
5.3.1	Optical lithography	96
5.3.2	Electron-beam direct-write lithography	97
5.3.3	Interference lithography	98
5.3.4	Dry etching	100
5.3.5	Focused Ion Beam etching	101
5.4	Characterization	101
5.5	Deposition	103
5.6	Packaging	105
6	Measurements	107
6.1	Measurement setup	107
6.1.1	Fibre in - fibre out	107
6.1.2	Fibre in - cleaved facet out	111
6.2	Measurement results	114
6.2.1	Coupling efficiency	114
6.2.2	With taper	115
6.2.3	Alignment sensitivity	117
6.2.4	With index-matching layer	117
6.2.5	Uniformity	117
6.2.6	Characterization of other components	119
6.2.7	Reflection measurements	122
6.2.8	Conclusions	124

7	2-D grating coupler	125
7.1	Introduction	125
7.1.1	Basic principle	125
7.1.2	Near vertical coupling	127
7.1.3	Polarization dependent loss	129
7.2	Grating design	132
7.2.1	Numerical methods	132
7.2.2	Design	133
7.3	Experimental results	135
7.3.1	Polarization splitter	135
7.3.2	Polarization diversity configuration	137
7.3.3	Coupling efficiency	139
7.4	Future perspectives	140
8	Conclusions and perspectives	143
8.1	Conclusions	143
8.2	Perspectives	144
A	CAMFR simulation example	147
B	Fabricated structures	151
List of figures		155
Bibliography		159

Nederlandstalige tekst

Dutch summary - Nederlandstalige samenvatting

Op de volgende bladzijden wordt een beknopte samenvatting gegeven van de belangrijkste verwijzingen in het kader van voorliggend doctoraatswerk. Voor verdere details en uitgebreidere achtergrondinformatie verwijzen we naar de Engelstalige tekst.

1. Inleiding

1.1 Achtergrond

Telecommunicatie speelt een belangrijke rol in ons dagelijks leven. Het internet laat toe om informatie van om het even waar op te vragen en te communiceren met mensen van over gans de wereld. Een van de basiselementen in het netwerk zijn de optische vezels die gigantische hoeveelheden informatie transporteren over onze planeet. De explosieve groei van het internet zou niet mogelijk geweest zijn zonder de enorme vooruitgang die de voorbije decennia gemaakt werd in het gebied van de optische communicatie. Maar er is nog ruimte voor verbetering. De optische vezels transporteren informatie van punt A naar punt B. Maar in de knooppunten van het netwerk, wordt het licht terug omgezet naar elektrische informatie. De routering en signaalverwerking gebeuren elektrisch en dan wordt het signaal weer omgezet in licht en over de volgende vezel verstuurd. Deze opto-elektronische omzettingen beperken de verdere groei van het netwerk en daarom is optische signaalverwerking een zeer actueel onderzoeksthema. Opto-elektronica wordt ook fotonica genoemd omdat er gewerkt wordt met licht of fotonen.

Alhoewel het ruggengraatnetwerk bijna uitsluitend optische vezel gebruikt, bestaan de laatste kilometers van het toegangsnetwerk naar de eindgebruiker nog steeds uit koperdraad. Een van de redenen hier voor is de kost van de vervanging van de draden. Maar ook de fotonische componenten die nodig zijn aan het uiteinde van de vezel zijn te duur om de thuisgebruiker aan te sluiten op optische vezel.

Een voorbeeld van een veelgebruikte fotonische component is een golflengte-multiplexer. Deze component combineert meerdere golflengtes in een vezel. Elk van deze golflengtes transporteert een signaal aan hoge datasnelheid (bvb. 10 Gbit/s). Dankzij golflengtemultiplexering is de capaciteit van de vezel veel hoger dan de datasnelheid in een kanaal, die beperkt wordt door de snelheid van de elektronica. Wanneer bijvoorbeeld 64 kanalen gebruikt worden, die elk 10 Gbit/s aankunnen, dan kan een vezel 640 Gbit/s transporteren. Aan het andere uiteinde van de vezel is een demultiplexer nodig om alle kanalen weer te scheiden.

Om meer geavanceerde en goedkopere fotonische componenten te kunnen maken, is het nodig om deze te integreren op een chip. Deze integratie zou het mogelijk moeten maken om grote, dure toestellen in de netwerkknooppunten te vervangen door enkele chips. Wanneer fotonische componenten geïntegreerd worden op een chip, spreken we over fotonische geïntegreerde schakelingen of fotonische ICs.

1.2 Golfgeleiders en fotonische geïntegreerde schakelingen

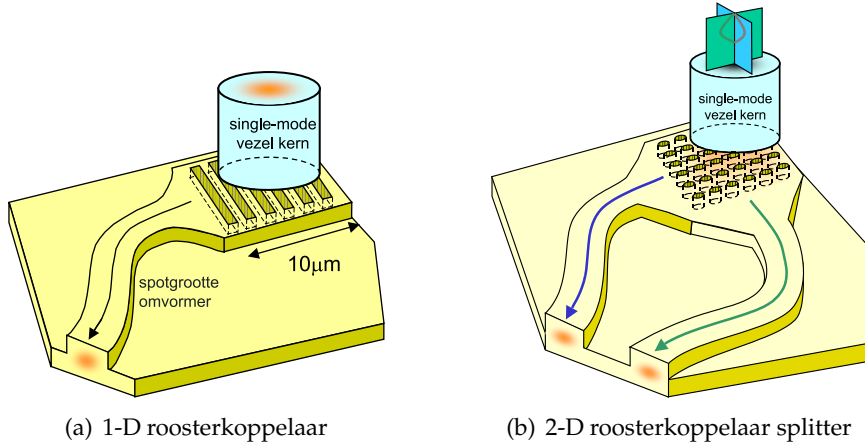
Een optische golfgeleider is een structuur die licht kan transporteren. In zo'n golfgeleider bevindt het licht zich in een kern die een hogere brekingsindex heeft dan de omringende mantel. Een optische vezel is een voorbeeld van een golfgeleider. Voor de meeste toepassingen worden single-mode golfgeleiders gebruikt, deze hebben slechts een geleide mode (voor elke polarisatie). Een optische vezel is meestal gemaakt uit glas en het brekingsindexcontrast tussen de kern en de mantel is typisch $< 1\%$. De diameter van de kern is ongeveer $9 \mu\text{m}$. Golfgeleiders in een fotonisch IC kunnen uit verscheidene materialen opgebouwd zijn, maar wij zullen ons beperken tot silicium gebaseerde structuren.

Golfgeleiders in silicium-op-isolator (SOI) hebben een heel hoog indexcontrast van ongeveer 3.5 op 1.5. Deze golfgeleiders moeten veel kleiner zijn om slechts een geleide mode te hebben. Typische afmetingen zijn $200 \times 450 \text{ nm}^2$. Omdat de afmetingen in nanometer uitgedrukt worden, spreken we van nanofotonische golfgeleiders. Mogelijke toe-

passingen van SOI fotonische ICs zijn niet alleen optische communicatie, maar ook interconnecties en sensors.

Het gebruik van nanofotonische golfgeleiders maakt het mogelijk om heel veel functionaliteit op een chip te integreren. Maar de kleine afmetingen zorgen ook voor een heleboel problemen. Het probleem dat wij zullen behandelen is de koppeling van licht tussen een optische vezel en een nanofotonische golfgeleider. Dit koppelprobleem is heel belangrijk omdat een geïntegreerd circuit niet erg nuttig is zonder koppeling met de buitenwereld. We hebben een structuur nodig die het verschil in spotgrootte kan overbruggen. Door het grote verschil in spotgrootte is dit een moeilijke opdracht. Een goede oplossing heeft niet alleen een hoge koppelefficiëntie, maar ook een grote bandbreedte en goede alignatietoleranties. Een ander probleem treedt op wanneer we een nanofotonisch IC willen gebruiken in optische communicatie links. Een nanofotonisch IC werkt enkel voor TE polarisatie, maar de polarisatietoestand van het licht dat uit een vezel komt kan variëren. Hierdoor zal het fotonisch IC niet goed werken, tenzij gebruik gemaakt wordt van een speciale polarisatiediversiteit configuratie. Deze problemen en mogelijke oplossingen worden in meer detail besproken in hoofdstuk 2.

Een roosterkoppelaar gebruikt een periodieke structuur of diffractierooster om het licht in een bepaalde richting te buigen. Een roosterkoppelaar kan gebruikt worden om licht efficiënt in een sub-micrometer SOI golfgeleider te koppelen. Maar traditionele roosterkoppelaars zijn smalbandig en redelijk groot. Daardoor zijn ze niet geschikt om licht naar een fotonisch IC te koppelen. We stellen voor om een compacte roosterkoppelaar te gebruiken om naar een vezel te koppelen. Omdat de koppellengte van het rooster zeer klein is, is de bandbreedte redelijk groot. Het concept van deze koppelaar wordt getoond in figuur 1(a). Het rooster voert de vertikale omvorming van de spotgrootte uit, voor de horizontale omvorming wordt een bundelexpansiestructuur gebruikt. De voorgestelde roosterkoppelaar werkt enkel voor TE polarisatie. Maar dit probleem kan opgelost worden door gebruik te maken van een 2-D rooster zoals voorgesteld in figuur 1(b). Deze 2-D roosterkoppelaar koppelt licht met een willekeurige polarisatie naar de TE modes van twee planaire golfgeleiders. Door deze manier van koppelen te gebruiken, kan het polarisatie-afhankelijkheidsprobleem van nanofotonische golfgeleiders misschien opgelost worden. Een gedetailleerde discussie over dit onderwerp wordt ook gegeven in hoofdstuk 2.



Figuur 1: Schematische voorstelling van golfgeleider roosterkoppelaars voor koppeling naar vezel. Voor de duidelijkheid zijn de structuren niet op schaal getekend.

1.3 Doel en structuur van dit werk

Het doel van ons onderzoek was het gebruik van roosterkoppelaars te onderzoeken om licht te koppelen tussen optische vezels en nanofootonische golfgeleiders en circuits. We hebben ons gefocusseerd op structuren in silicium-op-isolator omdat dit materiaal geschikt is voor massaproductie van toekomstige fotonische ICs.

In hoofdstuk 2 wordt het koppelprobleem in meer detail besproken en een overzicht van de state-of-the-art oplossingen gegeven. Het polarisatieprobleem wordt ook uitgelegd. Omdat ons werk gebaseerd is op roosters, worden de theorie van roosterkoppelaars en de simulatiemethodes die we gebruikt hebben, besproken in hoofdstuk 3. Hoofdstuk 4 behandelt het ontwerp van een 1-D roosterkoppelaar. Een kort overzicht van de technologie die nodig is om structuren te fabriceren wordt gegeven in hoofdstuk 5. De experimentele resultaten komen aan bod in hoofdstuk 6. Hoofdstuk 7 behandelt de 2-D koppelaars die gebruikt worden als polarisatiesplitter. Tenslotte worden de belangrijkste conclusies samengevat in hoofdstuk 8.

1.4 Publicaties

Het werk uitgevoerd in het kader van dit proefschrift heeft geleid tot een aantal publicaties in internationale vaktijdschriften

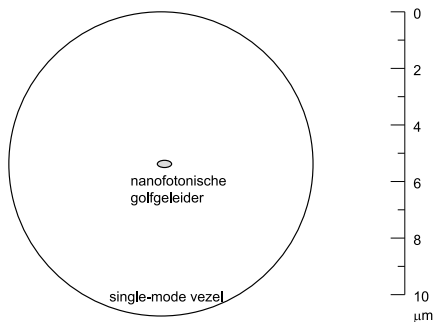
1. D. Taillaert, P. Bienstman, R. Baets, "Compact efficient broadband grating coupler for silicon-on-insulator waveguides," accepted for publication in *Optics Letters*, vol. 29, December 2004.
2. D. Taillaert, H. Chong, P. Borel, L. Frandsen, R. De La Rue, and R. Baets, "A compact two-dimensional grating coupler used as a polarization splitter," *IEEE Photonics Technology Letters*, vol. 15, pp. 1249–1251, September 2003.
3. D. Taillaert, W. Bogaerts, P. Bienstman, T. Krauss, P. Van Daele, I. Moerman, S. Verstuyft, K. De Mesel, and R. Baets, "An out-of-plane grating coupler for efficient butt-coupling between compact planar waveguides and single-mode fibers," *IEEE Journal of Quantum Electronics*, vol. 38, pp. 949–955, July 2002.
4. P. Sanchis, J. Garcia, J. Marti, W. Bogaerts, P. Dumon, D. Taillaert, R. Baets, "Experimental demonstration of high coupling efficiency between wide ridge dielectric waveguides and single-mode photonic crystal waveguides," accepted for publication in *IEEE Photonics Technology Letters*, October 2004.
5. P. Dumon, W. Bogaerts, V. Wiaux, J. Wouters, S. Beckx, J. Van Campenhout, D. Taillaert, B. Luyssaert, P. Bienstman, D. Van Thourhout, R. Baets, "Low-loss SOI photonic wires and ring resonators fabricated with deep UV lithography," *IEEE Photonics Technology Letters*, vol. 16, pp. 1328–1330, May 2004.
6. W. Bogaerts, D. Taillaert, B. Luyssaert, P. Dumon, J. Van Campenhout, P. Bienstman, D. Van Thourhout, R. Baets, V. Wiaux, S. Beckx, "Basic structures for photonic integrated circuits in silicon-on-insulator," *Optics Express*, vol. 12, pp. 1583–1591, April 2004.
7. W. Bogaerts, P. Bienstman, D. Taillaert, R. Baets, D. De Zutter, "Out-of-Plane Scattering in Photonic Crystal Slabs," *IEEE Photonics Technology Letters*, vol. 13, pp. 565–567, June 2002.
8. W. Bogaerts, V. Wiaux, D. Taillaert, S. Beckx, B. Luyssaert, P. Bienstman, R. Baets, "Fabrication of Photonic Crystals in Silicon-on-Insulator Using 248-nm Deep UV Lithography," *IEEE Journal on Selected Topics in Quantum Electronics*, vol. 8, pp. 928–934, 2002.
9. W. Bogaerts, P. Bienstman, D. Taillaert, R. Baets, D. De Zutter, "Out-of-plane scattering in 1-D photonic crystal slabs," *Optics and Quantum Electronics*, vol. 34, pp. 195–203, 2002.

Dit werk werd ook gepresenteerd op een aantal internationale conferenties, voor de lijst verwijzen naar de Engelstalige tekst.

Het concept van de 2-D koppelaar heeft aanleiding gegeven tot een octrooi-aanvraag :

Europese octrooi-aanvraag nummer EP-1353200

Amerikaanse octrooi-aanvraag nummer US-2003235370



Figuur 2: Spotgrootte van een typische nanofotonische golfgeleider en een single-mode optische vezel, op dezelfde schaal getekend.

2. Het koppelprobleem

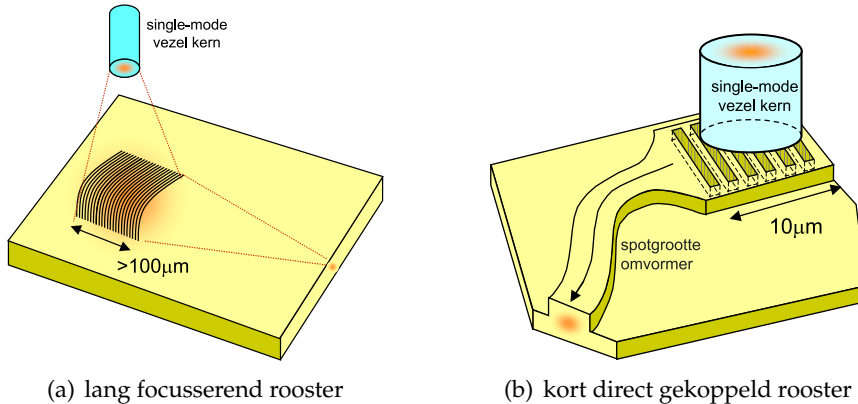
2.1 Nanofotonische golfgeleiders in SOI

Silicium-op-isolator (SOI) bestaat uit een dunne silicium laag bovenop een oxidebufferlaag bovenop een silicium substraat. Het bovenste silicium ($n=3.47$) is de golfgeleiderkern en het oxide de ondermantel. De bovenmantel is lucht, maar er kan ook een oxidelaag bovenop het silicium gelegd worden. SOI is beschikbaar in schijven met een diameter tot 30 cm en is geschikt voor massaproductie. Wij hebben SOI gebruikt met een 220 nm dikke Si toplaag en een 1000 nm dikke oxidebufferlaag. Dit materiaal is geschikt om nanofotonische golfgeleiders met lage propagatieverliezen te maken. Voorbeelden van zulke golfgeleiders zijn de zogenaamde fotonische kristalgolfgeleiders en fotonische draden. Een fotonische draad is in dit geval ongeveer 500 nm breed.

2.2 Koppeling naar optische vezels

De spotgrootte van een fotonische draad wordt vergeleken met die van een optische vezel in figuur 2. Het is duidelijk dat er een zeer groot verschil is. Beide golfgeleiders rechtstreeks met elkaar koppelen zou een koppelverlies van 26 dB opleveren, wat uiteraard onaanvaardbaar is. Er is een omvormer nodig die de spotgrootte aanpast, zowel in de horizontale als de vertikale richting. Het is vooral de vertikale richting die een groot probleem is. In de horizontale richting kan een planaire bundlexpansiestructuur gebruikt worden.

Heel wat onderzoekers hebben de voorbije jaren oplossingen gezocht voor dit koppelprobleem. Voor een literatuuroverzicht verwijzen we



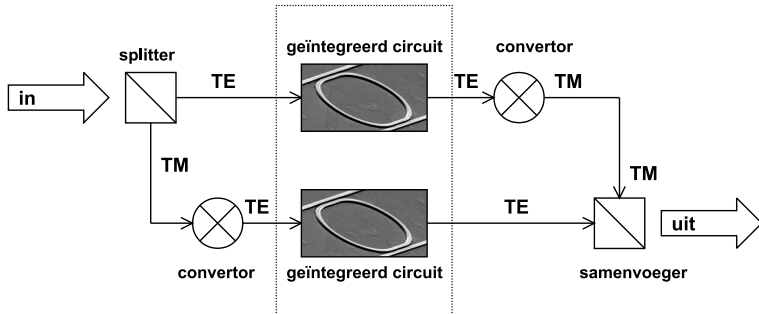
Figuur 3: Golfgeleider roosterkoppelaars.

naar de Engelstalige tekst. Hier beperken we ons tot de roosterkoppelaars. Een roosterkoppelaar kan licht in een golfgeleider koppelen langsboven. Op deze manier is het mogelijk om licht om het even waar in een circuit in en uit te koppelen en niet alleen aan de randen. Dit heeft als bijkomend voordeel dat de randen van de chip niet moeten gepolijst worden. Omdat de ganse chip oppervlakte kan gebruikt worden voor in- en uitgangen kan ook een groter aantal vezels met de chip verbonden worden. In de volgende paragraaf bespreken we bestaande roosterkoppelaars en vergelijken deze met de koppelaars die in dit werk behandeld worden.

Wanneer een roosterkoppelaar gebruikt wordt voor koppeling naar vezel, zijn er twee opties. Traditioneel wordt een lang zwak en dus ook smalbandig rooster gebruikt. Deze roosters hebben een hoge efficiëntie maar nemen veel plaats in en om naar een vezel te koppelen moet het rooster focuserend gemaakt worden (figuur 3(a)). Wij koppelen rechtstreeks de vezel met het rooster. Hiervoor moet het rooster veel korter zijn en dus een veel grotere koppelsterkte hebben. Als gevolg hiervan is de bandbreedte ook veel groter.

2.3 Polarisatie

De 1-D roosterkoppelaars werken slechts voor een polarisatie, in de meeste gevallen is dit voor TE-polarisatie. Ook nanofotonische circuits zijn polarisatiegevoelig. Licht dat van een single-mode optische vezel komt, kan echter elke elliptische polarisatietoestand hebben. In een optisch communicatienetwerk is die polarisatietoestand die uit de vezel



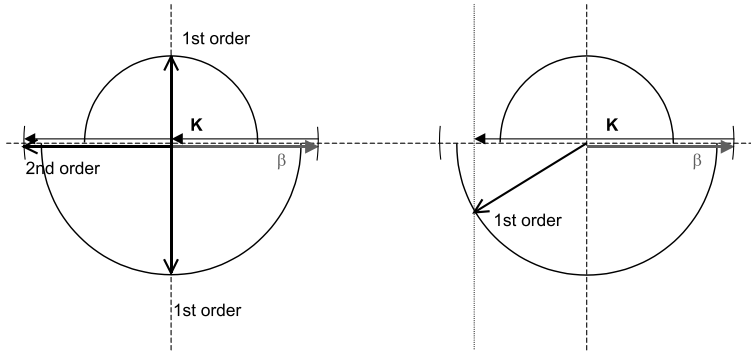
Figuur 4: Polarisatiediversiteit configuratie.

komt niet gekend, en dus moeten de componenten in de knooppunten polarisatie-ongevoelig zijn.

Er bestaan speciale types optische vezels, de zogenaamde polarisatiebehoudende vezels (PMF), waarin de polarisatiestoedant niet verandert gedurende de propagatie door de vezel. De huidige PMF kunnen slechts een goede uitdovingsverhouding garanderen over relatief korte afstanden, tot enkele honderden meters. Voor communicatie over langere afstand moeten we dus een andere oplossing vinden als we daarvoor ook nanofotonische circuits in de netwerkknooppunten willen gebruiken.

Een oplossing is het gebruik van een polarisatiediversiteit configuratie. Bij deze aanpak wordt het inkomende licht van de optische vezel gesplitst in twee orthogonale polarisaties. Een van de twee toestanden wordt geroteerd zodat twee gelijke polarisaties bekomen worden. Identieke operaties worden dan in parallel uitgevoerd. Aan de uitgang wordt een van de twee polarisaties opnieuw geroteerd en tenslotte worden beiden weer samengevoegd. Dit is schematisch geïllustreerd in figuur 4. De bestaande polarisatiesplitters en polarisatieconvertoren zijn echter moeilijk op een chip te integreren.

Om toch een geïntegreerde polarisatiediversiteit configuratie te kunnen implementeren stellen wij het gebruik voor van een golfgeleider-roosterkoppelaar met een 2-D rooster. Met de structuur van figuur 1(b) is het mogelijk om een compacte vezelkoppelaar te maken die tegelijkertijd polarisatiesplitter is. De koppelaar koppelt licht van de vezels naar de fundamentele TE-mode van twee golfgeleiders. De component vervult dus in feite de functie van polarisatiesplitter en convertor en is bovendien gemakkelijk te integreren. Deze 2-D roosterkoppelaar wordt besproken in hoofdstuk 7.



Figuur 5: Golfvector-diagram voor een roosterkoppelaar. Links is een tweede orde rooster te zien, rechts een rooster met slechts een diffractie-orde.

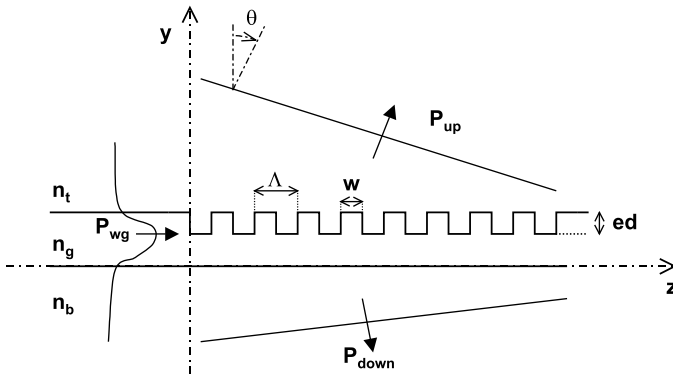
3. Roosterkoppelaar theorie

3.1 Introductie

Periodieke structuren spelen een belangrijke rol in de optica. In een periodieke structuur is het brekingsindexprofiel periodiek in een of meerdere dimensies. De structuren die ons interesseren hebben een periode van de grootte-orde van de golflengte van het licht en worden diffractieroosters of kortweg roosters genoemd. In dit hoofdstuk behandelen we enkel 1-D roosters, de 2-D roosters komen aan bod in hoofdstuk 7. Als de periodieke structuur zich in de nabijheid van een golfgeleiderstructuur bevindt, spreken we van golfgeleider-roosters.

Het gedrag van die roosters kan verklaard worden aan de hand van een golfvector-diagram. Enkele voorbeelden worden getoond in figuur 5. Bij een tweede orde rooster is de tweede orde diffractie reflectie in de golfgeleider. De eerste orde diffractie koppelt verticaal naar boven of beneden en kan gebruikt worden om naar een vezel te koppelen. Door de roosterperiode of de golflengte aan te passen, kan de uitkoppelrichting veranderd worden.

Om deze inleiding af te sluiten, geven we nog enkele definities aan de hand van figuur 6. Het rooster heeft een etsdiepte ed . De roosterperiode is Λ en de vulfactor $ff=w/\Lambda$. De assen en de hoek θ zijn gedefinieerd zoals in de figuur. Wanneer we de koppelaar als uitgangskoppelaar beschouwen, dan zal het vermogen in de golfgeleider exponentieel afnemen tengevolge van de aanwezigheid van het rooster (indien er geen koppeling is tussen de voorwaartse en achterwaartse geleide mode) : $P_{wg}(z) = P_{wg}(z=0) \exp(-2\alpha z)$



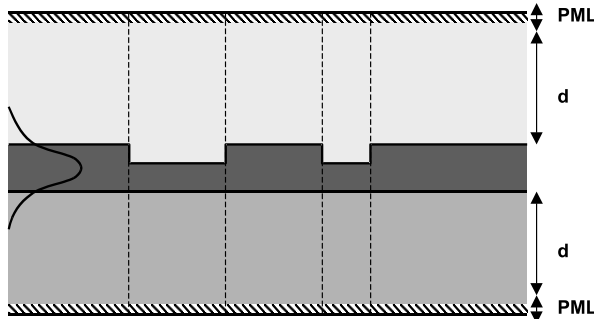
Figuur 6: Het 1-D roosterkoppelaar probleem.

2α is de koppelsterkte van het rooster. Wanneer α klein is spreken we van een zwak rooster, als α groot is van een sterk rooster. Deze exponentiële afname is enkel geldig in het geval van een zwak en ontstemd rooster. De gerichtheid van het rooster is de verhouding van het vermogen dat naar boven uitstraalt tot het vermogen dat naar onder uitstraalt. De koppelefficiëntie is het vermogen dat naar de vezel koppelt gedeeld door het vermogen in de geleide mode dat op het rooster invalt. De koppelefficiëntie van golfgeleider naar vezel is dezelfde als van vezel naar golfgeleider omwille van reciprociteit. We kunnen dan ook spreken van de efficiëntie.

3.2 Berekeningsmethodes

In de literatuur zijn heel wat numerieke methodes gepubliceerd om roosterkoppelaars uit te rekenen. Een veelgebruikte benadering is dat het rooster beschouwd wordt als een kleine periodieke perturbatie van de golfgeleider. Deze benadering maakt de berekeningen heel wat eenvoudiger. Er blijkt echter dat voor de roosters die wij gebruiken, deze benadering geen accurate resultaten oplevert. Deze perturbatie aanpak levert wel een aantal kwalitatieve inzichten in de eigenschappen van de koppelaars op.

Er bestaan ook methodes die sterkere roosters rigoreus kunnen uitrekenen. Deze methodes zijn meestal beperkt tot puur periodieke of oneindige structuren. Een oneindige structuur is uiteraard een puur mathematische beschrijving, maar onder bepaalde voorwaarden zijn de resultaten ook accuraat voor eindige roosters. Het geval van ver-



Figuur 7: Eigenmode expansie methode. De structuur is verdeeld in secties met een brekingsindex die niet verandert in de propagatierichting.

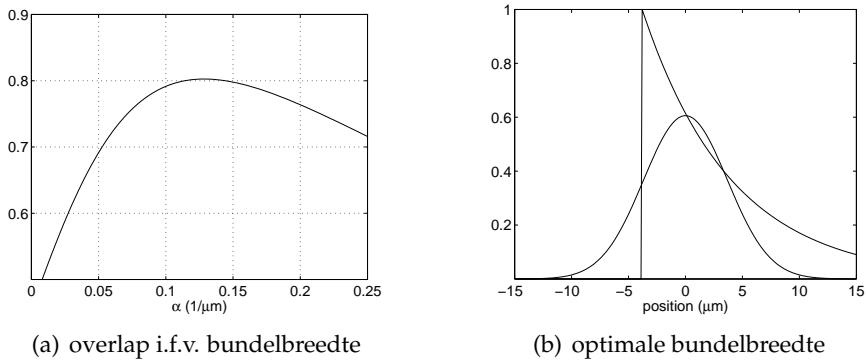
tikale koppeling waarbij er ook tweede orde rooster reflectie is, kan echter niet behandeld worden.

3.3 Eigenmode expansie

De eigenmode expansie methode is een methode die zeer algemene structuren kan simuleren, maar die ook uitermate geschikt is voor onze roosterkoppelaars. De structuur wordt opgedeeld in secties, waarbij de brekingsindex in iedere sectie niet verandert in de propagatierichting (figuur 7). Een binair rooster heeft dus slechts twee verschillende secties. In een eerste stap worden de eigenmodes van alle secties berekend. Deze modes zijn de geleide maar ook de stralende modes. Het totale elektromagnetisch veld in een sectie kan beschreven worden als een lineaire combinatie van de eigenmodes. In een 2-D probleem zijn de secties slabgolfgeleiders.

Door samenvoegen van alle secties wordt de totale structuur of stapel bekomen. Aan de overgang tussen verschillende secties wordt een mode-matching techniek gebruikt en zo kan de verstrooiingsmatrix van de volledige stapel berekend worden. Deze verstrooiingsmatrix levert ons ook de reflectie en transmissie van de volledige stapel op. Voor eindige periodieke structuren kan een speciaal berekeningsschema gebruikt worden, waardoor de rekentijd logaritmisch toeneemt met het aantal perioden in plaats van lineair. De velden en het uitgestraalde vermogen kunnen ook berekend worden voor een gegeven excitatie. We gebruiken altijd de fundamentele geleide mode als excitatie.

De randvoorwaarden zijn belangrijk. Om reflecties aan de randen van de berekeningsruimte te vermijden, worden perfect aangepast la-



Figuur 8: Overlap van een Gaussisch en een exponentieel profiel. De diameter van de Gaussische bundel is $10.4 \mu\text{m}$.

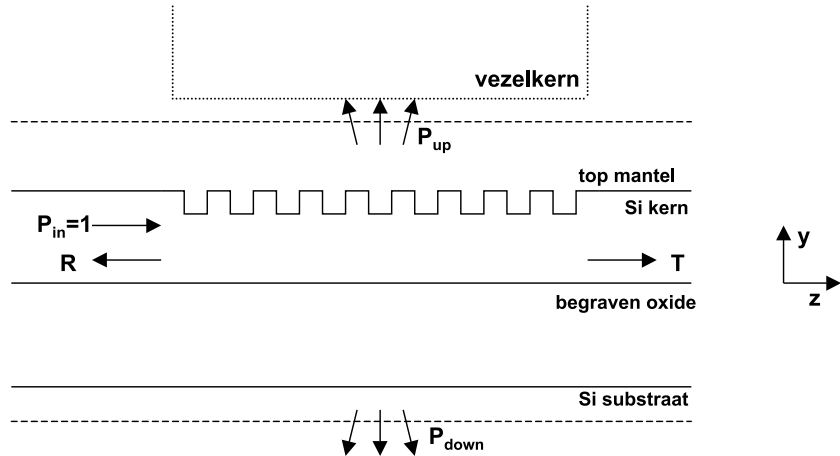
gen (PML) gebruikt. Een juiste keuze van de PML dikte is nodig. Indien de PML te klein gekozen wordt, zal er nog reflectie zijn aan de randen, die voor foute resultaten zal zorgen.

Het simulatieprogramma CAMFR implementeert deze methode. Wij hebben CAMFR gebruikt voor de simulatie van 1-D roosters in hoofdstuk 4. We hebben CAMFR gebruikt omdat het geschikt is voor zowat alle verschillende types roosters die we bestudeerd hebben. De accuraatheid van de resultaten werd uitgebreid onderzocht door vergelijking met resultaten uit de literatuur en met FDTD-simulaties.

3.4 Koppeling naar vezel

Om de koppelefficiëntie naar een vezel te berekenen wordt de vezelmode benaderd door een Gaussische bundel met een bundeldiameter van $10.4 \mu\text{m}$. De vezel zelf is niet aanwezig in de simulaties, maar we maken gebruik van een overlapintegraal om de koppeling te berekenen. We gebruiken 2-D simulaties, maar de resultaten zijn een goede benadering van het 3-D probleem omdat de breedte van de golfgeleider veel groter is dan de hoogte en de golflengte. De optimale golfgeleiderbreedte is ongeveer $12 \mu\text{m}$.

Een uniform rooster resulteert in een uitgestraald vermogen dat ongeveer exponentieel afneemt. Een exponentieel veld kan nooit volledig koppelen naar een Gaussische bundel. De maximale overlap is ongeveer 80%. Deze overlap als functie van de koppelsterkte van het rooster wordt getoond in figuur 8(a). In figuur 8(b), wordt de alignatie getoond in het geval van maximale koppeling.



Figuur 9: Simulatiemodel van een 1-D roosterkoppelaar structuur. De excitatie is de genormaliseerde golfgeleidermode. R is de reflectie aan het rooster. T is de transmissie doorheen het eindig rooster. P_{up} en P_{down} zijn het vermogen dat naar boven en beneden gestraald wordt.

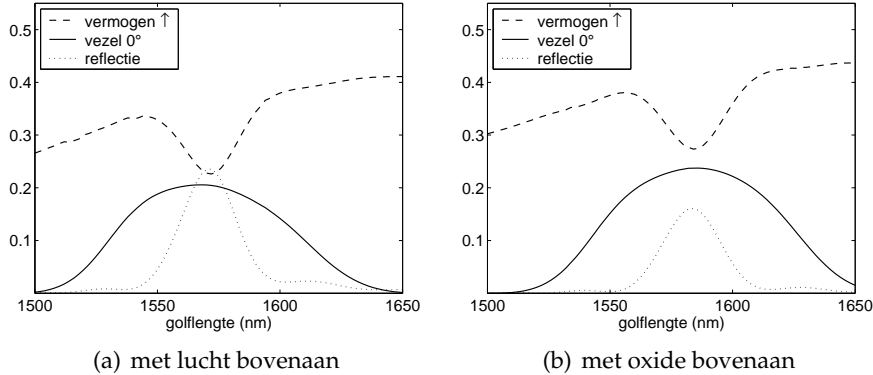
4. Ontwerp van de 1-D roosterkoppelaar

4.1 Introductie

Een goed ontwerp is nodig om een hoge koppelefficiëntie tussen de SOI golfgeleider en de vezel te bekomen. In dit hoofdstuk stellen we verschillende ontwerpen voor. We starten met een relatief eenvoudig uniform rooster. Daarna volgen complexere structuren. De resultaten in dit hoofdstuk zijn gebaseerd op CAMFR-simulaties (zie hoofdstuk 3) en enkel 2-D structuren (1-D roosters) worden behandeld. Het simulatiemodel wordt getoond in figuur 9. Alle resultaten zijn voor TE polarisatie, tenzij anders vermeld.

4.2 Uniforme rechthoekige roosters

We starten met een studie van uniforme roosters met rechthoekige tanden. Deze structuren zijn periodiek maar eindig. Rechthoekige roostertanden zijn het gemakkelijkst te fabriceren en te simuleren. De golfgeleider laagstructuur is 220 nm Si bovenop 1000 nm SiO_2 bovenop een Si substrate. Het rooster is geëtst in de Si toplaag. Bovenop de structuur is er lucht ($n=1$) of oxide ($n=1.46$).



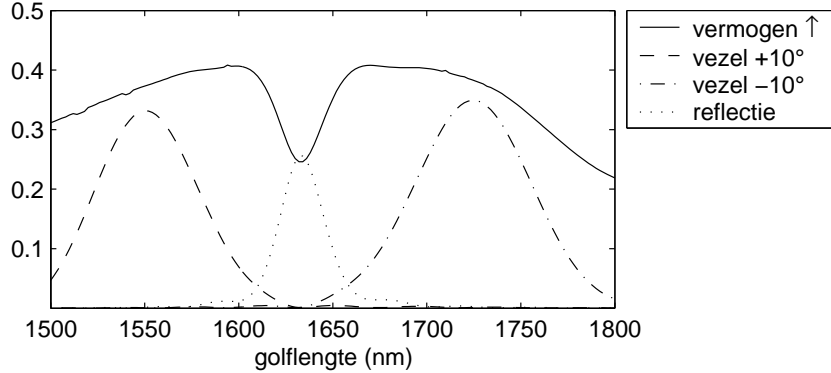
Figuur 10: Berekende koppelefficiëntie naar vezel voor vertikale koppeling.
 $\Lambda=580 \text{ nm}$, $ed=50 \text{ nm}$, $ff=0.5$, $N=20$, $\overbrace{\hspace{1cm}}$

Vertikale koppeling

Vertikale koppeling ($\theta = 0^\circ$) kan bereikt worden wanneer de roosterperiode Λ gelijk is aan de golflengte λ gedeeld door een brekingsindex. Voor een heel zwak rooster is deze brekingsindex de effectieve index van de golfgeleidermode. Zulk rooster wordt ook een tweede orde rooster genoemd. Maar het is de eerste orde diffractie die gebruikt wordt om naar vezel te koppelen. Om verwarring te vermijden zullen we dit rooster koppelrooster noemen. De tweede orde diffractie is reflectie terug in de golfgeleider. Deze reflectie neemt toe als de etsdiepte toeneemt. Ze is minimaal voor een vulfactor van ongeveer 50%. De optimale etsdiepte is ongeveer 50 nm en de simulatieresultaten voor deze structuur worden getoond in figuur 10. De piek reflectie bedraagt 23% en de maximale efficiëntie 21%. De 1 dB bandbreedte is 52 nm. Wanneer oxide op de structuur wordt gedeponeerd, neemt de efficiëntie toe tot 24% en neemt de reflectie af tot 16%.

Bijna vertikale koppeling

Om reflectie aan het rooster te vermijden, kunnen we een werkingspunt kiezen dat verder is van de tweede orde reflectie piek. Een kortere of langere golflengte kan gekozen worden. Het gevolg is dat het licht niet meer exact verticaal uitgekoppeld wordt, maar onder een kleine hoek θ ten opzichte van de oppervlaktenormaal. Dit wordt geïllustreerd in figuur 11. Het rooster wordt ontstemd (detuned) genoemd. In plaats van de golflengte te wijzigen kan de periode van het roos-



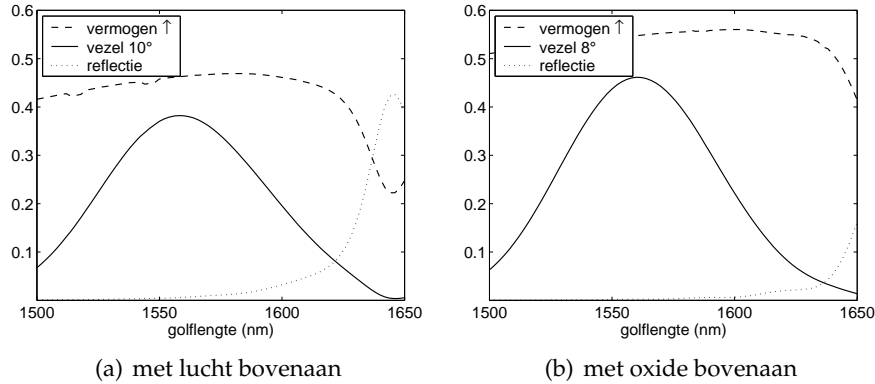
Figuur 11: Positief en negatief ontstemd rooster.
 $\Lambda=610 \text{ nm}$, $ed=50 \text{ nm}$, $ff=0.5$, $N=20$,

ter aangepast worden. We kiezen voor een positief ontstemd rooster, omdat dit de experimenten eenvoudiger maakt. In de experimenten meten we de transmissie van vezel naar vezel op een golfleider met een roosterkoppelaar aan beide uiteinden. Dit zou veel moeilijker zijn wanneer de hoek θ negatief is.

De optimale structuur heeft een etsdiepte van 70 nm. De periode is 630 nm omdat het spectrum rond 1550 nm gecentreerd zou zijn. De simulatieresulaten zijn voorgesteld in figuur 12. De maximale efficiëntie is 38% voor $\lambda=1558 \text{ nm}$ en de 1 dB bandbreedte is 46 nm. Met een oxidelaag bovenop het rooster, wordt de efficiëntie verhoogd naar 46%. De efficiëntie wordt beperkt door koppeling naar het substraat en door de mismatch tussen een exponentieel en een Gaussische profiel. De gerichtheid van de koppelaar kan verbeterd worden door de dikte van de oxidebufferlaag optimaal te kiezen.

Laagdiktes

De dikte van de begraven oxidelaag heeft een grote invloed op de efficiëntie van een SOI roosterkoppelaar. Dit effect kan als volgt uitgelegd worden. Het rooster creëert een opwaartse en een neerwaartse golf. De neerwaartse golf reflecteert gedeeltelijk aan de oxide-substraat overgang en interfereert met de rechstreekse opwaartse golf. Het faseverschil tussen de twee hangt af van de dikte van de begraven oxidelaag. De efficiëntie van de koppelaar zal het grootst zijn, wanneer er constructieve interferentie is tussen beide voorgenoemde golven. Als voorbeeld hebben we de efficiëntie uitgerekend van de structuur van figuur



Figuur 12: Berekende koppelefficiëntie naar vezel voor bijna vertikale koppeling en een optimaal uniform rooster. $\Lambda=630$ nm, $ed=70$ nm, $ff=0.5$, $N=20$,

12(b) als functie van de dikte van de begraven oxidelaag. De maximale efficiëntie is 55% voor een dikte van 900 nm of 1450 nm. Dit wordt getoond in figuur 13.

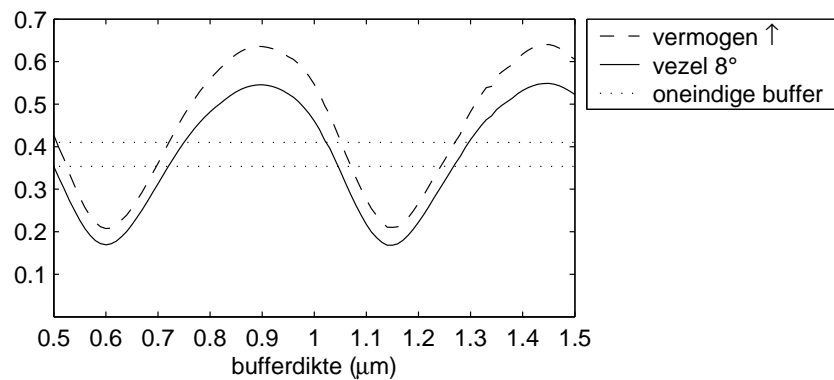
We hebben ook nog enkele andere gevallen bestudeerd, zoals de invloed van het brekingsindexcontrast. Hiervoor verwijzen we naar de Engelstalige tekst.

4.3 Koppelaar met reflectorrooster

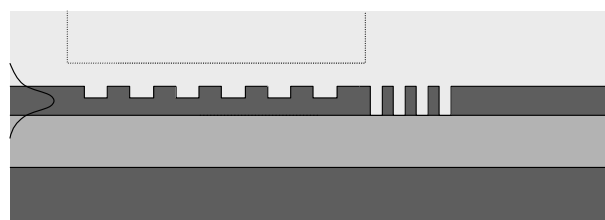
In het geval van exact vertikale koppeling is de efficiëntie altijd kleiner dan 50% voor een symmetrische structuur. Ook is er altijd een belangrijke tweede orde rooster reflectiepiek. Om dit te vermijden moet een asymmetrisch rooster gebruikt worden. Een optie is het gebruik van een tweede rooster, dat dienst doet als reflector. Dit tweede rooster bevindt zich na het eigenlijk koppelrooster (zie figuur 14). Bij een goed ontwerp kan ervoor gezorgd worden dat de reflectie aan het koppelrooster en de reflectie aan het reflectorrooster elkaar opheffen. Als gevolg is de reflectie aan de totale structuur heel laag.

De ontwerpprocedure voor deze structuur kan als volgt samengevat worden:

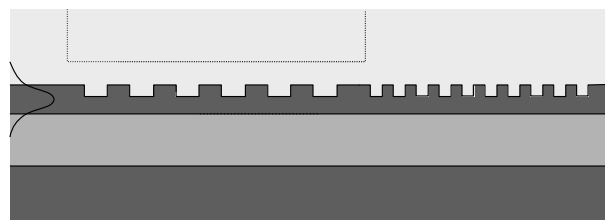
- ontwerp een koppelrooster voor vertikale koppeling dat voldoet aan $R = T^2$. Hierdoor zijn de eerste en tweede gereflecteerde golf even sterk en kunnen ze elkaar volledig opheffen.



Figuur 13: Efficiëntie i.f.v. oxidebufferdikte. De puntjeslijnen komen overeen met het vermogen en de efficiëntie voor een oneidige oxidebuffer. $\Lambda=630 \text{ nm}$, $ed=70 \text{ nm}$, $\lambda=1558 \text{ nm}$,



(a) met diepe reflector



(b) met ondiepe reflector (zelfde diepte als koppelaar)

Figuur 14: Roosterkoppelaar met reflectorrooster.

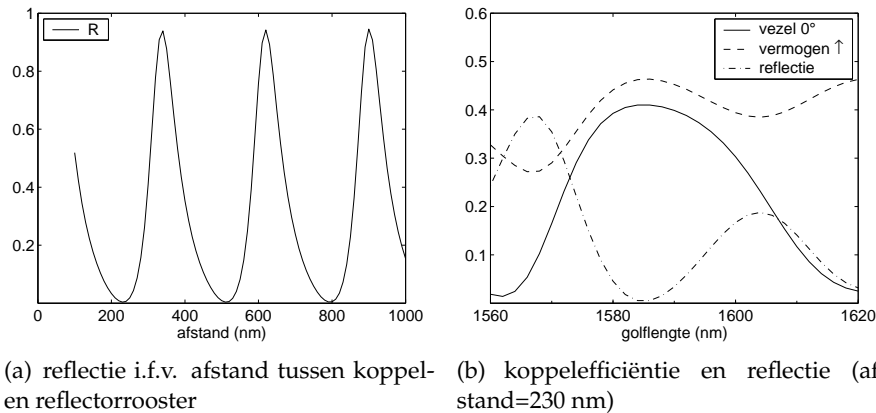
- Ontwerp een reflectorrooster met de gewenste etsdiepte en een hoge reflectie in het interessante golflengtegebied.
- Optimaliseer de afstand tussen beide roosters. We doen dit door de reflectie van de totale structuur te berekenen.
- Uiteindelijk kunnen we de efficiëntie van de koppelaar in functie van de golflengte berekenen. Ook de toleranties naar fabricagefouten toe kunnen uitgerekend worden.

We zullen dit nu toepassen om een koppelaar met een diepe reflector te ontwerpen. Het reflectorrooster heeft een periode van 340 nm en 50% vulfactor. Acht periodes zijn voldoende. De periode van het koppelrooster is 580 nm en de etsdiepte 40 nm. Deze etsdiepte is zodanig gekozen dat aan de vuistregel $R = T^2$ is voldaan. De enige parameter die nu nog moet gekozen worden is de afstand tussen de twee roosters. De reflectie aan de totale structuur in functie van deze afstand is berekend in figuur 15(a). De optimale afstand Δ is 230 nm (of $230 \text{ nm} + m\lambda/2$) en voor deze waarde is de reflectie kleiner dan 0.5%. De koppelefficiëntie naar vezel is berekend in figuur 15(b). De maximale efficiëntie is 41% en de 1 dB bandbreedte is 22 nm. Maar aan de rand van deze band is de reflectie al opgelopen tot 14%. Dit is meestal ongewenst. De reflectie is slechts kleiner dan 2% in een golflengtegebied van 6 nm breed. Voor $\lambda=1585 \text{ nm}$ is er geen reflectie en 46% van het licht wordt omhoog gestraald (en 53% naar beneden). De overlap met een Gaussiaan is 89%, wat resulteert in 41% koppelefficiëntie naar vezel. De gevoeligheid aan fabricagefouten wordt getoond in figuur 16. Een fout van 30 nm op de afstand tussen de twee roosters zorgt voor een kleine spectrale verschuiving, maar bijna geen reductie in koppelefficiëntie. Een fout van 10 nm op de etsdiepte resulteert in een kleine vermindering van de koppelefficiëntie en een golflengteverschuiving van 12 nm.

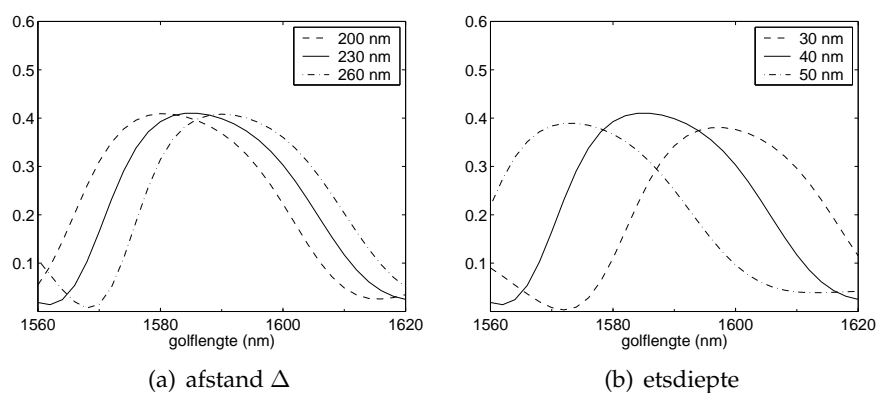
Een gelijkaardige structuur kan ontworpen worden met een reflectorrooster dat dezelfde etsdiepte heeft als het koppelrooster. De eigenschappen zijn gelijkaardig. Maar doordat het reflectierooster minder breedbandig is, is deze structuur gevoeliger aan fabricagefouten.

4.4 Bodemreflector

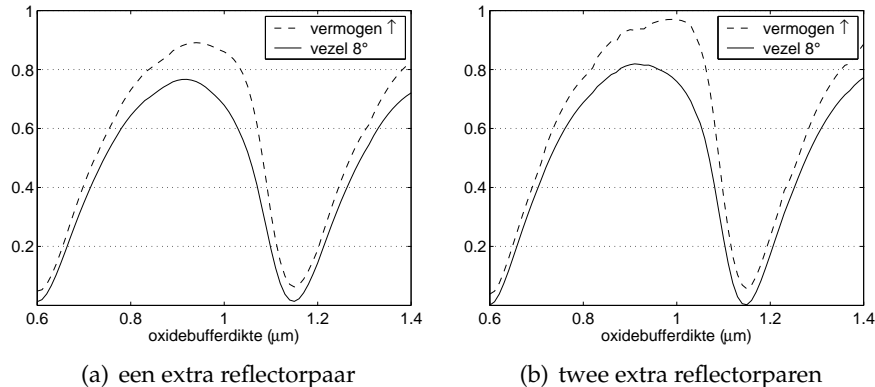
De efficiëntie wordt beperkt door koppeling naar beneden. Zelfs met een optimale dikte van de oxidelaag is de verhouding boven/beneden beperkt tot ongeveer 1.5. Een bodemreflector kan deze verhouding verbeteren en de efficiëntie van de koppelaar verhogen. Wij hebben



Figuur 15: Ontwerp van een koppelaar met diep reflectorrooster. 



Figuur 16: Efficiëntie van een koppelaar met diep reflectorrooster  : gevoeligheid aan fabricagefouten.



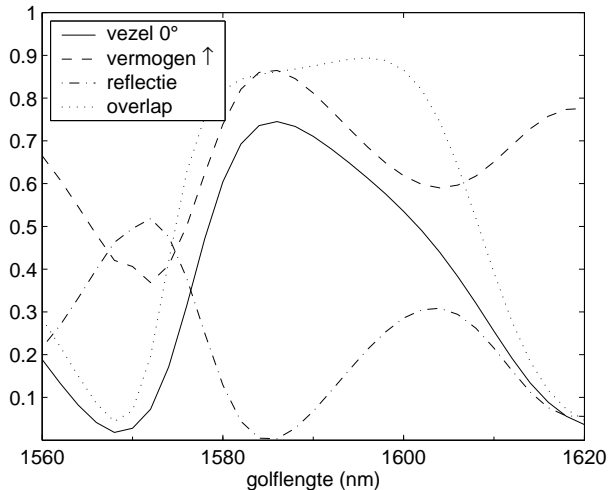
Figuur 17: Koppelefficiëntie i.f.v. de oxidebufferdikte. De koppelaar heeft een uniform rooster en een DBR-spiegel onder de golfgeleider. $\Lambda=630$ nm, $ed=70$ nm, $ff=0.5$, $\lambda=1566$ nm,

gekozen voor een silicium/oxide DBR spiegel. Dankzij het hoge brekingsindexcontrast is de reflectie breedbandig en zijn maar een paar lagen nodig. De efficiëntie van een koppelaar met een of twee bijkomende reflectorpallen wordt getoond in figuur 17. De maximale efficiëntie is 77% voor de structuur met een extra lagenpaar en 82% voor de structuur met twee extra paar. Zonder bijkomende bodemspiegel was de efficiëntie slechts 55% voor de optimale structuur.

4.5 Topreflector

In de vorige paragraaf werd een bodemreflector gebruikt om koppeling naar het substraat te vermijden en zo de efficiëntie te verhogen. Maar zulke bodemreflector maakt de fabricage moeilijker en SOI schijven met een bodemreflector zijn nog niet commercieel verkrijgbaar. De karakteristieken van een roosterkoppelaar kunnen ook gewijzigd worden door er lagen met verschillende brekingsindices bovenop te leggen. Op een conferentie werd verteld dat met een extra oxide en siliciumlaag de gerichtheid van de uitkoppeling kan verhoogd worden tot 95%.

We hebben uitgebreid onderzocht waarom dit werkt en onder welke omstandigheden dit werkt. Deze topspiegel zorgt ervoor dat het rooster zich in een caviteit bevindt. Deze caviteit wordt gevormd door de topspiegel enerzijds en de begraven oxidelaag van het SOI anderzijds. Als de afstanden goed gekozen worden kan inderdaad bijna alle ver-



Figuur 18: Efficiëntie van een koppelaar met reflectorrooster en topreflector.

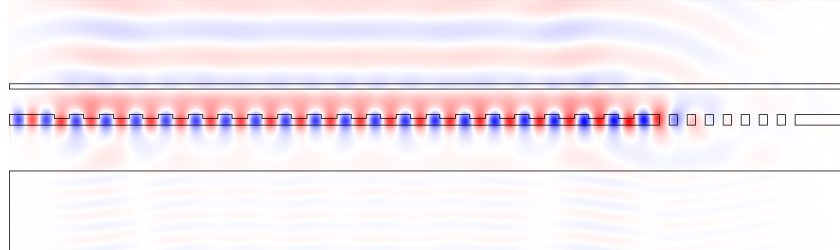
mogen naar boven uitgekoppeld worden. Voor de formules en berekeningen verwijzen we naar de Engelstalige tekst.

Deze topreflector lijkt zeer interessant omdat de efficiëntie sterk verhoogd kan worden zonder dat er een extra bodemreflector nodig is. Deze topreflector werkt echter slechts optimaal voor heel ondiepe roosters. Dit kan eenvoudig verklaard worden door de roostertanden te beschouwen als bronnetjes. Als een bron op een bepaalde plaats staat in de caviteit kan de fase van beide reflecties optimaal zijn. Wanneer zo'n bronnetje echter een kwartgolfelengte verplaatst wordt, zal alles naar beneden uitkoppelen in plaats van naar boven. Voor een diep rooster staan de bronnetjes allemaal op een verschillende plaats in de caviteit.

We hebben een topspiegel ontworpen voor de koppelaar met reflectorrooster. Door de geringe etsdiepte van 40 nm verwachten we dat de topspiegel goed zal werken. Het resultaat wordt getoond in figuur 18. De maximale efficiëntie is 74% voor $\lambda=1585$ nm. De structuur samen met een veldplot wordt getoond in figuur 19. De topspiegel heeft de efficiëntie verhoogd van 41% naar 74%

4.6 Gaussische bundel

Een roosterkoppelaar met een uniform rooster kan een maximale theoretische efficiëntie hebben van ongeveer 80% omdat de bundel een



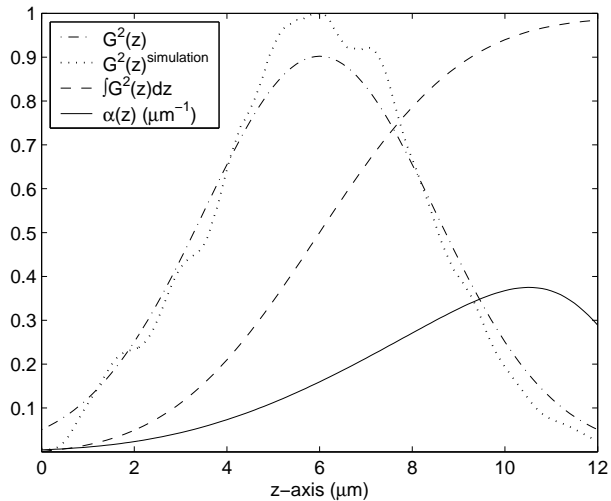
Figuur 19: Veldplot van een koppelaar met topreflector.

exponentieel dalend verloop heeft $P = P_0 \exp(-2\alpha z)$ in de z richting. 2α wordt de koppelsterkte van het rooster genoemd. Als het rooster niet uniform is, wordt α een functie van z en kan de bundel een andere vorm hebben. Om een Gaussische bundel te bekomen, wordt α gegeven door

$$2\alpha(z) = \frac{G^2(z)}{1 - \int_0^z G^2(t)dt}$$

waarbij $G(z)$ een genormaliseerd Gaussisch profiel is. Om deze z -afhankelijkheid van α te bekomen, kan zowel de vulfactor als de etsdiepte gevarieerd worden. In figuur 20 zijn $G^2(z)$ en de overeenkomstige theoretische α getekend voor een Gaussische bundel met een bundeldiameter van $10.4 \mu\text{m}$. De maximale α die nodig is, is $0.36 \mu\text{m}^{-1}$. Dit is veel hoger dan de optimale α voor een uniform rooster ($\alpha=0.13 \mu\text{m}^{-1}$). Bovenstaande formule is enkel correct voor zwakke roosters met een kleine α . Dit is niet het geval voor onze structuren. Daarom nemen wij de bovenstaande resultaten als een uitgangspunt voor een verdere numerieke optimalisatie van de roosterparameters.

We hebben een rooster ontworpen met een variërende vulfactor. Om de optimale roosterparameters te bepalen, hebben we een eenvoudig genetisch algoritme gebruikt. De details van de optimalisatie staan in de Engelstalige tekst, hier geven we enkel de resultaten. De efficiëntie als functie van golflengte staat afgebeeld in figuur 21. Voor de optimale SOI structuur is de koppeling naar vezel 63%. Met behulp van een bodemreflector kan dit verhoogd worden naar 95%. Deze structuur heeft een koppelverlies kleiner dan 1 dB in het golflengtegebied 1532-1567 nm. In dit gebied is de reflectie aan het rooster kleiner dan -24 dB. De etsdiepte is 120 nm en de smalste groefbreedte is slecht 30 nm. Door



Figuur 20: Gaussisch profiel en de overeenkomstige $\alpha(z)$.

een paar procent efficiëntie in te leveren, kan dit verhoogd worden naar 60 nm.

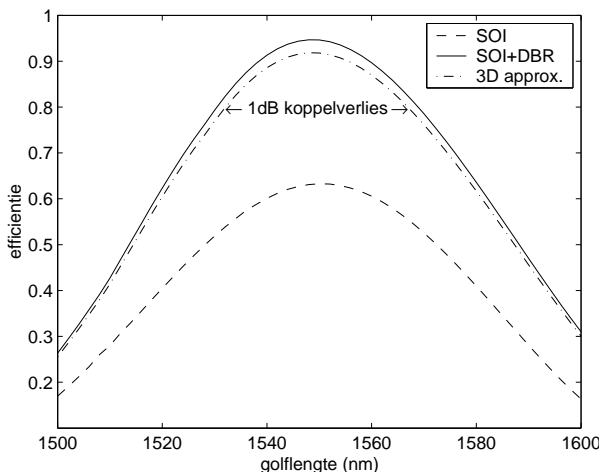
4.7 Samenvatting

Om hoofdstuk 4 af te ronden, geven we een overzicht van de belangrijkste resultaten. Deze samenvatting wordt gegeven in de vorm van overzichtelijke tabellen. We maken een onderscheid tussen vertikale koppeling (vezel 0°) en bijna vertikale koppeling (vezel 8°).

Vertikale koppeling

De resultaten voor vertikale koppeling zijn samengevat in de volgende tabel :

SOI rooster	efficiëntie	1 dB bandbreedte	reflectie
	21%	52 nm	24%
	41%	22 nm	0.5%
	50%	36 nm	3%



Figuur 21: Koppelefficiëntie naar vezel (8°) i.f.v. de golflengte voor SOI en SOI met een bodem DBR.

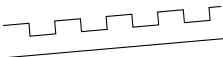
Een uniform rooster heeft de grootste bandbreedte, maar de kleinste efficiëntie. De reflectie rond de tweede orde Bragg golflengte is groot. De reflectie kan verkleind worden en de efficiëntie verhoogd door gebruik te maken van een koppelaar met bijkomend reflectorrooster. De hoogste efficiëntie wordt bereikt met een speciaal rooster met parallellogramvormige tanden. Maar dit rooster is heel moeilijk te fabriceren. De meest belovende structuur is de koppelaar met bijkomend reflectorrooster. De efficiëntie van die structuur kan verhoogd worden door een bodemspiegel of topspiegel te gebruiken :

	efficiëntie	zie ook
standaard SOI	41%	fig. 4.19
met bodem DBR (2 paar)	79%	fig. 4.24
met top spiegel	74%	fig. 4.29

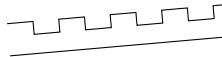
Voor deze structuur werkt de topspiegel goed, omdat de diepte van het rooster klein is.

Bijna vertikale koppeling

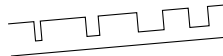
De resultaten voor bijna vertikale koppeling worden samengevat in de volgende tabel. De lagenstructuur is SOI met een optimale dikte voor het begraven oxide. Er wordt ook oxide als bovenlaag gebruikt.

rooster type	efficiëntie	1 dB bandbreedte	zie ook
	55%	43 nm	fig. 4.9
	63%	43 nm	fig. 4.33

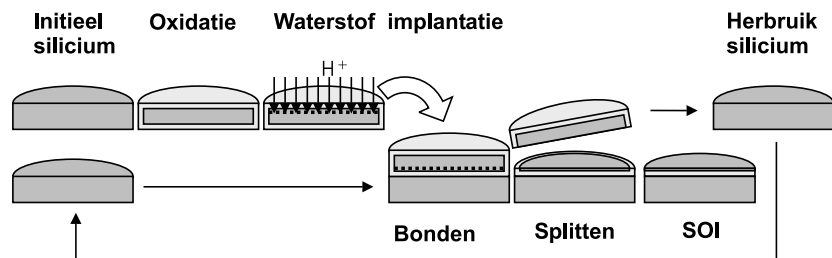
De efficiëntie van de koppelaar met een rooster met variërende vultfactor is hoger dan de efficiëntie van een uniform rooster. De reden is de betere overlap met een Gaussisch profiel. De bandbreedte is ongeveer dezelfde voor beide structuren. De volgende tabel toont het effect van de lagenstructuur op de koppelaar met uniform rooster.

	efficiëntie	zie ook
standaard SOI (1 μm oxide)	46%	fig. 4.8(b)
standaard SOI (1.45 μm oxide)	55%	fig. 4.9
met top spiegel	64%	fig. 4.28(b)
met bodem DBR (1 paar)	77%	fig. 4.23(a)
met bodem DBR (2 paar)	82%	fig. 4.23(b)

De laatste tabel vat de resultaten van de Gaussische bundel koppelaar met variërende vultfactor samen. In dit geval werkt de topspiegel niet goed wegens de relatief diepe ets.

	efficiëntie
standaard SOI	63%
met top spiegel	64%
met bodem DBR (2 paar)	95%

De getalwaarden die geciteerd werden zijn 2-D simulatieresulaten voor TE polarisatie.



Figuur 22: SmartCutTM proces om SOI schijven te fabriceren.

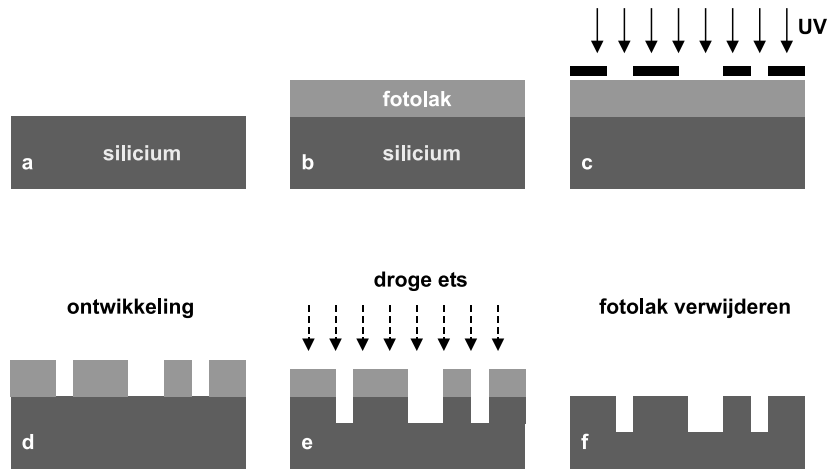
5. Fabricage

De fabricage van de roosters vereist geavanceerde halfgeleider productieprocessen omwille van de kleine afmetingen van de roostertanden. In dit hoofdstuk geven we een kort overzicht van de verschillende processen die nodig zijn en we bespreken de mogelijkheden en beperkingen. De fabricage werd uitgevoerd in samenwerking met andere universiteiten en onderzoeksinstellingen.

5.1 Substraat

We hebben SOI schijven gebruikt van de firma SOITEC. Deze schijven worden gefabriceerd met het gepatenteerde SmartCut proces. Dit proces is samengevat in figuur 22. Een silicium schijf wordt eerst thermisch geoxideerd om een oxidelaag te maken. Dan worden waterstofionen geïmplanteerd op een goed gecontroleerde diepte. Dit is de Smartcut. De schijf wordt ondersteboven gekeerd en gebond op een ander silicium schijf. Het substraat van de eerste schijf wordt nu verwijderd via de Smartcut. Uiteindelijk wordt de schijf nog gepolijst. Het resulterende SOI is van zeer hoge kwaliteit en laat lage propagatieverliezen toe voor golflengtes in het telecomspectrum. We hebben SOI gebruikt met 220 nm silicium op een 1000 nm dikke oxidelaag. Deze laag is dik genoeg om lekverliezen naar het substraat te vermijden, althans voor TE polarisatie. Dit proces werd ontwikkeld voor gebruik in de micro-elektronica industrie, maar daar zijn de lagen veel dunner.

Hetzelfde proces kan gebruikt worden om SOI schijven met meerdere oxidelagen te maken. Door het proces te herhalen met een SOI schijf in plaats van een silicium schijf, kan een schijf met twee oxidelagen gefabriceerd worden. Zulk SOIOSOI materiaal is zeer interessant voor roost-



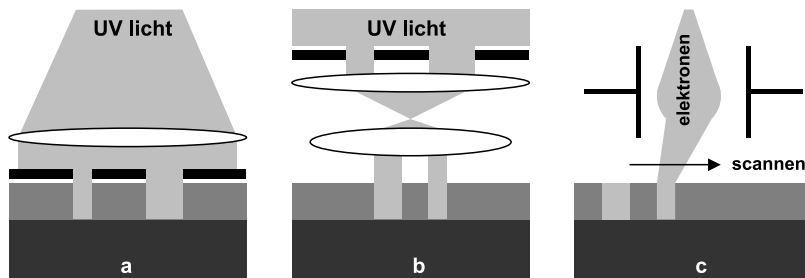
Figuur 23: Algemeen processchema: a) schijf kuisen, b) fotolak spinnen en bakken, c) belichting met masker, d) ontwikkeling fotolak e) droog etsproces om het patroon in silicium aan te brengen , f) fotolak verwijderen

erkoppelaars, maar deze schijven zijn nog niet commercieel verkrijgbaar.

5.2 Patroondefinitie

Verschillende technieken kunnen gebruikt worden patronen te definiëren, maar het proces schema is altijd gelijkaardig. Een algemeen proces-schema wordt getoond in figuur 23. De schijf wordt eerst gekuis en een fotogevoelige lak laag wordt aangebracht. Na spinnen en bakken is deze laklaag hard en klaar om belicht te worden. Tijdens de belichting wordt het patroon aangebracht in de laklaag. De belichte delen van de lak worden tijdens de ontwikkeling verwijderd. Deze lak wordt als een etsmasker gebruikt om het patroon in het silicium te etsen.

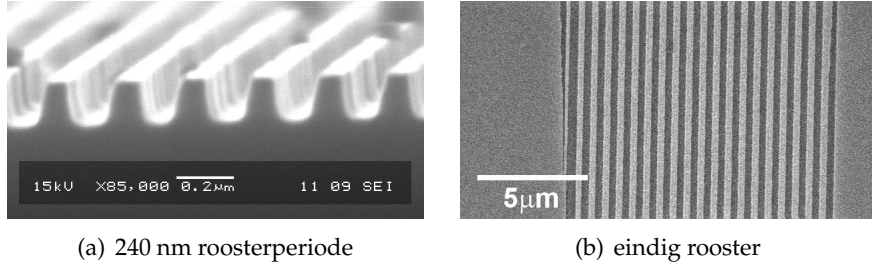
Optisch lithografie maakt gebruik van UV licht en een fotomasker om de laklaag te belichten. Elektronenbundellithografie gebruikt een scannende gefocusseerde elektronenbundel om het patroon in een laklaag te schrijven. We kunnen twee types optische lithografie onderscheiden : contact lithografie en projectie lithografie. In contact lithografie wordt het masker direct in contact gebracht met de laklaag. Deze methode wordt enkel gebruikt voor onderzoeksdoeleinden. Voor productiedoelen wordt projectie lithografie gebruikt. Het patroon van het fotomasker wordt met behulp van een lenssysteem op de laklaag



Figuur 24: Overzicht van verschillende lithografie processen : a) Optische contact lithografie, b) Optische projectie lithografie, c) Elektronenbundellithografie.

geprojecteerd. Deze projectie reduceert de afmetingen met een factor 4 of 5 en hetzelfde patroon wordt vele malen op een schijf herhaald. De resolutie die kan bereikt worden hangt af van heel wat factoren. De belangrijkste beperking wordt opgelegd door de golflengte van het gebruikte licht. Het systeem dat in INTEC gebruikt wordt kan lijn-breedtes definiëren tot $0.8 \mu\text{m}$. Dit is onvoldoende voor onze roosters. IMEC Leuven heeft toestellen die werken met een golflengte van 248 nm. Omwille van de zeer korte golflengte wordt deze techniek diep UV genoemd. 248 nm en 193 nm diep UV lithografie worden reeds gebruikt voor de productie van microprocessoren. Wij hebben 248 nm diep UV gebruikt voor de fabricage van roosters. De kleinste periode die kan gedefinieerd worden, is ongeveer 400 nm. De kleinste afmeting hangt niet alleen af van de golflengte, maar ook van de NA van het lenssysteem, de dikte van de laklaag, de belichtingscondities en enkele andere parameters. Voor details verwijzen we naar de literatuur. Alhoewel diep UV de techniek is voor massaproductie, is het minder geschikt voor onderzoeksdoeleinden omdat het heel heel duur is.

Elektronenbundellithografie is beter geschikt voor onderzoek. Omdat de bundel gescand wordt over het oppervlak is er geen masker nodig, het is een rechtstreekse schrijftechniek. De spotgrootte van de bundel kan enkele nanometers klein zijn. Het is de meest populaire techniek voor de fabricage van nanofotonische structuren voor onderzoeksdoeleinden. Deze techniek is niet beschikbaar in Gent, maar dankzij samenwerking in het kader van het IST-PICCO project kon deze techniek toch gebruikt worden. Structuren werden gefabriceerd in samenwerking met de universiteit van Glasgow, St.-Andrews en het on-



Figuur 25: Structuren gemaakt met holografie.

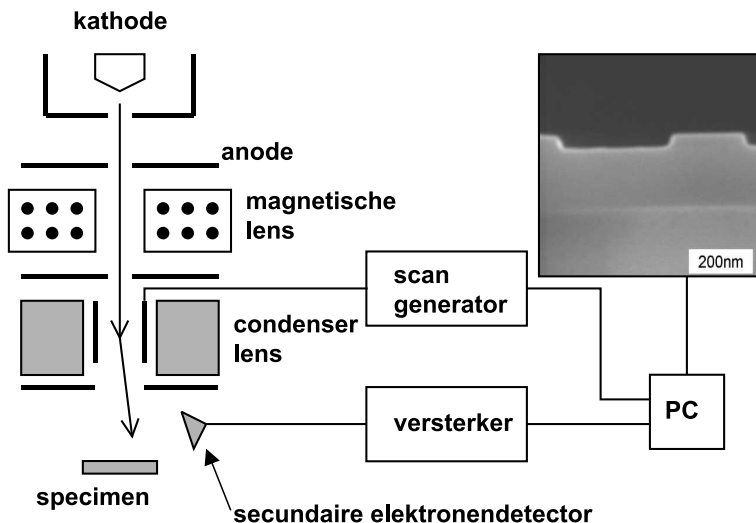
derzoekscentrum COM van de Deense technische universiteit. Ondanks de hoge resolutie is elektronenbundellithografie niet geschikt voor massaproductie omdat het een zeer trage techniek is.

Nog een andere techniek om roosters te definiëren is holografie. Holografie maakt gebruik van twee interfererende laserbundels om een periodieke structuur te definiëren. In INTEC is een holografie opstelling die gebruikt maakt van een Argon-laser beschikbaar. De kleinste periode die kan bereikt worden is ongeveer 240 nm. Deze techniek is echter weinig flexibel, enkel periodieke structuren kunnen gedefinieerd worden. We hebben dit proces uitgebreid om roosters met een beperkte oppervlakte te kunnen maken. De details van de opstelling worden beschreven in de Engelstalige tekst. Enkele voorbeelden van roosters zijn te zien in figuur 25.

Om het patroon van de laklaag over te brengen in het silicium wordt een etsproces gebruikt. Omwille van de kleine afmetingen van de structuren is een droog etsproces nodig. Een droog etsproces maakt gebruik van reactieve ionen in een plasma. Voor onze roosters is het belangrijk dat de etsdiepte nauwkeurig kan gecontroleerd worden en uniform is.

5.3 Karakterisatie

Door de kleine afmetingen van de roostertanden is het niet mogelijk om deze met een optische microscoop te zien. Het meest gebruikte instrument voor de karakterisatie is de elektronenmicroscoop of SEM. In een SEM wordt een elektronenbundel over een specimen gescand. Wanneer de elektronen op het specimen invallen worden secundaire elektronen gegenereerd. Deze secundaire elektronen worden gedetecteerd, synchroon met de scannende bundel. Omdat het aantal en de richting van deze verstrooide elektronen afhangt van de topografie en mate-



Figuur 26: Schema van een scannende elektronenmicroscoop.

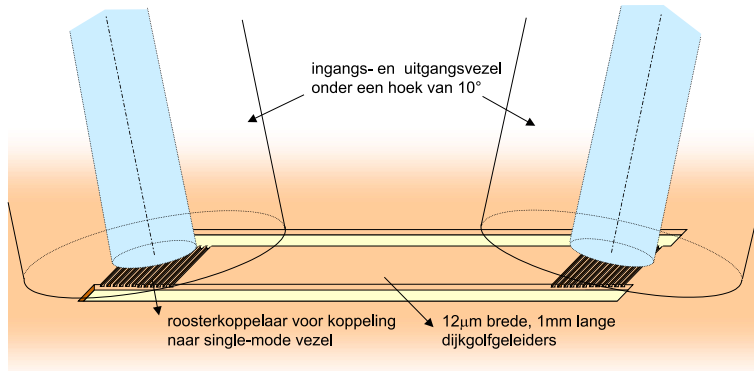
riaal van het specimen, kan een beeld gemaakt worden op basis van de intensiteit van het gedetecteerde signaal. De resolutie is typisch een paar nanometer, maar het bekijken van submicrometer structuren vereist geschikte specimen en een ervaren operator.

Om de etsdiepte te kunnen inspecteren met een SEM, moet het specimen gekliefd worden doorheen de roosters. Dat is moeilijk als de roosters maar $12 \mu\text{m}$ breed zijn en kliven is ook een destructief proces. Een andere techniek die kan gebruikt worden om de etsdiepte op te meten is de AFM of atoomkrachtmicroscoop. AFM maakt gebruik van een naald die over het specimen scant en kan gebruikt worden om de etsdiepte via de top op te meten.

5.4 Verpakking

De verpakking van de componenten is een belangrijk deel van de kostprijs van fotonische componenten. Onder verpakking verstaan we het aanbrengen van de optische vezels en eventueel hermetisch afsluiten van de componenten. Omdat roosterkoppelaars via de top inkoppelen is het niet nodig om de facetten van de chip te polijsten, zoals het geval is bij inkoppeling via de rand van de chip. De alignatie van de vezel ten opzichte van de koppelaar is relatief tolerant aan afwijkingen omdat er geen lenzen gebruikt worden.

Om veel vezels aan een chip te koppelen, wordt gebruik gemaakt van vezelrijen. De vezeluiteinden bevinden zich in silicium V-groeven, waardoor de positie van de vezels ten opzichte van elkaar zeer nauwkeurig is. De afstand tussen het centrum van twee vezels is typisch $250 \mu\text{m}$ en de absolute afwijking op de positie van het centrum van de vezels is kleiner dan $1 \mu\text{m}$ in commercieel verkrijgbare vezelrijen. Om deze vezelrijen aan de chip te bevestigen wordt lijm gebruikt die met UV licht uitgehard wordt. Deze lijm heeft een brekingsindex die ongeveer gelijk is aan de brekingsindex van de vezel. Het eindfacet van de vezelrij kan vlak zijn of onder een bepaalde hoek gepolijst.



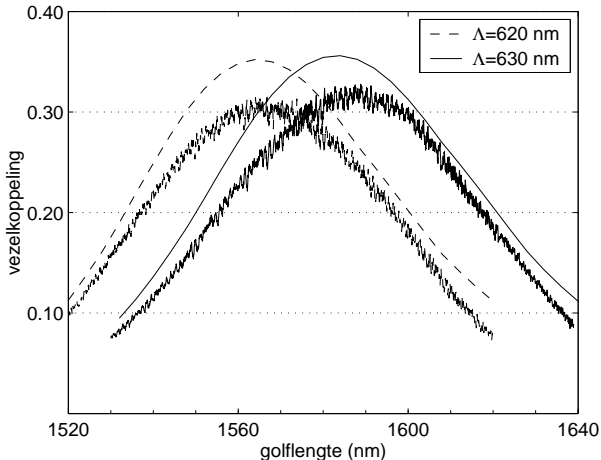
Figuur 27: Meetopstelling om de koppelefficiëntie van de roosterkoppelaars te meten. De ingangsvezel is verbonden met een afstembare laser en de uitgangsvezel met een vermogenmeter.

6. Metingen

6.1 Meetopstelling

In een conventionele meetopstelling om geïntegreerde golfgeleiders te karakteriseren wordt licht aan de randen van de chip in- en uitgekoppeld. In deze opstelling bevinden alle vezels zich in hetzelfde vlak en kan een microscoop boven de opstelling geplaatst worden om te helpen bij de alignatie. We hebben de opstelling aangepast om licht te kunnen inkoppelen van bovenuit.

De meetopstelling is schematisch weergegeven in figuur 27. De in- en uitvoervezel zijn gemonteerd op precisie translatietafels. Met behulp van speciale adapterplaatjes zijn de vezels gemonteerd onder een hoek van 10 graden ten opzichte van de oppervlaktenormaal. De invoervezel is verbonden met een afstembare laser met een afstembereik van 1500-1640 nm. De uitvoervezel is verbonden met een optische vermogenmeter om de vermogentransmissie te meten. Omdat we via de top inkoppelen is het niet mogelijk een microscoop boven de opstelling te plaatsen. We gebruiken een camera met microscopobjectief en een vezellamp om het specimen te belichten. De camera is gemonteerd onder een hoek van 30 graden en de objectieflens heeft een vergroting van 10 \times , dit laat toe om de structuren op het specimen en de vezels met voldoend hoge resolutie te bekijken.



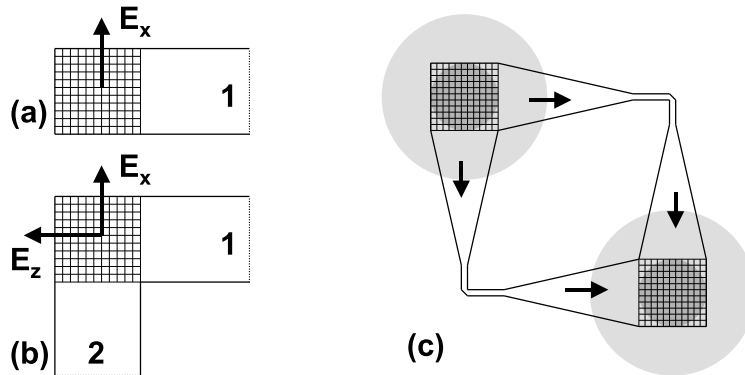
Figuur 28: Meetresultaat van de koppelefficiëntie i.f.v. golfleugte.

6.2 Meetresultaten

We meten de transmissie op een structuur met een roosterkoppelaar aan beide uiteinden. De efficiëntie van een roosterkoppelaar kan makkelijk afgeleid worden uit deze transmissie, omdat in- en uitkoppeling identiek zijn. De optimale parameters voor een uniform rooster werden voorgesteld in figuur 12(a). De etsdiepte van de gefabriceerde structuren is 55 nm in plaats van 70 nm. Hierdoor is de theoretische efficiëntie een paar procent lager. Maar de parameters van de gefabriceerde roosters liggen dicht bij de optimale parameters.

De opgemeten efficiëntie is 33% of -4.8 dB. De 1 dB bandbreedte is ongeveer 40 nm. De efficiëntie als functie van golfleugte wordt getoond in figuur 28. De streeppjeslijn komt overeen met een roosterperiode van 620 nm en de volle lijn met 630 nm. De overeenkomstige theoretische curves zijn ook getekend in figuur 28.

Een andere belangrijke eigenschap van de koppelaars zijn de alignatietoleranties. We hebben het koppelverlies opgemeten als functie van de horizontale positie van de vezel. Een alignatiefout van $\pm 1 \mu\text{m}$ resulteert in minder dan 0.5 dB bijkomend koppelverlies. Dit komt overeen met de theoretische verwachtingen. We hebben ook nog de uniformiteit opgemeten van koppelaars verspreid over de schijf silicium. Ook werd een vezel aan het specimen gelijmd met brekingsindextaangepaste lijm. Tenslotte werden de koppelaars ook gebruikt om andere nanofotonische componenten te karakteriseren.



Figuur 29: Bovenaanzicht van (a) 2-D roosterkoppelaar, (b) 2-D roosterkoppelaar gebruikt als polarisatiesplitter (c) ingangs- en uitgangskoppelaar gebruikt in een polarisatiediversiteit configuratie.

7. 2-D koppelaar en polarisatiesplitter

7.1 Introductie

Een 2-D rooster is periodiek in twee richtingen. Deze roosters worden ook gekruiste of bi-periodieke roosters genoemd. Een voorbeeld van een 2-D rooster is een vierkante matrix van gaatjes. 2-D roosters zijn interessant omwille van de polarisatie-eigenschappen. In dit hoofdstuk bespreken we golfgeleider-roosterkoppelaars gebaseerd op 2-D roosters. Deze structuren worden gebruikt als polarisatiesplitter in een speciale configuratie.

Een single-mode optische vezel heeft (bij benadering) twee orthogonale lineair gepolariseerde moden. Licht in de vezel bevindt zich in een elliptische polarisatietoestand. En deze polarisatietoestand wijzigt tijdens de propagatie doorheen de vezel. Zelfs als lineair gepolariseerd licht ingekoppeld wordt zal er aan de andere kant van de vezel niet noodzakelijk lineair gepolariseerd licht uitkomen.

Beschouwen we nu een golfgeleider met een roosterkoppelaar die bestaat uit een 2-D rooster, geëtst in een dijkgolfgeleider (figuur 29(a)). De koppeling van vezel naar golfgeleider is polarisatie-afhankelijk in het algemeen. Voor de golfgeleider-roosters die wij gebruiken, is de efficiëntie voor TE veel groter dan voor TM. De koppeling van vezel naar golfgeleider zal maximaal zijn als het inkomend licht lineair gepolariseerd is volgens E_x . De structuur van figuur 29(b) bestaat uit 2 dijkgolfgeleiders die loodrecht op elkaar staan. Het 2-D rooster is geëtst in

de intersectie van de 2 golfgeleiders. Licht komende van een vertikale vezel met polarisatie E_x zal koppelen naar golfgeleider 1 en de andere polarisatie met elektrisch veld E_z naar golfgeleider 2. In het algemeen zal elliptisch gepolariseerd licht zowel naar golfgeleider 1 en golfgeleider 2 koppelen. De koppelverhouding zal afhangen van de polarisatietoestand van het licht. Maar de totale koppeling naar beide golfgeleiders samen zal onafhankelijk zijn van de polarisatie. We hebben dit werkingsprincipe beschreven als uitkoppelaar maar het werkt ook als inkoppelaar.

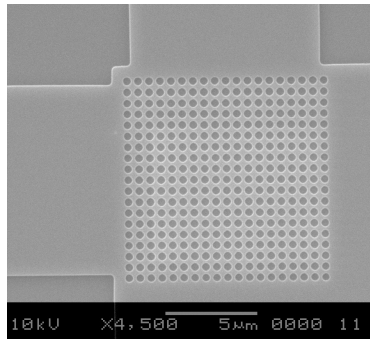
De koppelaar-splitter kan gebruikt worden als ingangs- en uitgangskoppelaar in een polarisatiediversiteit configuratie. Een heel eenvoudig voorbeeld wordt getoond in figuur 29(c). De transmissie van ingangsvezel naar uitgangsvezel is onafhankelijk van de polarisatietoestand van het inkomende licht, hoewel de golfgeleiders die in het circuit gebruikt worden wel polarisatiegevoelig zijn. De maatstaven om de performantie van deze structuur te beoordelen zijn het invoegverlies en het polarisatie-afhankelijk verlies of PDL (polarization dependent loss). De PDL wordt gedefinieerd als $10\log_{10}(P_{max}/P_{min})$ wanneer de polarisatie alle mogelijke toestanden aanneemt.

We weten uit de vorige hoofdstukken dat het heel moeilijk is om een rooster te maken voor vertikale koppeling dat weinig reflecteert. Een oplossing voor die reflectie is gebruik maken van bijna vertikale koppeling. De hierboven beschreven polarisatiesplitter structuur kan ook werken voor een lichte afwijking van de vertikale richting. De situatie wordt echter een heel stuk complexer. Onder andere is het nodig om de golfgeleiders ook te roteren. Voor een meer gedetailleerde studie van deze situatie verwijzen we naar de Engelstalige tekst.

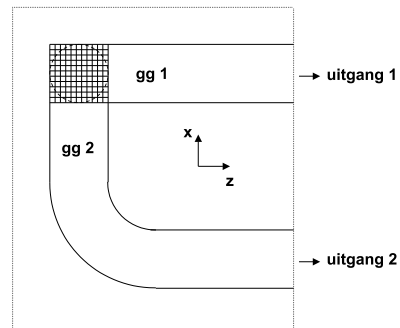
7.2 Experimentele resultaten

Polarisatiesplitter

De polarisatiesplitter die hier voorgesteld wordt, is gefabriceerd met behulp van elektronenbundellithografie. Het rooster is een vierkante matrix van ronde gaatjes met een periode van 580 nm. De diameter van de gaten is ongeveer 300 nm. Een SEM bovenaanzicht van het rooster is te zien in figuur 30(a). De breedte van de dijkgolfgeleiders is 10 μm . In een van de golfgeleiders is een 90 graden bocht geplaatst om beide uitgangen te kunnen detecteren aan hetzelfde facet van de chip. We hebben de structuur van figuur 30(b) gebruikt om de uitdovingsverhouding te meten. Een vertikale single-mode vezel koppelt licht



(a) SEM bovenaanzicht



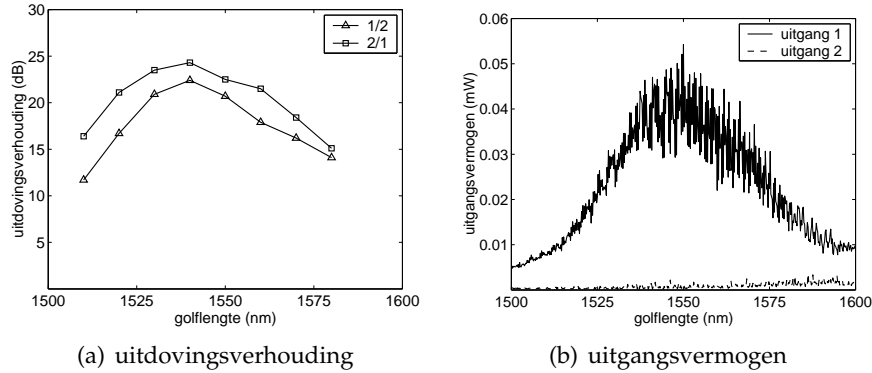
(b) splitter met bocht

Figuur 30: Polarisatiesplitter teststructuren.

van een afstembare laser in de golfgeleiders in via het rooster. We detecteren het uitgangsvermogen van golfgeleiders een en twee aan een gekliefd facet met behulp van een $40\times$ objectief en een vermogendetector.

De alignatie van de vezel is belangrijk omdat de opstelling symmetrisch moet zijn voor optimale performantie. Om zeker te zijn dat het centrum van de vezel zich centraal boven het rooster bevindt, wordt de x -positie geoptimaliseerd met behulp van uitgang 1 en de z -positie met behulp van uitgang 2. Na de alignatie wordt de positie van de vezel vastgehouden, enkel de polarisatie en de golflengte worden nog gewijzigd tijdens de meting. De polarisatie van het ingangslicht wordt veranderd om uitgang 1 of uitgang 2 te maximaliseren. Daarna meten we de uitdovingsverhouding op voor beide gevallen. Deze verhouding wordt getoond in figuur 31(a) voor verschillende golflengtes. De uitdovingsverhouding is groter dan 18 dB in het golflengtegebied 1530-1560 nm. Het verschil tussen de twee curves wordt veroorzaakt door verliezen in de bocht.

Het uitgangsvermogen in functie van de golflengte voor het geval waarin uitgang 1 maximaal is, wordt getoond in figuur 31(b). De oscillaties in deze curve worden veroorzaakt door een caviteit tussen het rooster (tweede orde reflectie) en het facet. De opgemeten vermogen-transmissie bedraagt slechts 5%. Een oorzaak van deze lage waarde is de slechte kwaliteit van het gekliefde facet. Zoals reeds vermeld is het moeilijk om een goed facet te klieven in silicium. Indien het facet perfect was, zou het opgemeten vermogen hoger geweest zijn, en de Fabry-Pérot franjes sterker.



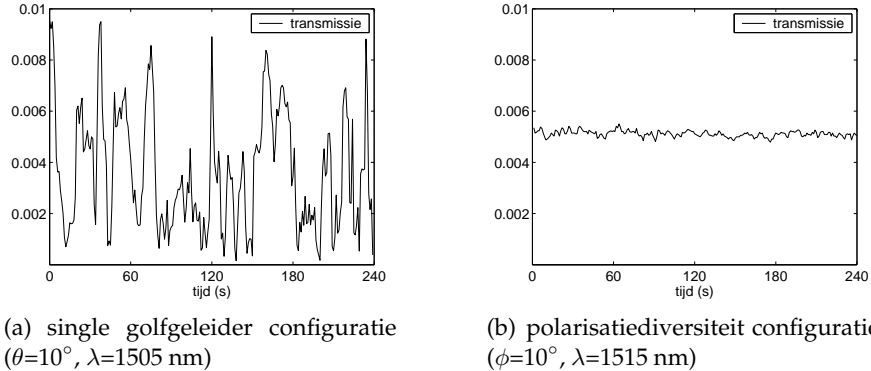
Figuur 31: Meetresultaten van een polarisatiesplitter.

Polarisatiediversiteit configuratie

We hebben ook enkele structuren opgemeten in een polarisatiediversiteit configuratie (figuur 29(c)). Een 2-D rooster wordt gebruikt als ingangs- en uitgangskoppelaar en we meten de vermogentransmissie. Tijdens de meting wordt de polarisatietoestand van het ingangslicht gewijzigd. Voor een perfecte structuur zou de transmissie onafhankelijk moeten zijn van de polarisatie. In een echte structuur zal het vermogen een beetje veranderen als functie van de polarisatie. Op deze manier kunnen we de PDL opmeten.

Het gebruikte rooster bestaat uit een vierkante matrix van ronde gaatjes. De roosterperiode is 580 nm en etsdiepte ongeveer 50 nm. De diameter van de gaten is 380 nm. Deze etsdiepte is niet optimaal, maar de gatgrootte is wel optimaal voor de gegeven etsdiepte.

In figuur 32(a) wordt de transmissie getoond voor een golfgeleider met een 2-D rooster aan beide uiteinden. Door veranderen van de polarisatie schommelt het vermogen zeer sterk, het valt zelfs tot bijna nul terug. Wanneer we een polarisatiediversiteit configuratie gebruiken dan is de transmissie bijna onafhankelijk geworden van de polarisatie (figuur 32(b)). De PDL is ongeveer 0.6 dB in dit geval. Hoewel we het principe experimenteel aangetoond hebben, zijn de gebruikte structuren verre van ideaal. Het invoegverlies is zeer groot. Dit is gedeeltelijk te wijten aan het nog niet optimale ontwerp. Voorstellen om de performantie te verbeteren zijn voorgesteld in Engelstalige tekst. Er is ook nog bijkomend onderzoek nodig om te bepalen wat de ultieme performantie van de voorgestelde structuren kan zijn.



Figuur 32: Opgemeten transmissie als functie van de polarisatie. De polarisatie van het ingangslicht wordt willekeurig veranderd gedurende de meting.

8. Besluit en toekomstperspectieven

Tenslotte vatten we de belangrijkste verwijzingen en conclusies samen. Het centrale thema van dit werk is de koppeling tussen optische vezels en nanofotonische geïntegreerde circuits. We zijn begonnen met een literatuuroverzicht te geven van de state-of-the-art oplossingen voor het koppelprobleem. Het concept van een heel compact rooster dat kan gebruikt worden om rechtstreeks naar een vezel te koppelen werd geïntroduceerd en vergeleken met bestaande roosterkoppelaars. De korte koppellengte van onze roosters resulteert in een grotere bandbreedte en een gemakkelijke koppelmethode. Mogelijke toepassingen zijn optische interconnecties, communicatielinks en sensoren.

In hoofdstuk 4 hebben we uitgebreid de eigenschappen van deze roosterkoppelaars bestudeerd. We hebben een aantal ontwerpen voorgesteld die een hoge efficiëntie met een relatief grote bandbreedte combineren. De belangrijkste beperking van de efficiëntie komt van de koppeling naar het substraat. Een goede keuze van de dikte van het begraven oxide is belangrijk. Maar om een heel klein koppelverlies ($<1 \text{ dB}$) te bekomen, is een bijkomende bodem- of topspiegel nodig.

We hebben experimenteel de koppeling aangetoond tussen single-mode vezels en sub-micrometer SOI golfgeleiders met behulp van compacte roosterkoppelaars. De hoogste opgemeten efficiëntie was 33% voor een uniform rooster en de eigenschappen komen goed overeen met de simulatieresultaten. De efficiëntie kan verhoogd worden door een geoptimaliseerd roosterontwerp en lagenstructuur te gebruiken.

De geoptimaliseerde structuren zijn redelijk moeilijk om te fabriceren, omdat een zeer goede controle van de etsdiepte noodzakelijk is. Bovendien zorgt de variatie op de dikte van de top siliciumlaag voor kleinere toelaatbare fouten op de etsdiepte.

Om het polarisatie-afhankelijkheidsprobleem van SOI fotonische ICs op te lossen hebben we een geïntegreerde polarisatiediversiteit configuratie onderzocht, gebaseerd op 2-D roosters. Het principe van de 2-D roosterkoppelaar als polarisatiesplitter werd experimenteel aange- toond. Ook hebben we polarisatie-onafhankelijke transmissie doorheen een heel eenvoudig polarisatiediversiteit circuit gedemonstreerd. Maar de performantie, in het bijzonder het invoegverlies, van de huidige structuren is niet goed genoeg voor praktische toepassingen. We hebben mogelijke verbeteringen voorgesteld, maar een optimalisatie van het ontwerp en een experimentele demonstratie ervan vergen verder onderzoek.

Het zou nuttig kunnen zijn om in de toekomst enkele van de behandelde onderwerpen verder te onderzoeken. Hierbij denken we in de eerste plaats aan de fabricage van de geoptimaliseerde 1-D rooster- ontwerpen en aan een optimalisatie van de 2-D roosters.

English text

Chapter 1

Introduction

In this work we will present grating couplers for coupling between optical fibres and nanophotonic waveguides. Before we discuss the theory and experiments, we will explain the research context and the possible applications. We start with a short introduction on optical communication and photonic integrated circuits. Afterwards the evolution towards nanophotonics and the related coupling problem are introduced.

1.1 Research context

Today it is difficult to imagine a world without telecommunication. The internet makes it possible to access information from everywhere and to communicate with people anywhere in the world. One of the key elements in the network are the optical fibres that transport the massive amounts of data all over the planet. The exponential growth of the internet would have been impossible without the tremendous progress made in optical communication in the past decades. But there is still room for improvement and optical communication is still a very active research field, in spite of the economical troubles in the telecom business in the past years.

The optical fibres are used to transport information in the form of light from point A to point B. In the network nodes, the light signals are converted to electrical signals. The routing and signal processing is performed electrically, and the electrical signal is converted back into light and sent on the next fibre. These opto-electronic conversions limit the further growth of the network. Therefore, all-optical signal process-

ing is a hot research topic. Opto-electronics is also called photonics, because it deals with the manipulation of light or photons.

Although the backbone networks use almost exclusively optical fibre, the last kilometres of the access network to the home-user are still copper wire. One reason is the cost of the replacement of the wires, but also the photonic equipment needed at the end of the optical fibre is too expensive to bring the fibre to the home.

A typical photonic component is a wavelength multiplexer. This component combines many different wavelengths into one fibre. Each of the wavelengths carries a high-bitrate (e.g. 10 Gbit/s) signal. Thanks to this wavelength division multiplexing, the transport capacity of the fibre is much higher than the bitrate in one channel, which is limited by the electronics. For example, if 64 channels are used, each modulated at 10 Gbit/s, the fibre can transport a massive 640 Gbit/s. At the other end of the fibre, a wavelength demultiplexer is used to split all these channels.

The key to making more advanced and cheaper photonic components is the integration of these photonic components on a single chip. This integration may make it possible to replace the large racks of equipment used in network nodes today by a few chips. When the photonic components are integrated on chip, we talk about photonic integrated circuits¹ or photonic ICs.

1.2 Waveguides and photonic integrated circuits

An optical waveguide is a structure that can confine light within a certain area and transport it. In most waveguides light is trapped in a core, which has a higher refractive index than the surrounding cladding. An optical fibre is a kind of waveguide. Most optical waveguides used in communications are single-mode, they support only one guided mode (for each polarization).

Different types of optical waveguides are shown in figure 1.1. An optical fibre is made of glass and the index contrast between the core and the cladding is typically 0.3%. The diameter of the core is approximately 9 μm . Waveguides in photonic ICs can be fabricated in a variety of materials. Doped silica waveguides have a typical index contrast of around 1% and the mode size is similar to that of an optical

¹Another commonly used name is planar lightwave circuit or PLC. We prefer the name photonic integrated circuits because it sounds similar to an electronic IC.

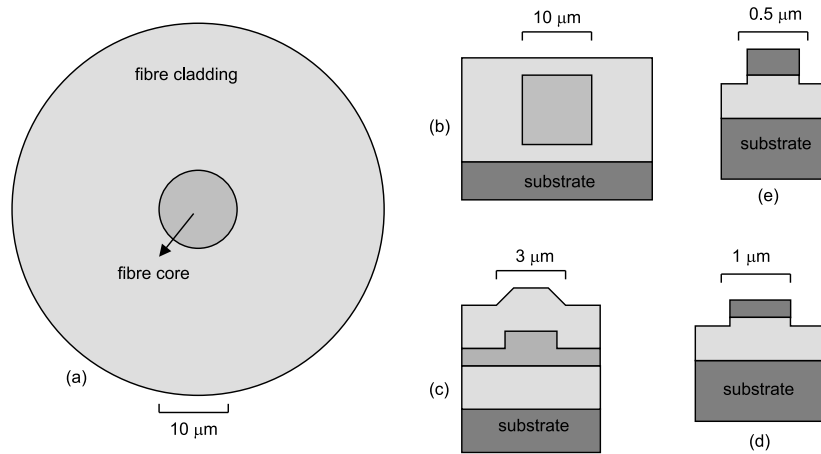


Figure 1.1: Cross-sections of different types of optical waveguides. A darker colour represents a higher refractive index. (a) fibre, (b) doped silica, (c) silicon oxynitride, (d) silicon nitride, (e) silicon-on-insulator

fibre. Because the silica is located on a Silicon carrier substrate, this technology is also called silica on Silicon. The best performing photonic ICs currently use silica waveguides. Waveguide demultiplexers in silica are commercially available products today, but these silica ICs are very large. For example, a 16×16 switching matrix in silica measures $10 \times 10 \text{ cm}^2$ [1]. The main reason for the large size is the low refractive index contrast. This results in a large bend radius [2] and as a consequence large structures.

Silicon oxynitride (SiON) waveguides [3] have an index contrast of about 5%. This can be increased to 50% by using silicon nitride as the waveguide core material [4]. As a result the same functionality can be integrated on a smaller chip. Silicon-on-insulator (SOI) has a very high contrast of approximately 3.5 to 1.5. SOI consists of a thin Si core layer on top a SiO_2 cladding on top of a Si substrate. If the index contrast is higher, the size of the waveguides has to be smaller to be single-mode. Typical dimensions of an SOI waveguide are $200 \times 450 \text{ nm}^2$. Therefore we will call them nanophotonic waveguides.

Although we have only discussed Si based waveguides, photonic ICs can also be made in compound semiconductor materials such as InP [5]. InP has the advantage that active components such as lasers and amplifiers can also be integrated. Silicon is known as a very bad light emitter because of its indirect bandgap. But recently efficient light

emission in Si has been demonstrated [6]. Other alternatives are doping Silicon with rare-earth metal ions or putting InP based lasers on top of a passive Silicon photonic IC. The latter is called heterogenous integration. Silicon is also better suited for mass production. We will focus on SOI waveguides. Possible applications of SOI photonic integrated circuits are not only telecom, but also optical interconnects and sensors.

1.2.1 Nanophotonics

Nanophotonic waveguides will make it possible to integrate a lot of functions on one chip. However, the small dimensions also create a lot of problems. The problem that we will address is the coupling of light between a nanophotonic waveguide and an optical fibre or in other words the interface between the nanophotonic waveguide and the outside world.

1.2.2 The coupling problem

Because of the small size of nanophotonic waveguides, the coupling of light to an optical fibre is an important issue. Some kind of mode-size converter is needed to couple from a large fibre mode to a small waveguide mode. Because the difference in mode-size is very large in the case of nanophotonic waveguides, the problem is more difficult. A good solution has to achieve a high coupling efficiency, large bandwidth and large tolerances to alignment errors.

Another problem occurs when we want to use nanophotonic ICs in communication networks. The nanophotonic ICs only work for TE-polarization. The polarization state of light coming from an optical fibre in a network is not known. As a result, the photonic IC will not work properly, unless a special polarization diversity configuration is used.

These problems and possible solutions are discussed in more detail in chapter 2. We have investigated the use of grating couplers to solve these problems.

1.2.3 Grating coupler

A grating coupler uses a periodic structure or diffraction grating to diffract the light in a certain direction. A grating coupler can couple light efficiently into sub-micrometre SOI waveguides [7]. However, conventional grating couplers have a very narrow bandwidth and are

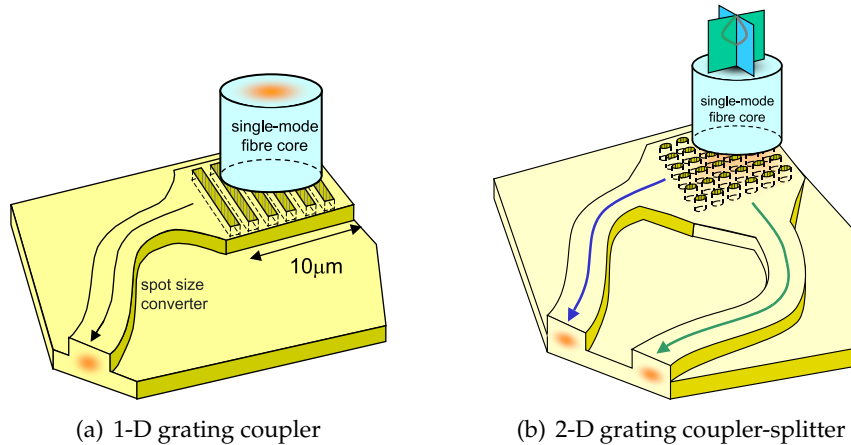


Figure 1.2: Waveguide grating couplers for coupling to fibre.

rather large. As a consequence, they are not suited for coupling to photonic ICs. We propose the use of a compact grating coupler to couple to fibre. Because the coupling length of the grating is very short, the bandwidth is quite large. This coupler is shown in figure 1.2(a). The grating performs the vertical mode-size conversion, for the horizontal mode-size conversion a taper is used.

The proposed grating coupler works only for TE-polarization. But when using a 2-D grating coupler, as shown in figure 1.2(b), this problem can be solved. This 2-D grating coupler couples the incoming light, which has an unknown polarization state, to the TE-modes of two planar waveguides. By using this coupling scheme, the polarization dependence problem of nanophotonic waveguides might be solved. An in depth discussion of this topic is also given in chapter 2.

1.3 Purpose and outline of this work

The purpose of our research was to investigate the use of grating couplers to couple light from optical fibres to nanophotonic waveguides and integrated circuits. We have focused our work on structures in silicon-on-insulator because that material is suitable for mass production of future photonic integrated circuits.

In chapter 2, the coupling problem is discussed in more detail and a summary of the state-of-the-art solutions is presented. The polarization issue is also explained. Because our work is based on gratings,

an overview of grating coupler theory and the numerical methods that we have used is given in chapter 3, followed by the actual design of the 1-D grating couplers in chapter 4. A short overview of the processes that are used to fabricate the couplers is given in chapter 5 and the experimental results are discussed in chapter 6. Chapter 7 deals with the 2-D gratings that are used as polarization splitter. Finally, in chapter 8 we present our main conclusions and perspectives for future work.

1.4 Publications

The results obtained within this work have been published in various papers and presented at various conferences. This paragraph gives an overview of the publications. They can also be found in the [publications](#) section of the photonics research group website : <http://photonics.intec.ugent.be>. These publications may be downloaded for personal use only. For any other use, the permission of the copyright owner (usually the publisher of the journal) must be obtained.

The following papers have been published in international peer reviewed journals or are accepted for publication:

1. D. Taillaert, P. Bienstman, R. Baets, "Compact efficient broadband grating coupler for silicon-on-insulator waveguides," accepted for publication in *Optics Letters*, vol. 29, December 2004.
2. D. Taillaert, H. Chong, P. Borel, L. Frandsen, R. De La Rue, and R. Baets, "A compact two-dimensional grating coupler used as a polarization splitter," *IEEE Photonics Technology Letters*, vol. 15, pp. 1249–1251, September 2003.
3. D. Taillaert, W. Bogaerts, P. Bienstman, T. Krauss, P. Van Daele, I. Moerman, S. Verstuyft, K. De Mesel, and R. Baets, "An out-of-plane grating coupler for efficient butt-coupling between compact planar waveguides and single-mode fibers," *IEEE Journal of Quantum Electronics*, vol. 38, pp. 949–955, July 2002.
4. P. Sanchis, J. Garcia, J. Marti, W. Bogaerts, P. Dumon, D. Taillaert, R. Baets, "Experimental demonstration of high coupling efficiency between wide ridge dielectric waveguides and single-mode photonic crystal waveguides," accepted for publication in *IEEE Photonics Technology Letters*, October 2004.

5. P. Dumon, W. Bogaerts, V. Wiaux, J. Wouters, S. Beckx, J. Van Campenhout, D. Taillaert, B. Luyssaert, P. Bienstman, D. Van Thourhout, R. Baets, "Low-loss SOI photonic wires and ring resonators fabricated with deep UV lithography," *IEEE Photonics Technology Letters*, vol. 16, pp. 1328–1330, May 2004.
6. W. Bogaerts, D. Taillaert, B. Luyssaert, P. Dumon, J. Van Campenhout, P. Bienstman, D. Van Thourhout, R. Baets, V. Wiaux, S. Beckx, "Basic structures for photonic integrated circuits in silicon-on-insulator," *Optics Express*, vol. 12, pp. 1583–1591, April 2004.
7. W. Bogaerts, P. Bienstman, D. Taillaert, R. Baets, D. De Zutter, "Out-of-Plane Scattering in Photonic Crystal Slabs," *IEEE Photonics Technology Letters*, vol. 13, pp. 565–567, June 2002.
8. W. Bogaerts, V. Wiaux, D. Taillaert, S. Beckx, B. Luyssaert, P. Bienstman, R. Baets, "Fabrication of Photonic Crystals in Silicon-on-Insulator Using 248-nm Deep UV Lithography," *IEEE Journal on Selected Topics in Quantum Electronics*, vol. 8, pp. 928–934, 2002.
9. W. Bogaerts, P. Bienstman, D. Taillaert, R. Baets, D. De Zutter, "Out-of-plane scattering in 1-D photonic crystal slabs," *Optics and Quantum Electronics*, vol. 34, pp. 195–203, 2002.

The following papers have been presented at international conferences and are published in the conference proceedings:

10. P. Sanchis, J. Garcia, F. Cuesta-Costo, A. Martinez, J. Blasco, J. Marti, W. Bogaerts, P. Dumon, D. Taillaert, R. Baets, "Experimental demonstration of a high efficiency coupling technique for planar photonic crystal circuits," presented at the fifth Photonic and Electromagnetic Crystal Structures conference (PECS V), Kyoto, Japan, p. 128, 2004.
11. D. Taillaert, W. Bogaerts, R. Baets, "Efficient coupling between submicron SOI-waveguides and single-mode fibers," IEEE/LEOS Benelux Annual Symposium 2003, Enschede, The Netherlands, pp. 289–292, 2003.
12. W. Bogaerts, P. Dumon, J. Van Campenhout, V. Wiaux, J. Wouters, S. Beckx, D. Taillaert, B. Luyssaert, D. Van Thourhout, R. Baets, "Deep UV Lithography for Planar Photonic Crystal Structures,"

in proceedings of the IEEE LEOS Annual Meeting 2003 (invited), Tucson, USA, pp. 754–755, 2003.

13. D. Taillaert, R. Baets, H. Chong, R. De La Rue, P. Borel, L. Frandsen, "A compact two-dimensional grating coupler used as a polarisation splitter," presented at the European Conference on Integrated Optics (ECIO 03), Czech Republic, pp. PD:5–8, 2003.
14. V. Volkov, S. Bozhevolnyi, D. Taillaert, "Near-field imaging of out-of-plane light scattering in photonic crystal slabs," in proceedings SPIE, vol. 5118, pp. 541–548, 2003.
15. D. Taillaert, W. Bogaerts, P. Bienstman, R. Baets, "Out-of-plane fiber coupler for coupling to high-index-contrast waveguides," presented at the fourth Photonic and Electromagnetic Crystal Structures conference (PECS IV), Los Angeles, USA, p. 155, 2002.
16. W. Bogaerts, V. Wiaux, D. Taillaert, S. Beckx, R. Baets, "Photonic Crystal Waveguides in SOI fabricated with deep UV lithography," European Conference on Optical Communication (ECOC 02), Copenhagen, Denmark, p. 4.4.5, 2002.
17. D. Taillaert, R. Baets, "Out-of-plane fiber coupler for coupling to high-index-contrast waveguides," Workshop 2D photonic crystals, Ascona, Switzerland, p. I-17, 2002.
18. D. Taillaert, W. Bogaerts, P. Bienstman, T.F. Krauss, I. Moerman, P. Van Daele, R. Baets, "A high-efficiency out-of-plane fibre coupler for coupling to high index contrast waveguides," European Conference on Optical Communication (ECOC 01), Amsterdam, The Netherlands, pp.30–31, 2001.
19. D. Taillaert, W. Bogaerts, P. Bienstman, D. De Zutter, R. Baets, "Design of an out-of-plane coupler for efficient butt-coupling from photonic crystal waveguides to single-mode fibres," presented at the third Photonic and Electromagnetic Crystal Structures conference (PECS III), St.-Andrews, UK, 2001.

The work on the 2-D couplers was the subject of a patent application.

European patent application number EP-1353200 (10/2003)

US patent application number US-2003235370 (12/2003)

Chapter 2

Coupling light from optical fibres to nanophotonic waveguides

Coupling light from an optical fibre to a nanophotonic waveguide is not an easy task. But it is a very important one, because an integrated circuit is useless without an interface to the outside world. We will first explain the problem in more detail. Then a short overview of the state-of-the art is given. Last but not least, we discuss the polarization sensitivity and its consequences.

2.1 Nanophotonic waveguides in SOI

2.1.1 Silicon-on-insulator

Silicon-on-insulator (SOI) consists of a thin Silicon layer on top of an oxide buffer layer on top of a Silicon substrate. SOI is a suitable material for low-loss optical waveguides. The top Silicon ($n=3.47$) is the waveguide core and the oxide ($n=1.44$) is the bottom cladding. The top cladding is air ($n=1$), but it is possible to deposit an oxide layer on top to create a vertically symmetric structure. SOI wafers are available in diameters up to 300 mm and are compatible with mass fabrication techniques (figure 2.1).

The oxide buffer has to be sufficiently thick to prevent leakage loss to the substrate. The thickness of the Silicon core has to be below

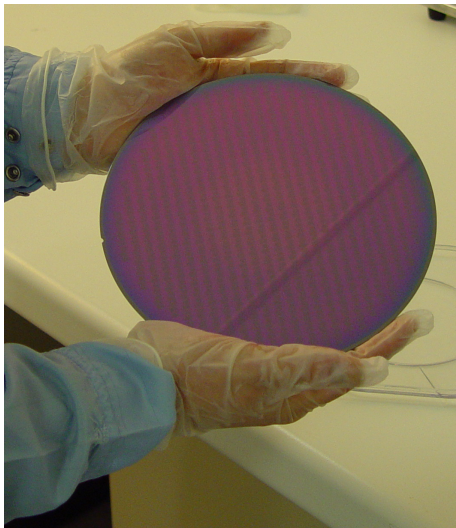


Figure 2.1: A lot of photonic integrated circuits fit on a 200 mm SOI wafer.

280 nm to keep the slab waveguide single-mode¹ for TE polarization². The wafers we have used have a 220 nm Silicon core and 1000 nm oxide cladding. The Silicon substrate is 750 μm thick. Nanophotonic waveguides can be fabricated on these wafers and very low propagation losses have been demonstrated [10] in the wavelength range 1500–1650 nm for TE polarization.

2.1.2 Nanophotonics

Compact photonic integrated circuits in SOI can be based on photonic wire or photonic crystal waveguides. Photonic wires are conventional waveguides with a high refractive index contrast. Because of this high contrast, the dimensions have to be very small to keep the waveguide single-mode. Typical dimensions are 220 nm by 500 nm. Because these dimensions and the related fabrication tolerances are in the nanometre range, we use the term nanophotonics. An example of a component based on photonic wires is a ring resonator [11]. The diameter of the resonator shown in figure 2.2(a) is approximately 10 μm .

¹It is also possible to create a single-mode ridge waveguide with a Silicon thickness of several micrometres [8, 9]. However that configuration is not suitable for nanophotonic waveguides.

²We use the waveguide definitions for TE and TM. TE means that the E-field is parallel with the substrate and perpendicular to the propagation direction.

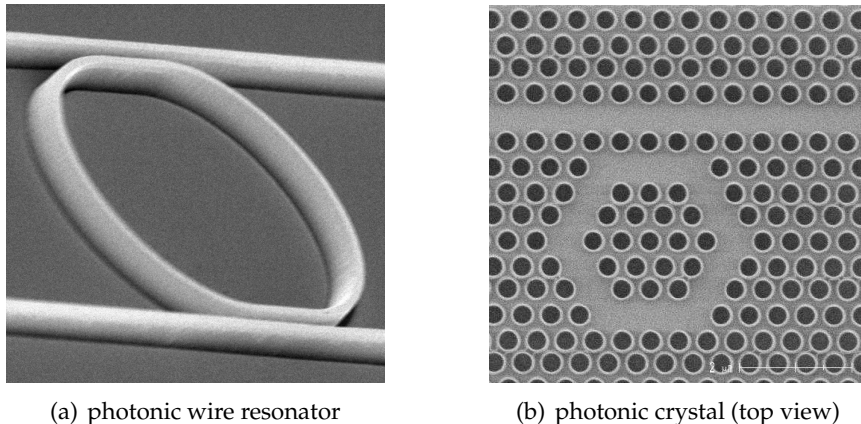


Figure 2.2: Examples of nanophotonic waveguides and components in SOI. Pictures courtesy of Wim Bogaerts.

Another example of a nanophotonic waveguide is a photonic crystal waveguide [12]. A photonic crystal is a periodic structure with a period on the order of the wavelength of light and a high refractive index contrast in each unit cell [10]. In some wavelength ranges, light cannot propagate through the structure in any direction and a photonic bandgap occurs. A photonic crystal made of a triangular array of holes in SOI has a large bandgap for TE polarization. If defects are introduced in the crystal, the light is confined in these defects and waveguides are created, because the light cannot propagate through the crystal. An example of a photonic crystal structure made in SOI is shown in figure 2.2(b). The lattice constant is of the order of 500 nm.

It is expected that these nanophotonic waveguides will make it possible to integrate a lot of functionality on a small chip. But the small size also creates some problems. The problem that we will discuss in more detail is the interface to the outside world, which is an optical fibre for most applications.

2.2 Coupling to fibre

2.2.1 The problem

The small size of nanophotonic waveguides makes the coupling to an optical fibre more difficult. This is illustrated in figure 2.3, where the spot-size of a typical SOI photonic wire and a single-mode fibre are

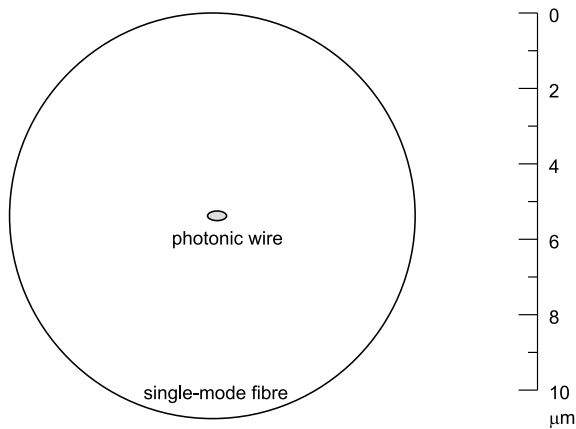


Figure 2.3: Spot-size of a typical nanophotonic waveguide and a single-mode fibre, drawn on the same scale.

shown on the same scale. It is obvious that there is a huge mismatch between the two modes. Simple butt-coupling of both waveguides would result in 26 dB coupling loss, which is of course unacceptable.

In theory a lens can be used to solve this problem. This lens can be a discrete component or be integrated on the fibre in the form of a microlensed fibre. However the sensitivity to alignment errors becomes very critical in the case of sub-micrometre waveguides. A better solution is an integrated spot-size converter which expands the small waveguide mode on chip [13, 14]. Such a spot-size converter can be a taper, but also a directional coupler or a waveguide grating coupler. In section 2.2.2 - 2.2.4 we present an overview of the relevant literature. We also discuss the properties of these spot-size converters in more detail.

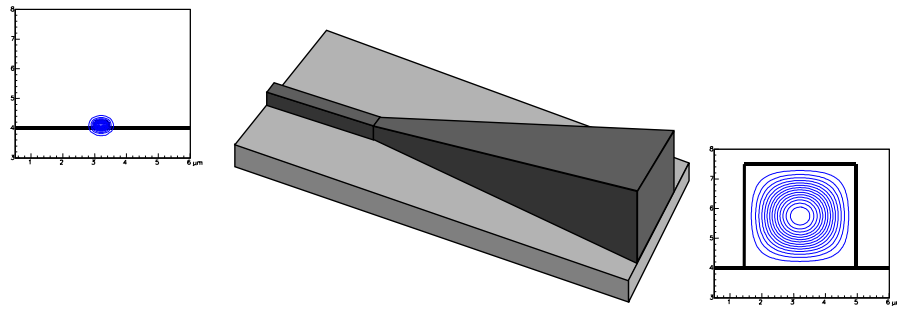
2.2.2 Tapered spot-size converters

A tapered spot-size converter or taper can convert the small mode from the nanophotonic waveguide into a larger mode that couples better to fibre. A taper is typically a waveguide whose dimensions change along the propagation direction, creating a transition from a small to a large mode size. If the variation is slow enough, the fundamental mode of the input waveguide is converted into the fundamental mode of the output waveguide with 100% efficiency and the taper is called adiabatic. The theoretically most straightforward solution to our problem is

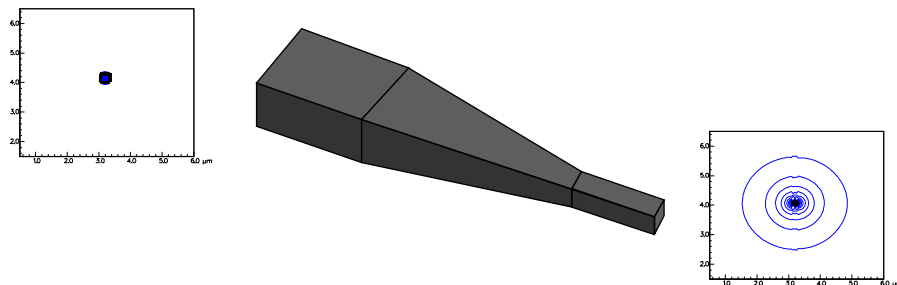
a 3-D taper, this is a structure that is tapered both laterally and vertically (figure 2.4(a)). Because of the huge difference in mode size between a nanophotonic waveguide and a fibre, such a taper is very long, almost 1 mm. Also the fabrication process of this 3-D structure is rather complicated. A so-called grayscale lithography and etch process is needed [15] to fabricate the vertical taper. Also an AR-coating is needed at the facet. Published experimental results achieve -4.5 dB conversion efficiency [16] and -3.5 dB efficiency [15] from a standard fibre to a 250 nm thin SOI waveguide. The length of the taper is 600 μm .

Another approach is a 3-D taper whose dimensions become smaller instead of larger towards the fibre (sometimes called inverted taper, see figure 2.4(b)). It is well known that if a waveguide core becomes too small, the mode size is also expanded. Such a taper is much shorter than the previous one, but the fabrication requirements are much harder to achieve because the dimensions are very small. A coupling loss of 0.2dB has been calculated [17] for a 10 μm long linear taper from 350x350 nm² to 155x155 nm². No experimental results are available which confirms the fact that this kind of taper is very difficult if not impossible to fabricate with the required accuracy.

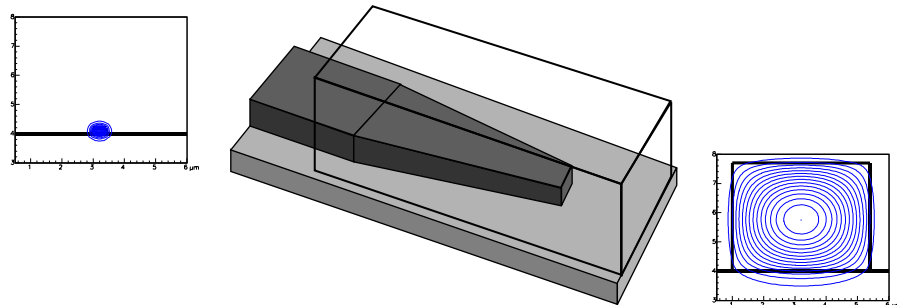
A more elegant solution that is compatible with planar processing techniques is the use of a 2-D taper (tapered only laterally) to achieve 3-D spot-size conversion. An example structure is shown in figure 2.4(c). The nanophotonic waveguide is tapered; its width is reduced to a few tens of nanometers. This forces the mode out of the Silicon nanophotonic waveguide into another fibre-adapted waveguide that is either on top or below the Silicon. This fibre-adapted waveguide can be a thick Silicon dioxide layer or a polymer waveguide that is made on top of the Silicon. These structures can be fabricated with conventional processing techniques, although very high resolution lithography is needed for the taper tip. This structure is also called an inverted lateral taper. A coupling loss of 0.8 dB between a 300x300 nm² Silicon waveguide and a standard single-mode fibre has been demonstrated by NTT [18]. They use a 3 μm wide polymer fibre-adapted waveguide and a 200 μm long taper with a tip width of 60 nm. The polymer waveguide is connected to 4 μm mode diameter high index contrast fibre. This special fibre is connected to standard fibre with very low loss using thermal diffusion expanded core (TEC) fibre, but the use of fibre with a smaller mode size increases the sensitivity to alignment errors. A similar structure has been demonstrated by IBM [19]. A coupling loss of 0.5 dB is demonstrated using tapered lensed fibres. A detailed com-



(a) 3-D Silicon taper



(b) 3-D inverted Silicon taper



(c) 2-D inverted Silicon taper with polymer waveguide on top

Figure 2.4: Examples of tapered spot-size converters. Note that the taper angles are strongly exaggerated, the length of the taper is typically a few 100 μm up to 1 mm.

Table 2.1: Details of inverted lateral tapers.

reference	NTT [18]	IBM [19]
taper length	200 μm	150 μm
tip width	60 nm	75 nm
waveguide width	300 nm	450 nm
waveguide thickness	300 nm	220 nm
polymer guide width	3 μm	2 μm
measured coupling loss	0.8 dB	0.5 dB
polarization	both	TE

parison of the characteristics of both structures is given in table 2.1. It is also possible to use a 3 μm thick buried oxide layer instead of polymer overlay waveguide [20]. In this case however, the end tip of the taper must be positioned exactly at the end facet, because the buried oxide does not provide lateral confinement.

2.2.3 Grating-assisted directional couplers

A directional coupler, consisting of two parallel waveguides close together, can be used to couple light between two waveguides. If the waveguides are identical, the directional coupler is called symmetric and 100% power transfer can be achieved. If the two waveguides are not identical (which is the case for coupling between fibre and nanophotonic waveguides), the coupler is called asymmetric. A simple asymmetric directional coupler cannot achieve 100% power transfer. By adding a grating to one of the waveguides, it is possible to achieve 100% efficiency with an asymmetric directional coupler. This structure is called a grating-assisted directional coupler (GADC).

A GADC for coupling between a 250 nm thin Silicon waveguide and a fibre-adapted SiON waveguide is presented in [21]. Because of the huge asymmetry, an intermediate Si_3N_4 waveguide is used. This dual grating-assisted directional coupler is shown in figure 2.5(a). The calculated coupling efficiency is 90% and the length is a few hundred μm to a few mm. This structure is polarization sensitive. Because only the vertical spot-size conversion is achieved, a lateral taper is still needed.

Based on the same principle, direct coupling between a fibre and a photonic crystal waveguide can be achieved with the structure shown in figure 2.5(b). However a fibre with a diameter of 1-2 μm is needed.

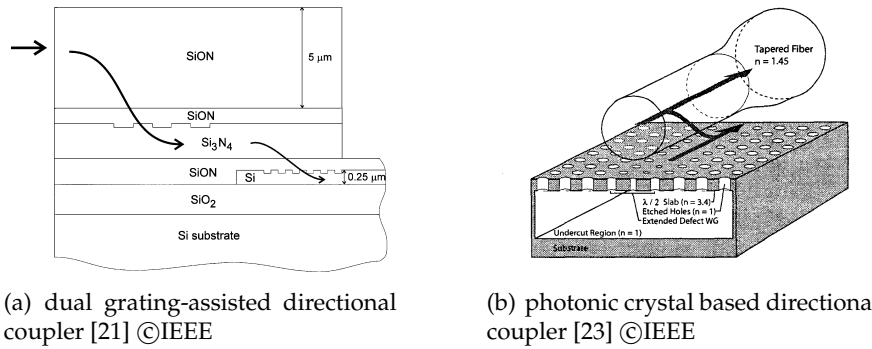


Figure 2.5: Grating-assisted directional couplers.

The photonic crystal waveguide performs the role of the grating. A theoretical efficiency of 90% was calculated in [22]. The small diameter fibre can be made by heating and stretching. Experimental results are presented in [23] and a drop in fibre transmission from 100% to 10% has been observed for a certain wavelength. This structure is of course wavelength and polarization sensitive. A major disadvantage is the very critical alignment that is needed.

2.2.4 Waveguide grating couplers

Waveguide grating couplers can couple light from the top into a planar waveguide. Therefore grating couplers can be used to inject or extract light anywhere in a photonic integrated circuit and not only at the edges. This type of coupler is also called surface coupler. Another advantage of surface couplers compared to edge couplers is that there is no need to polish facets. And because the entire surface of the chip can be used for input-output, a higher number of fibres can be connected to one chip. The main disadvantage of grating couplers is the limited bandwidth and/or coupling efficiency to fibre. In the next paragraphs we give an overview of published SOI grating couplers and compare them to the grating couplers we have investigated.

Traditional grating couplers [7, 24] use very long gratings that are several hundred micrometres long. These gratings can achieve high efficiencies, a value of 70% is cited in [24]. However this is not the coupling efficiency to a fibre, but only the power that is coupled out of the waveguide. When using such a long grating, a curved focusing

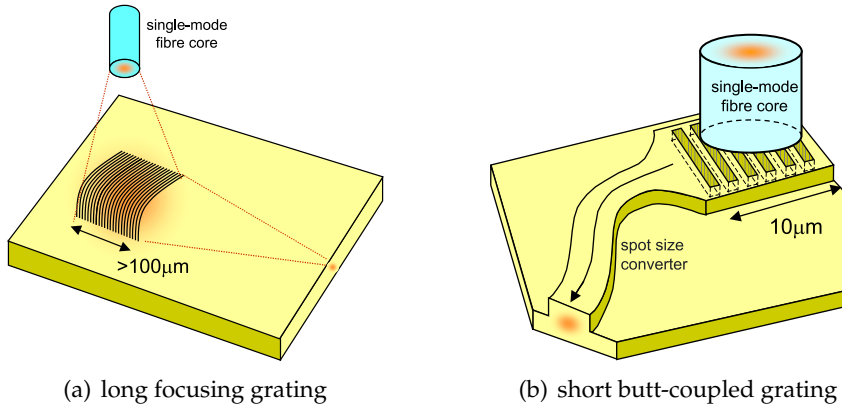


Figure 2.6: Waveguide grating couplers.

grating can be used to couple to a fibre. This is shown in figure 2.6(a). However, using a long grating with a small coupling strength results in a very narrow bandwidth. It should also be noted that a multi-mode SOI slab waveguide is used in [24].

There are some publications that use shorter gratings to couple to single-mode SOI slab waveguides. These shorter gratings are better suited for coupling to photonic integrated circuits. In [25], a measured coupling efficiency of 57% is published. The cited efficiency is for a Gaussian beam with beam diameter $48\ \mu\text{m}$. A top metal mirror and coupling through the substrate are used to achieve the high efficiency. However, this configuration is not suitable for fibre coupling unless additional lenses are used. In [26, 27], an efficiency of 40% is reported for a Gaussian beam with beam diameter $28\ \mu\text{m}$. Although this is a very nice result and the light is coupled in from the top, a lens is still needed to couple to a fibre. The beam diameter of a fibre is approximately $10\ \mu\text{m}$. The use of lenses to couple a $28\ \mu\text{m}$ wide beam to a fibre increases the cost and reduces the bandwidth of the grating coupler.

In this work, we use a short grating ($10\ \mu\text{m}$) and butt-couple the fibre to the grating. This configuration is shown in figure 2.6(b). No lenses or focusing gratings are needed. Moreover standard fibres or fibre arrays can be used. A larger bandwidth, up to $43\ \text{nm}$ ($1\ \text{dB}$ bandwidth) is achieved thanks to the large coupling strength of the grating. The tolerances to alignment errors are comparable to fibre-fibre alignment. Our simulation results are presented in chapter 4 and the experimental results in chapter 6.

These grating couplers only perform the vertical (out-of-plane) spot-size conversion. A lateral (in-plane) spot-size converter is still needed to couple from a wide waveguide to a narrow photonic wire. This lateral taper is rather easy. A simple adiabatic taper of 200 μm length can be used to connect a 12 μm wide waveguide to a 500 nm photonic wire. But more compact solutions³ may be preferred, especially in the case of a chip with a high number of input-output fibres. A 20 μm long spot-size converter for coupling between a 10 μm wide waveguide and a 500 nm photonic wire was demonstrated by our group in [28].

2.3 Polarization

2.3.1 Polarization in fibre optics

A single-mode fibre has in fact two orthogonal linearly polarized modes. These modes are degenerate and couple to each other in fibre bends or due to imperfections or random variations in the fibre [29]. As a result the state of polarization changes during propagation in the fibre and the output from a fibre can have any elliptical polarization state, even when linearly polarized light is launched into the fibre.

In optical communication networks, the state of polarization of the light coming from a fibre is unknown and thus every component in the network must be polarization insensitive. An important figure of merit used is the PDL or polarization dependent loss. For a perfectly polarization insensitive component, the PDL is zero.

There exist special types of fibre where the state of polarization does not change during propagation. These polarization maintaining fibres (PMF) are more expensive than standard single-mode fibres. Also currently available PMF's can only maintain good extinction ratios (>20 dB) over a short distance (few hundreds of metres). Over very long lengths random variations in the fibre properties limit the extinction ratio the fibre can maintain [30]. Therefore PMF can only be used for interconnections between components and systems and not for long distance communication links.

³The research on compact horizontal or in-plane spot-size converters has been carried out by Bert Luyssaert in the context of his PhD.

2.3.2 Issues in nanophotonics

Nanophotonic waveguides are polarization sensitive because of the high refractive index contrast. The boundary conditions at these index steps are very different for the tangential and normal E-field. As a result, the propagation constants of the TE and TM modes⁴ can be very different. Although a straight photonic wire can be made polarization insensitive by using a symmetric wire with square cross-section, this is not the case for more complicated components. Designing a polarization insensitive ring resonator for example is very difficult, if not impossible.

Photonic crystals are even worse. A triangular lattice of air holes in SOI has only a large bandgap for TE polarization. This fact has very important consequences for potential applications in optical fibre communications.

2.3.3 Polarization diversity approach

If we want to use components or circuits that are polarization sensitive in optical communication networks, a polarization diversity approach is needed. In this approach, the random polarization coming from the fibre is split into two orthogonal polarization states and one of the states is rotated. Identical operations are then performed in parallel. A schematic polarization diversity configuration is shown in figure 2.7. At the input, there is a polarization splitter that splits the incoming light in TE and TM parts. In the example, the circuit we want to use is a ring resonator that works only for TE-polarization. Therefore the TM part goes through a polarization rotator that converts TM into TE. In both branches there is an identical circuit or component. In one branch the TE output light is converted back into TM. And finally TE and TM are combined again with a polarization combiner (which is identical to the splitter).

In theory it is possible to combine both TE branches into one branch after the polarization converter. In this case the second circuit and the output converter and splitter would not be needed. However combining both TE branches is sensitive to the phase of the light and is very difficult to realize in practice. In the configuration where TE and TM are combined, this sensitivity to the phase is avoided because orthogonal polarization states are combined. A similar scheme can be given for

⁴Strictly speaking, we should talk about quasi-TE or TE-like modes, because TE and TM only exist in structures that are infinite in the lateral direction.

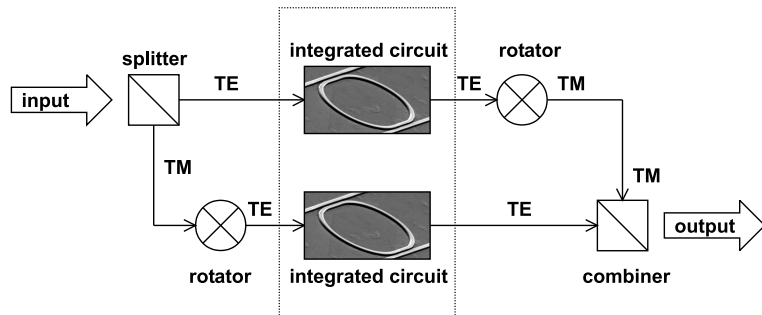


Figure 2.7: Polarization diversity configuration.

components or circuits that work in reflection instead of transmission. In that case the input side is also the output side and the incoming and outgoing light can be separated by using a circulator.

The polarization splitters and rotators can be implemented in conventional non-integrated optics, such as birefringent prisms and quarter-wave plates. These components have very good performance and low insertion loss to fibre is achieved by using lenses or fibre collimators. The disadvantage of this approach is the large size and expensive packaging. Therefore the preferred option is to integrate these components on the same chip as the nanophotonic circuits.

2.3.4 Integrated polarization diversity

Polarization splitters and rotators are difficult to make in a compact integrated version. Integrated polarization splitter devices have been demonstrated by several research groups, but these devices are typically >1 mm long. This is small compared to non-integrated devices, but large compared to nanophotonic devices.

A splitter in InGaAsP-InP that can be fabricated in one etch step is demonstrated in [31], the device is approximately 1 mm long. Another device based on high index contrast Bragg reflector waveguides is proposed in [32], but the length is also 1 mm. A very compact splitter based on photonic crystals is proposed in [33], but the results given in that paper are based on 2D-FDTD simulations and do not take into account possible out-of-plane scattering losses in the photonic crystal. The proposed device is shorter than $10\ \mu\text{m}$.

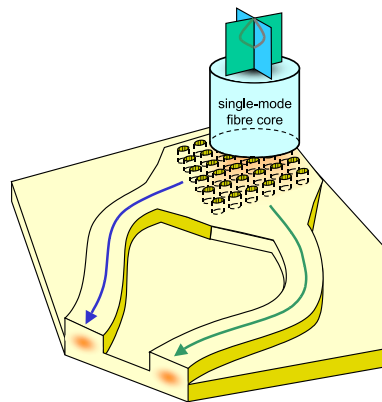


Figure 2.8: 2-D grating coupler splitter.

A design of a splitter and rotator is presented in [34]. The splitter is $150\ \mu\text{m}$ long and the rotator $400\ \mu\text{m}$. The device is Silicon-based, but requires three etch and deposition steps to fabricate it.

We use a completely different approach. By using a waveguide grating coupler with a 2-D grating, it is possible to make a compact integrated fibre coupler that is also a polarization splitter [35]. This device is shown in figure 2.8. Two identical waveguides intersect at a right angle and the grating is made in the intersection. The grating is designed in such a way that only the fundamental TE-mode of a waveguide couples to fibre. Light coming from the fibre is coupled to the TE-modes of both waveguides. The coupling ratio between both waveguides depends on the polarization in the fibre, but the total coupling efficiency to both waveguides together does not. In fact this device combines the functions of fibre coupler, polarization splitter and rotator. This 2-D grating coupler structure is studied in chapter 7.

A polarization diversity configuration based on a 2-D grating coupler is shown in figure 2.9. Compared to the previous polarization diversity scheme, the splitter and rotator are replaced by the 2-D grating coupler. The advantage is that everything can be integrated on the same chip. In this way, a photonic integrated circuit based on nanophotonic components can be made that is polarization independent, although the nanophotonic components itself are strongly polarization dependent.

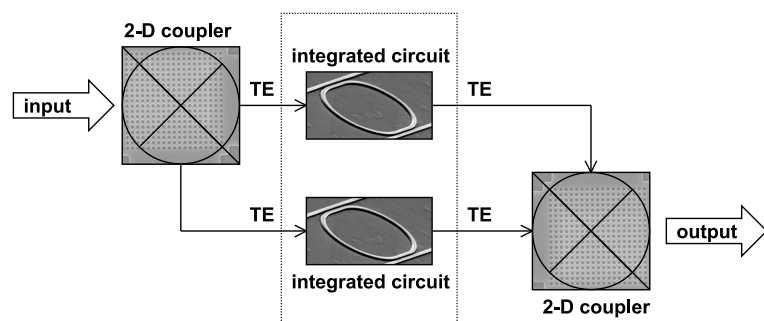


Figure 2.9: Polarization diversity configuration using 2-D waveguide grating fibre couplers.

Chapter 3

Grating coupler theory and numerical methods

In this chapter we will give a short overview of grating coupler theory and numerical methods. Only dielectric gratings are considered, no metals. First the basics of grating couplers are presented. Also the basic principles of different numerical methods are given. For the details of these methods the reader is referred to the literature. The methods that we have used for the simulations in chapter 4 are discussed in more detail. Finally the calculation of the coupling efficiency to or from a fibre is explained.

3.1 Introduction

3.1.1 Periodic structures

Periodic structures play an important role in optics. In a periodic structure, the refractive index profile is periodic in one or more dimensions. The structures we use, have a period on the order of the wavelength of the light and are called diffraction gratings or shortly gratings. In this chapter we only treat 1-D gratings, in chapter 7 we have a look at 2-D gratings. A special class of gratings are waveguide gratings, where the periodic structure is made in or close to a waveguide. These structures are also called corrugated waveguides.

In the last decade, the so-called photonic crystals have become very popular. Photonic crystals are periodic structures with a period on the order of the wavelength of the light and a relatively high index contrast. The name photonic crystal originates from the fact that these structures

Table 3.1: Number of papers listed in “Web of Science.”

search subject	result
grating	17000
photonic crystal	2110
grating and waveguide	1607
grating and coupler	615

can have a photonic bandgap, which is a range of wavelengths in which light cannot propagate through the structure. Usually a photonic crystal has a relatively large index contrast and a grating a small index contrast. In the previous definition, it is the refractive index contrast, felt by the waveguide mode, that matters.

To illustrate the importance of gratings and the extent of the research field, we have listed the number of published papers related to gratings in table 3.1. The numbers are based on the ISI Web of Science [36], which is a database with publications in international peer reviewed journals. The large number of papers on grating couplers and waveguide gratings shows that the field is very extensive.

Before starting with the theory, we would like to answer the following question : Do we call the couplers that we have studied in this work, grating couplers or photonic crystal couplers? Based on the refractive index contrast and the number of periods, the couplers fall somewhere in between the gratings and the crystals. So both names are acceptable. But based on the functionality and properties of the couplers, it is better to use the term grating couplers. For that reason we use the old-fashioned term grating instead of the trendy photonic crystal.

3.1.2 The Bragg condition

The most fundamental formula concerning periodic structures is the Bragg condition. It describes the relation between the wave-vectors of the incident and diffracted waves. For a grating with uniaxial periodicity along the z-axis between two materials with refractive index n_1 and n_2 the equation is :

$$\mathbf{k}_z = \mathbf{k}_{in,z} + m\mathbf{K} \quad (3.1)$$

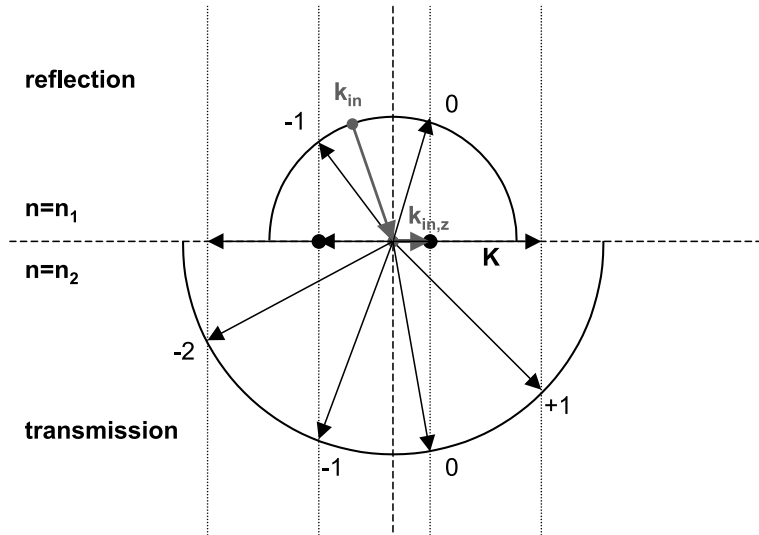


Figure 3.1: The Bragg condition : example wave-vector diagram. This is the graphical representation of equation (3.1).

$$|\mathbf{k}| = k_0 n_1 \text{ in material 1}$$

$$|\mathbf{k}| = k_0 n_2 \text{ in material 2}$$

$$|\mathbf{K}| = \frac{2\pi}{\Lambda}$$

where Λ is the grating period and the integer m is the diffraction order. This relationship between the incident and diffracted waves can also be shown in a wave-vector diagram. Such a diagram is the graphical representation of equation (3.1) and is easier to understand. An example is shown in figure 3.1. The Bragg condition only tells us which diffraction orders can occur. It does not say anything about the diffraction efficiencies. When there is no grating at the interface between the two materials ($K=0$), the Bragg condition is the same as Snell's Law, which describes refraction at the interface between two materials.

For a waveguide grating coupler, a similar formula and wave-vector diagram can be written. In this case, the incident wave is replaced by the guided mode of the waveguide, which is characterized by its propagation constant β . The equations become :

$$\mathbf{k}_z = \beta + m\mathbf{K} \quad (3.2)$$

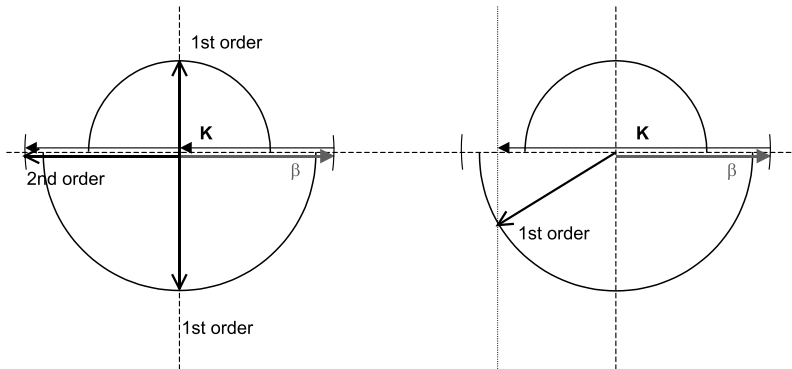


Figure 3.2: Wave-vector diagram for a waveguide grating coupler. The left diagram corresponds to a second-order grating. In the right diagram, a grating with only one diffraction order is shown.

$$|\mathbf{k}| = k_0 n_1 \text{ in material 1}$$

$$|\mathbf{k}| = k_0 n_2 \text{ in material 2}$$

$$|\mathbf{K}| = \frac{2\pi}{\Lambda}$$

$$\beta = \frac{2\pi}{\lambda_0} n_{\text{eff}}$$

Two examples of k-vector diagrams of grating couplers are shown in figure 3.2. The structure on the left is called a second-order grating, because the second order diffraction is reflection back into the waveguide. The first order diffraction is vertically coupling out of the waveguide. This first order diffraction is useful to couple to a fibre. This case of exactly vertical coupling occurs when $K=\beta$ or $\lambda=n_{\text{eff}}\Lambda$ and is also called the resonant case. If the grating period is slightly different, the coupling is no longer exactly vertical but near vertical and the grating is called detuned. In this case the second-order reflection is avoided. Even in the detuned case, there are still two possible diffraction orders, one up and one down. In figure 3.2 on the right, an example is shown of a coupler with only one possible diffraction order. The coupling is not near vertical but oblique.

It should be noted that the Bragg condition is only exact for infinite structures. In a finite structure, there is not exactly one discrete k-vector for which diffraction occurs, but a range of k-vectors around the one predicted by the Bragg condition. The extent of this range or

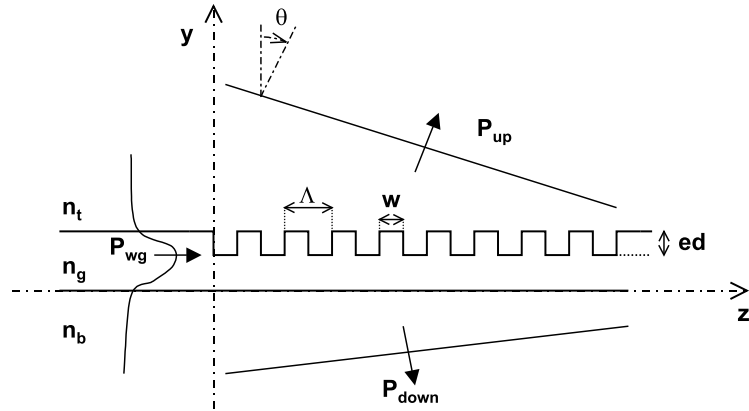


Figure 3.3: The 1-D grating coupler problem.

in other words the bandwidth will depend on the coupling strength of the grating.

3.1.3 Definitions

In this section we will define the grating coupler problem and some terms used in the rest of this work. This section is needed because some terms have different meanings in different articles in the literature. The problem is sketched in figure 3.3. The waveguide has a core ($n=n_g$) and a top ($n=n_t$) and bottom ($n=n_b$) cladding. In general there can be additional layers, such as a high index substrate, under the bottom cladding. The grating has an etch depth ed . The grating period is Λ and the filling factor is $ff=w/\Lambda$. The filling factor is also called duty cycle. The axes and the angle θ are defined as in figure 3.3.

When considering the coupler as an output coupler, the power in the waveguide will be exponentially decaying due to the presence of the grating (if there is no coupling between the forward and backward propagating guided mode) :

$$P_{wg}(z) = P_{wg}(z = 0) \exp(-2\alpha z) \quad (3.3)$$

2α is the coupling strength or leakage factor of the grating. The inverse of the coupling strength is the coupling length $L_c=(2\alpha)^{-1}$. When α is small, we talk about a weak grating, when α is large, the grating is strong. Equation (3.3) is only exact for weak detuned gratings. The

directionality of the grating is the power that is radiated upwards divided by the total amount of radiated power.

The coupling efficiency from waveguide to fibre is the power that is coupled to the fibre divided by the power of the incident guided mode. The coupling efficiency from fibre to waveguide is the power that is coupled to the waveguide mode divided by the input power in the fibre. Because single-mode waveguides are used, the coupling efficiency from fibre to waveguide is the same as from waveguide to fibre (see also section 3.7.4) and can be called the coupling efficiency¹. In some publications where coupling to a power detector instead of a fibre is considered, P_{up}/P_{wg} is called the coupling efficiency. To avoid any confusion we will label this quantity *power up* in the graphs with simulation results. The coupling efficiency to fibre will be labelled *fibre* θ° and θ is the angle between the fibre and the y-axis.

A finite grating has a limited number of periods. An infinite grating has an infinite number of periods and hence is a purely mathematical description. Infinite gratings are easier to model and under some circumstances the results are applicable for finite gratings too.

3.1.4 Symmetry arguments

Based on symmetry arguments, some limits on the efficiency of grating couplers can be explained. Figure 3.4(a) shows a horizontally symmetric structure. When light is coupled in from the top, the same amount will couple to the left and to the right due to the symmetry. To exceed 50% efficiency, the symmetry must be broken. This can be achieved by using an asymmetric grating or by coupling in not exactly vertically.

A coupler with vertical symmetry is shown in figure 3.4(b). The upward and downward radiated power are the same if the structure is symmetric. As a result, the coupling efficiency is always <50%, even for non-vertical coupling. A practical grating is not exactly vertically symmetric, but if the grating depth is much smaller than the waveguide thickness, there is approximately vertical symmetry. The symmetry can be broken by using different materials as top and bottom cladding or by adding a highly reflective substrate under the waveguide.

¹In some articles, a difference is made between the input and output coupling efficiency. When considering the coupling to a single-mode fibre or waveguide, there is no difference.

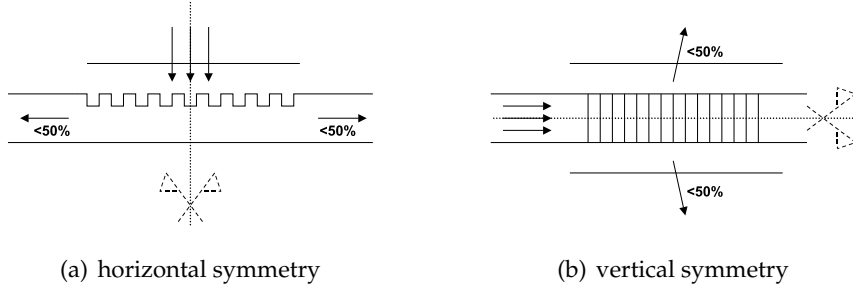


Figure 3.4: Symmetry arguments. In a symmetric structure, the coupling efficiency can never exceed 50%.

3.2 Perturbation analysis

3.2.1 Basic theory

In a perturbation analysis the grating is treated as a small perturbation of the waveguide structure without grating. It is expected that these results are only accurate for weak gratings. We will briefly explain the theory in 2-D and look at the validity for stronger gratings.

For the unperturbed waveguide, the TE-mode satisfies the following field equation (the axes are defined in figure 3.3) :

$$\left[\frac{\delta^2}{\delta y^2} + \frac{\delta^2}{\delta z^2} + k_0^2 n(y)^2 \right] E_x(y, z) = 0 \quad (3.4)$$

where

$$\begin{aligned} n(y) &= n_t & y \geq t \\ n(y) &= n_g & t > y > 0 \\ n(y) &= n_b & 0 \geq y \end{aligned}$$

When a periodic grating is etched into the waveguide, it creates a periodic change of the refractive index that is now a function of y and z . We can write the equation in the grating region $t > y > t - \delta$ as

$$\begin{aligned} \left[\frac{\delta^2}{\delta y^2} + \frac{\delta^2}{\delta z^2} + k_0^2 n(y, z)^2 \right] E_x(y, z) &= 0 \\ n^2(y, z) &= n_g^2 - \Delta n^2(y, z) \end{aligned} \quad (3.5)$$

We consider a solution of the form

$$E_x = E_x^0 + E'_x \quad (3.6)$$

where E_x^0 is the solution of (3.4) including the boundary conditions and E'_x is the perturbation term. Substituting (3.6) in (3.4) and (3.5) yields

$$\begin{aligned} \left[\frac{\delta^2}{\delta y^2} + \frac{\delta^2}{\delta z^2} + n_t^2 k_0^2 \right] E'_x &= 0 & y \geq t \\ \left[\frac{\delta^2}{\delta y^2} + \frac{\delta^2}{\delta z^2} + n_g^2 k_0^2 \right] E'_x &= \Delta n^2 k^2 E_x^0 & t > y > t - \delta \\ \left[\frac{\delta^2}{\delta y^2} + \frac{\delta^2}{\delta z^2} + n_g^2 k_0^2 \right] E'_x &= 0 & t - \delta > y > 0 \\ \left[\frac{\delta^2}{\delta y^2} + \frac{\delta^2}{\delta z^2} + n_b^2 k_0^2 \right] E'_x &= 0 & 0 \geq y \end{aligned} \quad (3.7)$$

where the term $\Delta n^2 E'_x$ has been neglected as second order perturbation. So the perturbation term E'_x satisfies the original wave equation with a source term added in the grating layer. In other words, the grating teeth have been replaced by (dipole) sources. This new problem can be solved, for example, with the Green's function method. A possible method to calculate the Green's function for a source in a multi-layer stack will be described in section 3.4.3.

An in depth analysis of grating couplers using this perturbation analysis is given in [37, 38]. In [37] both the Green's function method and a transmission line method are used to solve the equations containing sources. The coupling efficiency for a plane wave and a Gaussian beam is also calculated. With some more approximations, the perturbation equations can be solved analytically. It can be shown that the directionality can never exceed $\frac{n_t}{n_t + n_b}$ for near vertical coupling.

3.2.2 Improved perturbation theory

Several improved versions of the perturbation approach are presented in literature. These methods try to improve the accuracy of the analysis in the case of deeper gratings. In [39], the refractive index in the grating region is replaced by an averaged refractive index. This reduces the coupling strength of deep gratings compared to the original perturbation theory.

In [40], closed form expressions are given for a three layer structure and also for a four layer structure in the case of near vertical radiation. These expressions can be used to estimate the effect of a high index substrate under the bottom cladding. A comparison between the calculation results of different methods is given in section 3.6.

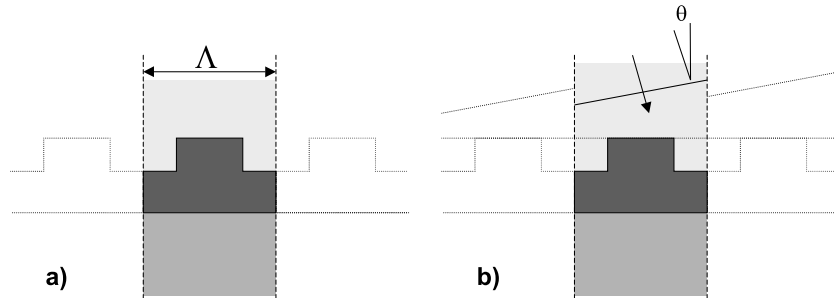


Figure 3.5: (a) Definition of the 1-D periodic structure. The grating period or lattice constant is Λ . (b) A plane wave is incident on the periodic structure from the top.

3.3 Theory of periodic structures

3.3.1 The Floquet-Bloch theorem

In this section, we describe some numerical methods that do not treat the grating as a small perturbation, in contrast to the previous section. These methods are rigorous and can be used for strong gratings, but they are limited to infinite gratings.

Consider the structure of figure 3.5a. It consists of an infinite number of repetitions of the same basic period in the z -direction. We know from Bloch theory [41] that the solutions of the wave equations in such a periodic structure take the following form :

$$\psi_{k_z}(z) = e^{-jk_z z} \cdot u_{k_z}(z) \quad (3.8)$$

where ψ represents any component of the electromagnetic field and u_{k_z} is a function with the same periodicity as the grating, i.e. $u_{k_z}(z) = u_{k_z}(z + \Lambda)$. There are different functions ψ corresponding to each k_z . The propagation constant is in general a complex number

$$k_z = \beta + j\alpha \quad (3.9)$$

and the imaginary part α results in an exponentially decaying wave along the z -direction. Such a wave is sometimes also called leaky surface-wave. The α in equation (3.9) corresponds to α in equation (3.3). If we can calculate the complex propagation constant of such a Bloch-mode in a grating coupler, then we have also found the coupling strength of the grating coupler.

An analysis of grating couplers with the Floquet-Bloch expansion method was first described by Neviere [42] and Peng [43]. They use different numerical methods to solve the problem but both start with Fourier expansion of the periodic function u_{k_z} . We will not give more details here, because the mathematics involved are rather tedious. These methods are rigorous because there are no approximations used, apart from the fact that the infinite Fourier series is truncated, so care should be taken to achieve convergence and avoid numerical stability problems. Different methods are found in literature that start from the exact formulation of the periodic problem and use some approximations to solve the problem without having to use complex mathematics. One example is given in [44].

We have used the eigenmode expansion method from section 3.4.3 to calculate these Bloch modes. A simulation result of a 10 nm and 50 nm deep grating is shown in figure 3.6.

For a detuned grating, the leakage parameter α is only slightly wavelength dependent. When comparing these results with a calculation on a finite structure, it turns out that the results match very well as expected (see example in section 3.6). The field of the Bloch mode can also be calculated and used to determine the power that is coupled to the substrate or superstrate.

The situation is rather different around the second order Bragg wavelength, β becomes zero and α reaches a minimum value. At this wavelength, there is no propagating mode, but a standing wave. Because of this second order Bragg reflection, it is not a priori known if the results for an infinitely periodic structure are still valid for a finite structure. We have simulated finite structures with the method from section 3.4 and found that for this particular structure, infinite means > 100 periods. Therefore the results for a fibre coupler with approximately 20 periods can be very different.

The results of the Bloch modes are valid for infinite structures. In the case of a sufficiently detuned grating, they are also valid in the bulk of a finite structure. But at the start of the grating, there can be a mode mismatch between the waveguide mode and the Bloch mode of the waveguide grating.

3.3.2 Waveguide grating resonances

A very different way to look at grating couplers is from the viewpoint of resonant waveguide grating structures. In these structures, the wave-

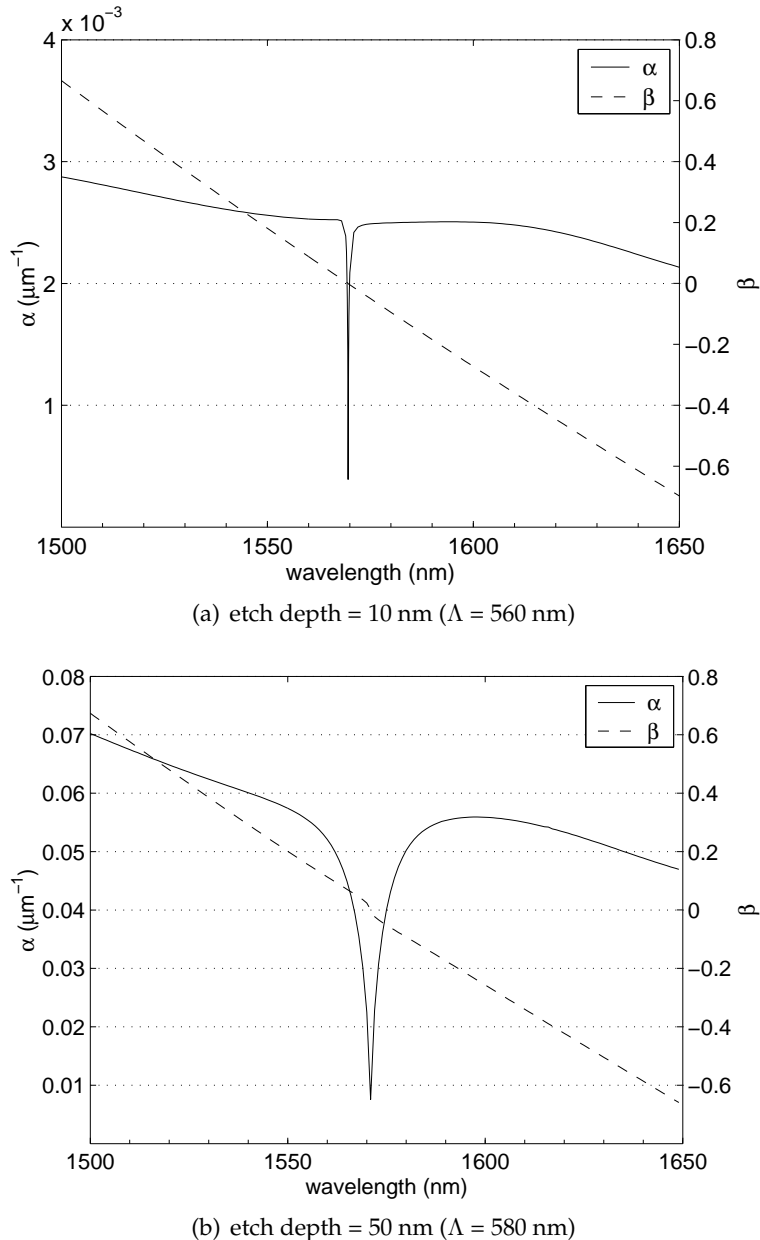


Figure 3.6: Simulation results of a Bloch mode using CAMFR. The simulated structure is shown in figure 3.5a. The SOI waveguide has a 220 nm thick Si core and an infinite SiO_2 bottom cladding. The real and imaginary part of the propagation constant are plotted on a different scale for clarity.

guide grating is illuminated by a plane wave from the top, as shown in figure 3.5b. A resonance phenomenon can occur in waveguide grating structures and those resonances are related to the excitation of guided modes of the waveguide [45].

When such a structure (figure 3.5b) is illuminated by an incident plane wave from the top, part of the wave is directly reflected and transmitted and part is diffracted and coupled to a waveguide mode. Part of this light in the waveguide is rediffracted and interferes with the directly reflected and transmitted part of the light beam. For certain wavelengths and angular orientations, the structure resonates and 100% zeroth order reflection or transmission occurs.

In the vicinity of the resonances, the reflectance spectrum can be explained with a pole-zero model [45, 46]. The shape of the resonance depends on the relative positions of the pole and zero. Maxima or minima in the transmission can occur. The width of these resonances is related to the imaginary part of the propagation constant β of the waveguide mode and thus the coupling strength of the grating [47]. This relation is given by :

$$\alpha = \frac{\pi \Delta\lambda}{\Lambda \lambda_{peak}} \quad (3.10)$$

When the zeroth order reflection is calculated as a function of incidence angle θ for a fixed wavelength, similar resonance peaks are obtained. The relation between the peak width $\Delta\theta$ and the coupling strength of the gratings is given by :

$$\alpha = \frac{\pi \Delta\theta \cos(\theta_{peak})}{\lambda} \quad (3.11)$$

In the vicinity of vertical coupling, two counter-propagating guided modes are excited and the grating also acts as Bragg-reflector for the waveguide mode. The resonance in the reflection is influenced by both the first order coupling of the grating and the second order reflection. As a consequence it is no longer possible to derive the coupling strength from the width of the resonance.

We will illustrate this by showing some calculated reflectance spectra of the SOI fibre coupler. We used the simulation tool RODIS² for

²RODIS is a simulation tool originally written by Bart Dhoedt and extended by Danaë Delbeke. Thanks to Lieven Vanholme a version with a user-friendly interface is now available for download from <http://photonics.intec.ugent.be>.

these calculations, which is based on the rigorous coupled wave analysis method [48, 49].

The calculated reflection spectrum of a shallow grating is shown in figure 3.7(a). The grating period is 560 nm and the etch depth 10 nm. The wavelength of the reflection peak for normal incidence corresponds to $n_{\text{eff}} = \lambda/\Lambda = 2.8$. In the limit of a very shallow grating, the n_{eff} of the waveguide is found. In the case of non-normal incidence, two peaks are present. These peaks correspond to the excitation of a forward and backward propagating mode. The width (FWHM) of the peaks is 0.6 nm which corresponds to a coupling strength $\alpha = 0.0022 \mu\text{m}^{-1}$.

In figure 3.7(b), the grating period is 610 nm and the etch depth 50 nm. The picture looks similar as in the $\text{ed}=10$ nm case, but the peaks are broader, because the coupling strength is higher. The reflection peaks are also asymmetric. The width of the peak around 1550 nm is 20 nm. This corresponds to a coupling strength $\alpha = 0.066 \mu\text{m}^{-1}$.

3.3.3 Coupled mode theory

A coupled mode approach is a phenomenological description, the behaviour of the structure is described by the coupled mode equations. These contain a number of parameters, the coupling constants. The most difficult part is the calculation of these constants for a particular structure.

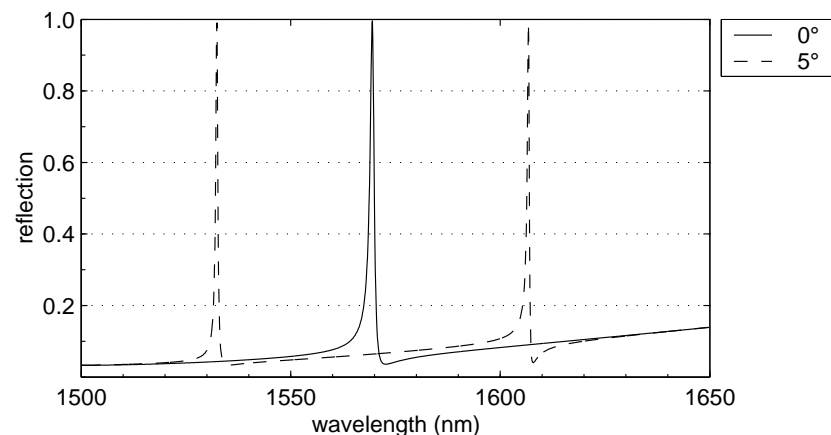
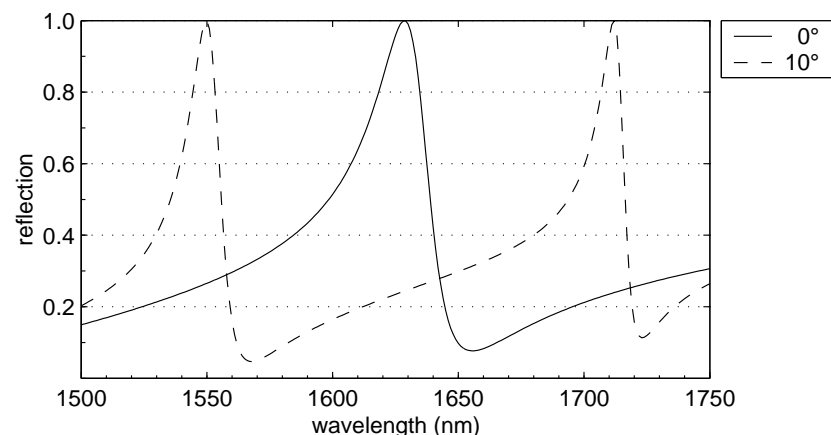
Coupled mode theory is a convenient way to describe Bragg reflectors [50]. A coupled mode analysis that includes radiation effects in higher order Bragg gratings is presented in [51]. This method can be used to calculate the out-of-plane radiation for second-order gratings, both in the resonant and non-resonant case. We will give a short outline of the coupled mode theory here, but for the mathematics and details we refer to [52]. The structure is shown in figure 3.8.

The field in the waveguide grating is expanded in partial waves

$$E_x(y, z) = \sum_{m=-\infty}^{+\infty} E_m(y, z) \exp(j\beta_m z) \quad (3.12)$$

where $\beta_m = \beta_0 + 2\pi m/\Lambda$ and β_0 and $E_m(y, z)$ are to be determined. Because the grating is a second-order grating, the guided modes are expressed in the form

$$\begin{aligned} E_0(y, z) &= R(z)E_0(y) \\ E_{-2}(y, z) &= S(z)E_0(y) \end{aligned} \quad (3.13)$$

(a) etch depth = 10 nm ($\Lambda = 560$ nm)(b) etch depth = 50 nm ($\Lambda = 610$ nm)**Figure 3.7:** Reflection spectrum of a plane wave incident from the top.

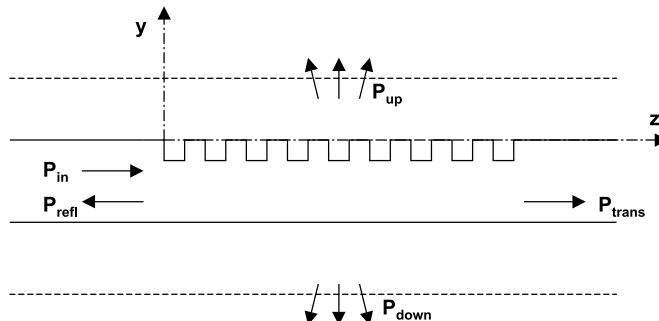


Figure 3.8: Structure that is calculated in [52] with coupled-mode theory.

where $E_0(y)$ is the unperturbed guided mode profile. Under the assumption that all the partial waves have a similar z -dependence and after substantial manipulation it is found in [52] that $R(z)$ and $S(z)$ satisfy the following coupled-mode equations :

$$\begin{aligned} \frac{dR}{dz} + (\alpha - j\delta - j\zeta_1)R &= j(\kappa^* + \zeta_2)S \\ -\frac{dS}{dz} + (\alpha - j\delta - j\zeta_1)S &= j(\kappa + \zeta_4)R \end{aligned} \quad (3.14)$$

where α is the material gain and δ is the deviation from the Bragg condition ($\delta = \beta - \beta_0$). κ is the conventional coupled mode constant that is also present in the analysis of DBR gratings. The ζ constants are related to radiation effects, the imaginary part of ζ corresponds to power loss due to radiation. The calculation of the coupled mode constants involves overlap integrals and the partial waves are solutions of the wave equation with a source term. For a sufficiently detuned grating, the cross-coupling constants κ , ζ_2 and ζ_4 are zero. In this case $R(z)$ becomes an exponentially decaying term as expected.

Reflection, transmission, and radiated power can be calculated as a function of the coupled mode constants. The formulas for the calculation of the constants itself are also given in [52] and the theory is also extended there to arbitrary groove shapes. The partial waves used in [52] are a first order perturbation solution of the Floquet-Bloch expansion method. It can be shown that the coupled-mode formalism is equivalent to the Floquet-Bloch formalism if a first order perturbation is used [53, 54]. The resonant waveguide grating structures from section 3.3.2 can also be described with a coupled mode theory [55].

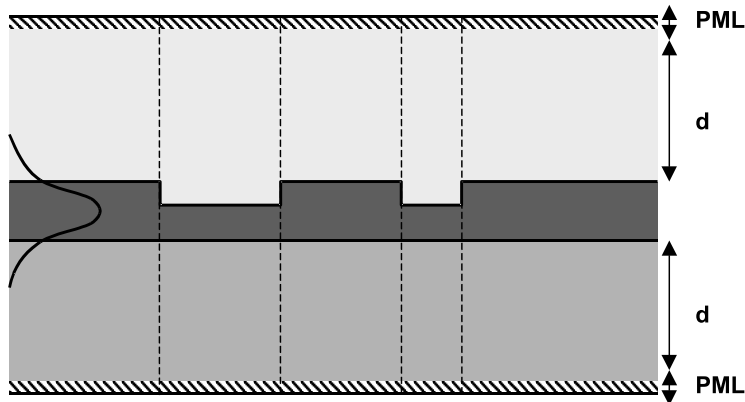


Figure 3.9: Eigenmode expansion method. The structure is divided into sections. In each section the refractive index does not change along the propagation direction.

3.4 Eigenmode expansion

3.4.1 Introduction

The eigenmode expansion method can be used to analyze very general structures but is also very well suited for waveguide grating couplers. We will only describe the basic theory in order to better understand the advantages and limitations of the method. For an in depth review of the eigenmode expansion method, we refer to [56].

The structure is divided into sections. In each section the refractive index does not change along the propagation direction. This is shown in figure 3.9. In a first step the eigenmodes of every section are calculated. These modes are the guided modes, but also the radiation modes. The total field can be written as a linear combination of the eigenmodes. In a 2-D problem, the sections are slab waveguides.

All these sections together form the total structure or stack. By using a mode-matching technique at the interfaces between the sections, the scattering matrix of the entire stack is calculated. This scattering matrix gives us the reflection and transmission of the total stack. For finite periodic structures, a special calculation scheme can be used that makes the calculation time logarithmic in the number of periods instead of linear. The fields and the radiated power can also be calculated at any position in the stack, for a given excitation. We always use the guided mode of the input waveguide as excitation.

3.4.2 Boundary conditions

The eigenmode method can only simulate structures of a limited size in the vertical direction. At the boundaries of the simulations space, reflections can occur that are not present in the real, open structure. These reflections cause wrong results and should be avoided. This problem can be solved by using perfectly matched layers (PML) at the top and bottom boundaries. This PML is a kind of artificial material [57, 58] that absorbs the incident radiation and does not reflect it back into the simulation space.

As with most numerical methods, the parameters must be carefully chosen to obtain accurate results. The most important parameters are the number of modes N , the distance d between the structure and the boundaries of the computational domain, and the thickness of the PML. If N is too small, the results will be wrong. In the case of the grating coupler, a relatively large number of (radiation) modes is needed to accurately describe the radiation coming out of the waveguide. If the required N is too large, the calculation time becomes very long and numerical problems may also occur. If d or PML are too small, light may reflect at the boundaries of the computational domain and couple back to the waveguide. Again this may give wrong results. If d or PML are chosen too large, the calculation becomes very slow and numerical problems may occur. So a good choice of these parameters is important. The situation is even more complicated because the required number of modes N depends on d . Also the optimal PML thickness depends on d .

Fortunately, it is possible to find values for these parameters that give accurate results. In figure 3.10, we have plotted the total radiated power of a waveguide grating as a function of d for different PML values. The number of modes used is 120. It can be seen that without PML, the results do not converge at all. Increasing the PML thickness helps a lot and for a PML thickness of $0.5 \mu\text{m}$, the residual oscillation has become very small (<1%).

Similar calculations can be performed as a function of the number of modes for a fixed d or PML thickness. We have discovered that $d=7 \mu\text{m}$, $\text{PML}=0.4 \mu\text{m}$ gives accurate and numerically stable results for the SOI grating couplers in the wavelength range around $\lambda=1550 \text{ nm}$. The number of modes used is between 100 and 130, depending on the layer structure used. With these parameters, the error on the results is smaller than a few percent.

The eigenmode expansion method we have described, is also called the bi-directional eigenmode method, because the guided modes prop-

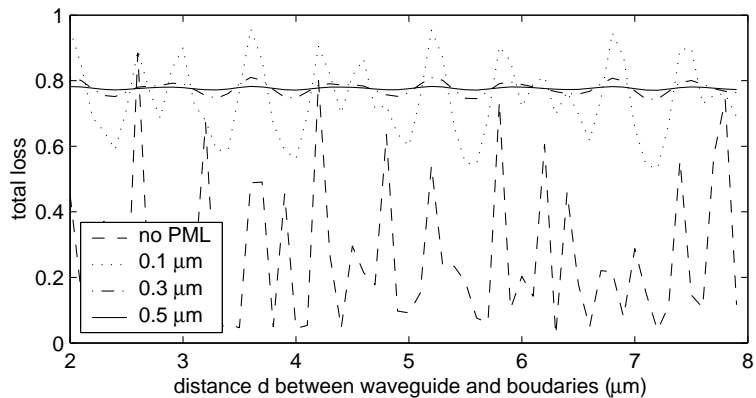


Figure 3.10: Convergence of the eigenmode expansion method with PML.

agate from left to right and from right to left. A quadri-directional eigenmode expansion scheme is described in [59]. In this scheme, the guided modes also propagate in the vertical direction. The advantage is that no PML is needed. Without PML, a real mode solver can be used instead of a complex mode solver. The disadvantage is that two sets of eigenmodes must be calculated. One set are the regular eigenmodes that propagate horizontally, the modes of the second set propagate vertically. In the case of a grating with 20 periods, it is very difficult to calculate this second set of eigenmodes.

3.4.3 CAMFR

The simulation tool CAMFR [60] implements the eigenmode expansion method with PML boundary conditions. We have used CAMFR for most of the simulations in chapter 4, because it is very versatile. For a complete overview of the possibilities of this tool, we refer to the CAMFR manual [60]. An example script to perform SOI waveguide grating coupler calculations is given in appendix A.

This tool is very well suited for modelling finite waveguide gratings. It can handle both the resonant and non-resonant case and is not limited to purely periodic structures. It is also possible to add sources to a structure. In this way Green's functions can be easily calculated. CAMFR can also calculate the complex propagation constants of Bloch modes in periodic structures.

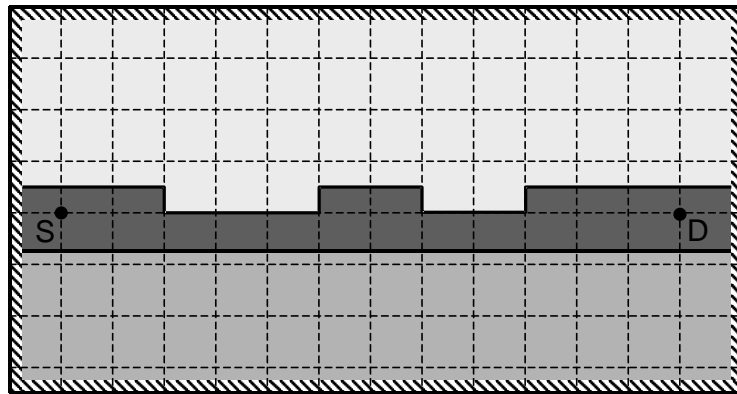


Figure 3.11: FDTD method. In reality the grid size will be much smaller than drawn in the figure. S represents a source and D a detector. Sources and detectors can be placed everywhere.

3.5 FDTD

The finite-difference time-domain method (FDTD) uses a brute-force discretisation of Maxwell's equations [61]. The structure is discretised using a uniform grid (see figure 3.11) and the derivatives in Maxwell's equations are replaced by finite differences. The grid size used is very important, a small grid size is required to get accurate results. However using more grid points results in longer calculation times. The grid size also imposes an upper limit on the time step that can be used, because of stability requirements.

FDTD can in theory handle almost any 2-D or 3-D structure, but computation time and memory requirements limit the size of the problems that can be handled. For the SOI grating coupler, a grid size of 10 nm is typically needed. To calculate the coupler, sources are placed in the waveguide to excite the waveguide mode and detectors are placed above the grating to detect the outcoupled power. Appropriate boundary conditions (e.g. PML) are used to avoid reflections at the boundaries of the computational domain and model open structures.

Because of the long calculation times for the structures, it is not feasible to use FDTD as a design method for the grating coupler. We used it sometimes to verify the results obtained with other numerical methods.

3.6 Comparison of simulation results

In this section we compare some simulation results calculated with different methods. Figure 3.12 shows the coupling strength α as a function of etch depth for a SOI grating coupler. The grating period and wavelength are chosen with the intention of staying away from the second order reflection peak. The numerical methods used are :

- Calculation of the complex propagation constant of a leaky guided *Bloch* wave in a periodic structure. The simulation tool CAMFR was used for the calculation.
- Eigenmode expansion and propagation method for the simulation of *finite* grating coupler structures. The coupling strength is derived from the transmitted power through a finite grating with the formula $2\alpha = \frac{-\ln(T)}{m\Lambda}$. The simulation tool CAMFR is used.
- α derived from the width of the resonance in a resonant waveguide grating analysis using equation (3.11). The reflection of a plane wave as a function of incidence angle θ is calculated with RODIS.
- *Perturbation* analysis using a Green's functions method and an averaged refractive index in the grating region. The Green's functions for a source in the SOI waveguide are calculated with CAMFR.
- Closed form expressions for α given by Parriaux et al. in [40]. The grating is supposed to be sinusoidal in this method, while the other methods use a rectangular grating. We have chosen the amplitude of the sinus corresponding to the first Fourier component of the rectangular profile ($\sigma = \frac{2}{\pi}ed$).

For shallow gratings ($ed < 20$ nm), all the results match very well. The simple perturbation theory overestimates the coupling strength for deeper gratings. This was expected because the assumption of a small perturbation is not valid for deeper gratings. Also the results based on RODIS go wrong for gratings deeper than 30 nm. The reason for this can be seen in figure 3.7(b). The resonance peaks become asymmetric, because the two resonances are no longer completely separated. As a result the width of the resonances is too large and α is overestimated. It is the extraction of α that goes wrong, not the calculation of the resonances itself.

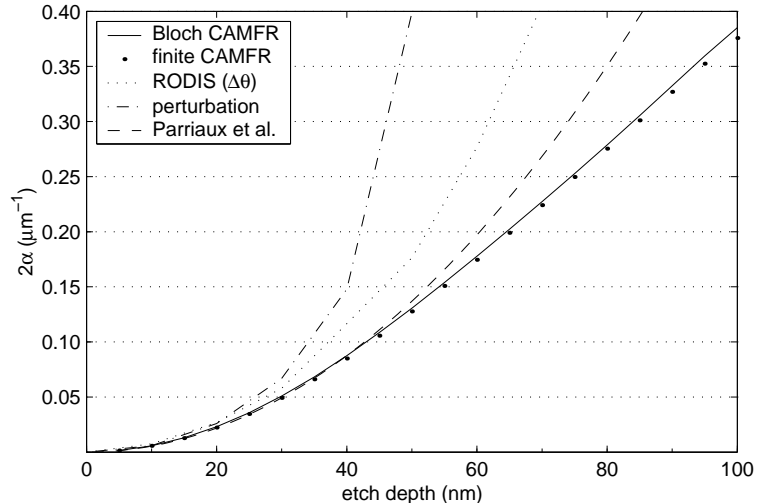


Figure 3.12: Simulation results obtained with different numerical methods. The coupling strength α is calculated as a function of the etch depth. The SOI waveguide has a 220 nm thick Si core and an infinite SiO_2 bottom cladding. $\Lambda=630 \text{ nm}$, $\text{ff}=0.5$, $\lambda=1550 \text{ nm}$

The results from the finite grating and the Bloch mode match perfectly. Only for very deep gratings there is a small difference. The cause of this is the second order reflection peak. For a 100 nm deep grating and the other parameters used, the second order reflection can not be neglected anymore. The analytical results from [40] match the CAMFR results for grating depths $< 50 \text{ nm}$. For deeper gratings the coupling strength is overestimated. According to [40], the analytical equations are valid for gratings with $\frac{\sigma}{\Lambda} < 7\%$. This is consistent with our results.

To verify our results, we have also simulated some other grating couplers that are described in the literature. A first example is the structure shown in figure 3.13(a). The next table compares our results with [62]. Reference [62] uses the Fourier modal method [63].

$t_g = \lambda = 1.5 \mu\text{m}$	t_f	ref. [62]	CAMFR
TE mode	λ/π	$1.582 + 0.0023j$	$1.582 + 0.0022j$
TM mode	$\lambda/2$	$1.609 + 0.00072j$	$1.609 + 0.00069j$

The results are in excellent agreement. In [43], the coupling strength is calculated as a function of the grating thickness for the same structure, but only for TE polarization. Figure 3.14(a) compares the CAMFR results with the results given in figure 9 in reference [43]. The results

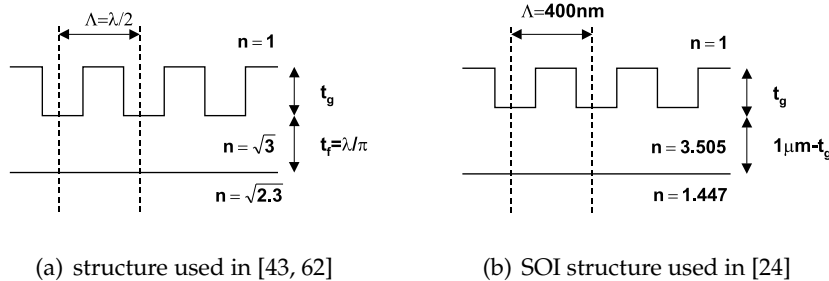


Figure 3.13: Grating coupler structures used for comparison with our simulation results.

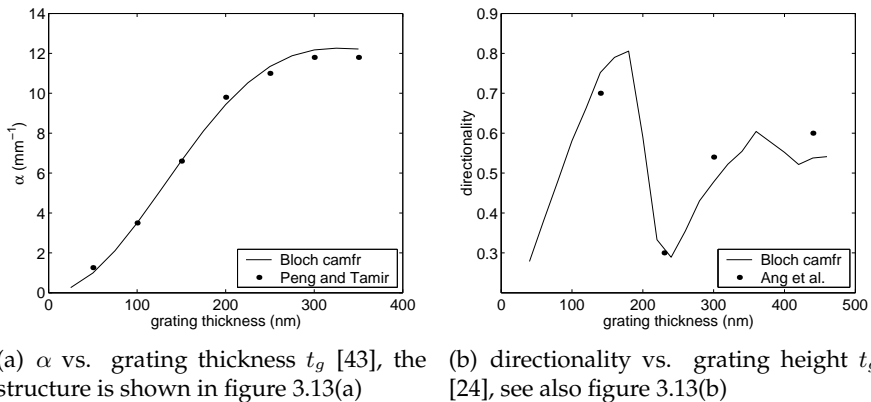


Figure 3.14: Comparison between simulation results and literature.

match very well. It should be noted that only a figure is given in [43] and as a result there is a small error on the values derived from that figure.

A last example is the SOI structure shown in figure 3.13(b). It should be noted that the waveguide in this example is a thick multi-mode SOI waveguide and $\lambda=1.3\mu\text{m}$. In figure 3.14(b), we have compared our simulation results with experimental results from [24]. There is also a good agreement.

3.7 Coupling to fibre

3.7.1 Introduction

Because we want to use the grating coupler to couple to optical fibres, we do not only have to calculate how much light is coupled out of the waveguide but also how much couples to a fibre. Although in theory it is possible to include a fibre directly in the simulated structure in some methods, this is not the best option because it will increase the complexity of the problem. Therefore the fibre mode is approximated by a Gaussian profile. The fibre is characterized by the spot-size or beam diameter instead of the core diameter and refractive index. Most suppliers of optical fibres supply the beam diameter in the data sheet. The Gaussian beam approximation is very accurate for calculating the launching efficiency at the input of a fibre³. As beam diameter we use 10.4 μm , because this value is given in the data sheet of the fibres we have used for experiments. This beam diameter is in fact also wavelength dependent, but we neglect this in our calculations. Before giving the equations used to calculate the fibre coupling efficiency, we briefly discuss the basic properties of Gaussian beams.

3.7.2 Gaussian beams

A Gaussian beam is a paraxial solution of the wave equation. The beam size at the origin is also called the beam waist. The amplitude has a Gaussian profile at the origin and remains Gaussian during propagation through free space :

$$|E(\rho, z)| = \frac{w_0}{w(z)} \exp\left(-\frac{\rho^2}{w^2(z)}\right) \quad (3.15)$$

$$w(z) = w_0 \sqrt{1 + \frac{2z^2}{kw_0^2}} \quad (3.16)$$

The equations are presented in most textbooks on the fundamentals of optics or photonics [64] and we will not repeat them all here. But as an illustration, we have plotted a Gaussian beam with waist radius $w_0=5 \mu\text{m}$ in figure 3.15. The origin ($z=0$) represents the end facet of the

³The Gaussian approximation underestimates the evanescent field in the fibre cladding [29], but this is only important when calculating bend losses for example. For our work this is not relevant.

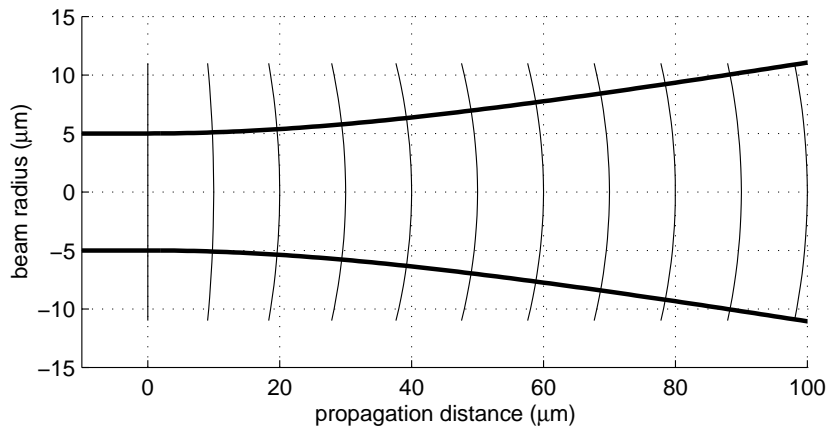


Figure 3.15: Diffraction of a Gaussian beam with waist radius $5 \mu\text{m}$.

fibre. The thick line is the beam radius $w(z)$ and the thin lines represent the phase at certain positions.

At the origin, the beam has a planar phase front, which is a property of a plane wave. Far away from the origin, the phase front becomes spherical, as in a spherical wave. At $z=10 \mu\text{m}$, the phase is approximately 10° at the beam radius. For $z=20 \mu\text{m}$, the phase is already 20° at the beam radius and further away the beam is expanding rapidly. We can conclude that for butt-coupling to fibre, the distance to the fibre should be kept as small as possible and certainly $< 10 \mu\text{m}$.

There exist some papers that describe the modelling of a grating coupler illuminated by a focused Gaussian beam. In [65] a beam propagation method is used to calculate the coupling of an elliptical beam. In [66] a coupled mode formalism is described. Because we butt-couple to fibre, we can use a simpler approach.

3.7.3 Equations and approximations

In a numerical method that uses plane waves, the coupling to a Gaussian beam can be calculated by expansion of the Gaussian beam in plane waves. In the eigenmode expansion method, the coupling to a Gaussian beam can be calculated with an overlap integral. When we know the electromagnetic fields at the position of the fibre facet, the coupling to fibre is calculated with the following integral [29] :

$$\gamma = \frac{\left| \iint E \times H_{fib}^* \right|^2}{\operatorname{Re} \iint E \times H^* \cdot \iint E_{fib} \times H_{fib}^*} \quad (3.17)$$

Equation (3.17) is only exact in uniform media and for weakly guiding structures. It does not take into account the reflection at the interface, but it is very accurate when an index matching layer is present between the grating and the fibre. It can also be used when there is air between the grating and the fibre, but in this case, the approximation is less accurate because the reflection is larger. Yet it is still sufficiently accurate to optimize a grating structure for maximum coupling efficiency.

In equation (3.17), γ is the overlap between the field and the fibre mode. To calculate the coupling efficiency from waveguide to fibre, γ must be multiplied by the outcoupled power efficiency. If the waveguide mode and the fibre mode are normalized, the coupling efficiency to fibre becomes :

$$\eta = \left| \iint_S E \times H_{fib}^* dS \right|^2 \quad (3.18)$$

where S is the facet of the fibre.

The complete coupler problem is a 3-D problem. In the case of 1-D gratings, the problem can be reduced to two 2-D problems with high accuracy. The reason for this is that the width of the SOI ridge waveguide used is much larger than the height and the wavelength. In figure 3.16 the fundamental TE mode of a $12 \mu\text{m}$ wide SOI ridge waveguide is shown. Because of the large width of the waveguide it is a very good approximation [50] to write the field $\psi(x, y)$ as $\psi_1(x) \cdot \psi_2(y)$ where $\psi_2(y)$ represents a field component of the slab mode and $\psi_1(x)$ is a lateral mode profile. The validity of this approximation is confirmed by the fact that the effective index of the ridge waveguide mode, calculated with a fully vectorial mode solver (2.8302) is almost identical to the effective index of the SOI slab mode (2.8309). Therefore we consider only the 2-D grating problem in the (y, z) plane for TE-polarization, as is done in most grating coupler literature.

To calculate equation (3.18), the fibre mode is approximated by a Gaussian beam with beam diameter $2w_0=10.4 \mu\text{m}$ and the field $E(y, z)$ resulting from the 2-D grating calculation is multiplied by $E(x)$ to take into account the lateral direction. When neglecting the smaller field components, taking into account that $\cos(\theta) \approx 1$, and neglecting the

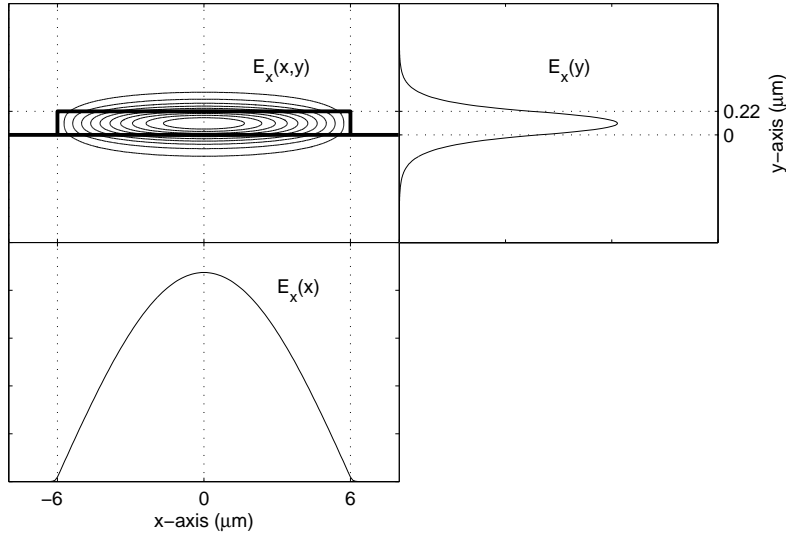


Figure 3.16: Fundamental TE mode of a 12 μm wide SOI waveguide. $E_x(x,y) \approx E_x(x).E_x(y)$ because of the large width of the waveguide.

beam divergence in the x -direction, equation (3.18) can be further simplified to :

$$\eta = \left| \iint E(x)E(y=y_0,z)Ae^{-\frac{(x-x_0)^2+(z-z_0)^2}{w_0^2}}e^{(jn\frac{2\pi}{\lambda}z\sin\theta)}dxdz \right|^2 \quad (3.19)$$

The constant A represents the normalization of the Gaussian beam. This formula can be separated in two terms, one dependent on x and the other dependent on z . If we call the x -dependent term ξ , the coupling efficiency to fibre is the coupling efficiency of a 2-D problem multiplied by the correction factor ξ . For a 12 μm wide SOI ridge waveguide and $w_0=5.2 \mu\text{m}$, we calculated $\xi=0.97$. For a 10 μm wide SOI ridge waveguide we get $\xi=0.93$.

The refractive index n in equation (3.19) is 1.46 when an index matching layer is present on top of the grating. In this case $n=n_{\text{fib}}=1.46$ and it does not matter if the fibre is cleaved straight or angle cleaved⁴. When there is air between the grating and the fibre, $n=n_{\text{air}}=1.0$, but only if the

⁴We call a fibre straight cleaved when the facet is perpendicular to the fibre axis. When there is an angle θ between the fibre axis and the surface normal to the facet, the fibre is angle cleaved.

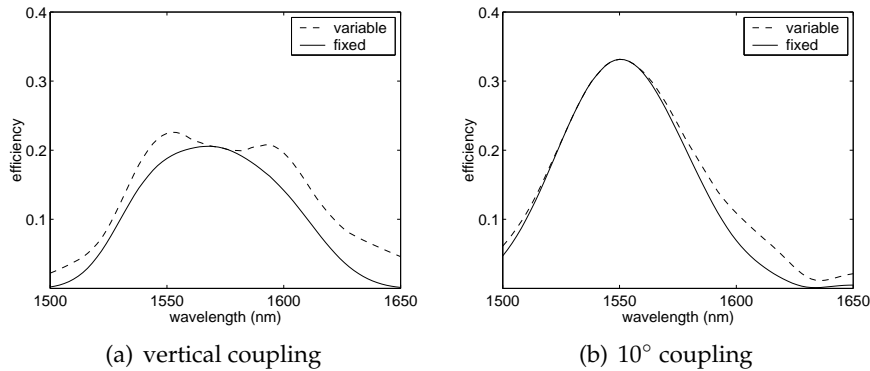


Figure 3.17: Calculation of coupling efficiency to fibre : difference between fixed and optimal position.

fibre is cleaved straight. If the fibre is angle cleaved, the situation is more complicated. Because we have only used straight cleaved fibres in our measurements, we have used $n=1$ in the air case and $n=1.46$ in the index matching layer case in the simulations.

For the position of the fibre, we have used $y_0=1.5 \mu\text{m}$ as the height of the fibre above the waveguide. The longitudinal position of the fibre z_0 was chosen optimal. This optimal z_0 depends on the grating and the wavelength used. For the calculation of the efficiency as a function of wavelength, we used a fixed position z_0 . This fixed position is the optimal position for the wavelength with the highest efficiency. This is illustrated in figure 3.17.

Finally, we calculate the maximum overlap between a Gaussian profile and some other profiles. In figure 3.18(a) the overlap with an exponential profile as a function of α is shown. The maximum is 80% for $\alpha=0.13 \mu\text{m}^{-1}$. This corresponds to a coupling length $L_c=3.8 \mu\text{m}$. This agrees with the formula $w_0 = 1.37L_c$ given in [25]. The field profiles corresponding to this optimal situation are shown in figure 3.18(b). In the second example (figure 3.19) we use a rectangular profile. The maximum overlap is 89% when the beam width equals the 1/e width of the Gaussian profile. The field profiles corresponding to the optimal situation are shown in figure 3.19(b).

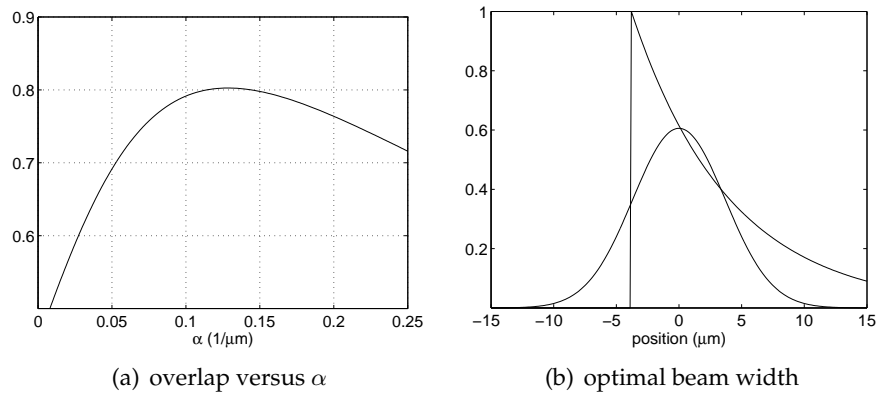


Figure 3.18: Overlap between Gaussian and exponential profile. The diameter of the Gaussian is $10.4 \mu\text{m}$.

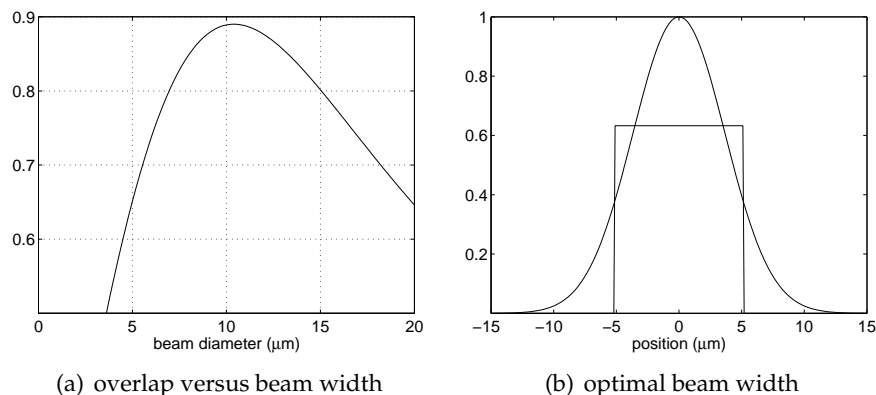


Figure 3.19: Overlap between Gaussian and rectangular profile. The diameter of the Gaussian is $10.4 \mu\text{m}$.

3.7.4 Reciprocity

The reciprocity theorem is very powerful and it can be proven based on Maxwell's equations [67], but one should take care not to misinterpret the results. Consider a linear optical system with N ports. These ports are the modes of one or several waveguides. The system can be described by a scattering matrix S which gives the relation between the inputs and the outputs of the system

$$\mathbf{B} = \mathbf{S} \cdot \mathbf{A} \quad (3.20)$$

where A and B are vectors containing the amplitudes of input and output modes. The element S_{ij} is the transmission from input mode j to output mode i . When the materials used are reciprocal⁵, the optical system is also called reciprocal and the scattering matrix is symmetric :

$$S_{ij} = S_{ji} \quad (3.21)$$

or in others words, the transmission from port i to port j is the same as from port j to port i . Although we have described reciprocity for the case of a system with N modes, it can be proven that it is also valid in the case of an open system, where energy can leak away [68]. In the case of the fibre couplers, this means that the transmission from a fibre mode to a waveguide mode is the same as from a waveguide mode to a fibre mode. Because we use single-mode fibres and waveguides, we can calculate the coupling efficiency either from waveguide to fibre or from fibre to waveguide. The reciprocity theorem tells us that the coupling efficiency is the same in the two cases.

⁵All materials used in this work are isotropic and thus also reciprocal. An example of a non-reciprocal material is a ferromagnetic material (such as Fe,Co) in the presence of a magnetic field.

Chapter 4

Design of a 1-D grating coupler

A good design of the grating couplers is needed to achieve a high coupling efficiency to fibre. In this chapter we present different optimized designs and discuss the properties of the couplers. We start with a simple uniform grating and introduce enhanced structures afterwards. At the end, a summary of the results is given.

4.1 Introduction

We use the simulation tool CAMFR, which is based on eigenmode expansion for the simulations. This method, which was described in section 3.4, can handle all the different grating coupler configurations we have looked at. Sometimes a simplified model is used to explain the physics. All the results given in this chapter are for TE-polarization, with the exception of section 4.2.5 where we have a look at the TM case.

Only 1-D gratings are treated in this chapter. The results are obtained using 2-D calculations. This 2-D model is a good approximation for the real 3-D structure as was discussed in section 3.7. The simulation model is shown in figure 4.1. The waveguide mode is incident from the left. The reflection and transmission at the finite grating are calculated. Also the power that is coupled up and down and the coupling efficiency to fibre are calculated. The fibre itself is not present in the simulated structure, but the coupling efficiency is calculated using an overlap integral with a Gaussian profile as was discussed in section 3.7.

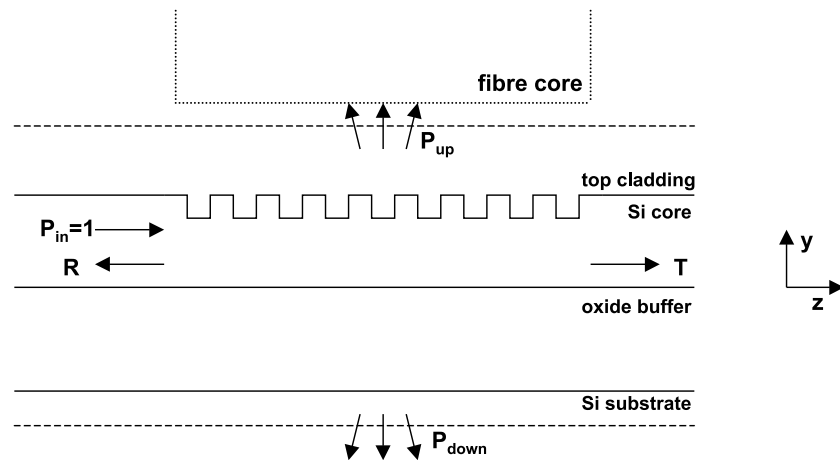


Figure 4.1: Simulation model of a 1-D grating coupler structure. The input is the normalized waveguide mode. R is the reflection at the grating. T is the transmission through the finite grating. P_{up} and P_{down} are the power that is radiated up and down.

Table 4.1: Approximate conversion factors.

coupling loss	0.5	1	3	6	10	20	dB
coupling efficiency	90	80	50	25	10	1	%
loss (dB) = $-10 \log(\text{efficiency})$							

We use SOI waveguides in this work. Results for GaAs/AlOx material, which has similar refractive indices are given in [69]. Waveguides in other interesting materials, that have a different refractive index contrast between the core and cladding, are briefly treated in section 4.2.8.

The results are sometimes presented in linear units and sometimes in logarithmic units (dB). For the reader who is not used to these units, table 4.1 can help to convert between linear and dB units. The cited values are rounded for easy conversion.

We have verified the accuracy of the results obtained with CAMFR by simulating some grating couplers presented in the literature. This comparison was presented in chapter 3. Because we did not find publications with results on couplers with a very short coupling length, we have also verified some results, in particular the couplers with a

high efficiency, with FDTD-simulations. The difference in calculated efficiency was always below 3% (absolute error).

4.2 Uniform rectangular grating

We will start with a study of uniform gratings with rectangular grating teeth. These are structures that are purely periodic but of finite extent. Rectangular grating teeth are the easiest structures to fabricate and to simulate. The waveguide layer structure is 220 nm Si on top of 1000 nm SiO₂ on top of a Si substrate. The grating is etched in the Si core layer. On top of the structure there is either air ($n=1$) or an index matching layer ($n=1.46$).

4.2.1 Vertical coupling

The case of vertical coupling ($\theta = 0^\circ$) is very interesting from a practical point of view. Vertical coupling can be achieved when the grating period Λ equals the wavelength λ divided by the refractive index. For a very shallow grating, this index is the effective index of the waveguide mode. As mentioned in chapter 3, this grating is called a second order grating. But for the grating coupler, the first order diffraction is used. The second order diffraction is reflecting back into the waveguide. To avoid any confusion, we will use the term coupler grating instead of second order grating in the rest of this work.

Figure 4.2 shows the reflection R as a function of wavelength for different etch depths. As the etch depth increases, the reflection increases. Also the peak reflection shifts to shorter wavelengths because the average refractive index becomes smaller when the grooves are deeper. The reflection peak corresponds to exactly vertical coupling and in this case the grating is called resonant. In the wavelength ranges outside the reflection peak, the grating is not resonant, but detuned.

Figure 4.3 shows the reflection as a function of wavelength for different filling factors. The smallest reflection peak corresponds to a filling factor of 50%. In fact the filling factor that results in the smallest reflection peak is 47% for an etch depth of 50 nm. Because the etched grating reduces the average refractive index, the optical length of the grating grooves and teeth is the same for a filling factor slightly smaller than 50%. For larger or smaller filling factors, the reflection peak is higher and broader. For very large or very small filling factors, the re-

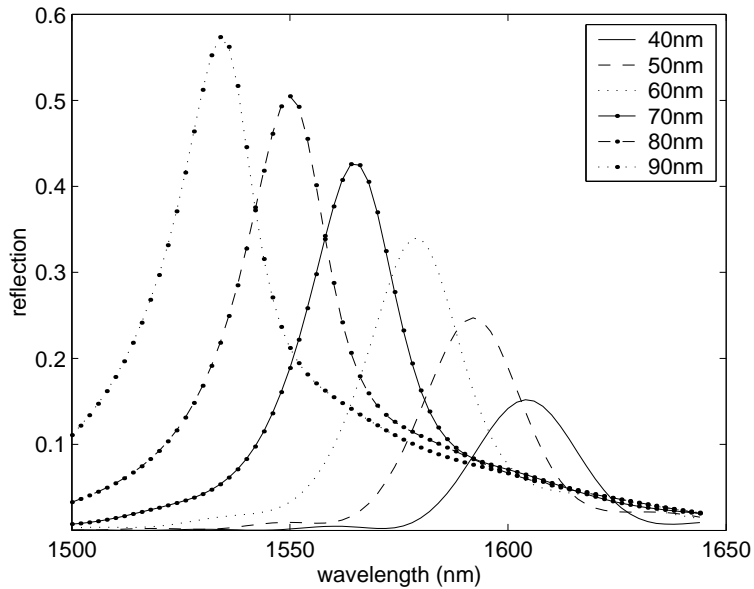


Figure 4.2: Grating reflection versus wavelength for different etch depths. $\Lambda=590$ nm, ff=0.5, N=20

flection drops again. In the limit of 0% or 100% filling factor, there is no grating any more and the reflection becomes zero.

There exists an optimal etch depth for the vertical coupler. If the grating is too shallow, little light will be coupled out by the finite grating. If the grating is too deep, the reflection will be very high. We have optimized the grating parameters for coupling to a vertical fibre. The resulting structure has an etch depth of 50 nm and the simulation results are shown in figure 4.4(a). The peak reflection is 23% and the coupling efficiency to fibre is 21%. The 1 dB bandwidth is 52 nm. When an index matching layer is deposited on top of the structure (figure 4.4(b)), the efficiency is increased to 24% and the reflection is decreased to 16%. In most applications the reflection back into the waveguide is not wanted. One possible solution to avoid this reflection is discussed in the next section.

4.2.2 Almost vertical coupling

To avoid the reflection at the grating, we have to choose a working point away from the second order reflection peak. Either a shorter or longer wavelength can be chosen. As a result, light is coupled out not

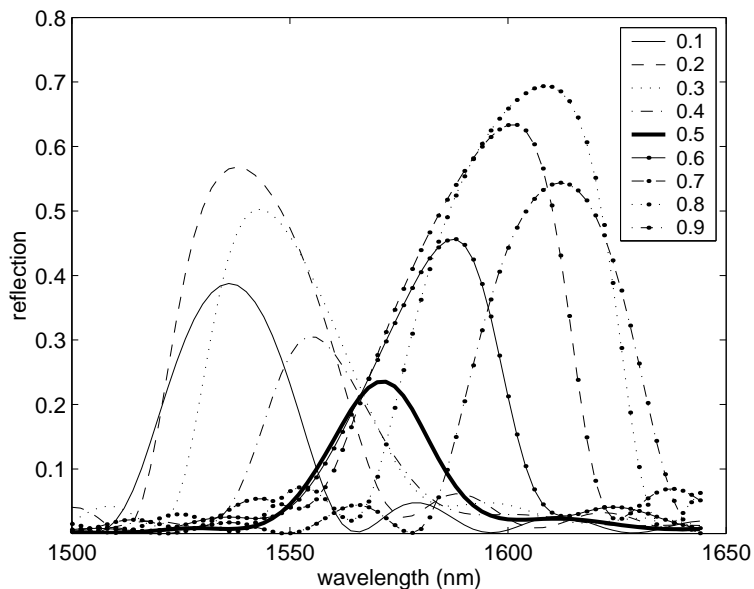


Figure 4.3: Grating reflection versus wavelength for different filling factors.
 $\Lambda=580$ nm, $ed=50$ nm, $N=20$

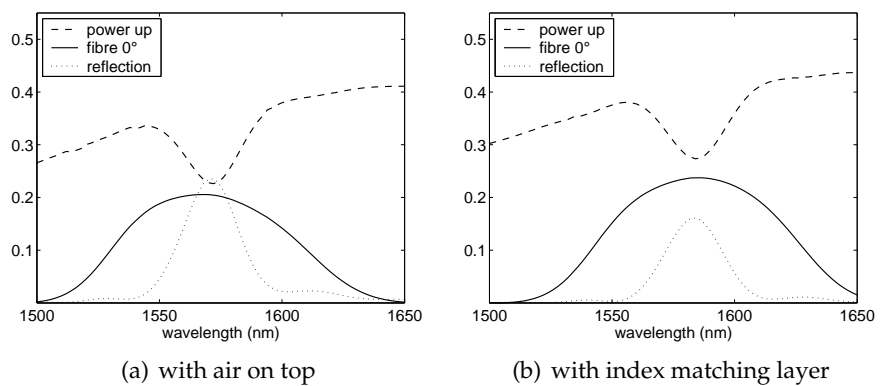


Figure 4.4: Calculated coupling efficiency to fibre for vertical coupling.
 $\Lambda=580$ nm, $ed=50$ nm, $ff=0.5$, $N=20$,

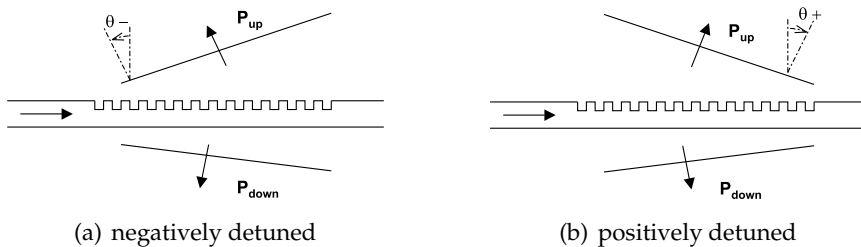


Figure 4.5: Detuned grating and near vertical coupling.

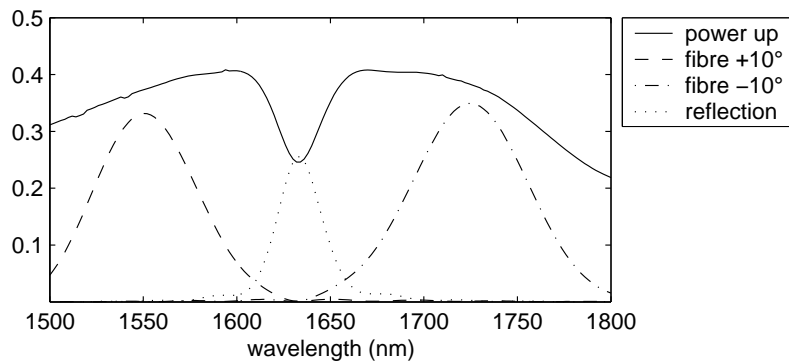


Figure 4.6: Positive and negative detuning. $\Lambda=610$ nm, $ed=50$ nm, $ff=0.5$, $N=20$

exactly vertical, but at a small angle θ with respect to the vertical direction. This grating is also called a detuned grating. Instead of changing the wavelength, the grating period can be changed. The grating can be negatively or positively detuned (figure 4.5). In a negatively detuned grating, the grating period is smaller (K is larger) or the wavelength is longer (β is smaller) compared to the case of vertical coupling. In a positively detuned grating, the grating period is larger (K is smaller) or the wavelength is shorter (β is larger) compared to the case of vertical coupling.

Figure 4.6 shows the coupling efficiency as a function of wavelength for a positive and negative angle. The $\theta=10^\circ$ curve has a maximum for $\lambda=1550$ nm. The case of vertical coupling corresponds to $\lambda=1640$ nm and the $\theta=-10^\circ$ curve has a maximum for $\lambda=1730$ nm. The upwards coupled power curve is not flat away from the resonance wavelength because we use a finite grating. The coupling strength is wavelength dependent and as a result also the total outcoupled power. Also the effect of the finite buried oxide layer is wavelength dependent.

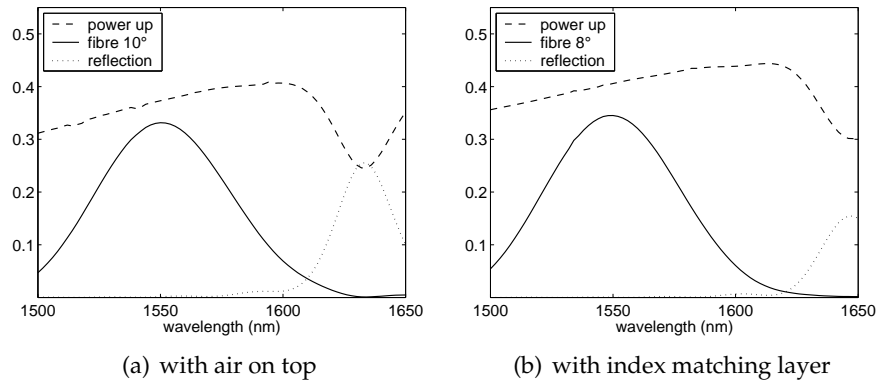


Figure 4.7: Calculated coupling efficiency to fibre for a uniform grating and near vertical coupling. $\Lambda=610$ nm, $ed=50$ nm, $ff=0.5$, $N=20$,

We have chosen to use a positively detuned grating, because this makes the experiments easier. In the experiments, we measure the fibre to fibre transmission on a waveguide with a grating coupler at both ends. In the case of a negative θ , it is much more complicated to make a suitable experimental setup. A positively detuned grating also has a larger period than a negatively detuned grating, which makes fabrication easier.

The coupling efficiency for a 50 nm deep detuned grating is shown in figure 4.7. The efficiency is 33% for $\lambda=1550$ nm and the 1 dB bandwidth is 37 nm. In this wavelength range, the reflection is smaller than 0.2%. With an index matching layer on top, the efficiency is slightly increased. In this case, we have chosen a different angle θ to make the central wavelength the same as in the air case. This grating with 50 nm etch depth is not the optimal structure.

The optimal structure has an etch depth of 70 nm. A period of 630 nm is chosen to shift the wavelength range back to 1550 nm and the simulation results are shown in figure 4.8. The maximum coupling efficiency is 38% for $\lambda=1558$ nm and the 1 dB bandwidth is 46 nm. The reflection is < -18 dB in this wavelength range. With an index matching layer on top of the grating, the efficiency is 46%. The main limitations to the efficiency are the coupling to the substrate and the mismatch between an exponential and a Gaussian profile. The directionality can be improved by optimizing the thickness of the buried oxide layer. This is discussed in detail in the next paragraph.

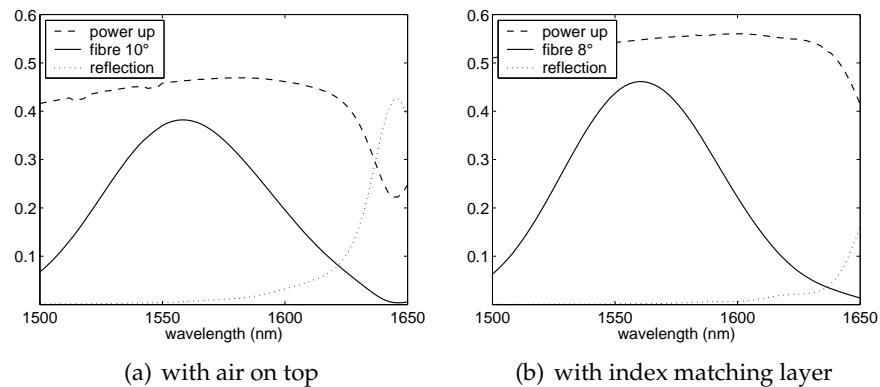


Figure 4.8: Calculated coupling efficiency to fibre for an optimized uniform grating and near vertical coupling. $\Lambda=630$ nm, $ed=70$ nm, $ff=0.5$, $N=20$,

4.2.3 Layer thickness

The thickness of the buried oxide layer has a major effect on the efficiency of SOI grating couplers. This was shown for the first time by Suhara [70]. The effect can be explained as follows : The grating coupler creates an upward and downward propagating wave. The downward wave partially reflects at the oxide-substrate interface and interferes with the direct upward wave. Depending on the oxide buffer thickness there is constructive or destructive interference. The reflected wave also interacts with the grating and the buffer thickness influences the coupling strength. This effect is studied in detail in [7] and in the same paper an up/down ratio of 1.5 is calculated for an optimized SOI layer structure. Approximate closed form expressions for grating couplers with a reflecting substrate are given in [40].

The optimal buffer thickness depends on the grating, the wavelength and the angle used. As an example we have calculated the coupling efficiency versus buffer thickness for the structure of figure 4.8(b). The results are shown in figure 4.9. The maximum efficiency is 55% for a buffer thickness of 900 nm or 1450 nm. The efficiency can be > 50% because the coupling is not exactly vertical. The minimum efficiency is 18% or approximately three times less than the maximum. In the theoretical case of an infinite buffer, there is no reflection at the buffer-substrate interface and the efficiency is 35%. As discussed before, the SOI wafers we have used for experiments have a 1000 nm thick oxide buffer, resulting in 46% efficiency for this structure. Similar results are

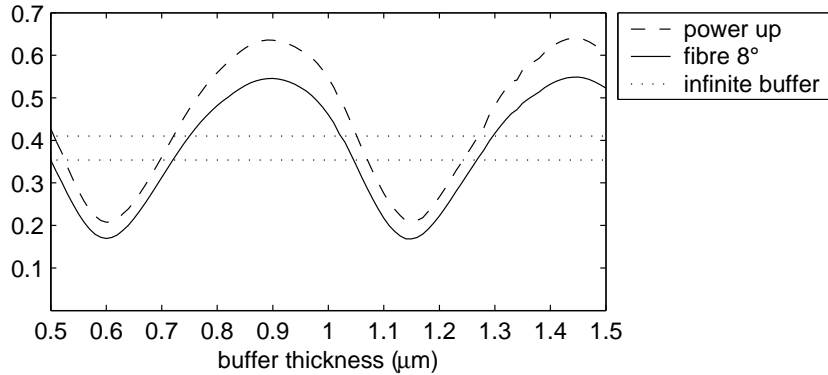


Figure 4.9: Efficiency versus buried oxide thickness. The dotted lines correspond to the power and fibre coupling efficiency in the case of an infinite buffer. $\Lambda=630$ nm, $ed=70$ nm, $\lambda=1558$ nm, 

obtained in the case of vertical coupling. But in this case, also the reflection is strongly dependent on the buried oxide thickness.

In [27] a directionality of 80% is achieved, which is larger than the maximum value of 64% that we have found. But the layer structure used in [27] is 400 nm Si on top of 700 nm SiO_2 and $\lambda = 1.3 \mu\text{m}$. This is a multimode slab waveguide for TE polarization.

4.2.4 Sensitivity to fabrication errors

In this section, we will look at the sensitivity of the grating couplers to variations in the grating parameters. We use the structure from figure 4.8(a) and introduce errors on the etch depth, filling factor and Si core thickness. The effect of the oxide buffer thickness was discussed in the previous section. Finally, we introduce random errors on the widths of the different grooves and look what happens. The resulting coupling efficiency as a function of wavelength is shown in figure 4.10.

An error of 10 nm on the etch depth has almost no effect on the maximum coupling efficiency, but the wavelength is shifted. This wavelength shift is approximately 18 nm. If the grating is etched too deep, there is not only a shift to longer wavelengths, but the second order reflection is also increased. This explains the asymmetry in the 80 nm curve in figure 4.10(a).

Figure 4.10(b) shows the effect of a different filling factor. Changing it from 50% to 40% or 60% has only a small effect on the coupling efficiency curves. However, in the case of 60% filling factor, the second

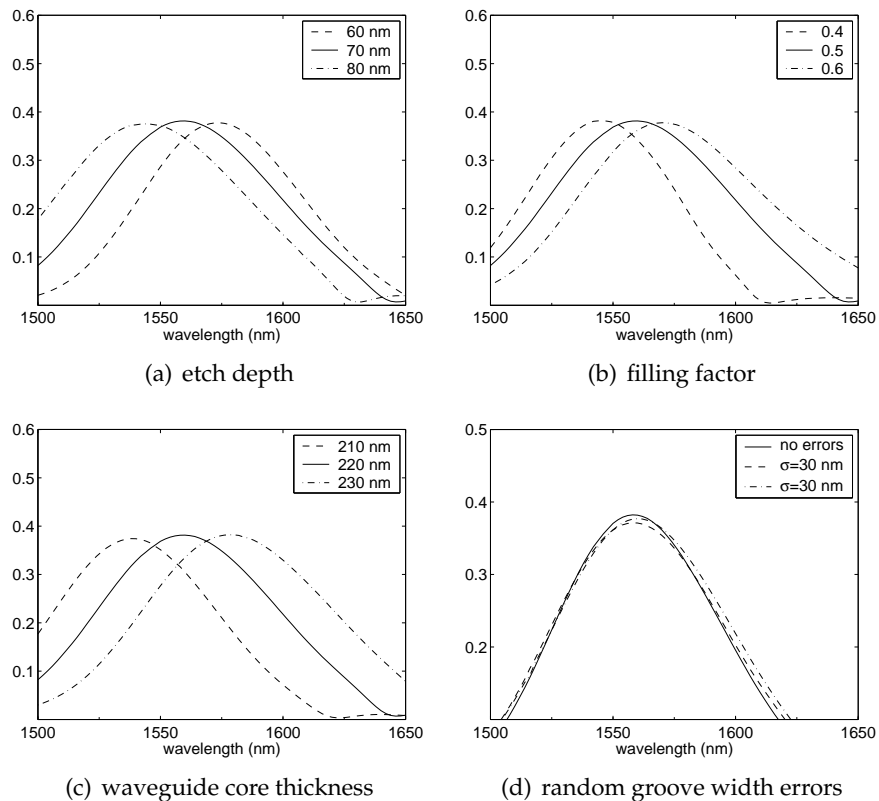


Figure 4.10: Sensitivity to fabrication errors. The coupling efficiency to fibre (10°) is plotted as a function of wavelength. The grating parameters are $\Lambda=630 \text{ nm}$, $ed=70 \text{ nm}$, $ff=0.5$, $N=20$,  , waveguide core thickness=220 nm. One of these parameters is varied : the etch depth in (a), the filling factor in (b) and the core thickness in (c). In (d) random errors are imposed on the groove widths. These errors have a Gaussian distribution with half width $\sigma=30 \text{ nm}$.

order reflection is also increased. This is not visible in the efficiency curve but may be relevant for some applications.

The effect of the thickness of the Si waveguide core is similar to the effect of the etch depth variations. A thicker core causes a shift to longer wavelengths because the effective index increases. For standard 200 mm SOI wafers, the error on the thickness of the Si top layer is within +/- 10 nm (3σ value). Wafers with an error of +/- 5 nm are also available at a higher price.

The effect of random errors on the groove widths is shown in figure 4.10(d). The errors have a normal (Gaussian) distribution with half width $\sigma=30$ nm. The grating period is kept constant, when e.g. a groove is 20 nm too narrow, the accompanying grating tooth is made 20 nm wider. Compared to the perfect structure, the coupling efficiency is slightly reduced and the bandwidth slightly increased.

In real fabricated structures these errors on the different parameters are present all at the same time. In the worst case scenario everything adds up, but it is also possible that one error cancels the other. We can conclude that the tolerances to fabrication errors are very tight, but achievable. The high accuracy needed is typical for all nanophotonic structures.

4.2.5 TE versus TM

Until now we have only considered TE-polarization. We can also calculate the coupling efficiency for TM-polarization. For the structure that has the highest coupling efficiency for TE-polarization (figure 4.8(a)), the efficiency for TM-polarization is below -25 dB in the wavelength range of interest (1536-1582 nm). This results in a TE-TM extinction ratio above 21 dB. The main reason for this high extinction ratio is the difference in effective index between the TE and TM waveguide mode. For the SOI structure, the effective index¹ is 2.83 for the TE slab mode and 1.89 for the TM mode. As a result the light is coupled out at a different angle and the coupling efficiency to fibre is very different.

For some applications it might be useful to have a grating coupler that works for TM polarization instead of TE. It is possible to design a fibre coupler grating for TM-polarization, but the grating parameters are different. Two examples are given in figure 4.11. In the TE case, the outcoupled light is linearly polarized in the x-direction. The TM

¹The effective index is wavelength dependent. The cited values correspond to $\lambda=1550$ nm.

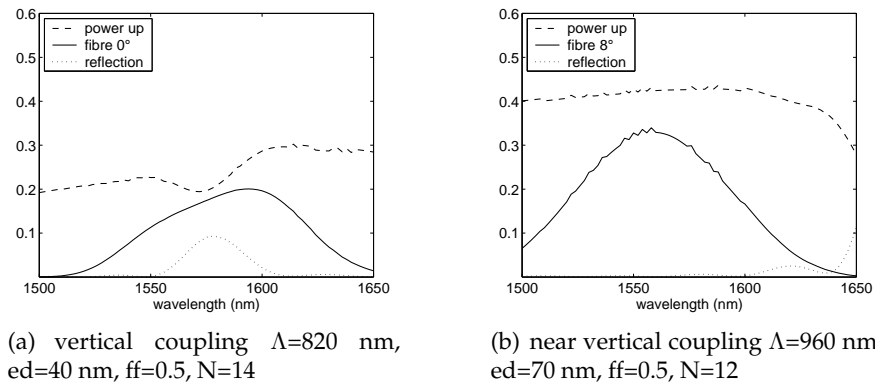


Figure 4.11: Coupling efficiency for TM-polarization.

waveguide mode has an E_y and E_z component, but only the E_z component radiates in the vertical direction. As a result, the outcoupled light is linearly polarized in the z-direction (in the case of exactly vertical coupling).

It should be noted that SOI with a $1\ \mu\text{m}$ thick oxide buffer layer is not suited for low loss TM waveguides because the leakage loss to the substrate is too large [10]. So in practice, a thicker oxide buffer should be used. And for a high coupling efficiency, the buffer thickness must be carefully chosen to achieve a high directionality of the grating coupler. We have not studied the TM case in more detail, because TE is the interesting polarization for our applications.

4.2.6 Oblique coupling

Until now, we have only considered vertical and almost vertical coupling. Another interesting situation occurs when the angle θ is negative and very large, i.e. close to -90° . In that case, it is possible to have only one diffraction order. If there is a layer on top of the Silicon waveguide with a refractive index that is higher than the refractive index of the oxide bottom cladding, then it may be possible to achieve near 100% coupling efficiency. This structure is shown in figure 4.12 together with the wave-vector diagram. The structure looks like a contra-directional grating-assisted directional coupler, but it is much shorter. The polymer waveguide on top of the Silicon captures the light that is coupled out by the grating and can be used to couple to a fibre at the edge of the

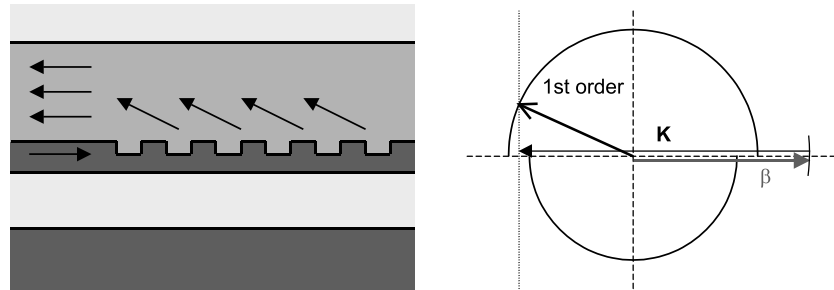


Figure 4.12: Coupling between Silicon and polymer waveguide.

chip. Because this structure is not a surface coupler, it is not studied in more detail in this work².

4.2.7 Very deep grating

In order to fabricate the couplers, it would be interesting to have a coupler that is etched completely through the Silicon core. However, it is not possible to design such coupler that has a high efficiency. Because of the very deep etch, a suitable coupling strength can only be achieved by either a very small or very large filling factor. With a filling factor around 50%, all light is coupled out in a few grating periods and the coupling efficiency to fibre is low. A very small filling factor does not work because there is no waveguide left when using deep etch and a small filling factor. So the only option left is a large filling factor (grating with very narrow grooves). To reduce the coupling strength, we use an oxide layer ($n=1.46$) instead of air on top of the grating.

Because of the deep etch, the second order reflection peak is very wide and a large detuning is needed. The reflection versus grating period is shown in figure 4.13(a). The first, second and third order reflection band can be seen. The reflection can be reduced by using very narrow grooves (few tens on nanometres), but in that case the coupling strength of the grating also becomes too small for butt-coupling to fibre. If the period becomes too large a higher order reflection peak occurs. So there exists an optimal structure, but it is not possible to make the reflection very small.

The best structure found has a 740 nm period and 80% filling factor which corresponds to 148 nm wide grooves. Light is coupled out at

²The research on coupling between parallel Silicon and polymer waveguides is being carried out by Gunther Roelkens in the context of his PhD.

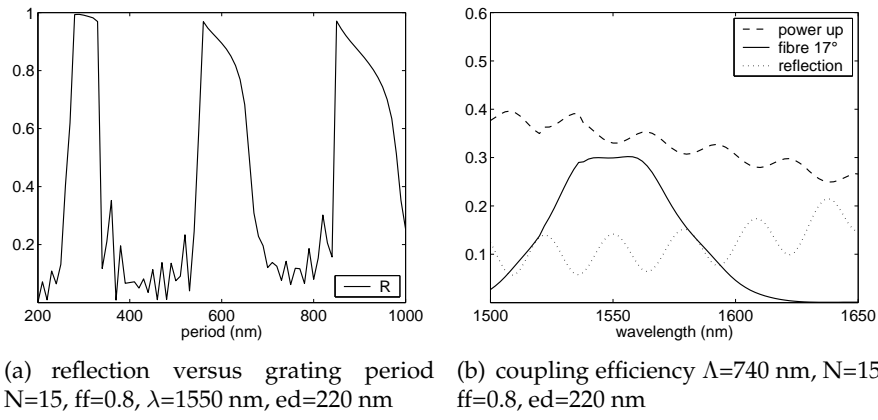


Figure 4.13: Coupler grating etched completely through Si core.

an angle of 17° , but there is still 14% reflection. It is not possible to reduce this reflection as discussed before. The coupling efficiency to fibre is approximately 30%. The reflection and efficiency as a function of wavelength are plotted in figure 4.13(b). We can conclude that it is not possible to design a good surface coupler with a deep etch of 220 nm.

4.2.8 Other index contrast waveguides

SOI has a high refractive index core and a high index difference between the core and the cladding. Other waveguides have a high index core, but a low index difference between the core and the cladding. Examples are GaAs/AlGaAs and InP/InGaAsP compound semiconductors. Other Si based waveguides, such as SiN or SiON waveguides, have a medium index core and an oxide cladding. In this section we briefly investigate grating couplers in SiN ($n=2$) and GaAs ($n=3.37$) based waveguides. A comparison of the slab waveguides used is given in figure 4.14. The guided TE mode is also shown in that figure.

Based on a perturbation analysis [40], we can try to predict the coupling efficiency for the different waveguides :

$$P_{up,max} = \frac{n_{top}}{n_{top} + n_{bottom}} \quad (4.1)$$

where n_{top} is the refractive index of the top cladding, which is 1 in the case of air and n_{bottom} is the index of the bottom cladding, which

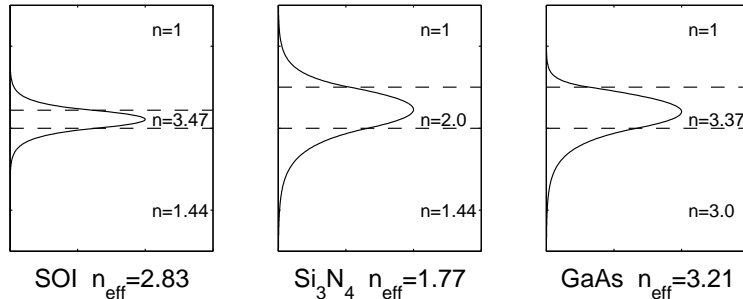


Figure 4.14: Comparison of the TE slab mode of different types of waveguides. The E-field is shown. The substrate is not shown in these figures.

is 1.44 in the case of SiO₂ or 3.0 in the case of AlGaAs with high Al-content. When a high index substrate with refractive index n_{substrate} is present under the bottom cladding, equation (4.1) becomes

$$P_{up,max} = \frac{n_{top}}{n_{top} + \frac{n_{bottom}}{n_{substrate}} n_{bottom}} \quad (4.2)$$

in the case of an optimized buffer thickness [40]. The substrate increases the efficiency because the downward wave is partially reflected at the interface between the bottom cladding and the substrate. This reflected wave interferes constructively with the direct upward wave if the buffer thickness is optimized. The results based on these approximate formulas are listed in the next table :

material	SOI	Si ₃ N ₄	GaAs
P _{up,max} without substrate	41%	41%	25%
P _{up,max} with substrate	63%	63%	27%

These values are the upper limit for the power that is coupled upwards. In the case of an optimized grating, the coupling efficiency to fibre will be approximately 0.8P_{up,max}. So it is expected that the efficiency of the Si₃N₄ coupler will be similar to the efficiency of the SOI coupler. The predicted efficiency of the GaAs coupler is much lower, because of the high refractive index of the bottom cladding layer.

We have also performed the rigorous calculations for these waveguide gratings. The efficiency as a function of wavelength is shown in figure 4.15. The efficiency of the Si₃N₄ coupler is 36% for λ=1558 nm. This is comparable to the SOI coupler of figure 4.8(a). These results confirm the predictions of the approximate formulas. In the GaAs/AlGaAs

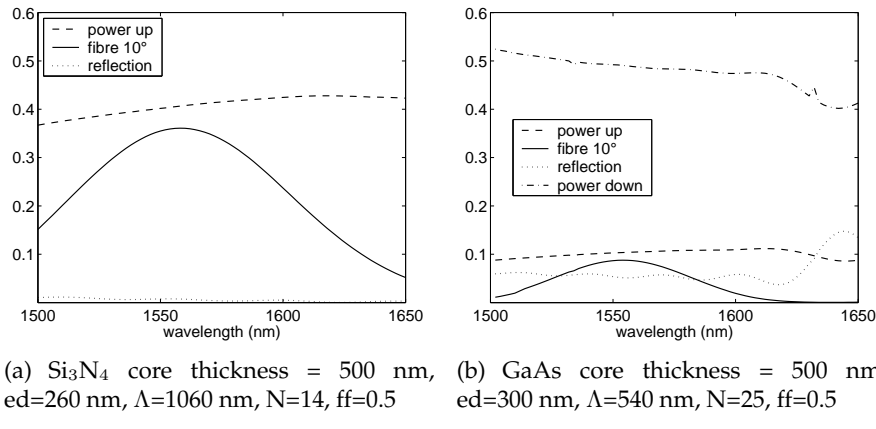


Figure 4.15: Efficiency of uniform grating couplers based on Si_3N_4 and GaAs waveguides.

case, the results are very different. The efficiency < 10%, which is even lower than expected. For smaller etch depths (< 200 nm), the results match with the perturbation formulas, but the coupling length is too long to butt-couple efficiently to fibre. For deeper gratings, reflection and scattering occur at the beginning of the grating. This may be explained by the mode mismatch between the waveguide mode and the Bloch mode of the grating. In the $\text{GaAs}/\text{AlGaAs}$ case, we did not find a suitable grating coupler design for butt-coupling to fibre.

Finally, we compare standard SOI with SOI with an oxide top cladding and a Silicon membrane. The membrane has air as top and bottom cladding and is made by etching away the buried oxide with a selective wet etch. The results based on equations (4.1) and (4.2) are given in the following table :

SOI bottom/top	SiO_2/air	$\text{SiO}_2/\text{SiO}_2$	air/air
$P_{up,max}$ without substrate	41%	50%	50%
$P_{up,max}$ with substrate	63%	71%	78%

The Silicon membrane has the highest efficiency, because the index contrast between the bottom cladding and the substrate is very high. As a result, a large part of the downward wave is reflected upwards. A membrane structure is not well suited for photonic integrated circuits, because the Silicon membrane must be suspended in air. SOI with oxide on top has a higher efficiency than the SOI with air as top cladding. This is confirmed by the rigorous simulation results (see e.g. figure 4.8).

4.3 Coupler with rear reflector

4.3.1 Introduction

When the coupler grating is horizontally symmetric, there is always a significant reflection peak around the second order Bragg wavelength. In the case of vertical coupling, the only solution is to make the grating asymmetric. Another argument in favour of an asymmetric grating is found when considering the coupling from fibre to waveguide. In the case of vertical coupling and a symmetric structure, the efficiency can never exceed 50%, because of the symmetry.

One way to make the grating asymmetric is to add a second grating, which acts as a reflector behind the coupler grating (figure 4.16). If the structure is properly designed, it is possible to reduce the reflection at the coupler and couple all light out. How this structure works, can be explained as follows : At the coupler grating, part of the light is reflected, part is coupled out and part is transmitted and reaches the reflector grating. This reflected light goes back to the coupler grating. If the direct reflection at the coupler grating and the reflection from the reflector grating interfere destructively, the resulting reflection at the coupler can be eliminated. It is obvious that the distance between the two gratings is critical. An error of $\lambda/4$ will transform the best possible structure into the worst.

We have used the following procedure to design a grating coupler with a rear reflector grating:

- Design a coupler grating without reflector for vertical coupling. The reflection at this coupler grating is R and the transmission is T . If a reflector is added behind the coupler, the secondary reflection at the total structure will be approximately T^2 , if R is small. If the coupler grating satisfies the condition $R = T^2$, it is expected that the direct and secondary reflection at the coupler with reflector have approximately the same magnitude and can cancel out each other.
- Design a reflector grating with the proper etch depth and high reflectivity in the wavelength range of interest.
- Optimize the spacing between the two gratings. We do this by calculating the reflection of the total structure as a function of the spacing between the two gratings. This calculation is performed at a fixed wavelength (the central wavelength of the coupler).

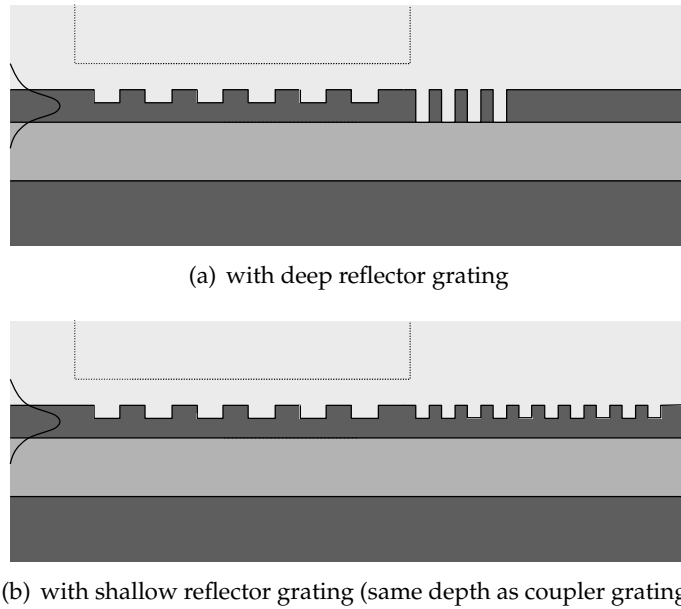


Figure 4.16: Grating coupler with reflector grating.

- Finally the coupling efficiency is calculated as a function of wavelength. Also the tolerances to fabrication errors can be calculated.

The reflector grating is a distributed Bragg reflector (DBR). The best option is a first order grating, etched completely through the waveguide core. Only a few periods are needed to achieve near 100% reflection (figure 4.17(a)). The disadvantage of this structure is that both gratings have a different etch depth and thus need to be fabricated in separate etch steps. This may be a problem because the distance between the two gratings is very critical. A detailed analysis and design of this structure is given in section 4.3.2.

To be able to etch both gratings in one step, a reflector grating with the same etch depth as the coupler grating is needed. It is possible to design a shallow grating with a high reflectivity, but the number of periods needed is much higher. The bandwidth is smaller but still sufficient (figure 4.17). However the major disadvantage is that the structure becomes more sensitive to fabrication errors. A small error in etch depth will shift the reflection spectrum and also change the phase of the grating reflection. It is expected that this structure is more sensitive to fabrication errors than the structure with a deep reflector grating. A detailed analysis and design of this structure is given in section 4.3.3.

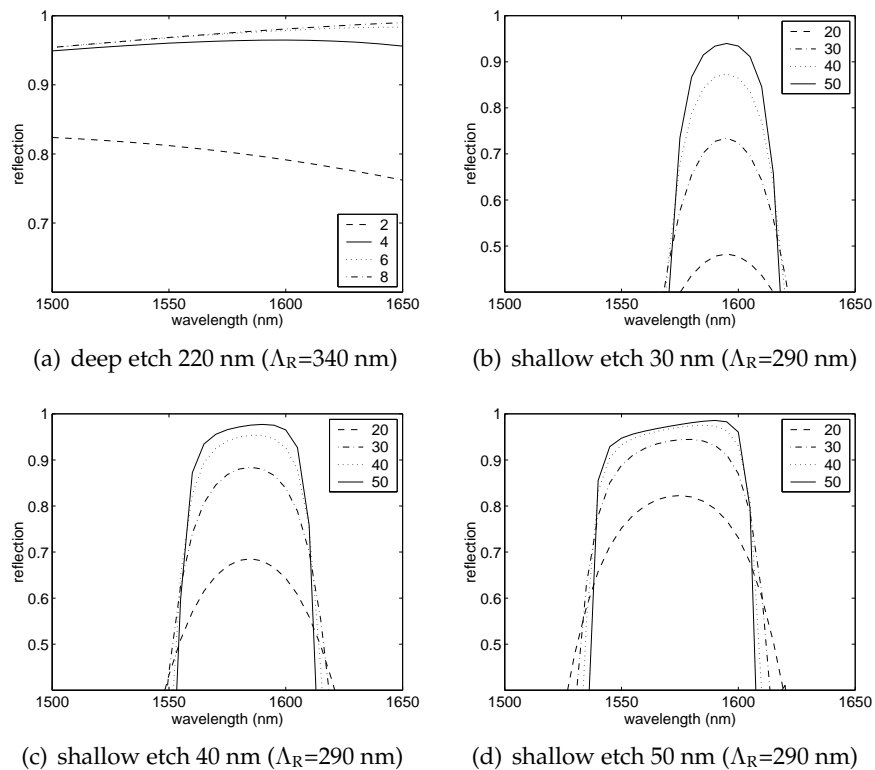


Figure 4.17: Reflection of a first order reflector grating as a function of the number of periods. The filling factor is 50%.

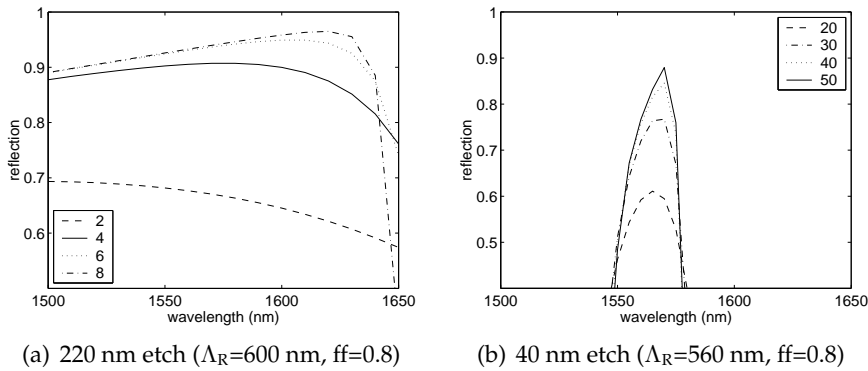


Figure 4.18: Reflection of a second order reflector grating as a function of the number of periods.

Another option for the reflector grating is a second order grating. If the filling factor of the grating is chosen well, it is possible to obtain a high reflectivity (see e.g. figure 4.3). This grating may be easier to fabricate than a first order grating because the grating period is larger. However the width of the grooves is similar to a first order grating, because a large filling factor is needed to make a good reflector. A reflection spectrum of a properly designed second order reflector is shown in figure 4.18(a) (deep grating) and figure 4.18(b) (shallow grating).

4.3.2 Coupler with deep reflector grating

The deep reflector grating is etched completely through the Silicon top layer. The grating period Λ_R is 340 nm, the filling factor is 0.5 and the number of periods is 8. This grating is a good reflector in a broad wavelength range (figure 4.17(a)). The 50% filling factor is chosen because it is the easiest to fabricate. The coupler grating period Λ_C is 580 nm and the etch depth is 40 nm. This etch depth is chosen to satisfy approximately the design rule $R=T^2$. The only parameter that is still to be determined now is the spacing between the two gratings. The reflection of the entire structure as a function of this spacing³ is shown in figure 4.19(a). The optimal spacing Δ is 230 nm (or $230 \text{ nm} + m\lambda/2$) and for this value the reflection is lower than 0.5%.

³The actual width of the unetched part between the exterior grooves of both gratings is $\Delta + 0.5\Lambda_C$.

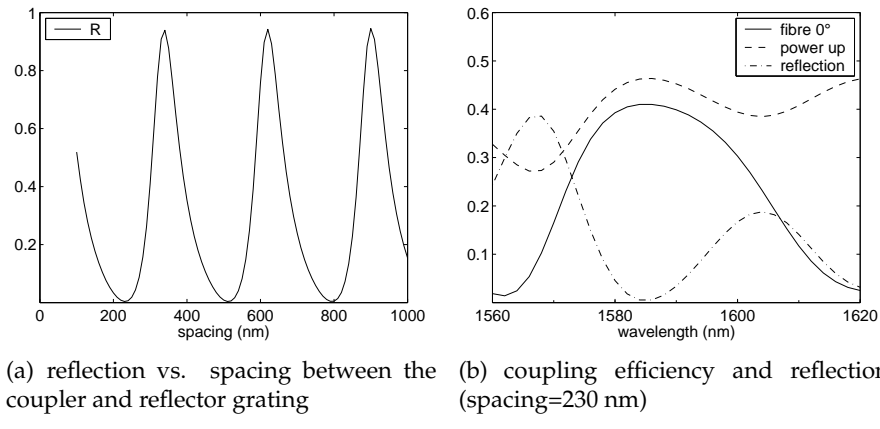


Figure 4.19: Design of a coupler with deep reflector.

The coupling efficiency to fibre is shown in figure 4.19(b). The maximum coupling efficiency is 41% and the 1 dB bandwidth is 22 nm. However at the edges of this band, the reflection is already 14%, which is unwanted for most applications. The reflection is only below 2% in a 6 nm wavelength range. At $\lambda=1585$ nm, there is no reflection and 46% of the light is coupled upwards (and 53% downwards). The overlap with a Gaussian is 89%, which results in 41% coupling efficiency to fibre. The sensitivity to fabrication errors is shown in figure 4.20. An error of 30 nm on the spacing results in a small wavelength shift, but almost no reduction in efficiency. An error of 10 nm on the etch depth results in a slight reduction in efficiency and a wavelength shift of approximately 12 nm.

4.3.3 Coupler with shallow reflector grating

The shallow reflector grating has the same etch depth⁴ as the coupler grating. The coupler grating period Λ_C is 580 nm and the etch depth is 40 nm. This etch depth is chosen to satisfy approximately the design rule $R=T^2$. The reflector grating period Λ_R is 290 nm, the filling factor is 0.5 and the number of periods is 50. This grating is a good reflector in the wavelength range 1560-1620 nm (figure 4.17(c)), but is more sensitive to fabrication errors than a deep grating. The 50% filling factor

⁴If the two gratings are made in the same etch step, it is expected that the etch depth is approximately the same. But depending on the etch process it may happen that the smaller grooves are etched less deep. This is undesirable.

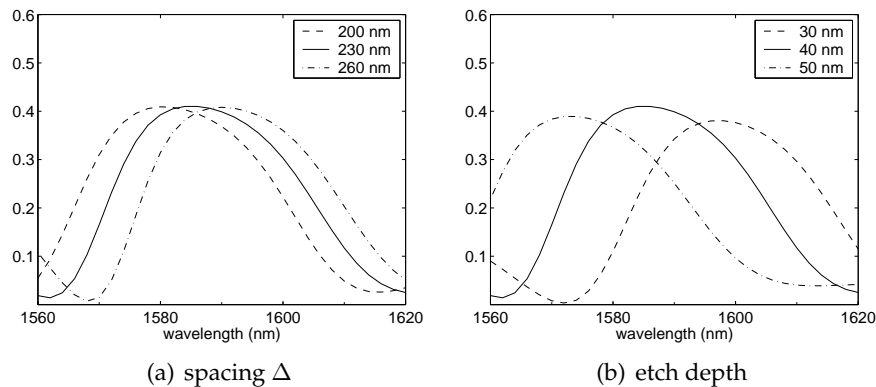
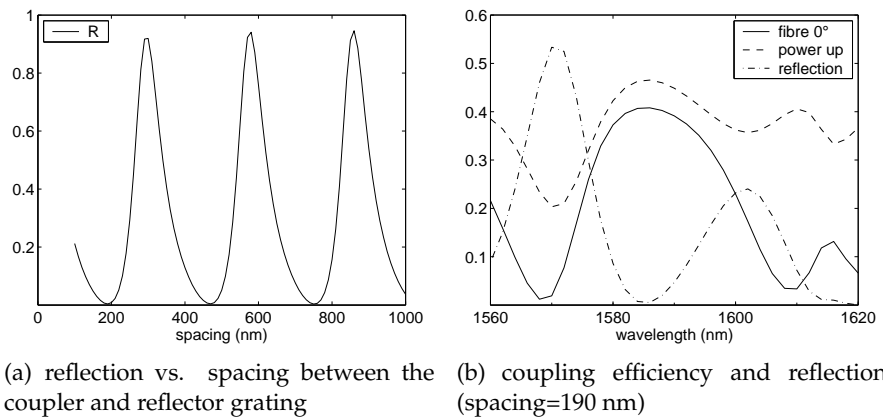
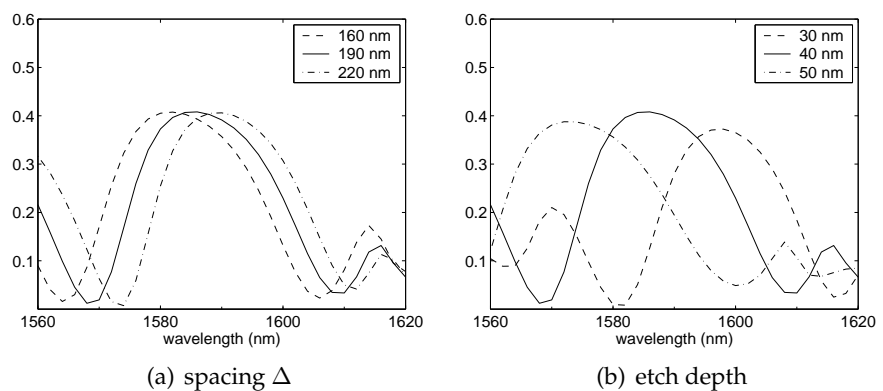


Figure 4.20: Efficiency of a coupler with deep reflector : sensitivity to fabrication errors.

is chosen because it is the easiest to fabricate. The only parameter that is still to be determined now is the spacing Δ between the two gratings. The reflection of the entire structure as a function of this spacing is shown in figure 4.21(a). The optimal spacing Δ is 190 nm (or 190 nm + $m\lambda/2$) and for this value the reflection is lower than 0.5%.

The coupling efficiency to fibre is shown in figure 4.21(b). The maximum coupling efficiency is 41% and the 1 dB bandwidth is 18 nm. However at the edges of this band, the reflection is already 17%, which is unwanted for most applications. The reflection is only below 2% in a 6 nm wavelength range. At $\lambda=1585$ nm, there is no reflection and 46% of the light is coupled upwards (and 53% downwards). The overlap with a Gaussian is 88%, which results in 41% coupling efficiency to fibre. The coupler with a shallow reflector performs almost as good as the coupler with a deep reflector. The sensitivity to fabrication errors is shown in figure 4.22. An error of 30 nm on the spacing results in a small wavelength shift, but almost no reduction in efficiency. An error of 10 nm on the etch depth results in a slight reduction in efficiency and a wavelength shift of approximately 12 nm.

The sensitivity to fabrication errors of the structure with a shallow reflector grating is similar to the sensitivity of the structure with a deep reflector grating for the error values considered. In a real structure, the errors on the different parameters may add up. For larger errors, the coupler with a deep reflector performs slightly better, because the bandwidth of the reflector grating is very large.

**Figure 4.21:** Design of a coupler with shallow reflector. **Figure 4.22:** Efficiency of a coupler with shallow reflector : sensitivity to fabrication errors.

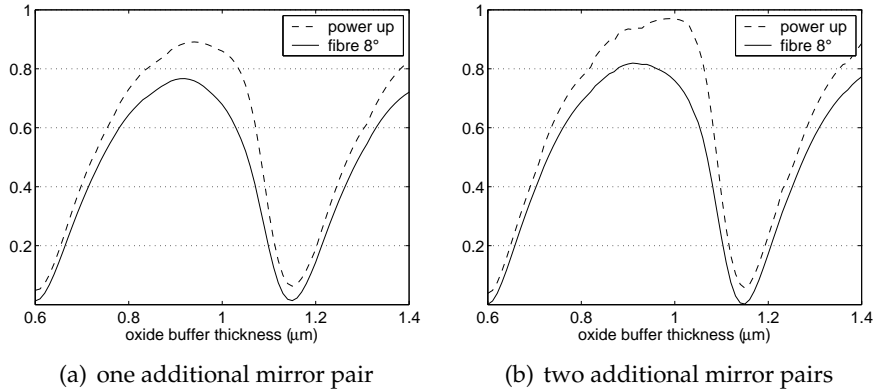


Figure 4.23: Coupling efficiency as a function of oxide buffer thickness. The coupler has a uniform grating and a DBR mirror under the waveguide. $\Lambda=630$ nm, $ed=70$ nm, $ff=0.5$, $\lambda=1566$ nm,

4.4 Bottom mirror

The main limitation to the efficiency of the grating couplers is the coupling to the substrate. Even with a good choice of oxide buffer thickness, the up/down ratio is limited to approximately 1.5. A bottom reflector can further improve this ratio and the coupling efficiency to fibre. This bottom reflector can be a multi-layer dielectric mirror or a metal mirror.

We have chosen for a DBR consisting of Si/SiO₂ pairs. Thanks to the high refractive index contrast, only a few pairs are needed and the reflection is broadband. The coupling efficiency to fibre for a coupler with one or two additional reflector pairs is shown in figure 4.23. The maximum coupling efficiency is 77% for the structure with 1 additional Si/SiO₂ pair and 82% with 2 pairs. Without an additional mirror, this efficiency was only 55% for an optimized buffer thickness.

Even with a highly reflecting bottom mirror, the correct choice of buffer thickness is important. The optimal buffer thickness is 920 nm or 1470 nm in our case. If the buffer thickness is wrong, the phase of the reflection is wrong and the efficiency is very low. In this case, the coupling length of the grating becomes very long.

As a second example, we have designed a grating coupler for vertical coupling with a rear and a bottom reflector. The coupling efficiency as a function of wavelength is shown in figure 4.24. The structure itself together with a field plot is shown in figure 4.25. The efficiency is 79%

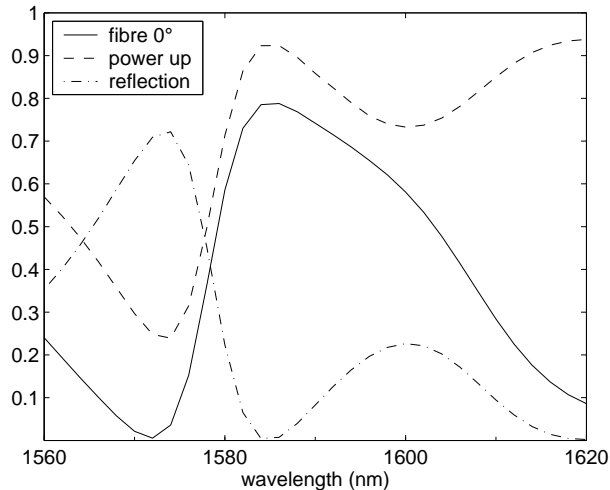


Figure 4.24: Coupling efficiency of a coupler with rear and bottom reflector.

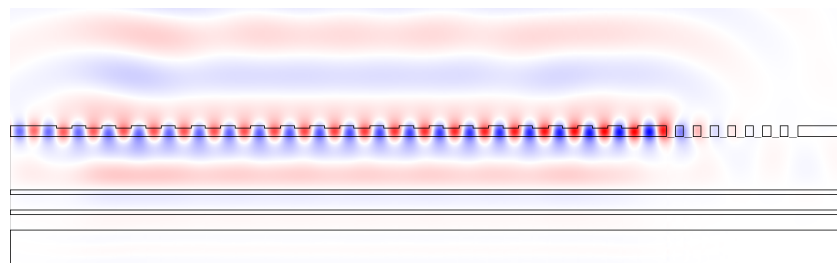


Figure 4.25: Field plot of a coupler with rear and bottom reflector. The two pair DBR can be seen under the waveguide.

for $\lambda=1585$ nm. The useful bandwidth is only a few nm, this limitation is due to the rear reflector, not the bottom reflector.

4.5 Top mirror

In the previous section, a bottom reflector was used to avoid coupling to the substrate and achieve high efficiencies. However, such a bottom reflector makes the fabrication process more complex, and SOI substrates with a bottom reflector are not commercially available products. The characteristics of a grating coupler can also be changed by adding dielectric layers on top of the grating. It has been suggested [71] that

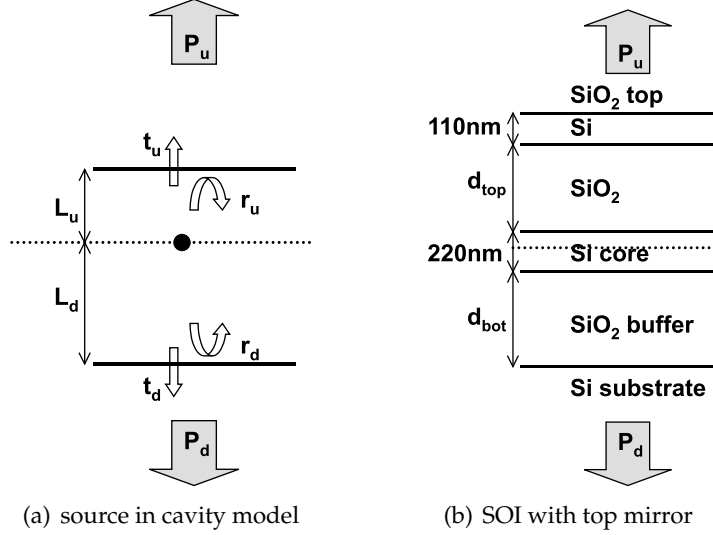


Figure 4.26: Vertical cavities.

depositing an additional oxide and Silicon layer on top of a SOI coupler can improve the directionality to values $> 95\%$. In this section we will explain why and in which cases this technique works.

The additional layers form a top mirror and the buried oxide layer is also a bottom mirror. The grating is embedded in a vertical cavity. In a perturbation analysis the grating can be represented by a source. The simplified model of a source in a 1-D cavity can be solved analytically. The formulas are given in [72] for example.

Consider the cavity of figure 4.26(a). A top mirror is placed at a distance L_u above the source and a bottom mirror L_d below the source. The reflection coefficients of the mirrors are r_u and r_d . These coefficients are complex numbers. This model is also valid for distributed reflectors, because such a DBR can be represented by an equivalent mirror. The reflection and transmission coefficients are related by $|r|^2 + |t|^2 = 1$. The up/down ratio of the emitted power is given by :

$$\frac{P_u}{P_d} = \frac{n_u}{n_d} \left| \frac{E_u}{E_d} \right|^2 \quad (4.3)$$

$$\left| \frac{E_u}{E_d} \right|^2 = \left| \frac{t_u}{t_d} \right|^2 \left| \frac{1 + r_d \exp(-jkL_d)}{1 + r_u \exp(-jkL_u)} \right|^2 \quad (4.4)$$

The position of the mirrors can be chosen to maximize this ratio. In the best case scenario, the reflected wave at the top mirror interferes destructively with the direct downward wave and the reflected wave at the bottom mirror interferes constructively with the direct upward wave. For this optimal position of the mirrors, equation (4.4) becomes :

$$\left| \frac{E_u}{E_d} \right|^2 = \left| \frac{t_u}{t_d} \right|^2 \left| \frac{1 + |r_d|}{1 - |r_u|} \right|^2 \quad (4.5)$$

The magnitude of the reflectivity $|r_d|$ of the bottom mirror is fixed because we want to use a regular SOI layer structure. According to equation (4.5), it is good to choose the reflectivity of the top mirror very high. However there is a second effect that has to be taken into account. The cavity does not only change the directionality but also the total extraction efficiency:

$$\left| \frac{E_u}{E_{source}} \right|^2 = |t_u|^2 \left| \frac{1 + |r_d|}{1 + |r_u| |r_d|} \right|^2 \quad (4.6)$$

If the reflectivity of the top mirror is chosen very high, the extraction efficiency becomes very low. The extraction efficiency of the source in a cavity model is related to the coupling strength of a grating in a cavity. If the coupling strength becomes smaller, a longer grating is needed to couple all the light out. It turns out that the structure of figure 4.26(b) provides a good compromise between directionality and coupling strength.

We have calculated the up/down ratio of the emitted power for the structure of figure 4.26(b) as a function of the thickness of the buffer oxide layers. In figure 4.27 the result is shown when the source is placed 50 nm below the top of the Silicon guiding layer. For the optimal layer thickness (bottom oxide = 895 nm and top oxide = 495 nm), the up/down ratio is 11.5, which corresponds to a directionality of 92%. This value is similar to 95% given in [71] for a slightly different layer structure. In figure 4.27, it can also be seen that the performance of the cavity is more sensitive to the thickness of the top oxide buffer layer than to the bottom oxide thickness.

Until now we have only considered a source at a certain position in a cavity. It is important to note that the position of the source in the cavity is very important. If this position is changed $\lambda/4$, the structure will couple everything downwards instead of upwards. In Silicon $\lambda/4 \approx 120 \text{ nm}$ for wavelengths around 1550 nm. So it is expected that this technique will only work well for shallow gratings. In the

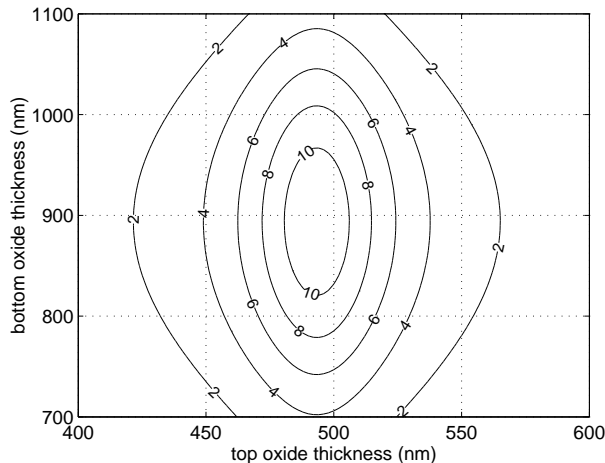


Figure 4.27: Calculated P_u/P_d for the structure of figure 4.26(b).

next paragraphs, we will give some examples of simulation results of grating couplers embedded in a cavity and look in which cases the top mirror can considerably improve the coupling efficiency to fibre.

The coupling efficiency of a uniform grating with a top mirror is shown in figure 4.28. In figure 4.28(a), the period is 630 nm and the etch depth is 70 nm and the thickness of the top and bottom oxide are optimized. These were the optimal grating parameters for a grating without top mirror. The coupling efficiency with the top mirror is not higher than without the top mirror. Although the up/down ratio is improved to 4:1, the coupling strength has become lower. It is needed to optimize the grating parameters as well.

The etch depth of the optimal structure is 110 nm. The coupling efficiency is shown in figure 4.28(b). The maximum efficiency is 64%. The up/down ratio is approximately 5:1. It may seem a contradiction that the up/down ratio is better when the etch depth is deeper. The reason for this, is that we optimized the structure for coupling efficiency to fibre and the maximum efficiency does not necessarily correspond to the maximum up/down ratio case. In conclusion, the top mirror only improves the efficiency from 55% to 64%. This is only a small improvement because the top mirror works only well for shallow gratings.

We have also designed a grating coupler with rear reflector and top mirror. Because the etch depth is smaller, it is expected that the improvement will be larger. The design procedure from section 4.3 is used. First a coupler grating is designed that has a high directionality

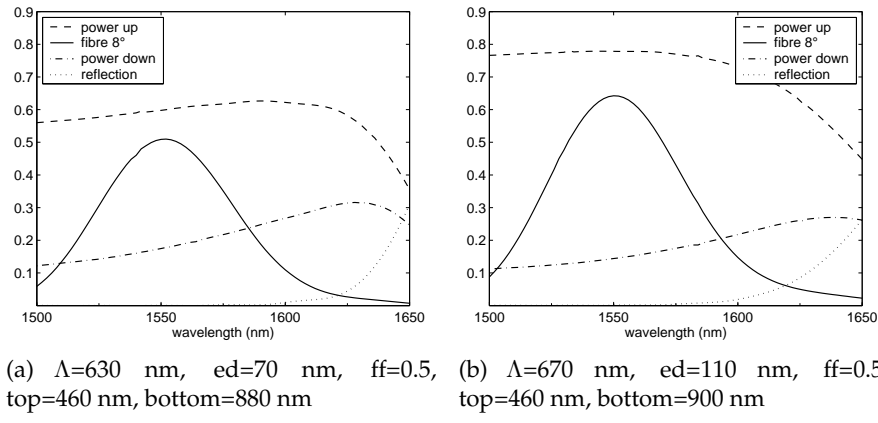


Figure 4.28: Efficiency of a uniform grating with top mirror.

and satisfies approximately the design rule $R=T^2$. The coupler grating period Λ_C is 594 nm and the etch depth is 70 nm. The thickness of the top oxide is 500 nm and the bottom oxide thickness is 900 nm. The deep reflector grating is etched completely through the Silicon top layer and the grating period Λ_R is 360 nm, the filling-factor is 0.5 and the number of periods is 8. The optimal spacing Δ between the two gratings is 230 nm (or $230 \text{ nm} + n\lambda/2$) and for this value the reflection is lower than 0.5%. The coupling efficiency to fibre is shown in figure 4.29. The maximum coupling efficiency is 74% and the 1 dB bandwidth is 18 nm. However at the edges of this band, the reflection is already above 20%, which is unwanted for most applications. The reflection is only below 2% in a 6 nm wavelength range. For $\lambda=1585$ nm, there is no reflection and 86% of the light is coupled upwards (and 13% downwards, so the up/down ratio is 6:1). The overlap with a Gaussian is 86%, which results in 74% coupling efficiency to fibre. The structure together with a field plot is shown in figure 4.30. The top mirror has increased the efficiency from 41% to 74% for the coupler with rear reflector.

4.6 Gaussian beam

4.6.1 Introduction

A grating coupler with a uniform grating can have a maximum theoretical coupling efficiency of approximately 80% because the output beam has an exponentially decaying power profile $P=P_0 \exp(-2\alpha z)$ along the

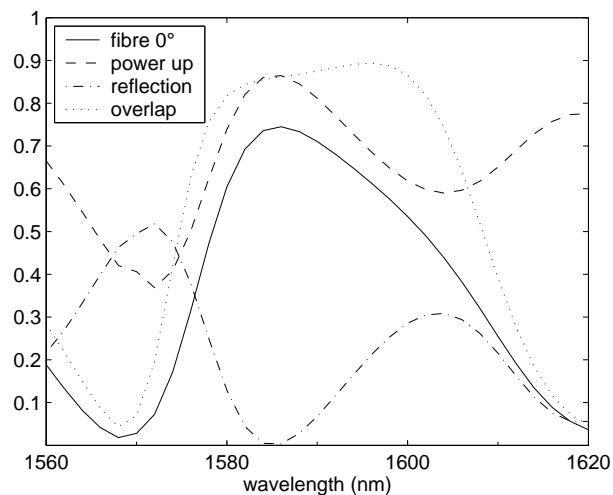


Figure 4.29: Coupling efficiency of a coupler with rear and top reflector.

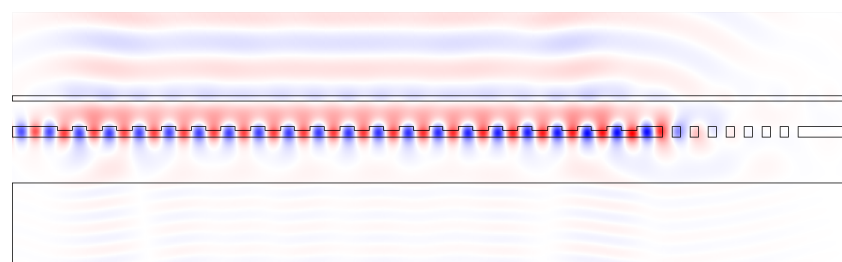


Figure 4.30: Field plot of a coupler with rear and top reflector.

propagation direction. 2α is called the leakage factor or coupling strength of the grating. For a non-uniform grating, α becomes a function of z and the output beam can be shaped differently. In order to achieve a Gaussian output beam, $\alpha(z)$ is given [73, 74] by

$$2\alpha(z) = \frac{G^2(z)}{1 - \int_0^z G^2(t)dt} \quad (4.7)$$

where $G(z)$ is a normalized Gaussian profile. To achieve this z -dependence of α , either the etch depth [73] or the duty cycle [74] of the grating can be varied. In figure 4.31, $G^2(z)$ and the corresponding theoretical $\alpha(z)$ are plotted for a Gaussian beam with a beam diameter of $10.4 \mu\text{m}$. The maximum α needed is $0.36 \mu\text{m}^{-1}$, this much higher than the coupling strength of an optimal uniform grating, which is $\alpha = 0.13 \mu\text{m}^{-1}$. It should be noted that (4.7) is only exact for a long grating with small α , which is not the case for our structure. Therefore we use the results of (4.7) as a starting point and do a further numerical optimization of the grating structure.

4.6.2 Optimization

We will now discuss our design procedure in more detail. Based on the maximum coupling strength that is needed, the etch depth is chosen. A grating period is chosen so that the output beam has the desired angle $\theta=8^\circ$. For this etch depth and period, α is calculated for different duty cycles. Based on these results the groove widths are chosen to match $\alpha(z)$ from figure 4.31. The resulting structure however has an output beam that has only 75% overlap with $G(z)$ instead of the 100% expected. The main reason for this is that because of the large coupling strength, not only the coupling strength is dependent on the duty cycle, but also the phase difference between two grating teeth. As a result, the resulting output field has a more or less Gaussian amplitude but a curved phasefront. By changing the spacing between the grating teeth, we can correct this phase mismatch. A second reason is that (4.7) is only very accurate for small α . Therefore we have decided to numerically optimize the structure to achieve a maximum coupling efficiency to fibre.

We define the grating as 20 groove widths and 19 spacing widths and use a very simple genetic algorithm [75] for the optimization. The groove widths and the spacings between the grooves are allowed to

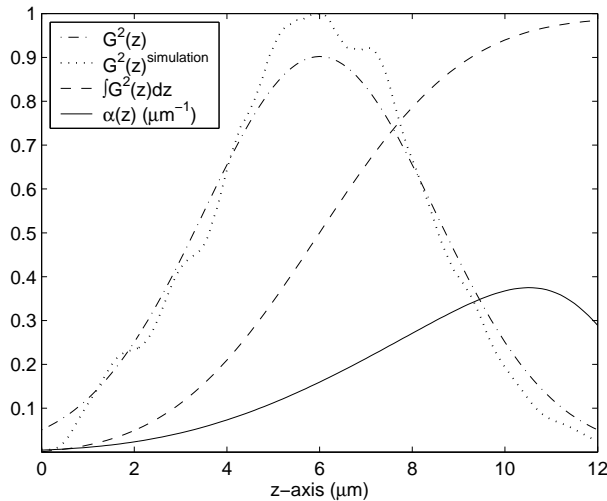


Figure 4.31: Gaussian profile and the corresponding $\alpha(z)$.

change in steps of 5 nm. In a first iteration we optimize only the spacing between grooves to correct the phase mismatch. In a second run we also allow the groove widths to change. As a result of this optimization, the overlap with a Gaussian profile is increased from 75% to 97%. The resulting output after optimization is also drawn on figure 4.31, next to the theoretical Gaussian profile.

For a SOI waveguide, we have repeated this procedure for different thicknesses of the buried oxide layer, because the thickness of this layer has a major influence on the coupling strength and efficiency as discussed before. For the structure with optimized oxide buffer thickness (925 nm) the maximum coupling efficiency to fibre is 63%. The efficiency versus wavelength is shown in figure 4.33. The efficiency is limited because approximately 35% light is lost to the substrate. The efficiency can be further improved by using SOI with a bottom reflector. For SOI with a 2 pair DBR under the waveguide, the maximum coupling efficiency after optimization is 95%. The evolution of the coupling efficiency during the optimization is shown in figure 4.32. After 160 generations an optimal structure is found. In this structure with bottom reflector, only 2% is lost to the substrate. The other 98% is coupled upwards, but there is still a small mismatch with the fibre mode, which results in maximum 95% coupling efficiency to fibre ($0.95=0.98 \cdot 0.97$). This value is the coupling efficiency in the 2-D model used in this chap-

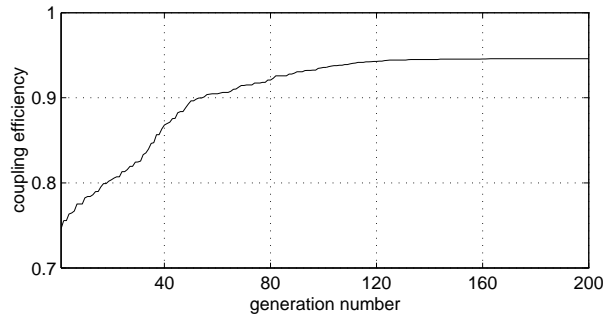


Figure 4.32: Evolution of the coupling efficiency using a genetic algorithm.

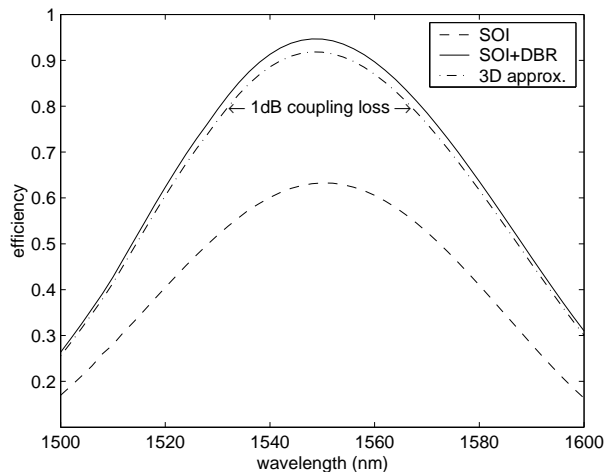


Figure 4.33: Coupling efficiency to fibre (8°) as a function of wavelength for SOI and SOI with a bottom DBR.

ter. If we also take into account the lateral dimensions as explained in section 3.7.3, the coupling efficiency to fibre is 92%.

The optimal grating parameters are also different for SOI and SOI with a DBR bottom reflector, because the reflector not only influences the up/down ratio, but also the coupling strength of the grating. The optimal structure is shown in figure 4.34 together with a field plot. The smallest groove width is 30 nm. The coupling loss to fibre for this structure is less than 1 dB in the wavelength range 1532-1567 nm (see figure 4.33). In this wavelength range the unwanted reflection at the waveguide grating interface is less than -24 dB.

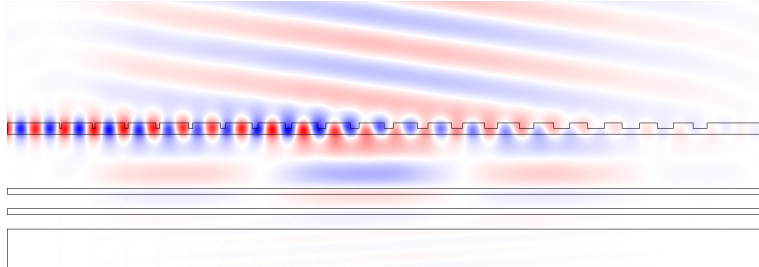


Figure 4.34: Structure with bottom DBR and field plot.

4.6.3 Sensitivity to fabrication errors

We have looked at the influence of variations in etch depth and groove width to see if the proposed device has reasonable tolerances to fabrication errors. In figure 4.35 the resulting coupling efficiency for different etch depths is shown. For an error of 10 nm, the maximum coupling efficiency remains approximately the same but the wavelength is shifted. This wavelength shift can be compensated by adjusting the angle of the fibres, but for most applications the etch depth will have to be controlled very accurately. To assess the influence of groove width errors, we have simulated the structure with statistic errors on the width of the grooves (Monte Carlo analysis). When the errors have a normal (Gaussian) distribution with a half width $\sigma=10$ nm, the resulting coupling efficiency is between 91% and 95%. Also the spectrum is shifted a few nanometre up or down. It should be noted that in practice the narrow grooves will probably etch less deep than the wider grooves. But this is not a problem because if the etch depth versus groove width characteristic is known, then this can be taken into account in the modelling and optimization of the design. Although the width of the smallest groove is only 30 nm in the optimal structure, an increase of the smallest groove width to 60 nm results only in a few percent lower efficiency.

4.6.4 Remarks and perspectives

We have also tried to increase the efficiency of this SOI coupler by using a top dielectric stack instead of a bottom mirror. It is found that the efficiency is not higher than for regular SOI. The reason is the rather deep etch depth. For regular SOI, the etch depth is 120 nm. Because the top mirror reduces the coupling strength, an even larger etch depth is needed. As a result, the beneficial effect of the top mirror is lost.

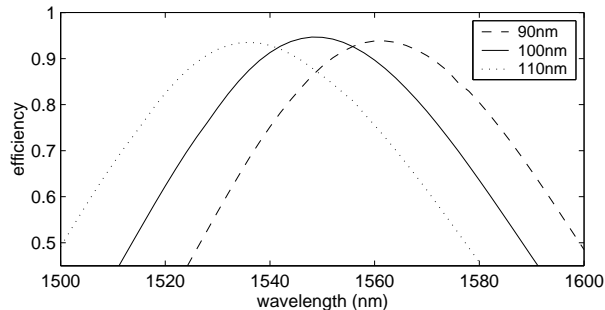


Figure 4.35: Coupling efficiency versus etch depth.

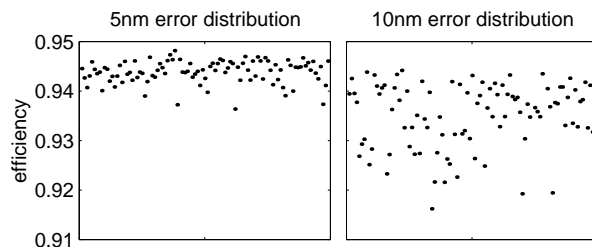


Figure 4.36: Sensitivity to errors on groove widths.

A possible solution is to make the output beam slightly wider (e.g. 20 μm diameter). This would reduce the required α and the etch depth. In this case, a focusing grating is needed to couple to fibre and the bandwidth is also reduced. A focusing grating is both chirped and curved [76]. The chirping of the grating period creates the focusing effect in the z-direction. In the transverse x-direction focusing is realized by curving the grating teeth. The grating teeth are part of concentric circles.

Another possible option is to use metal strips instead of etched grating teeth. Because the metal strips are very thin (approximately 20 nm for the coupling strength needed), it is expected that a top mirror can increase the efficiency. Preliminary simulation results show that 25-30% of the input power is lost by absorption in the metal. If these results are confirmed, it would be possible to achieve up to 70% coupling efficiency with a non-uniform metal grating, without the use of a bottom mirror.

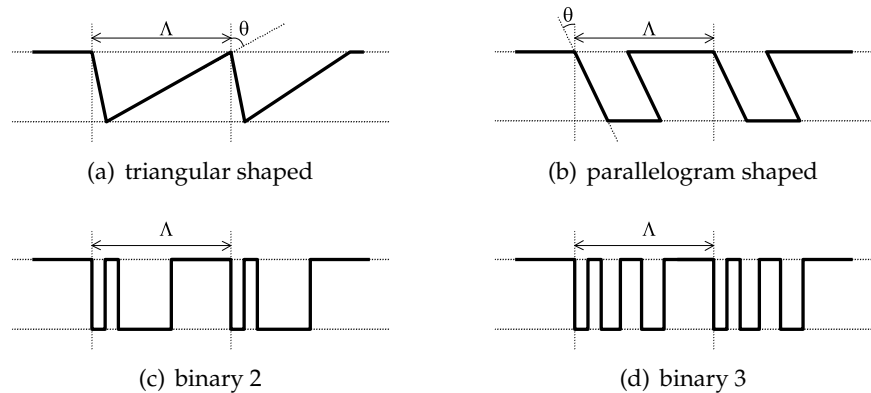


Figure 4.37: Examples of blazed gratings.

4.7 Blazed grating

A blazed grating is a grating with only one efficient diffraction order. To achieve the blazing effect, a special asymmetric tooth shape has to be used. A blazed grating may be used to suppress the second order reflection and/or enhance the directionality of the gratings.

Different types of blazed gratings are shown in figure 4.37. The most common type is the triangular shaped grating. This type is also called sawtooth or échelette grating. Another type used in grating couplers is the parallelogram shape. These shapes cannot be fabricated with standard etch processes. Blazed binary gratings [77] may be easier to fabricate. These gratings are a kind of binary version of the triangular tooth shape.

A theoretical study in [54] concludes that only the parallelogram shape can be used to suppress the second order reflection and not the triangular shape. Several experimental demonstrations of parallelogram gratings are found in the literature. In [78], the fabrication with a modified RIE process is described and a directionality of 90% is observed. Similar results are obtained with grating coupled surface emitting lasers in [79]. In these examples, long shallow gratings are used.

We have only studied parallelogram shaped gratings in the case of vertical coupling. A stepwise approximation is used to simulate the structure with the eigenmode expansion method. The calculation times are much longer than for binary gratings. We have used four levels to approximate the parallelogram. To find an optimized structure, we

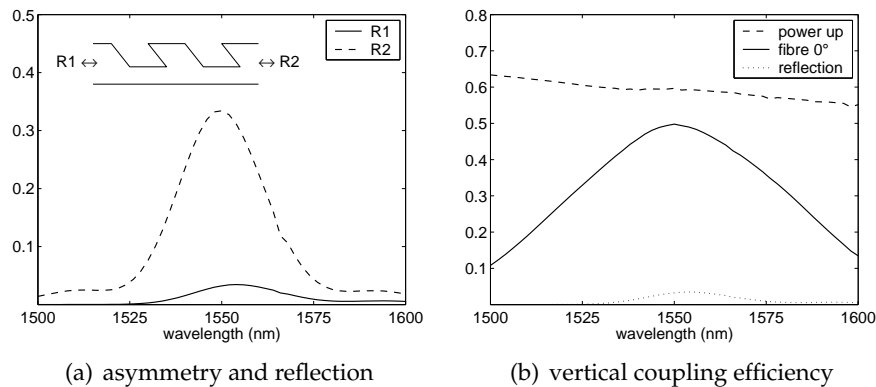


Figure 4.38: Efficiency of a blazed grating coupler with parallelogram teeth.
 $\Lambda=625 \text{ nm}$, $ed=110 \text{ nm}$, $ff=0.38$, $\text{angle}=63^\circ$, $N=20$,

have looked for a low reflection around the second order Bragg wavelength. The grating reflection versus wavelength for the optimal structure is shown in figure 4.38(a). The maximum reflection is only 3%. There is a strong asymmetry, the reflection is much higher when the waveguide mode is incident from the other side.

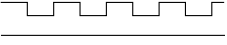
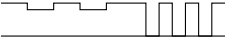
The coupling efficiency is shown in figure 4.38(b). The maximum efficiency is 50% and the 1 dB bandwidth is 36 nm. This type of grating allows vertical coupling with a low reflection and large bandwidth, but the disadvantage is the very difficult fabrication.

4.8 Summary

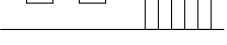
To finish this chapter, we give a summary of the simulation results. This is not a complete overview, but the highlights are presented in conveniently arranged tables. A clear distinction is made between the case of vertical coupling (fibre 0°) and almost vertical coupling (fibre 8°).

4.8.1 Vertical coupling

The results for different vertical SOI couplers are summarized in the following table :

SOI waveguide grating	efficiency	1 dB bandwidth	reflection
	21%	52 nm	24%
	41%	22 nm	0.5%
	50%	36 nm	3%

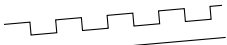
A uniform grating has the largest bandwidth but the smallest efficiency. The reflection around the second order Bragg wavelength is large. This reflection can be reduced and the efficiency increased by using a coupler with a rear reflector grating. The highest efficiency is achieved for a blazed grating with parallelogram teeth. But this blazed grating is very difficult to fabricate. The most promising structure is the coupler with rear reflector grating. The efficiency of this structure can be improved by using a top or bottom mirror :

	efficiency	see also
regular SOI	41%	fig. 4.19
with bottom DBR (2 pair)	79%	fig. 4.24
with top mirror	74%	fig. 4.29

For this structure, the top mirror works very well, because the coupler grating is rather shallow.

4.8.2 Almost vertical coupling

The results for near vertical coupling are summarized in the next table. The layer structure is SOI with an optimized buried oxide thickness and an oxide top cladding layer.

grating type	efficiency	1 dB bandwidth	see also
	55%	43 nm	fig. 4.9
	63%	43 nm	fig. 4.33

The efficiency of the coupler with varying filling factor is higher than the efficiency of the uniform grating because of the better overlap with a Gaussian profile. The bandwidth is approximately the same.

The next table shows the effect of the layer structure for a uniform grating coupler with oxide on top.

	efficiency	see also
regular SOI (1 μm oxide)	46%	fig. 4.8(b)
regular SOI (1.45 μm oxide)	55%	fig. 4.9
with top mirror	64%	fig. 4.28(b)
with bottom DBR (1 pair)	77%	fig. 4.23(a)
with bottom DBR (2 pair)	82%	fig. 4.23(b)

The last table summarizes the results of the Gaussian beam coupler with varying filling factor (see also figure 4.33). In this case the top mirror does not work well because of the rather deep etch.

	efficiency
regular SOI	63%
with top mirror	64%
with bottom DBR (2 pair)	95%

The values cited in this summary are 2-D simulation results and for TE polarization. As discussed in section 3.7.3, a 3-D approximation is obtained by multiplying these values with $\xi=0.97$ for a 12 μm wide ridge waveguide.

Chapter 5

Fabrication technology

The fabrication of the gratings requires advanced semiconductor processing technology because of the small feature sizes. In this chapter, we briefly describe the techniques used and discuss the possibilities and limitations. The fabrication itself was performed in collaboration with other universities and research institutes.

5.1 Introduction

The process flow for fabricating passive photonic integrated circuits can be summarized as follows: All structures are fabricated on a wafer or substrate. These substrates are discussed in section 5.2. To define patterns on this wafer, a lithography process is used. The pattern is first defined in a resist layer on top of the wafer. This resist pattern is transferred to the wafer using an etching process. It is also possible to add additional layers on top of the structure using deposition. Finally, the optical fibres are connected to the circuit.

Another important aspect is the characterization or inspection of the fabricated structures. If the feature size is a few hundred nanometres, it is not possible to inspect the structures with an optical microscope, so we use a scanning electron microscope.

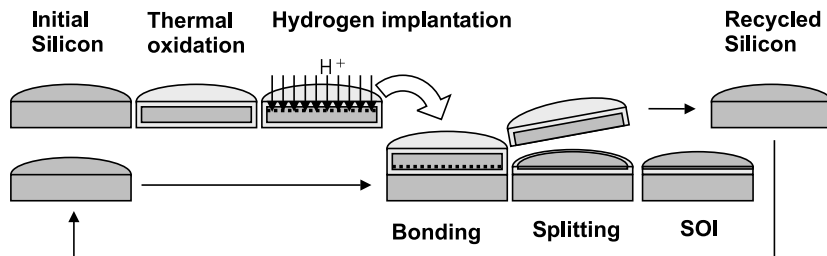


Figure 5.1: SmartCut™ process for fabricating SOI wafers.

5.2 Substrate

5.2.1 SOI

We have used commercially available SOI wafers from SOITEC [80]. These wafers are fabricated with the patented SmartCut™ process. This process is shown in figure 5.1. First a Silicon wafer is thermally oxidized to create the oxide layer. Then hydrogen ions are implanted at a well-controlled depth, creating a smart cut. This wafer is turned upside down and bonded to another Silicon wafer. The substrate of the first wafer can now be separated along the implanted smart cut. Finally the wafer is annealed and polished. The resulting SOI wafers are of very high quality and the optical propagation losses are very low in the telecom wavelength range. We have used wafers with a top Silicon thickness of 220 nm and a buried oxide layer of 1 μm . This buffer is sufficiently thick to prevent leakage loss to the substrate for TE polarization [10]. This process was originally developed to fabricate SOI wafers for high-speed and low-power electronics. In those wafers the buried oxide layer is much thinner.

The same waferbonding process can be used to fabricate SOI wafers with multiple oxide layers. By repeating the process with a SOI wafer instead of a Silicon wafer, a wafer with two oxide layers can be fabricated [81]. Such a “SOIOSOI” wafer is interesting for grating couplers, because the buried layers can be used as a bottom reflector. However these wafers are not commercially available yet.

5.2.2 GaAs

Because of the available technology, we have also performed experiments on GaAs layer structures in the beginning. In the GaAs/AlGaAs

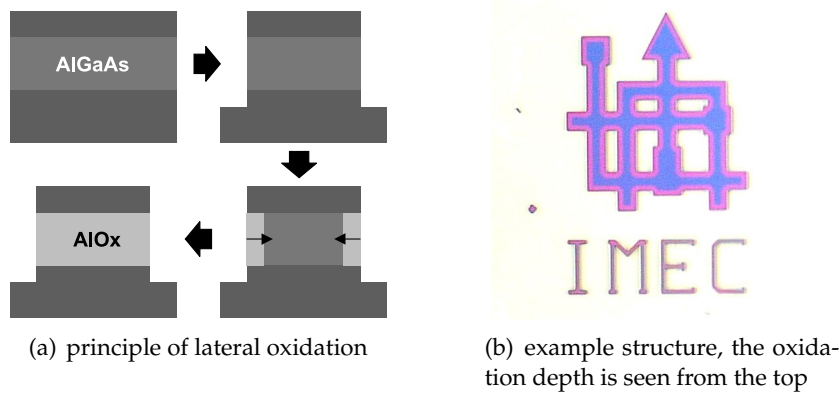


Figure 5.2: Wet thermal oxidation of AlGaAs to create a low refractive index AlOx layer.

material system, a low refractive index material can be created by oxidizing a high Al-content AlGaAs layer. The principle is shown in figure 5.2(a). In a first step, trenches are etched completely through the AlGaAs layer to expose this layer. In a second step the AlGaAs layer is oxidized. The oxidation front propagates laterally from the edges. Depending on the oxidation time, the layer can be partially or completely oxidized. Because of the change in refractive index it is also possible to see this through an optical microscope. As an example, the partially oxidized IMEC logo is shown in figure 5.2(b).

Technical details of the process used are given in [13]. It should be noted that the oxide layers used here are much thicker than in [13]. The resulting refractive index and the quality of the layers are not well known. Because of this and due to technical problems, we have abandoned the GaAs/AlOx route later on.

5.3 Pattern definition

Different techniques can be used to define a pattern on a wafer, but the processing scheme is very similar in all cases. A general scheme is shown in figure 5.3. The wafer is cleaned and a resist layer is spun on the wafer. After spinning and baking, this resist layer has become solid and is ready for exposure. During exposure, the pattern is written in the resist. The exposed parts of the resist are removed during the

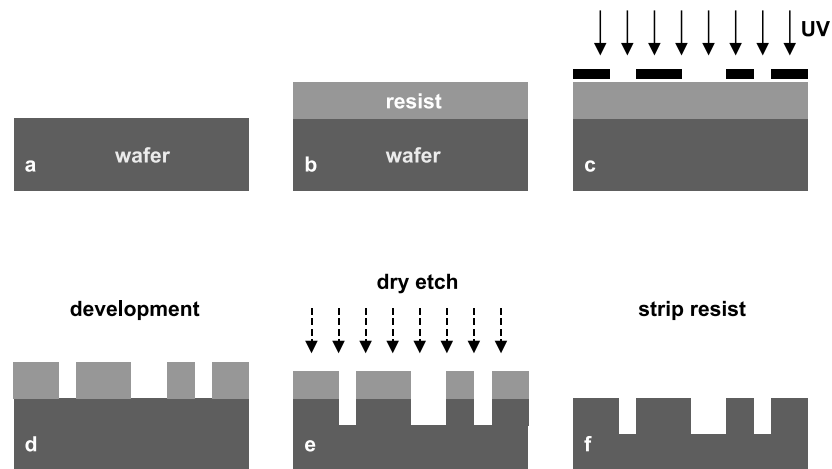


Figure 5.3: General processing scheme: a) wafer cleaning, b) spinning and baking resist, c) exposure with mask, d) resist development, e) dry etch transfers pattern to wafer, f) stripping and final cleaning

development. This patterned resist is used as an etch mask to transfer the pattern into the wafer.

In optical lithography, UV light and a mask are used to expose a photoresist layer. Interference lithography uses two laser beams to define a periodic structure in the resist. Electron-beam lithography uses a scanning electron-beam to write a pattern in a resist layer. These three different techniques have been used to define grating couplers and will be presented in the next sections.

5.3.1 Optical lithography

Optical lithography uses light to image a pattern, that is present on a predefined mask, in a photosensitive resist layer. In contact lithography, the mask is positioned directly on top of the resist layer (figure 5.4a). Contact lithography is used only for research purposes. For mass-production, projection lithography is used. As shown in figure 5.4b, the pattern from the mask is projected using a lens system. Typically, this projection reduces the size of the pattern 4 or 5 times and a stepper is used to print the same patterns many times on a whole wafer.

The resolution depends on a number of factors. The main limitation is imposed by the wavelength of the light that is used. The contact lithography system available in INTEC uses a UV-lamp ($\lambda=305\text{ nm}$) and

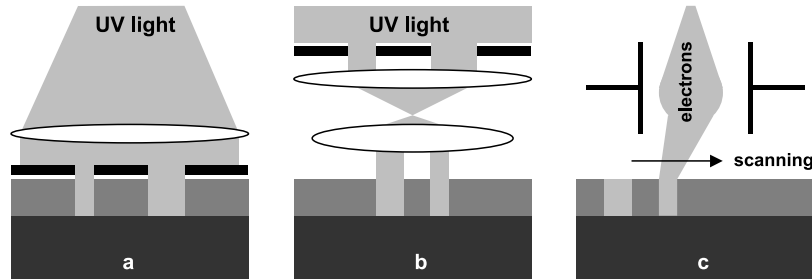


Figure 5.4: Overview of different lithography processes : a) Optical contact lithography, b) Optical projection lithography, c) Electron-beam direct-write lithography.

the minimum linewidth is approximately $0.8 \mu\text{m}$. This is not sufficient for our gratings, but can be used to define wide waveguides. The stepper in IMEC Leuven uses an excimer laser ($\lambda=248 \text{ nm}$) and can achieve linewidths $< 200 \text{ nm}$. Because of the very short wavelength, this is called deep UV lithography or shortly DUV. 248 nm and 193 nm DUV are already used for mass-production of microprocessors. We have used 248 nm DUV for the fabrication of grating couplers, the smallest grating period that can be achieved is approximately 400 nm. The minimum feature size that can be achieved depends not only on the wavelength but also on the NA of the lens system, the thickness of the resist, the exposure conditions and some other parameters. For details we refer to [10, 82].

5.3.2 Electron-beam direct-write lithography

Direct write electron-beam lithography uses a focused electron beam to write a pattern in the resist. The beam is scanned over the resist and no mask is needed (figure 5.4c). Therefore it is very flexible and the spot-size of the beam can be as small as 5 nm. It is the most popular technique for defining nanophotonic structures for research. Electron-beam lithography is not available in INTEC, but thanks to collaboration within the IST-PICCO-project¹, it was possible to fabricate some grating coupler samples with this technique.

Despite the high resolution, direct write electron-beam lithography is not suitable for mass-production, because it is very slow. To address

¹Samples have been fabricated in collaboration with Glasgow University, St.-Andrews University and the Technical University of Denmark.

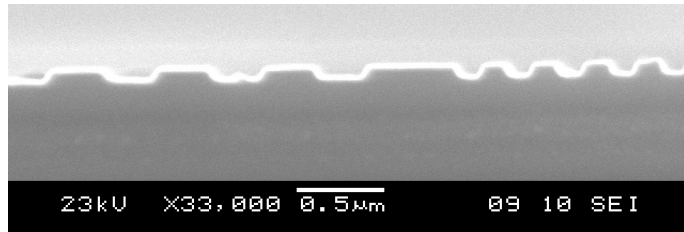


Figure 5.5: Example structure defined by electron-beam lithography.

this throughput issue, electron-projection lithography systems are being developed. The performance of the current systems is insufficient to be able to compete with DUV for mass-production [82].

5.3.3 Interference lithography

A relatively simple technique to define periodic structures is interference lithography or holography. In this technique, two coherent light beams coming from a laser are combined, resulting in a periodic intensity pattern. The angle between the two beams determines the grating period. At INTEC, an Argon laser ($\lambda=363.8$ nm) is used and it is possible to create gratings with a period down to 240 nm. More details can be found in [48], but this process can only define gratings on the entire sample.

We have added an additional optical lithography step to this processing in order to define gratings of finite extent. The complete processing scheme is shown in figure 5.6. An anti-reflective coating (ARC) is used to avoid vertical standing wave patterns in the photoresist. After the illumination with the laser, but before the development of the resist, the grating areas are defined using a conventional lithography step with a mask. After development, oblique evaporation of Ti is used to define the filling factor of the grating. The Ti acts as the etch mask for the etching of the grating.

Some examples of gratings fabricated with this setup are given in figure 5.7. A cross-section of a grating with a period of 240 nm is shown in figure 5.7(a). A top view of a finite grating with a period of 580 nm is shown in figure 5.7(b). The outermost grooves of the grating can have a different width, because it is not possible to align the edge of the grating area exactly with the grating pattern. In the example, the grating is also slightly rotated. This rotation should be avoided and can be reduced to less than 0.5° by carefully aligning the holography setup.

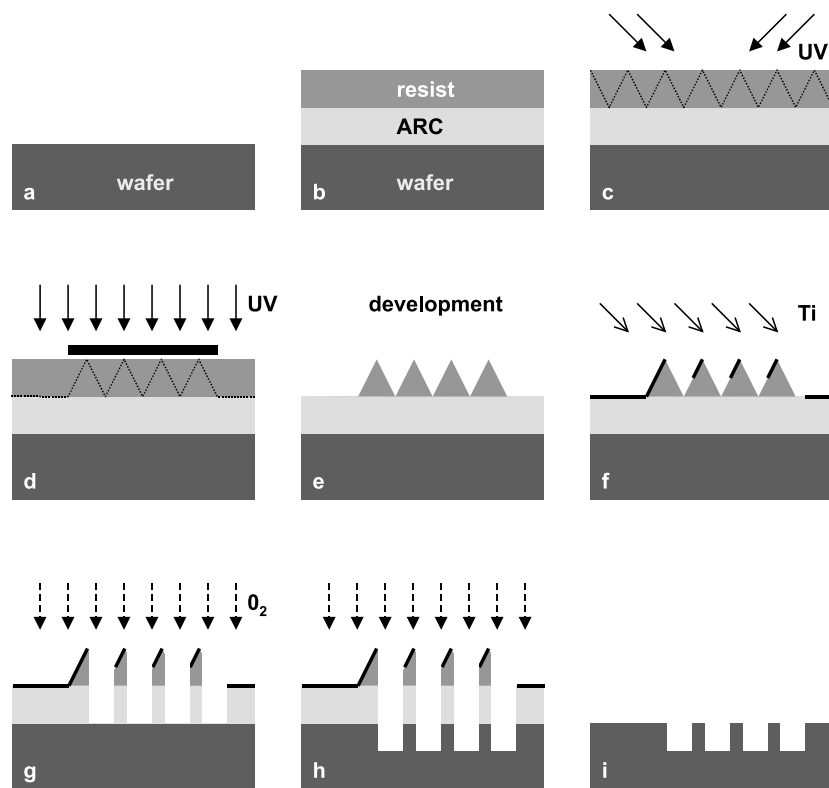


Figure 5.6: Fabrication of gratings of finite extent with interference lithography. a) wafer cleaning, b) spinning and baking ARC and resist, c) exposure with two interfering beams, d) exposure with mask, e) resist development, f) oblique Ti evaporation, g) oxygen plasma etch, h) dry etch transfers pattern to wafer, i) stripping and final cleaning

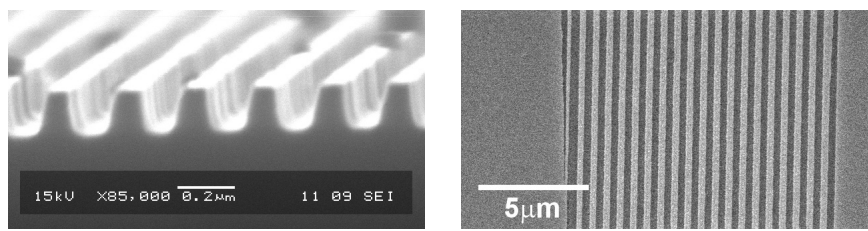


Figure 5.7: Structures fabricated using interference lithography.

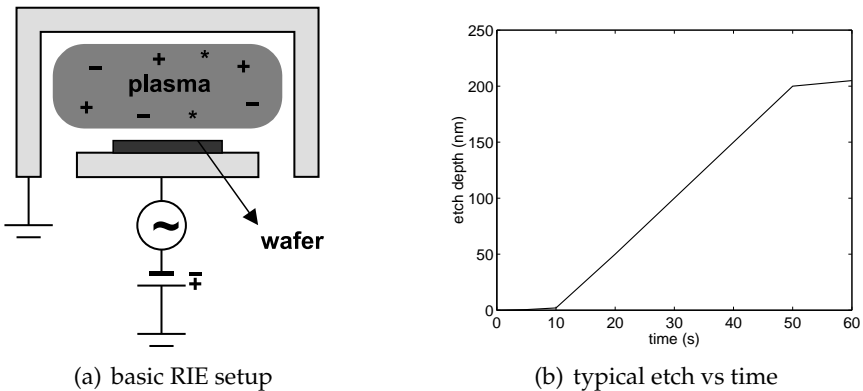


Figure 5.8: Typical reactive ion etching setup and etch characteristic.

It is also possible to define 2-D gratings by using two illumination steps and rotating the sample 90° in between the two illuminations [48]. However, it is very difficult to control the hole shape and size with this technique.

5.3.4 Dry etching

To transfer the resist pattern into the semiconductor, an etching process is used. Simple wet chemical etching is not suitable for fabricating sub-micrometre structures because of the underetch. More complicated dry etching processes are used. Dry etching or plasma etching is a collective name for a whole range of slightly different etch processes. We will only briefly describe reactive ion etching (RIE). The most basic RIE setup is shown in figure 5.8(a). The wafer is placed in a vacuum chamber on an electrode. The chamber is filled with gases and a high voltage is applied to the electrodes. In this way a plasma is created. The reactive ions in the plasma are accelerated towards the wafer and perform the etching². The gases used determine which materials can be etched. In INTEC, RIE etching is available for GaAs and InP compound semiconductors. The Silicon etching was performed in external laboratories.

With our gratings in mind, it is interesting to have a look at a typical etching characteristic. In figure 5.8(b), the etch depth is shown as a function of etch time. We can distinguish three different regions. In the beginning, almost no etching occurs, there is a kind of threshold.

²This description of the etch process is simplified. The actual physics can be much more complicated.

Then there is a linear regime, where the etch depth increases linearly with time. From a certain depth, the etch rate decreases and etching may stop completely. This etch characteristic depends on the width of the grooves, the details of the etch process used and also the treatments of the wafer prior to etching. For shallow gratings, it is important to take into account the threshold when calculating the etching time. In a well-controlled fabrication environment, such as the IMEC pilot line, the error on the etch depth can be less than 5 nm.

5.3.5 Focused Ion Beam etching

A Focused Ion Beam (FIB) machine resembles an electron-beam machine, but ions are used instead of electrons. These relatively heavy ions can be used to etch a semiconductor or metal directly. FIB machines were originally developed for etching and depositing metals to correct masks or interconnects in the micro-electronics industry.

A FIB can also be used to etch Silicon. FIB etching is slow because it is a serial process and also the etch rate is not so high, but that is not a problem for small grating couplers. A slow etch rate also results in an accurate control of the etch depth. Gratings having a different etch depth for each groove can also be fabricated. Using this technique, it is possible to make a non-uniform grating with varying groove width and depth. As a result, the very narrow grooves in the structure of figure 4.34, may be replaced by wider, shallower grooves that have the same coupling strength.

Another interesting option may be to make nanophotonic integrated circuits with DUV lithography and add the grating couplers afterwards with the FIB. In this way, it is possible to compensate for variations in the Silicon core thickness, by adapting the etch depth for each die.

At the time of writing, a FIB was not available to us.

5.4 Characterization

A grating with a 600 nm period is still visible under an optical microscope with very high magnification, but it is not possible to measure the filling factor or etch depth optically. Therefore other characterization tools are required.

The most common tool for viewing and measuring very small structures is the scanning electron microscope or SEM. The principle of the SEM is shown in figure 5.9. In the SEM, an electron-beam is scanned

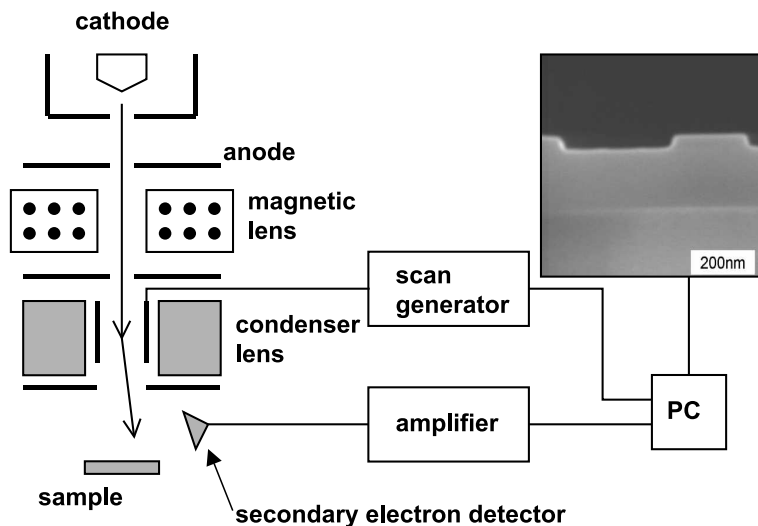


Figure 5.9: Schematic view of a scanning electron microscope.

across a part of the sample. When the electron-beam strikes the sample, backscattered and secondary electrons are created. These secondary electrons are detected synchronously with the scan of the incident beam. Because the number and direction of the scattered electrons depend upon the material composition and topography of the sample over which the incident beam is scanned, the intensity of the detected signal varies so that an image can be created. Usually, secondary electron imaging (SEI) is used because SEI has a higher resolution than backscattered electron imaging [83]. Samples can be viewed from the top (e.g. figure 5.7(b)) or in cross-section (e.g. figure 5.9). A birds-eye view (e.g. figure 5.10) can result in nice pictures, but is not useful for measuring distances.

The resolution is typically a few nanometres, but viewing of sub-micrometre structures requires a skilled operator and suitable samples. Accurate measurements of linewidths or etch depths with the SEM are not so easy. Measurements of resist structures are very tricky, because photoresist is not electrically conducting. The charging of the resist can affect the measured linewidth [82].

The INTEC and ELIS departments have a JEOL 5600 SEM. IMEC Leuven has a number of Hitachi and KLA-Tencor high-end semiconductor inspection SEMs.

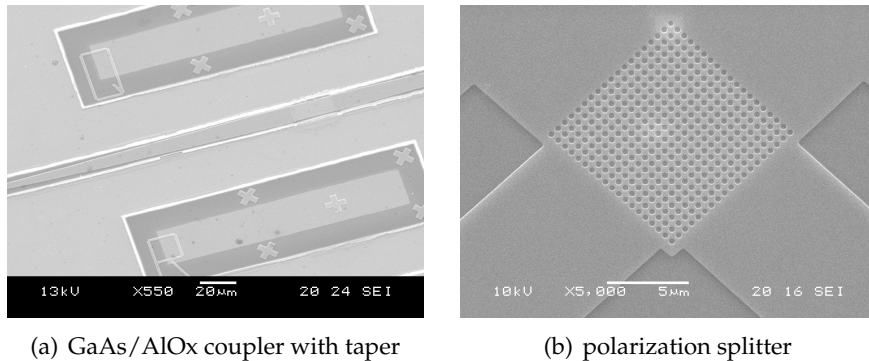


Figure 5.10: Examples of SEM pictures.

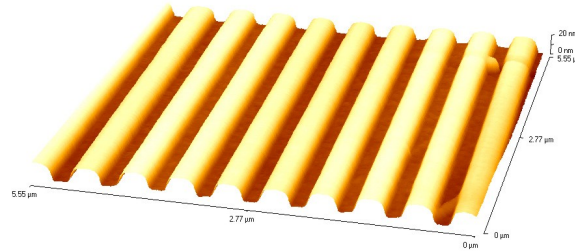


Figure 5.11: AFM measurement of shallow grating (15 nm depth).

To inspect the etch depth using the SEM, the sample has to be cleaved exactly through the structures. If the structures are only $12 \mu\text{m}$ wide, this is not so easy. Cleaving the sample is also destructive.

Another tool that can be used to measure the etch depth of the gratings is the atomic force microscope or AFM. AFM is a scanning probe technique that allows to measure the etch depth from the top. A probe with a very sharp tip is used to scan the topography of the sample. AFM is available in Ghent University in the solid-state physics research group. An example of a very shallow grating is shown in figure 5.11. Another example of a structure with two different etch depths is shown in figure 5.12(a).

5.5 Deposition

A chemical vapour deposition process can be used to deposit additional layers on top of the grating structures. Different materials can be de-

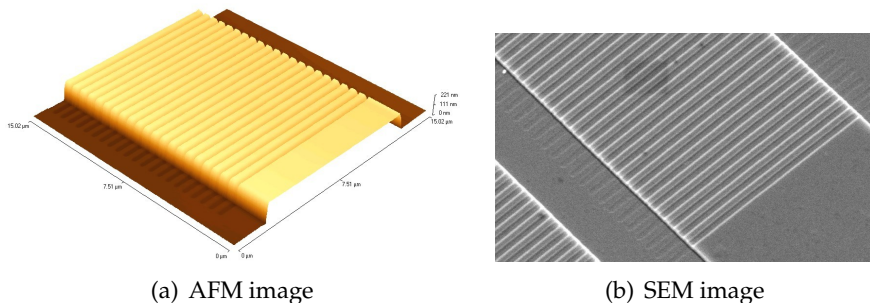


Figure 5.12: Structures fabricated with DUV using two etch steps. The depth of the grating is 50 nm and the wide trenches are almost 220 nm deep.

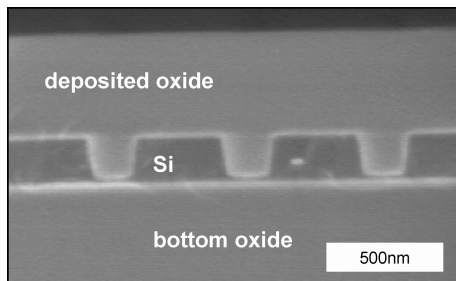


Figure 5.13: Oxide deposited on top of a deeply etched grating.

Posed, oxide and (poly)silicon are the most important for us. With an optimized process, even deep and narrow holes can be filled without voids and the structure becomes planarized [10]. An example of oxide deposition performed in IMEC Leuven is shown in figure 5.13. The 200 nm deep holes are completely filled and the top interface is perfectly flat.

Unfortunately, the standard SiO_2 deposition process used in INTEC is not so optimized. The top surface of a 500 nm SiO_2 layer on top of a 50 nm deep grating is not completely flat. Also the refractive index of the deposited layer is not very reproducible. This refractive index is very important when fabricating couplers with a top mirror. It should be possible to improve this process.

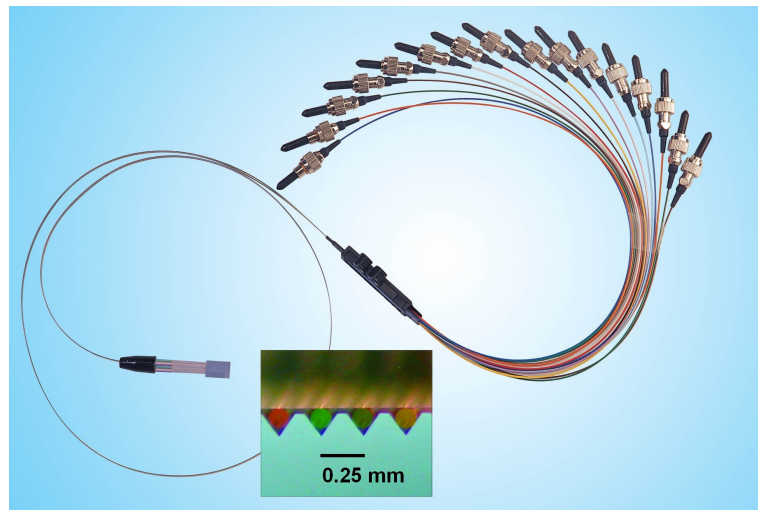


Figure 5.14: Array of 16 fibres mounted in V-grooves. The inset shows a close up of the end face of the fibre array.

5.6 Packaging

Packaging accounts for a major part of the cost of optical components. The use of grating couplers has several advantages. Because light is coupled in and out from the top, there is no need to polish the facets of the chip. Also the sensitivity to alignment errors is good because standard fibres are used without additional lenses.

To attach a lot of fibres to one chip, fibre arrays consisting of fibres mounted in Silicon V-grooves can be used. An example with 16 fibres is shown in figure 5.14. The fibre pitch is $250 \mu\text{m}$ and the deviation of the centre of the fibres from the optimal position is less than $1 \mu\text{m}$ in commercially available components [84]. These fibre arrays can be glued to the chip using UV-curable glues. These glues are available with a refractive index that matches the refractive index of the fibre. The top cover layer of the V-groove chip is transparent to allow the UV-curing of the glue. The end face of the fibre array can be flat or angle polished.

Usually, these fibre arrays are used to couple light in and out at the edge of a chip. But they can also be mounted vertically on top of a chip when using grating couplers.

Chapter 6

Measurements

In this chapter our experimental results are presented. We explain the measurement setup used, because it differs from the conventional waveguide measurement setup. The most important result is the coupling efficiency as a function of wavelength, but also the alignment tolerances and the uniformity measurements are presented.

6.1 Measurement setup

In a conventional measurement setup for the characterization of integrated optical waveguides, light is coupled in and out at the edges of the chip. In this setup the fibres and the chip are all in the same plane. We have adapted this setup for coupling from the top. We will describe two possible setups. In the first setup, light is coupled in and out with fibres on a structure with a grating coupler at both ends. In the second setup we couple light in using a vertical fibre, but measure the output power at a cleaved facet.

6.1.1 Fibre in - fibre out

This measurement setup is shown in figure 6.1. The input and output fibres are mounted on high-precision 3-axis translation stages. By using custom adapter plates, the fibres can be mounted vertically or at a 10° angle with respect to the vertical direction. The sample is mounted on a vacuum chuck on a two-axis stage. The input fibre is connected to a tunable laser with a tuning range of 1500-1640 nm. The output fibre is connected to a power detector to measure the transmitted power. Both the laser and detector can be connected to a PC using the GPIB

interface. An alternative to using a widely tunable laser is to use a broadband light source at the input and an optical spectrum analyzer at the output.

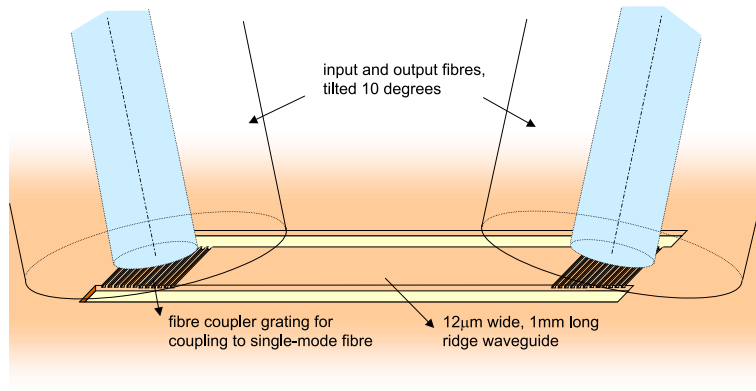
When coupling in from the top, it is not possible to position a microscope above the sample as in a conventional setup. We use a fibre lamp to illuminate the sample and a ccd-camera instead of a microscope. A microscope objective lens with a magnification of $5\times$ or $10\times$ and a long working distance is mounted on the camera. The angle between the optical axis of the camera system and the horizontal plane is 30° . This setup allows the observation of the structures on the sample and the fibres with sufficient resolution.

For the initial alignment, the camera image is used. The fibres are positioned relatively high ($500\ \mu\text{m}$) above the grating. This results in a low coupling efficiency, but easy alignment. As soon as there is some light transmitted, we can switch to active alignment. The position of the fibres is changed to maximize the power transmission at a fixed wavelength. This fixed wavelength is preferably the central wavelength of the coupler spectrum. The height of the fibre can be determined from the camera image, because both the fibre and its shadow can be seen. This alignment procedure is summarized in figure 6.2. When the fibres are aligned, the wavelength of the laser is swept to measure the transmission as a function of the wavelength.

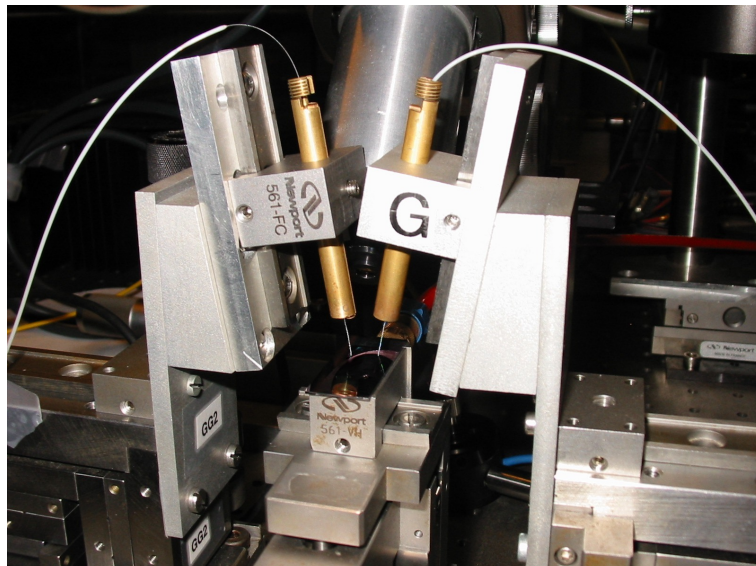
To control the polarization of the input light, we can use two different techniques. One is to use polarization maintaining fibre (PMF). The laser output is linearly polarized and has a PMF output. By rotating the input fibre, we can couple in any linear polarization. The second option is to use standard single-mode fibre in combination with a polarization controller¹. This allows to change the polarization state without having to realign the fibre. The disadvantage is that the polarization state is not known. But if we know that the structures have the highest efficiency for TE-polarization, we can simply optimize the transmission by changing the polarization state.

An example of a transmission measurement is shown in figure 6.3. In the case of vertical coupling ($\theta=0^\circ$), a lot of resonances are present, because of the second-order reflection of the grating. The resonances make the interpretation of the results more difficult. In the case of near vertical coupling ($\theta=10^\circ$), these resonances are avoided. The calculation of the coupling efficiency from this transmission is rather simple. If we

¹We have used a Lefevre-type [85] polarization controller. In this device, the light does not leave the fibre.



(a) coupling in and out with fibres



(b) photo of the measurement setup

Figure 6.1: Measurement setup to measure the coupling efficiency of the grating couplers. The input fibre is connected to a tunable laser and the output fibre to a power detector.

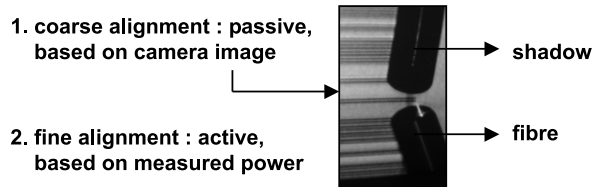


Figure 6.2: Summary of the alignment procedure.

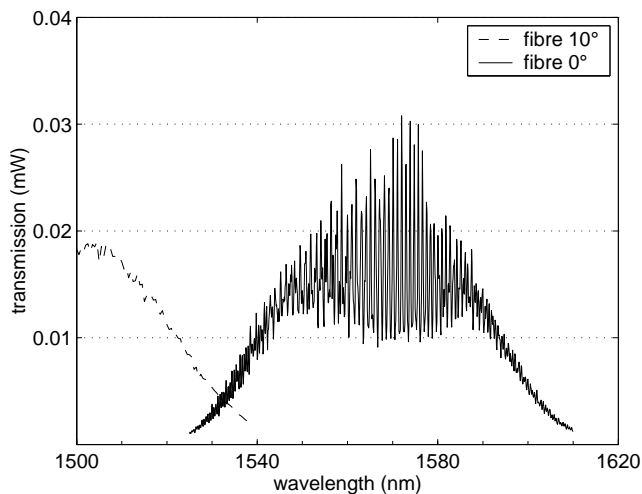


Figure 6.3: Comparison of vertical and almost vertical coupling. The grating period $\Lambda=580$ nm.

take into account that the input and output coupling efficiency are the same, the relation between the transmission T and the efficiency η is given by :

$$T = \eta_{in}\eta_{out} = \eta^2 \Rightarrow \eta = \sqrt{T} \quad (6.1)$$

If the coupling conditions at the input and output are not exactly the same, the efficiency is slightly underestimated and the bandwidth overestimated. The transmission T in equation (6.1) is the measured power P divided by the reference power P_{ref} . P_{ref} is measured by connecting the laser directly to the power detector with a fibre patchcord. It is important to verify that the power detector is working in its linear regime. Equation (6.1) also neglects the propagation losses in the waveguide, but these losses are very low for the SOI waveguides used.

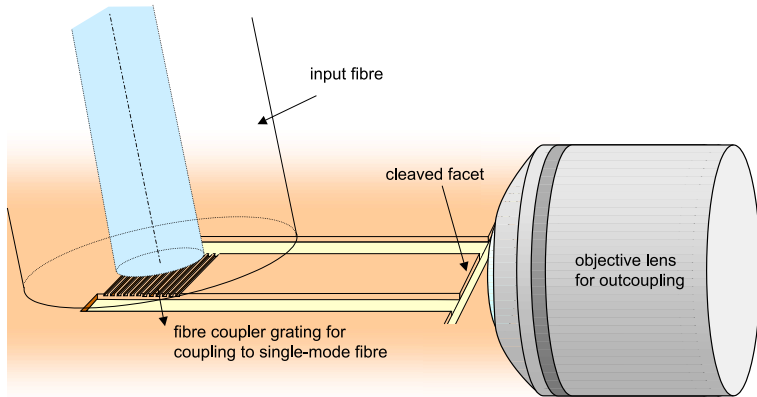
6.1.2 Fibre in - cleaved facet out

An alternative technique is using a fibre to couple light in, but measure the output power at a cleaved facet. This setup is shown in figure 6.4. The input side is the same as in the previous setup. At the output side, a $40\times$ microscope objective is used to collect the light from the output facet. This light is imaged onto a power detector or an infrared camera. The objective is mounted on a 3-axis translation stage. During the initial alignment, the infrared camera is used to monitor the light coming from the facet. When the objective lens is properly aligned, the output light is focused onto the power detector and the power transmission can be measured. Active alignment is used for the final alignment.

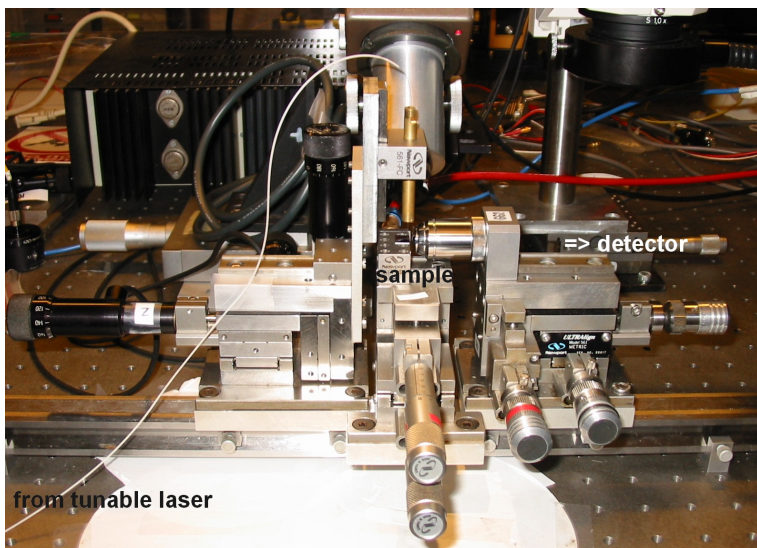
If a perfect AR-coating is present on the cleaved facet, then the measurement of the coupling efficiency is easy. In this case, all the light that is coupled from the fibre to the waveguide reaches the power detector and the measured transmission equals the coupling efficiency from fibre to waveguide. Unfortunately, it was not possible to deposit a good AR-coating on these waveguides.

In the case of a cleaved facet without AR-coating, the interpretation of the measurement results is not so easy, because of the high reflectivity of the facet. To calculate the coupling efficiency, we cannot simply divide the transmitted power by the input power. Also averaging the wavelength dependent output power is not correct. We have to take into account the effect of the cavity between the grating and the facet. If the facet reflectivity is known, it is possible to calculate the transmission for different grating reflectivities. An example is shown in figure 6.5. A simple transfer matrix method was used to calculate these transmission curves. The ratio of the maxima and minima only depends on the grating reflectivity if the facet reflectivity is fixed and the propagation losses are neglected. In this way, the grating reflectivity can be estimated from the measurement results. A correction factor can be calculated that gives the relation between the coupling efficiency and the transmission peaks. When there is no reflection at the grating, the measured transmission is $1-R_{\text{facet}}$ times the coupling efficiency, so the efficiency is higher than the measured transmission.

As an illustration, some measurement results are shown in figure 6.6. The measured structures are grating couplers on GaAs/AlOx waveguides. The waveguides are cleaved very short (approx. $200\ \mu\text{m}$) to reduce the propagation losses. In figure 6.6(a), the peak transmission is 7% and the ratio between the maxima and minima is $7/2$. This situation corresponds to the dash-dot line in figure 6.5. The peaks correspond to



(a) coupling in with fibre and out at a cleaved facet



(b) photo of the measurement setup

Figure 6.4: Measurement setup to measure the coupling efficiency with only one grating coupler. The input fibre is connected to a tunable laser and the output light is collected with an objective and imaged onto a power detector or infrared camera.

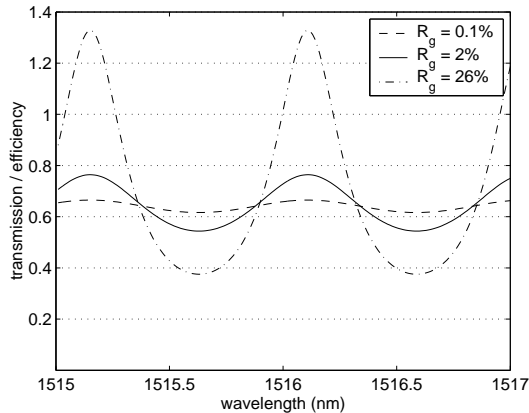


Figure 6.5: Calculation of the power transmission as a function of wavelength for different grating reflectivities. The values on the y-axis are the normalized transmission divided by the coupling efficiency from fibre to waveguide. A facet reflectivity of 36% is used.

1.3 times the coupling efficiency in this case. So the coupling efficiency is only 5.4%. In figure 6.6(b), the peak transmission is 14% and the ratio between the maxima and minima is 14/10. This situation corresponds to the solid line in figure 6.5. The peaks correspond to 0.75 times the coupling efficiency. In contrast to the previous case, the efficiency is higher than the peak transmission. The calculated coupling efficiency is 19%. This value is the transmission that we would measure if a perfect AR-coating were present on the facet.

This method has some disadvantages compared to the fibre in - fibre out method. A high quality facet is needed. Cleaving a facet is easy if the substrate is GaAs or InP. In the case of a Silicon substrate, it is difficult to make a good facet by cleaving. Even when the facet is perfect, a lens with a very high NA is needed to capture all the light. We have used a lens with $NA=0.65$ and to verify that all the light is collected with this lens, we have also used a lens with $NA=0.8$. The results obtained with both lenses were equal, indicating that all the output light is captured. But it is no guarantee, because there may be some reflection at the objective. Although the lenses have an AR coating, a very low reflection is only guaranteed for a smaller NA. The light that is reflected at the objective lens is lost and cannot reach the power detector. We can conclude that this method may underestimate the coupling efficiency. It is better to use the fibre in - fibre out method for an accurate measurement of the coupling efficiency.

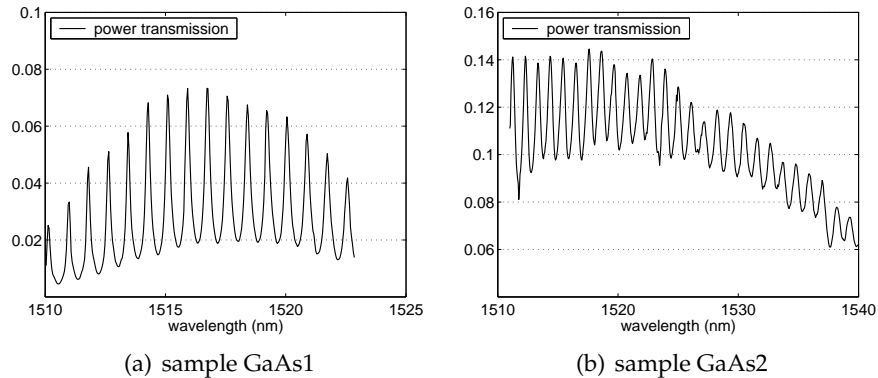


Figure 6.6: Measurement of the power transmission as a function of wavelength in the case of a cleaved facet without AR-coating. The actual coupling efficiency from fibre to waveguide can be estimated using figure 6.5.

6.2 Measurement results

In the next sections, our experimental results are presented. These are the result of a number of iterations. A lot of samples have been fabricated, but only the best results are discussed here. A longer list of samples that have been fabricated and characterized is given in appendix B.

6.2.1 Coupling efficiency

We will present the measurement results of the fabricated couplers with uniform gratings. As discussed before, we perform a transmission measurement on a waveguide with a grating coupler at both ends. The coupling efficiency of one coupler is calculated from this transmission value.

The optimal grating parameters were given in figure 4.8(a). The actual depth of the fabricated gratings is approximately 55 nm. As a result, the theoretical efficiency is 37% instead of 39% for the optimal depth. In any case the grating parameters of the fabricated structures are close to the optimal parameters. The waveguides are $12 \mu\text{m}$ wide and 1 mm long. The trenches that define the waveguides are $5 \mu\text{m}$ wide and etched in the same step as the gratings. As a result, the trenches are only slightly deeper than the gratings, but this is sufficient to create wide waveguides with very low propagation loss. These structures

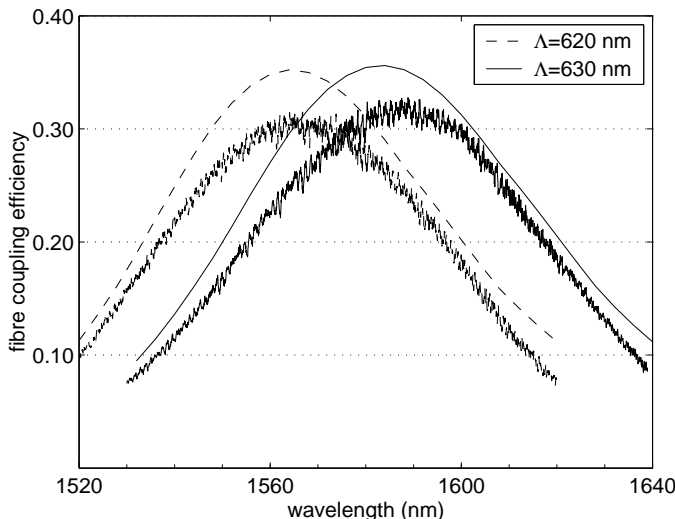


Figure 6.7: Measurement of the coupling efficiency versus wavelength. The smooth curves are the corresponding theoretical simulation results.

have been fabricated at Glasgow University using electron-beam lithography.

The measured coupling efficiency is 33% or -4.8 dB. The 1 dB bandwidth is between 35 and 40 nm. The coupling efficiency as a function of wavelength is shown in figure 6.7. The dashed curve is for a grating with $\Lambda=620 \text{ nm}$ and the solid curve is for a 630 nm period. The corresponding theoretical results are also shown in figure 6.7. The experimental results agree well with the theoretical curves, but the efficiency is a few percent lower. In part, this difference is due to the 2-D model used in the theoretical calculations. Also the distance between the grating and the fibre is $11 \mu\text{m}$ in the experiments and only $2 \mu\text{m}$ in the theoretical model used. It is not possible to position the fibre closer to the grating, because we used straight cleaved fibres mounted at a 10° angle.

6.2.2 With taper

In most applications, the light has to be coupled to a single-mode waveguide. The wide waveguide from the grating coupler is connected to a narrow single-mode photonic wire using a horizontal spot-size converter. We have used a linear taper as spot-size converter. The fabrication requires two steps with a different etch depth. First the gratings

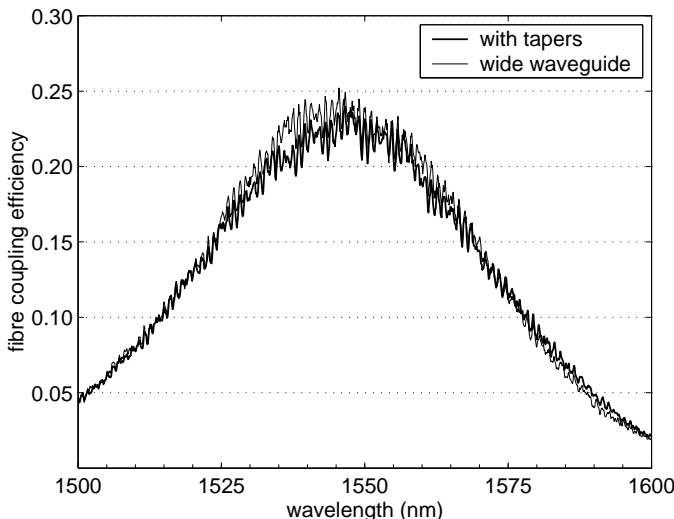


Figure 6.8: Measurement of the coupling efficiency versus wavelength with and without taper.

are defined and etched 45-50 nm deep. Afterwards the waveguides and tapers are defined and etched 220 nm deep. This processing was performed in IMEC Leuven using 248 nm DUV lithography.

The total length of the waveguides connecting the input and output couplers is 7 mm. The wide waveguide is 10 μm wide and the single-mode wire approximately 500 nm. The length of the linear tapers is 1 mm and the narrow wire is 100 μm long. The measured coupling efficiency for the structure with tapers is shown in figure 6.8. The efficiency measured on a 10 μm wide waveguide without tapers is also shown on the same figure.

The two curves match quite well. This confirms the assumption that light is only coupled to the fundamental waveguide mode if the fibre is accurately centered above the waveguide. The higher order waveguides modes are filtered out by the tapers and the single-mode wire and coupling to these modes would result in a lower transmission efficiency. Coupling to higher order modes may occur when the fibre is not centered. Also a lateral tilt of the fibre or a slightly rotated waveguide will cause coupling to higher order modes. This is discussed in more detail in section 7.1.2.

For the wide waveguide, the measured transmission for TE is 45 dB higher than the transmission for TM polarization. If we take into ac-

count that the TM-propagation loss is approximately 1 dB/mm, the resulting extinction ratio of one coupler is 19 dB.

6.2.3 Alignment sensitivity

An important property of the couplers is the sensitivity to alignment errors. We have measured the coupling loss as a function of the horizontal (in plane) position. In figure 6.9, the additional loss caused by alignment errors is shown. An alignment error of $\pm 1 \mu\text{m}$ results in less than 0.5 dB additional coupling loss. In other words, the diameter of the -0.5 dB contour is $2 \mu\text{m}$. These experimental results agree with the theoretical predictions. To measure the curve of figure 6.9(b), the position of the fibre is first optimized for maximum coupling efficiency. Afterwards the position of the fibre is scanned in the xz-plane.

6.2.4 With index-matching layer

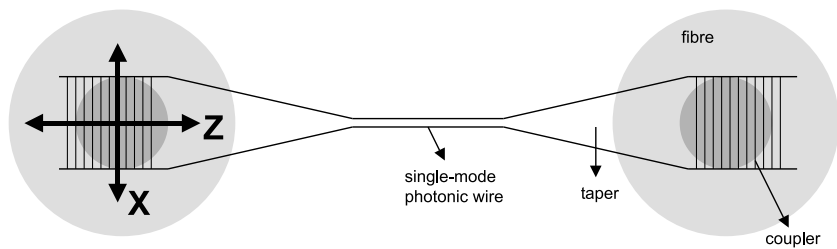
We have experimentally verified the effect of an index-matching layer or glue. We have measured the coupling efficiency as a function of wavelength with and without glue between the Silicon and the fibres. The results are shown in figure 6.10. The grating period Λ is 610 nm, the filling factor 50%, the etch depth 50 nm and the angle $\theta=10^\circ$.

As a result of the glue, the central wavelength is shifted from 1550 nm to 1520 nm and the efficiency is slightly increased. These effects confirm the theoretical predictions (see also figure 4.7). The spectrum can be shifted to longer wavelengths by reducing the angle θ or increasing the period Λ . To achieve a higher efficiency, a deeper grating (70 nm) is needed.

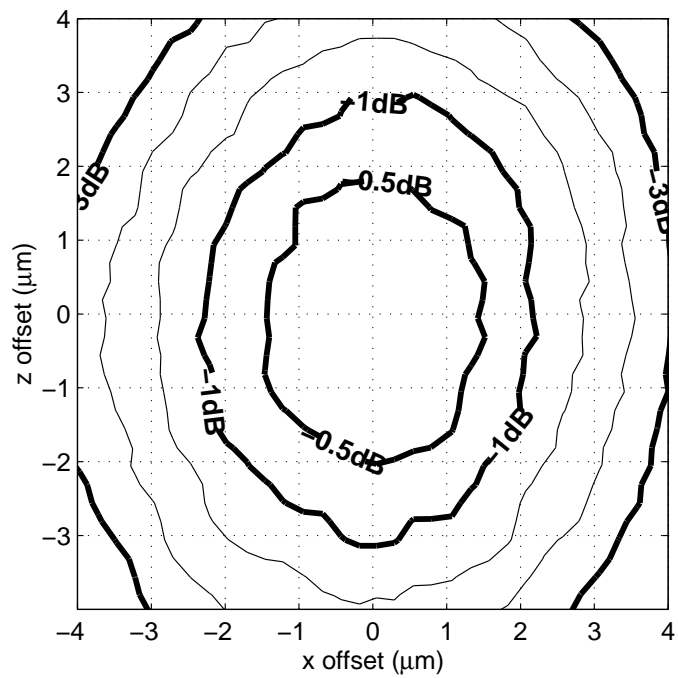
The glue may also affect the waveguide propagation losses, because there is no oxide layer on top of the Silicon core in our structures. In practical applications, an oxide passivation layer will be present on top of the Silicon. Also fibre arrays mounted in V-grooves instead of single fibres will be glued to the SOI chip.

6.2.5 Uniformity

In this section, we have a look at the uniformity of the fabricated gratings. For the characterization of other nanophotonic components (section 6.2.6), the same grating coupler is repeated many times on a wafer. We have compared couplers on one sample to avoid the effect of the non-uniformity of the Silicon layer thickness across the wafer.



(a) measurement setup



(b) measurement results

Figure 6.9: Experimental alignment tolerances.

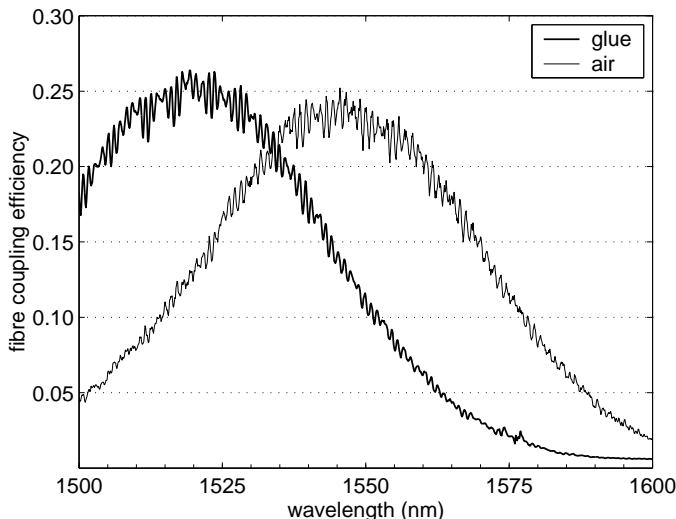


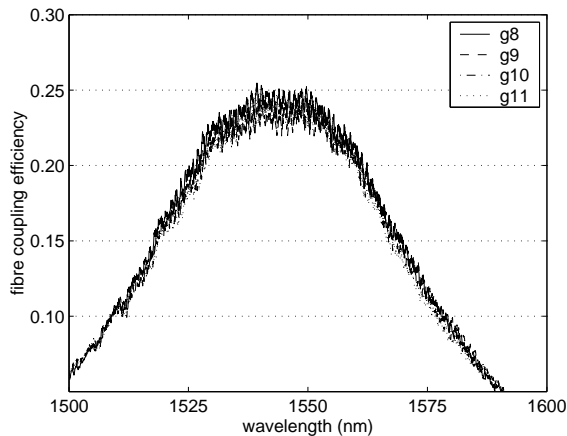
Figure 6.10: Measurement of the coupling efficiency versus wavelength with and without an index-matching glue between the Silicon and the fibre.

We have measured the efficiency of the same coupler on different parts of a sample. The distance between the different couplers is approximately $500 \mu\text{m}$. The resulting efficiency curves are shown in figure 6.11. The curves roughly coincide. The measured etch depth of the grooves of different gratings is also shown in figure 6.11(c). There is only a difference of a few nanometre between the different gratings.

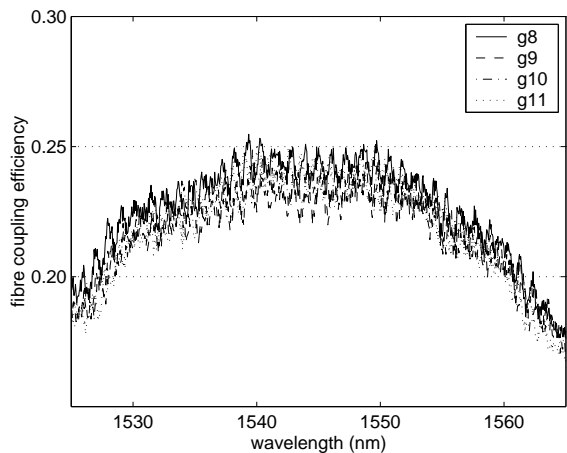
6.2.6 Characterization of other components

The grating couplers can be used for the characterization of other nanophotonic components. The setup used is shown in figure 6.12. The alignment is much easier than in a conventional edge coupling setup. In addition, there is no stray light that can reach the detector. The only tricky part is the height of the fibre above the sample. In the case of 10° coupling, it is not a problem if the fibre accidentally touches the sample. There is no damage because it is the edge of the fibre that touches the chip next to the grating. An additional camera may be used to view the distance between the fibre tip and the sample. The main disadvantage of the grating couplers is the limited bandwidth.

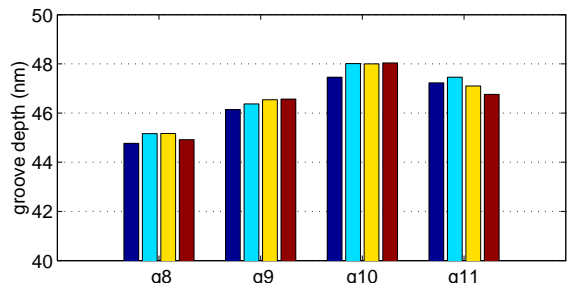
When using the couplers to measure the loss of other components, the following procedure must be used to ensure that the coupling conditions are the same. First the fibres are aligned on a reference wave-



(a) coupling efficiency



(b) coupling efficiency zoomed in



(c) measurement of groove depth (AFM)

Figure 6.11: Uniformity measurements on identical structures on the same die. The distance between two adjacent groups is approximately $500 \mu\text{m}$.

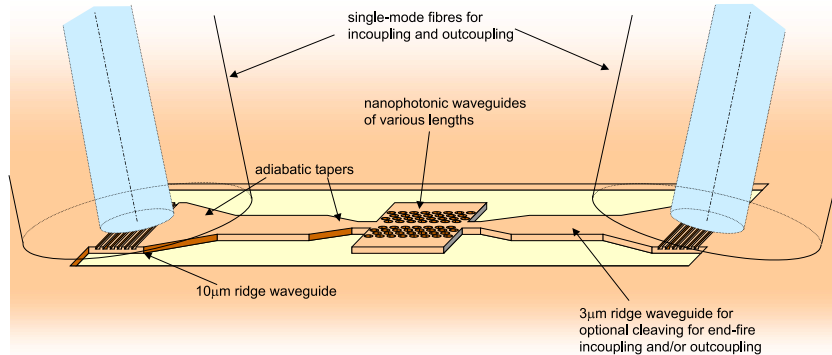


Figure 6.12: Setup for the characterization of other nanophotonic components.

guide that is close to the structures of interest. The transmission as a function of wavelength is measured on this reference waveguide. To move to the next structure, only the sample stage is moved and the lateral alignment of the fibres optimized, always at the same wavelength. The height of the fibres is not changed. The structures that are compared must be close together on the sample. In the design, a reference waveguide must be included in every group of components.

It is difficult to accurately measure low propagation losses with this method, because the different gratings differ slightly. Also there is some noise on the measured curves. This noise can be the result of different causes :

- Vibrations of the fibre tips. To reduce this effect, the time averaging function of the power meter can be used. This increases the measurement time. Another solution is to glue the fibres to the chip, but this is not so practical for the characterization of many components.
- Dirty or worn-out fibre connectors. This problem can be avoided by always carefully cleaning the connectors and replacing connectors that show any obvious sign of wear. Fibre connectors wear out rapidly by connecting and disconnecting them.
- Reflection at the cleaved fibre facets. A cavity is formed between the fibre facet and the grating coupler. This cavity is short and would result in a large fringe spacing. The cavity between the two couplers or fibres is long and may be responsible for some

of the noise. But in the case of 10° coupling, the reflection at the coupler back into the fibre is very small.

- Reflection at the power detector results in a cavity between the fibre connector and the detector surface. This problem may be avoided by using a new detector with a good AR coating.
- Variations in the polarization of the input light. When regular single-mode fibre together with a polarization controller is used, it is not possible to verify the polarization of the light in the fibre.
- Coupling to higher order modes due to bad alignment. These are filtered out by tapering to a single-mode wire. But if the wire supports a few guided modes instead of a single mode, an oscillation in the transmission versus wavelength characteristic is seen.

To find the main cause of the noise, a Fourier transform of the measured spectrum may help. We found a significant peak for a cavity length of 1 mm in air which corresponds to the fibre-detector cavity. We did not see a cavity corresponding to the length of the waveguide between the two gratings. The transmission curves can be smoothed by filtering out high-frequency components, but care should be taken not to filter out useful information.

6.2.7 Reflection measurements

Another interesting experiment is a reflection measurement. By adding a 3 dB splitter between the laser and the input fibre, the backreflection into the input fibre can be measured with a power detector. The measured reflection of a cleaved fibre facet is approximately 2.5%.

When the fibre is aligned with a grating coupler, the reflection becomes wavelength dependent. The reflection at the fibre facet and the reflection at the sample that couples back into the fibre, interfere. The phase difference is wavelength dependent. This is illustrated in figure 6.13(a). Two examples are shown in figure 6.14. The slow oscillation is caused by a cavity between the fibre facet and the sample. The distance between the fibre and the sample is related to the period of this oscillation by

$$L = \frac{\lambda^2}{2\Delta\lambda} \quad (6.2)$$

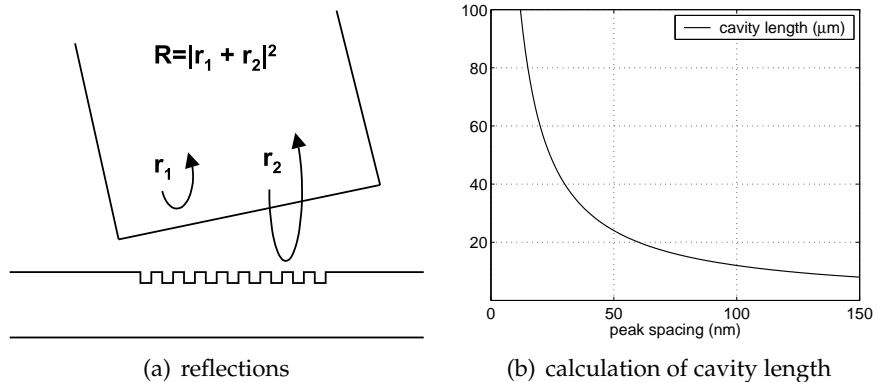


Figure 6.13: Reflection at the fibre facet and the sample.

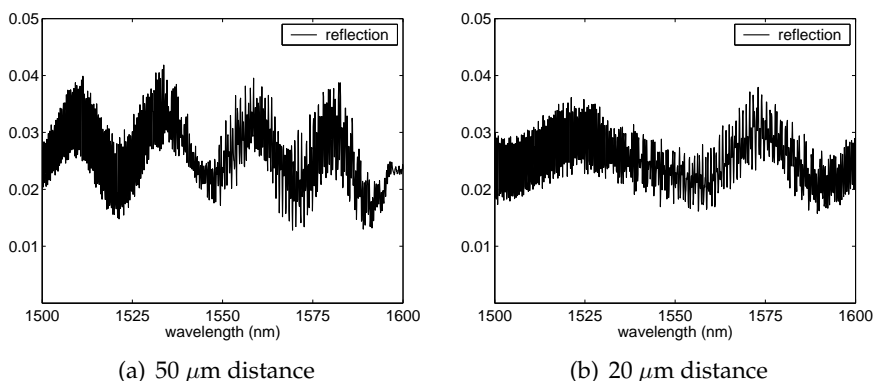


Figure 6.14: Examples of reflection measurements.

This relation is plotted in figure 6.13(b) and is valid if the cavity length is much larger than the wavelength. In the example of figure 6.14(a), $\Delta\lambda \approx 25$ nm and the distance ≈ 50 μm . In the second example (figure 6.14(b)), $\Delta\lambda \approx 55$ nm and the distance ≈ 20 μm . These values are approximate because the reflection at the coupler is wavelength dependent in the experiments. The rapid oscillation seen in figures 6.14(a) and 6.14(b) has a periodicity of approximately 0.5 nm and is caused by the fibre-detector cavity. A 10° angle between the fibre and the vertical direction is used in both examples. When the fibre tip is as close as possible to the sample, the distance ≈ 11 μm and the oscillation period becomes very large.

Not only the cavity length but also the amount of reflection from the coupler can be estimated. The reflection $|r_2|^2$ is between 0.1% and 0.2% in both examples. The reflection $|r_1|^2$ is approximately 2.5%, which agrees with the measured reflection from a fibre facet. The small reflection from the coupler has a visible effect because it is significant compared to the reflection of the fibre facet. The effect is less visible in a transmission measurement.

6.2.8 Conclusions

We have experimentally demonstrated efficient coupling between single-mode fibres and sub-micrometre SOI waveguides using compact grating couplers. The highest measured coupling efficiency is 33% for a uniform grating and the measured coupling characteristic is in good agreement with the simulation results. A measurement setup has been constructed for the characterization of the grating couplers using (near) vertical fibres. This measurement setup also provides a convenient way for the characterization of other SOI nanophotonic components.

The easiest way to improve the efficiency of the couplers is the use of SOI wafers with an optimal thickness of the buried oxide layer. Unfortunately, SOI wafers with a custom oxide thickness can only be bought in large quantities. To achieve a very high efficiency ($> 70\%$), SOI with a bottom reflector would be needed.

The efficiency may be further improved by using an optimized grating design instead of a uniform grating. However, these optimized structures are very challenging to fabricate, because a very accurate control of the etch depth and the line width is required. In addition, the variations on the Silicon top layer thickness across a wafer reduce the acceptable errors on the etch depth.

Chapter 7

2-D grating coupler

A coupler based on a 2-D grating is discussed in this chapter. This coupler is used as a polarization splitter. The principle of the splitter is explained, followed by some design considerations and a brief overview of numerical methods that can be used to simulate 2-D grating couplers. Finally some experimental results are presented.

7.1 Introduction

A 2-D or crossed grating is periodic in two directions. Other names are bi-gratings or doubly periodic gratings. An example of such a grating is a square array of holes etched in a semiconductor. 2-D gratings are interesting for the polarization properties. Examples of applications are polarization converters [86] and polarization independent resonant grating filters [87]. In this chapter, we will discuss waveguide grating couplers that use a 2-D grating. A 2-D waveguide grating is a 3-D problem and cannot be approximated by a 2-D model anymore. We use these 2-D waveguide grating couplers as a polarization splitter in a special configuration.

7.1.1 Basic principle

It is well known that a single-mode fibre can carry two orthogonal linearly polarized modes. When launching light into the fibre, the total field will be in an elliptical state of polarization. Also the state of polarization changes during propagation in a real fibre due to polarization mode dispersion [29].

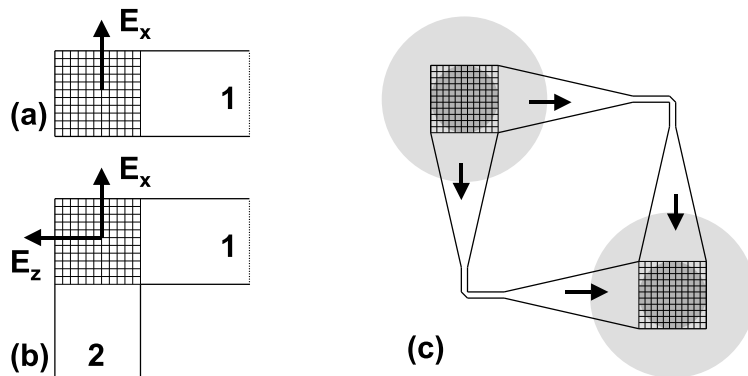


Figure 7.1: Top view of (a) 2-D grating coupler, (b) 2-D grating coupler used as polarization splitter (c) input and output coupler used in a polarization diversity configuration.

Consider a grating coupler consisting of a 2-D grating etched in a ridge waveguide (figure 7.1(a)). In general, the coupling efficiency from fibre to waveguide is polarization dependent. For the waveguides and gratings we use, the coupling efficiency for TE is much larger than the coupling efficiency for TM. The coupling from fibre to waveguide will be maximized if the input is linearly polarized in the x-direction. The structure of figure 7.1(b) consists of two ridge waveguides that are orthogonal with regard to each other. The 2-D grating is etched into the intersection of the waveguides and is invariant for a 90° rotation. Light from the vertical fibre with linear polarization with electric field E_x will couple to waveguide 1 and the other polarization with electric field E_z to waveguide 2. In general, elliptically polarized light from a single-mode fibre will couple to both waveguide 1 and 2. The coupling ratio will depend on the state of polarization, but the total coupling to waveguide 1 and waveguide 2 together, will be independent of it. We have described the working principle as input coupler, but the device can also be used as output coupler. The coupling efficiency from waveguide to fibre is the same as from fibre to waveguide when considering the coupling from one mode to another mode because of reciprocity.

The coupler can be used as input and output coupler in a polarization diversity configuration. A very simple configuration is shown in figure 7.1(c). The transmission from input fibre to output fibre is independent of the polarization of the input light, although the waveguides used in the circuit are polarization sensitive. The figures of merit for

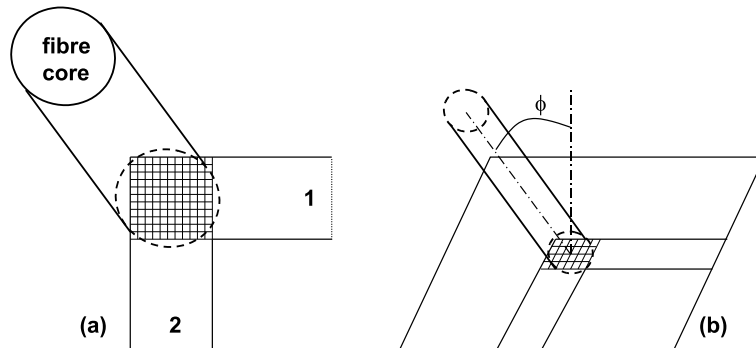


Figure 7.2: Near vertical coupling. (a) top view, (b) definition of the angle ϕ .

this circuit are the fibre-to-fibre insertion loss and the polarization dependent loss (PDL). The PDL is defined as $10 \log_{10}(P_{max}/P_{min})$ when the polarization state of the input is changed to all possible states. In the ideal case, the PDL is zero and the insertion loss depends only on the coupling efficiency of the gratings for TE-polarization. In the real world, the input or output coupling conditions at both waveguides are not exactly the same and also the TE/TM extinction ratio is limited. These effects will increase the insertion loss and the PDL.

From chapter 4, we know that it is very difficult to make a grating for vertical coupling that has a low reflection. Therefore we will discuss the effect of near vertical coupling in the next section.

7.1.2 Near vertical coupling

The second order reflection can be avoided by using near vertical coupling. The angle between the fibre axis and the surface normal is called ϕ . Because of symmetry reasons, the fibre axis cannot lie in the plane formed by the waveguide axis and the surface normal any more. This is illustrated in figure 7.2. Compared to vertical coupling, the situation has become more complicated. The angle $\phi \neq 0^\circ$ has an effect on the insertion loss and the PDL.

The coupling efficiency is reduced because the tilted fibre couples less power to the fundamental waveguide mode and increases the coupling to higher order waveguide modes. The reason is the phase mismatch due to the lateral tilt of the fibre. Only the fundamental waveguide mode survives the transition to a single-mode wire, the higher order modes are lost. We have estimated the effect of the angle θ using

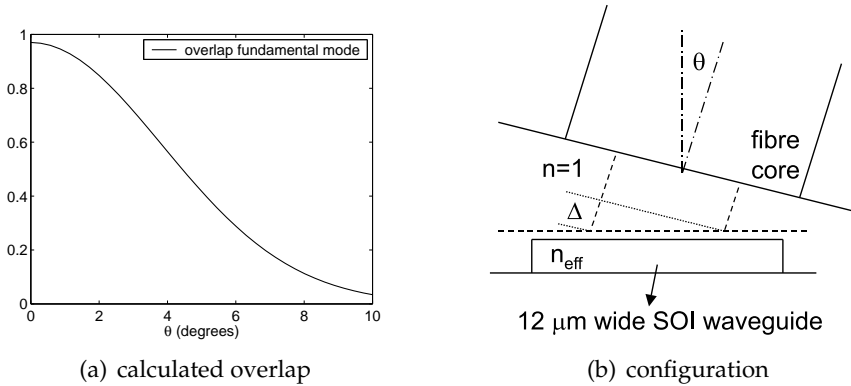


Figure 7.3: Overlap between the fibre mode and the fundamental waveguide mode as a function of incidence angle θ .

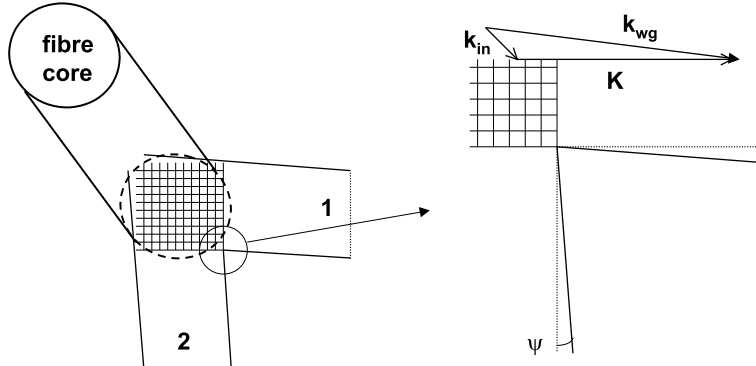


Figure 7.4: Rotated waveguides and definition of ψ . The k-vector diagram is also shown.

a 2-D model¹. The results are given in figure 7.3. If $\theta=0^\circ$, the calculated overlap between the fundamental waveguide mode (figure 3.16) and a Gaussian profile is 97%. For $\theta=7^\circ$, this overlap is only 20%. As a result the polarization diversity configuration has a very high insertion loss, which is unacceptable. This effect is important, even for small θ .

This problem may be solved by rotating the grating or the waveguides. The configuration with rotated waveguides is shown in figure 7.4. It should be noted that the symmetry of the structure is preserved. When $\psi \approx \theta/n_{eff}$, the phase mismatch due to the tilted fibre is com-

¹The angles θ and ϕ are different and are related by $\tan(\theta) = \tan(\phi)\cos(45^\circ)$. The case $\phi = 10^\circ$ corresponds to $\theta \approx 7^\circ$.

pensated by the rotation of the waveguide. This effect can also be explained with a wave-vector diagram. In figure 7.4, the projection of the k-vectors on the xz-plane is shown. The relation $\mathbf{k}_{wg} = \mathbf{k}_{in,xz} + \mathbf{K}$ results in the following equations:

$$\frac{2\pi}{\lambda} n_{\text{eff}} \sin(\psi) = \frac{2\pi}{\lambda} \sin(\phi) \cos(45^\circ) \quad (7.1)$$

$$\frac{2\pi}{\lambda} n_{\text{eff}} \cos(\psi) = \frac{2\pi}{\lambda} \sin(\phi) \cos(45^\circ) + \frac{2\pi}{\Lambda} \quad (7.2)$$

These equations can be simplified to :

$$\sin(\psi) = \frac{\sin(\phi)}{n_{\text{eff}}} \cos(45^\circ) \quad (7.3)$$

$$n_{\text{eff}} \cos(\psi) = \sin(\phi) \cos(45^\circ) + \frac{\lambda}{\Lambda} \quad (7.4)$$

For a given angle ϕ of the fibre, equation (7.3) can be used to calculate the corresponding rotation of the waveguide ψ . And for these values of ϕ and ψ , equation (7.4) gives the corresponding grating period Λ . The index n_{eff} is the effective index of the waveguide mode in the case of very weak grating. Although the explanation that we have given is qualitatively correct, an accurate calculation of these effects for stronger gratings may require full 3-D calculations.

We also know from figure 3.18(b) that the optimal position of the fibre in the case of a uniform grating coupler is not the centre of the grating. As a result the coupling efficiency of a uniform 2-D grating in the polarization splitter configuration will be lower than the efficiency of the same 2-D grating in single waveguide configuration. Also the optimal position for maximum coupling to waveguide 1 will be different from the optimal position for coupling to waveguide 2 in this case. To enhance the overall coupling efficiency of the splitter, a grating is needed for which the optimal fibre position is the centre of the grating. The optimal grating may be a 2-D version of the grating with varying filling factor that was described in section 4.6.

7.1.3 Polarization dependent loss

In the previous section, we have discussed the effect of near vertical coupling on the insertion loss. One of the conclusions is that the gratings or the waveguides must also be rotated. In this section, we will

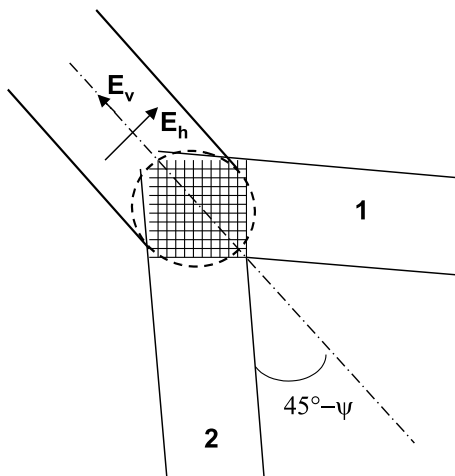


Figure 7.5: The symmetric problem. E_h and E_v represent two orthogonal linear polarization states in the fibre.

investigate the PDL in the case of near vertical coupling with rotated waveguides.

A general elliptical polarization state in the fibre can be written as a linear combination of two orthogonal polarization states. The polarization state is represented by its Jones vector

$$\mathbf{E}_{\text{fibre}} = \begin{bmatrix} h \\ v \end{bmatrix} \quad (7.5)$$

in which h and v are complex numbers. Normalization results in $|h|^2 + |v|^2 = 1$. We choose the two linear orthogonal polarization states E_h and E_v defined in figure 7.5 as basis for the Jones vector. E_h and E_v lie in a plane perpendicular to the fiber axis.

If the coupling from polarization state E_v to the fundamental TE mode of waveguide one is t_v , then the coupling from E_v to waveguide two is also t_v due to symmetry. And if the coupling from E_h to the fundamental TE mode of waveguide one is t_h , then the coupling to waveguide two is $-t_h$. These coupling coefficients are also complex numbers.

We can now express the coupling from the fibre to waveguide one and two as a function of the polarization state of the input. The coupling from fibre to waveguide one is $ht_h + vt_v$ and from fibre to waveguide two the coupling is $-ht_h + vt_v$. The coupling to the output fibre

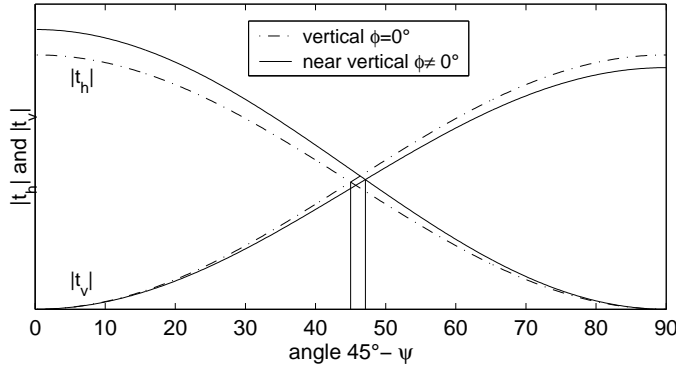


Figure 7.6: Qualitative effect of the waveguide rotation ψ . These curves are not calculation results, but it is expected that the curves for near vertical coupling differ only slightly from the curves for vertical coupling if ϕ is small.

can also be calculated because the coupling from waveguide to fibre is the same as from fibre to waveguide. This results in

$$h_{\text{out}} = (ht_h + vt_v)t_h + (-ht_h + vt_v)(-t_h) = 2ht_h^2 \quad (7.6)$$

$$v_{\text{out}} = (ht_h + vt_v)t_v + (-ht_h + vt_v)t_v = 2vt_v^2 \quad (7.7)$$

The power coupled to the output fibre is

$$P_{\text{out}} = |h_{\text{out}}|^2 + |v_{\text{out}}|^2 = 4|h|^2|t_h|^2 + 4|v|^2|t_v|^2 \quad (7.8)$$

If P_{out} is independent of h and v , the transmission is independent of the polarization state of the input. This is the case if $|t_h| = |t_v|$. In this case $P_{\text{out}} = 4|t_h|^2$.

In the case of vertical coupling, $|t_h| = |t_v|$ if $\psi=0^\circ$. This corresponds to the simple case of vertical coupling and a right angle between the two waveguides. But in the case of non vertical coupling, there may also be a situation where $|t_h| = |t_v|$. But the corresponding angle ψ will differ from 0° . This is illustrated in figure 7.6.

In this section, we have considered a perfectly symmetric structure. In a real structure, there is always a small asymmetry and there will always be some PDL. In addition, the phase difference between the light in the two waveguides at the output coupler will play a role if the two waveguides are not orthogonal anymore. Therefore it is important to keep the angles ϕ and ψ as small as possible.

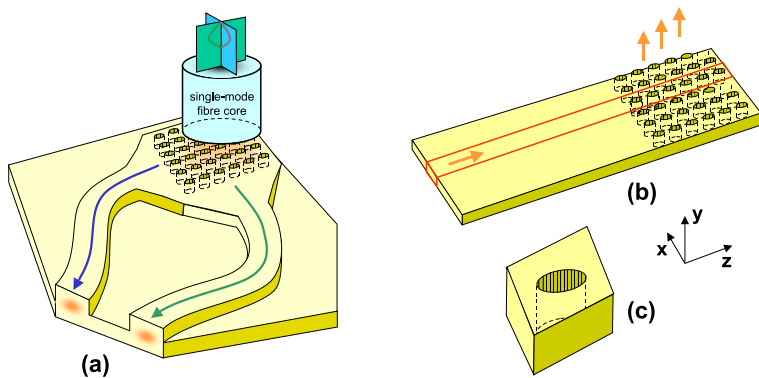


Figure 7.7: The 2-D grating coupler problem is a full 3-D problem (a). Some useful information may be obtained by simulating the problem as a 1-D periodic structure (b) or a 2-D periodic structure (c).

7.2 Grating design

7.2.1 Numerical methods

The 2-D coupler problem is a fully vectorial 3-D problem. Simulating the entire structure rigorously is almost impossible. In theory, very general methods such as FDTD or eigenmode expansion can be used. But simulating the entire structure (i.e. half the structure and using symmetry) with 3-D FDTD and a 10 nm grid requires 16 GBytes of memory and a month of computation time on a single-processor machine². However on a high-end supercomputer or large computer cluster, it would be reasonable to use parallelized 3-D FDTD. Also the eigenmode expansion method has difficulties with this structure. The main problem is finding all the modes of the 2-D cross-sections. A very large number of modes would be needed.

The general 3-D problem can be approximated by a simpler purely periodic problem. If periodicity in the lateral direction is introduced, the grating may still be non-periodic in the propagation direction (figure 7.7(b)). If the periodicity in two directions is used, the unit cell consists of only one grating period (figure 7.7(c)). These reduced problems may provide some useful information for the design of the coupler.

A perturbation analysis in which the grating is replaced by dipole sources may yield some qualitative results. But we know from chap-

²The cited values are an extrapolation based on experimental results with a smaller structure.

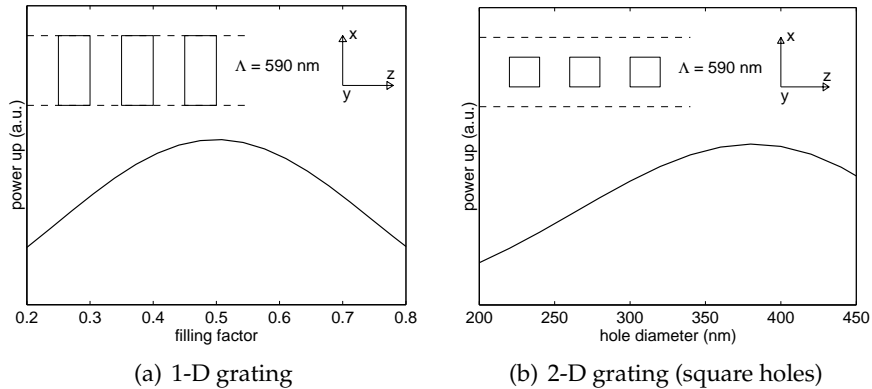


Figure 7.8: Results from a perturbation calculation. For a 1-D grating the optimal filling factor is 50%. The optimal hole diameter is 380 nm for a 2-D grating ($\Lambda=590$ nm).

ter 3 that the results are not accurate for gratings with a large coupling strength.

Most numerical methods for 2-D gratings are limited to purely periodic structures. An overview is given in the last chapter of [42]. An analysis of 2-D resonant waveguide gratings is given in [88, 89]. Although the analysis in [88] is valid for any grating, it is difficult to extract the coupling strength α from the resonances in the case of a strong grating. A perturbative coupled mode theory for 2-D textured waveguides is presented in [90], but these results are also not accurate for strong gratings. Moreover the case of vertical coupling requires the simulation of a finite grating instead of an infinite structure.

7.2.2 Design

Because the calculation of 2-D grating couplers is more difficult, we only present a few simulation results here. Results based on a perturbation analysis are shown in figure 7.8. In this approach, the grating is replaced by dipole sources and we have used a Green's functions method to calculate the resulting output coupling for the fundamental TE waveguide mode. For a 1-D grating, it is found that the optimal filling factor of the grating is 50%. For a 2-D grating, the optimal hole diameter is 380 nm in the case of $\Lambda=590$ nm. The optimum hole diameter is larger than 50% of the grating period, but the hole area is smaller than 50% of the area of the unit cell. This perturbation analysis gives us

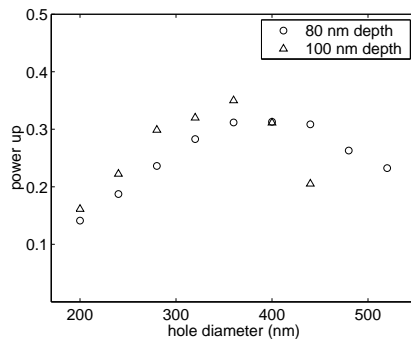


Figure 7.9: Simulation results from a 3-D FDTD calculation with 20 nm grid size. The upward radiated power is shown as a function of the hole diameter. A square lattice ($\Lambda=620$ nm) with round holes and SOI without substrate are used.

the optimal hole diameter for very shallow gratings, but does not tell anything about the efficiency of deeper gratings.

Therefore we have also tried to simulate some structures with 3-D FDTD. A 20 nm grid and SOI without substrate is used to keep the size of the computational domain as small as possible. Only one unit cell is used in the lateral direction (figure 7.7b). Absorbing boundary conditions are used at only 4 boundaries. At the left and right boundary, the tangential E-field is kept zero to simulate an infinite structure in the lateral direction. The upward radiated power is calculated as a function of the hole diameter. The results for an etch depth of 80 nm and 100 nm are shown in figure 7.9. The optimal hole diameter is 360-400 nm. The coupling strength $2\alpha=0.16 \mu\text{m}^{-1}$ for 80 nm depth and 400 nm hole diameter. For 100 nm depth and 360 nm hole diameter, the upward radiated power is 35% and the coupling strength $2\alpha=0.19 \mu\text{m}^{-1}$. This is still lower than the theoretical optimal coupling strength $2\alpha=0.26 \mu\text{m}^{-1}$ for coupling to fibre. However with a Silicon substrate and an optimized buried oxide thickness, α will be slightly higher for the same etch depth and the values of the radiated power will be approximately $1.5\times$ higher. These predictions are based on the results obtained for 1-D gratings in chapter 4.

Complete 3-D simulations of a 2-D coupler with a non-uniform grating are not feasible at the moment. However these simulations may be needed for an accurate calculation of the coupling to fibre. We do not know yet if a 2-D grating can achieve the same coupling efficiency to fibre as a 1-D grating.

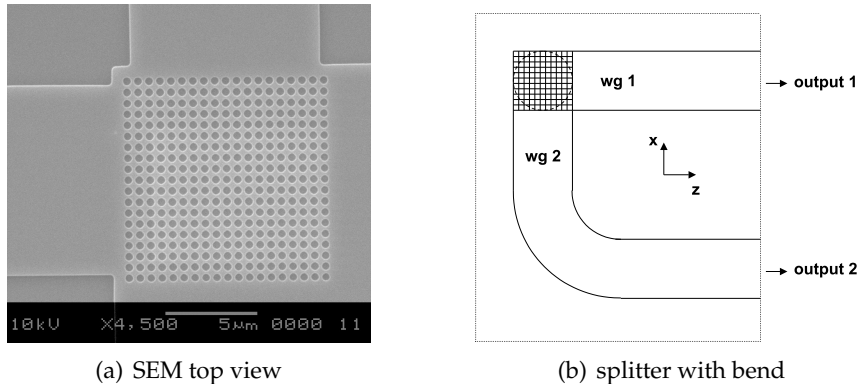


Figure 7.10: Polarization splitter test structures.

7.3 Experimental results

The results presented in the next paragraphs use structures with a 90° angle between the two waveguides. We do not have fabricated any structures with rotated waveguides yet.

7.3.1 Polarization splitter

The polarization splitter presented here was fabricated in Glasgow using electron-beam lithography. The grating is a square array of holes, the lattice period is 580 nm and the etch depth³ is approximately 90 nm. The hole diameter is 300 nm. A SEM top view of the grating is shown in figure 7.10(a). The width of the ridge waveguides is 10 μm . A 90° bend is inserted in one of the waveguides to be able to detect both outputs at one cleaved facet. The length of waveguide 1 is 850 μm .

We have used the structure from figure 7.10(b) to measure the extinction ratio and check the polarization of the light in the waveguides. A vertical single-mode fibre is used to couple light from the tunable laser into the waveguides via the grating. We detect the output power of waveguides 1 and 2 at the cleaved facet using a 40× objective and a power detector.

The alignment of the fibre is important, because the whole setup must be symmetric for optimal performance. To be sure that the centre

³The cited value is the measured depth of 5 μm wide trenches on the sample. The holes are etched slightly less deep.

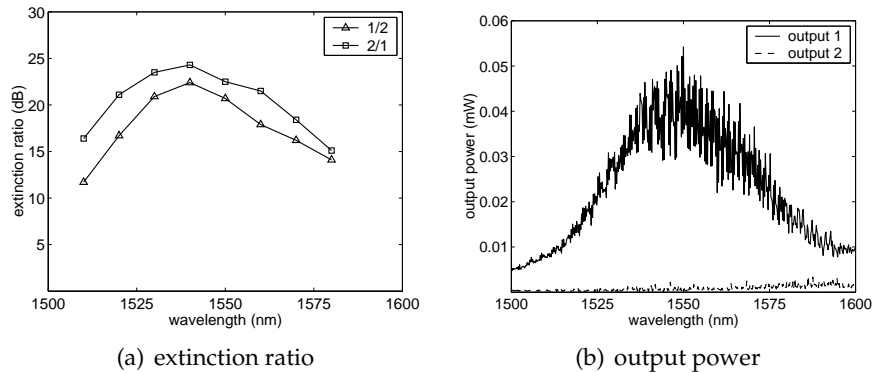


Figure 7.11: Measurement results of a polarization splitter.

of the fibre is aligned with the centre of the grating, the x position is optimized using output 1 and the z position using output 2.

After the initial alignment, the position of the fibre is fixed and only the polarization and the wavelength are changed during the measurements. The polarization of the input light is changed to maximize either output 1 or output 2. Then the extinction ratio between the two outputs is measured for both cases. The extinction ratio is shown in figure 7.11(a) for different wavelengths. The extinction ratio is better than 18 dB in the wavelength range 1530-1560 nm. The difference between the two curves is caused by radiation losses in the 90° bend in waveguide 2.

The output power versus wavelength for the case when output 1 is maximized is shown in figure 7.11(b). The polarization of the input was changed to maximize output 1 at $\lambda=1550$ nm before this measurement was done. The fringes in these curves are caused by a cavity between the grating (second order reflection) and the facet. The fringe spacing is approximately 0.5 nm, this is consistent with the waveguide length and effective index of the fundamental guided mode. The transmitted power is approximately 5%. One reason for this low value is the bad quality of the facet. As discussed before, it is difficult to cleave a good facet in Silicon. If the facet would have been perfect, the transmitted power would have been higher and the Fabry-Pérot fringes stronger.

The extinction ratio we have measured might be limited by our measurement setup, because the extinction ratio of the input light, measured with a rotatable polarizer, is only 25 dB. Also connecting the wide waveguides to single-mode wires will increase the extinction ratio, be-

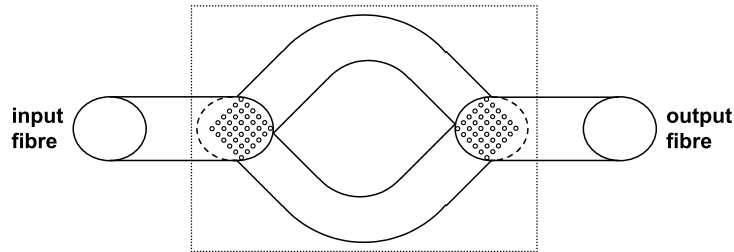


Figure 7.12: Polarization diversity configuration. Top view of the setup for measuring the transmission as a function of the polarization of the input. The angle $\phi=10^\circ$ but cannot be seen on this top view.

cause the small amount of TM light in the waveguide will be filtered out.

We have published these results also in [35]. This was the first demonstration of a very compact polarization splitter, based on a 2-D waveguide grating.

7.3.2 Polarization diversity configuration

We have also measured some structures in a polarization diversity configuration (figure 7.1c). A 2-D coupler is used as input and output coupler and the transmission is measured. The polarization of the input light is also changed during the measurement. In a perfect structure the transmission should be independent of the polarization. In a real structure there will be a small variation in the transmitted power. In this way, we can measure the polarization dependent loss or PDL.

The grating used is a square array of holes, the lattice period is 580 nm and the etch depth is approximately 50 nm. The hole diameter is 380 nm, this is the optimal hole diameter for the cited etch depth. These structures have been fabricated in IMEC Leuven using DUV lithography. When using exactly vertical coupling, the ripple on the transmission is very high. The reason is that there is a cavity between the two gratings that is caused by the second order reflection of the gratings. In fact there are two cavities of slightly different length. This can cause strong variations in the output power when the polarization changes. Therefore we have also performed these measurements for near vertical coupling.

The measurement setup of the polarization diversity configuration is shown in figure 7.12. As a comparison we have also measured the



Figure 7.13: Single waveguide configuration. Top view of the setup for measuring the transmission as a function of the polarization of the input. The angle $\theta=10^\circ$ but cannot be seen on this top view.

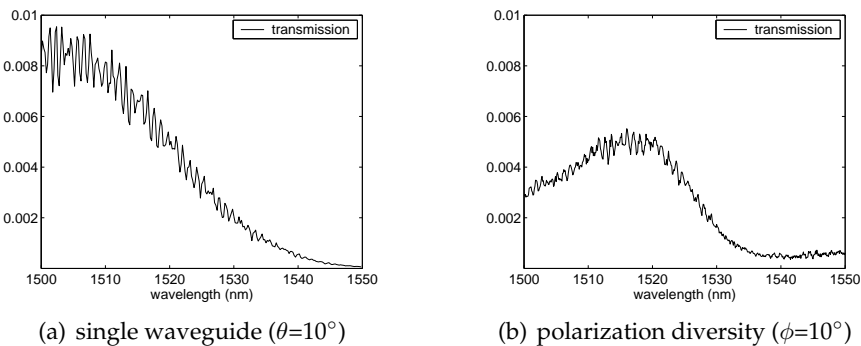


Figure 7.14: Transmission as a function of wavelength for the couplers shown in figure 7.12 and figure 7.13

transmission on a single waveguide with the same 2-D grating coupler at both ends (figure 7.13). The transmission as a function of wavelength for both configurations is shown in figure 7.14. The transmission in the polarization diversity configuration is approximately 50% of the transmission in the single waveguide configuration. The reasons for this lower transmission were discussed in section 7.1.2; the lateral tilt of the fibre and the fact that the alignment cannot be optimal for both waveguides together, because a uniform grating is used. However the transmission is much higher than predicted by figure 7.3(a). The reason is that wide waveguides are used that are not tapered to single-mode wires. The lateral tilt of the fibre causes less coupling to the fundamental mode, but more coupling to higher order waveguide modes. These higher order modes are also transmitted because we have used wide waveguides.

By changing the polarization of the input, we have measured the transmission as a function of polarization for both structures. The results are shown in figure 7.15. In the single waveguide configuration, the transmission drops to almost zero and the PDL is very high, as ex-

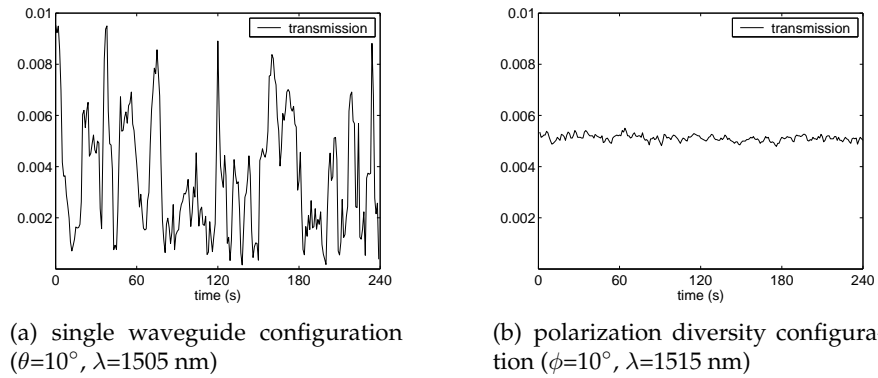


Figure 7.15: Measured transmission as a function of polarization. The polarization of the input light is randomly changed. The couplers are the same as in figure 7.14

pected. In the polarization diversity configuration, the ripple on the transmission is quite small, the PDL is approximately 0.6 dB. To achieve a low PDL, it is important that the symmetry of the structure is preserved. To align the fibre, we used input light that was linearly polarized in the x-direction. As a results, the coupling to both waveguides is equal and optimization of the fibre position puts the fibre in the right position.

7.3.3 Coupling efficiency

In the previous section, we have presented experimental results on two-dimensional grating couplers in a polarization diversity configuration. However, the insertion loss was rather high, because the coupling efficiency of the grating coupler was rather low. We have measured higher efficiencies on 2-D grating couplers in a single waveguide configuration (figure 7.13) on another sample. The etch depth is approximately 60 nm and the grating period 630 nm, the width of the waveguide is 12 μm . The measured coupling efficiency is shown in figure 7.16.

The maximum efficiency that we have measured for a 2-D grating is 23% compared to 33% for a 1-D grating. Part of this difference is caused by the fact that a 2-D grating has a lower coupling strength than a 1-D grating with the same depth. Further research is needed to find out the maximum efficiency that can be achieved with a 2-D grating.

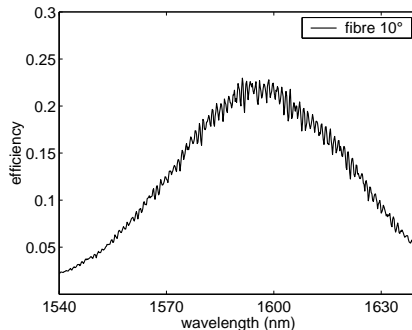


Figure 7.16: Measured coupling efficiency of 2-D grating coupler in a single waveguide configuration. The grating period $\Lambda=630$ nm, the hole diameter=350 nm and the etch depth=60 nm.

7.4 Future perspectives

We have demonstrated the principle of the polarization splitter and the polarization diversity configuration based on 2-D grating couplers. But there is still room for improvement of the coupling efficiency. The insertion loss of the fabricated structures is too high for practical applications. We propose two structures that may combine a low insertion loss and a low PDL. The concepts of the two most promising structures are shown in figure 7.17.

The coupler of figure 7.17(a) is suitable for vertical coupling. It is the 2-D version of the coupler with a rear reflector grating that was presented in section 4.3. The coupling efficiency of the 1-D version is 74% when a top mirror is used. The disadvantage of this approach is the smaller bandwidth. Another option to achieve vertical coupling with low grating reflection is a blazed grating with parallelogram teeth, but that structure is very difficult to fabricate.

A coupler concept for near vertical coupling is shown in figure 7.17(b). The grating is a 2-D version of the grating with a varying filling factor presented in section 4.6. The coupling efficiency of the 1-D version is 63% or 95% when a bottom DBR is used. However the 2-D structure is much more complicated and the maximum achievable efficiency may be lower. Because near vertical coupling is used, the waveguides or the grating must be rotated.

We have given only a qualitative description of the proposed couplers. Quantitative results will require extensive numerical simulations.

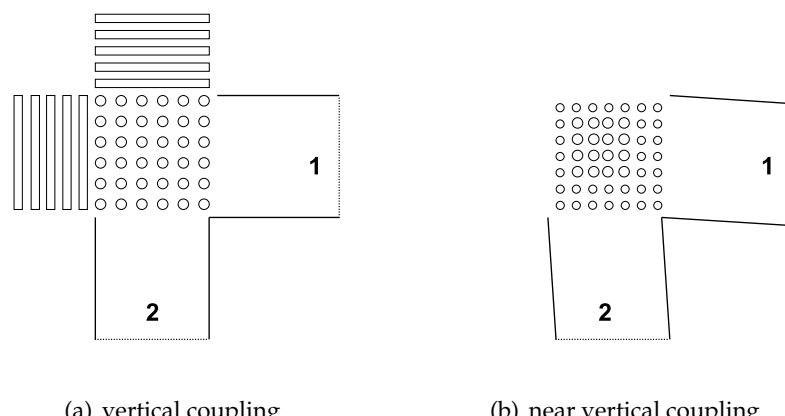


Figure 7.17: Two coupler concepts that look the most promising for future work. A top view of the structures is shown.

Chapter 8

Conclusions and perspectives

In this final chapter, we summarize the main conclusions of our work. We also discuss some options for future research work that builds on the results that we have presented.

8.1 Conclusions

The key aspect of this work is the coupling between optical fibres and nanophotonic integrated circuits. In chapter 2, an overview of the state-of-the-art was presented. The concept of a short grating that can be used to butt-couple to fibre was introduced and compared with existing larger grating couplers. The short coupling length of our coupler results in a larger bandwidth and an easy coupling method. Possible applications are optical interconnects, communication links and sensors.

In chapter 4, we have extensively studied the properties of these grating couplers. We have presented some designs that combine a high efficiency and a relatively large bandwidth. The main limitation on the efficiency is the coupling to the substrate. The correct choice of the buried oxide thickness helps a lot, but to achieve a very low coupling loss (<1 dB), a bottom or top reflector is needed.

We have experimentally demonstrated efficient coupling between single-mode fibres and sub-micrometre SOI waveguides using compact grating couplers. The highest measured coupling efficiency was 33% for a uniform grating and the measured coupling characteristic was in

good agreement with the simulation results. This efficiency can be improved by using an optimized SOI layer structure and grating design. However, these optimized structures are challenging to fabricate, because a very accurate control of the etch depth is required. In addition, the variations on the Silicon top layer thickness across a wafer reduce the acceptable errors on the etch depth. It may be needed to measure the exact thickness of the Silicon layer and adapt the grating parameters according to this thickness.

To solve the polarization problem of SOI nanophotonic ICs, we have investigated an integrated polarization diversity scheme based on 2-D grating couplers. The principle of a 2-D grating coupler alias polarization splitter was experimentally demonstrated. Also polarization independent transmission using a very simple integrated polarization diversity circuit was demonstrated. However the performance of these structures, in particular the insertion loss, is not good enough for practical applications. Possible improvements were also presented, but an optimization of the design and an experimental demonstration thereof require more research.

8.2 Perspectives

There are several topics that could be the subject for further work. The most obvious one is the fabrication and experimental demonstration of the non-uniform coupler design with the highest efficiency. But this structure is very challenging to fabricate. It requires a very accurate control of the linewidth and the etch depth and the smallest grooves are only a few tens of nanometres wide. However, if a technique is available that can etch grooves with different depths, these very narrow grooves can be replaced by wider shallower grooves. Focused ion beam etching may be very well suited to fabricate this coupler.

To further improve the efficiency, SOI wafers with a bottom DBR are needed. The top mirror as an alternative for the bottom DBR works only well for shallow gratings. With this in mind, it is interesting to investigate metal strip gratings instead of etched gratings. To achieve the same coupling strength, the thickness of a metal layer is lower than the depth of an etched grating. Another option may be to use a slightly weaker grating and sacrifice some bandwidth in favour of a higher coupling efficiency.

A very challenging task is the further development and optimization of the 2-D grating coupler for use in a in polarization diversity

configuration. Both the theoretical optimization and the practical realization will require state-of-the-art technology. The ultimate goal is to demonstrate a compact SOI photonic integrated circuit, with low insertion loss and low PDL, that uses these couplers.

Finally, the grating couplers presented in this work can be combined with shorter lateral spot-size converters [28] instead of linear tapers. This will further reduce the size of the interface between the fibres and the photonic IC.

Appendix A

CAMFR simulation example

In this appendix, an example python script is presented that can be used to calculate the efficiency of a grating coupler with CAMFR. For more information on CAMFR, we refer to the user's manual [60]. Most parts of the script are self-explanatory and additional information is provided in the form of comments.

```
1 #####  
2 # Example python script for calculating the fibre coupling      #  
3 # efficiency of a SOI waveguide grating coupler                 #  
4 #####  
  
6 # we use CAMFR  
7 from camfr import *  
8 from Numeric import *  
  
10 # define parameters (see CAMFR manual)  
11 set_lambda(1.55) # wavelength  
12 set_N(130)       # number of modes  
13 set_polarisation(TE)  
14 set_chunk_tracing(0)  
15 set_degenerate(0)  
16 set_orthogonal(False)  
  
18 # define materials  
19 substrate=Material(1.444)  
20 guiding=Material(3.476)  
21 nfib=1.46  
22 iml=Material(nfib)  
  
25 # create output file  
26 outfile = open("testje.txt",'w')
```

```

28 # define our own parameters
29 ff = 0.5
30 d = 7.0
31 pml=0.4
32 set_lower_PML(-pml)
33 set_upper_PML(-pml)
34 guide_thickness = 0.220
35 dclad = 1.0
36 period=0.630
37 groove_depth=0.070

39 # sweep the wavelength
40 for P in arange(1500,1651,2):
41     set_lambda(P/1000.0)
42     # define slabs
43     waveguide = Slab(guiding(d-dclad)+ substrate(dclad) +
44                         guiding(guide_thickness) + iml(d))
45     etched = Slab(guiding(d-dclad) + substrate(dclad) +
46                     guiding(guide_thickness-groove_depth) +
47                         iml(groove_depth + d))

49     # define stack
50     stack = Stack(waveguide(1.0) + 20*(etched(period*(1.0-ff)) +
51                                         + waveguide(period*ff)) + waveguide(2.0))

53     # find the guided mode
54     waveguide.calc()
55     guided=0
56     niguided=1
57     for t in range(0,60):
58         if abs(waveguide.mode(t).n_eff().imag) < niguided :
59             guided=t
60             niguided=abs(waveguide.mode(t).n_eff().imag)

62     # set input for calculating the fields
63     inc = zeros(N())
64     inc[guided] = 1
65     stack.set_inc_field(inc)

67     stack.calc()

69     R = abs(stack.R12(guided,guided))
70     T = abs(stack.T12(guided,guided))
71     up=stack.lateral_S_flux(d+1.5)
72     down=stack.lateral_S_flux(d-1.5)
73     x=d+1.5

75     # calculate the coupling efficiency to fibre
76     powerup = 0.0 + 0.0*1j

```

```

77     overlapint = zeros(100,Complex)      # 0 degrees
78     soverlapint = zeros(100,Complex)    # 8 degrees
79     align=zeros(100) # to find optimal fibre position
80     pfib=0.0
81     # normalization gaussian profile
82     Zzero=377
83     nZ=nfib/Zzero
84     for z in arange(-10.0,10.0,0.01):
85         pfib+=0.01*exp(-((z/5.2)**2))*nZ*exp(-((z/5.2)**2))

87     # calculate different fibre position simultaneously
88     for counter in range(100):
89         align[counter]=-1.0-period*(counter/5.0)
90     for z in arange(0.01, 23 * period , 0.01):
91         powerup+= 0.01*stack.field(Coord(x,0,z)).E2()*
92             conjugate(stack.field(Coord(x,0,z)).Hz())
93         overlapint+= 0.01*(stack.field(Coord(x,0,z)).E2())*
94             nZ*exp(-(((align+z)/5.2)**2))
95         soverlapint+= 0.01*(stack.field(Coord(x,0,z)).E2())*
96             nZ*exp(-(((align+z)/5.2)**2))*exp(0.85*1j*z)

98     coupling=((abs(overlapint))**2)/(pfib*powerup.real)
99     scoupling=((abs(soverlapint))**2)/(pfib*powerup.real)

101    print >> outfile, P,groove_depth,R*R,T*T,powerup.real,
102                    powerup.real*max(scoupling),
103                    argmax(scoupling),
104                    powerup.real*scoupling[33]
105    outfile.flush()
106    print P
107    free_tmpls()
108 outfile.close()

```


Appendix B

Fabricated structures

In this appendix, we give an overview of the grating coupler samples that have been fabricated during this work. Our best experimental results are presented in chapter 6. In this appendix we list most of the samples that have been fabricated and characterized. In addition, a number of samples did not yield any experimental results because the fabrication failed.

We start with couplers in the GaAs/AlOx material. In the beginning that material was used because of the available technology. Later on, this route was abandoned.

GaAs/AlOx

Grating couplers with a rear reflector grating were fabricated using electron-beam lithography. The reflector had the same etch depth as the coupler and the target etch depth was 40 nm. The experimental results for vertical coupling are given in the following table :

sample ID		efficiency	see also
CMS0083	GaAs/AlOx	5.5%	fig. 6.6(a)
TFK1406	with bottom DBR	19%	fig. 6.6(b)

The actual etch depth of sample TFK1406 was 65 nm instead of 40 nm. As a result, the theoretical efficiency is only 35% instead of 70%. The measured efficiency was 19%. This difference may be caused by the fact that the exact refractive index and thickness of the buried AlOx layers were not well known.

Grating couplers with uniform gratings were fabricated using interference lithography, because this technique is available in INTEC. Several test runs were used to optimize the processing. It was very difficult to accurately control the etch depth of the gratings with the available RIE and ICP etching processes. The efficiency of the first samples was low because the grating was slightly rotated with regard to the waveguides. Finally, an efficiency of 10% was achieved.

The GaAs/AlOx route was abandoned later on due to technical problems with equipment and because SOI processing technology became available.

SOI

The first SOI structures were fabricated on standard SOI wafers from SOITEC. These standard wafers have a 200 nm top Silicon layer and a 400 nm buried oxide layer. A large leakage loss to the substrate occurs in this structure because the buried oxide layer is too thin. These wafers were used for the first experimental SOI work until other wafers became available. We have later obtained custom SOI wafers with 220 nm Silicon and 1 μ m buried oxide. This is the layer structure that has been used for all the SOI nanophotonic work in the photonics research group in INTEC in the last two years.

When the DUV work started, a target etch depth of 50 nm was chosen. The measured etch depth on the processed wafers is 45-50 nm. The process is reproducible, but to achieve the optimal etch depth, additional process development is required. A relatively large delay occurred between the mask design and the fabrication of the actual structures. Grating coupler test structures were included on the PICCO_01, PICCO_03 and PICCO_04 masks. The DUV lithography and subsequent reactive ion etching was performed in IMEC, Leuven.

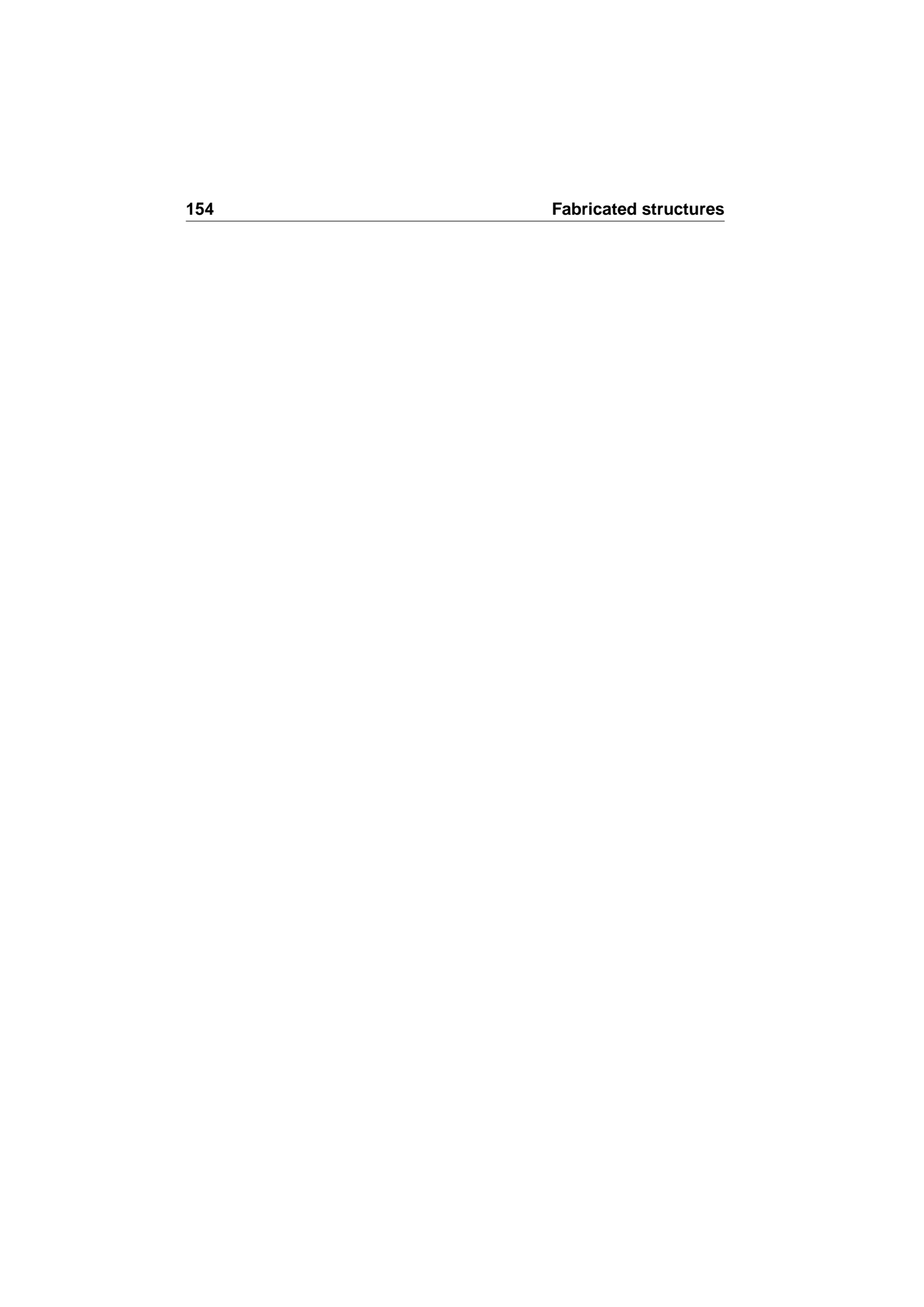
On the PICCO_03 and PICCO_04 mask, structures were included for a two-step processing. In this two-step processing, the gratings are etched 50 nm and the waveguides and other structures 220 nm. With this processing scheme, the grating couplers can be used for the characterization of other nanophotonic components.

Several samples have been fabricated using electron-beam lithography. This technique is more flexible and the delay time between design and fabrication is shorter. The electron-beam lithography was performed in the university of Glasgow. The reactive ion etching was performed in the university of Glasgow and the research centre COM of

the technical university of Denmark. An overview is given in the next table :

sample ID	etch profile	etch depth	efficiency
GUCOM1,2	too shallow	15 nm	3%
GUCOM3	almost ok	40 nm	13%
GU1,2		90 nm	20%
GU3,4	ok	55-60 nm	33%

The highest measured efficiency is 33%. This is close to the maximum efficiency that can be achieved with a uniform grating on the SOI wafers with a 1 μm buried oxide layer.



List of figures

1.1	Different types of optical waveguides.	3
1.2	Waveguide grating couplers for coupling to fibre.	5
2.1	SOI wafer (200 mm diameter)	10
2.2	Nanophotonic waveguides and components.	11
2.3	The coupling problem.	12
2.4	Tapered spot-size converters.	14
2.5	Grating-assisted directional couplers.	16
2.6	Waveguide grating couplers.	17
2.7	Polarization diversity configuration.	20
2.8	2-D grating coupler splitter.	21
2.9	Polarization diversity using 2-D grating couplers.	22
3.1	The Bragg condition.	25
3.2	Wave-vector diagram for a waveguide grating coupler. .	26
3.3	The 1-D grating coupler problem.	27
3.4	Symmetry arguments.	29
3.5	Periodic structures.	31
3.6	Bloch calculation results.	33
3.7	Reflection of a plane wave incident from the top.	36
3.8	Coupled-mode theory.	37
3.9	Eigenmode expansion method.	38
3.10	Convergence of eigenmode expansion with PML.	40
3.11	FDTD method	41
3.12	Comparison of different methods.	43
3.13	Grating coupler structures from literature.	44
3.14	Comparison between simulation results and literature. .	44
3.15	Diffraction of a Gaussian beam with waist radius 5 μm . .	46
3.16	Fundamental TE mode of a 12 μm wide SOI waveguide. .	48
3.17	Effect of fibre position on coupling efficiency.	49

3.18 Overlap between Gaussian and exponential profile.	50
3.19 Overlap between Gaussian and rectangular profile.	50
4.1 1-D grating coupler	54
4.2 Grating reflection versus etch depth.	56
4.3 Grating reflection versus filling factor.	57
4.4 Coupling efficiency for vertical coupling.	57
4.5 Detuned grating and near vertical coupling.	58
4.6 Positive and negative detuning.	58
4.7 Coupling efficiency.	59
4.8 Coupling efficiency.	60
4.9 Efficiency versus oxide buffer thickness.	61
4.10 Sensitivity to fabrication errors.	62
4.11 Coupling efficiency for TM-polarization.	64
4.12 Coupling between Silicon and polymer waveguide.	65
4.13 Coupler grating etched completely through Si core.	66
4.14 Different index contrast waveguides.	67
4.15 Couplers based on Si_3N_4 and GaAs waveguides.	68
4.16 Grating coupler with reflector grating.	70
4.17 Reflection of a first order reflector grating.	71
4.18 Reflection of a second order reflector grating	72
4.19 Design of coupler with deep reflector.	73
4.20 Efficiency of coupler with deep reflector.	74
4.21 Design of coupler with shallow reflector.	75
4.22 Efficiency of coupler with shallow reflector.	75
4.23 Coupler with bottom mirror.	76
4.24 Efficiency of coupler with rear and bottom reflector.	77
4.25 Coupler with rear and bottom reflector.	77
4.26 Vertical cavities.	78
4.27 Calculated P_u/P_d for the structure of figure 4.26(b).	80
4.28 Efficiency of uniform grating with top mirror.	81
4.29 Coupling efficiency of coupler with rear and top reflector.	82
4.30 Field plot of coupler with rear and top reflector.	82
4.31 Gaussian profile and the corresponding $\alpha(z)$	84
4.32 Evolution of the efficiency using a genetic algorithm.	85
4.33 Coupling efficiency versus wavelength.	85
4.34 Structure with bottom DBR and field plot.	86
4.35 Coupling efficiency versus etch depth.	87
4.36 Sensitivity to errors on groove widths.	87
4.37 Examples of blazed gratings.	88

4.38 Efficiency of blazed grating coupler.	89
5.1 SmartCut™ process for fabricating SOI wafers.	94
5.2 Wet thermal oxidation of AlGaAs.	95
5.3 General processing scheme.	96
5.4 Different lithography processes.	97
5.5 Structure defined by electron-beam lithography.	98
5.6 Interference lithography processing.	99
5.7 Structures fabricated using interference lithography.	99
5.8 Dry etching.	100
5.9 Schematic view of a scanning electron microscope.	102
5.10 Examples of SEM pictures.	103
5.11 AFM measurement of shallow grating.	103
5.12 Structures fabricated with DUV using two etch steps.	104
5.13 Oxide deposited on top of a deeply etched grating.	104
5.14 Fibre array.	105
6.1 Measurement setup with two fibres.	109
6.2 Summary of the alignment procedure.	110
6.3 Comparison of vertical and almost vertical coupling.	110
6.4 Measurement setup with one fibre and a lens.	112
6.5 Transmission as a function of grating reflectivity.	113
6.6 Transmitted power.	114
6.7 Coupling efficiency measurement results.	115
6.8 Coupling efficiency measurement results.	116
6.9 Experimental alignment tolerances.	118
6.10 With index-matching layer.	119
6.11 Uniformity measurements	120
6.12 Characterization of other components.	121
6.13 Reflection at the fibre facet and the sample.	123
6.14 Examples of reflection measurements.	123
7.1 2-D grating couplers.	126
7.2 Near vertical coupling.	127
7.3 Overlap with fundamental mode.	128
7.4 Rotated waveguides.	128
7.5 Symmetric problem.	130
7.6 Qualitative effect of waveguide rotation ϕ	131
7.7 The full 3-D problem.	132
7.8 Perturbation calculation.	133
7.9 3-D FDTD simulation result.	134

7.10	Polarization splitter	135
7.11	Measured extinction ratio.	136
7.12	Transmission measurement setup.	137
7.13	Transmission measurement setup.	138
7.14	Measured transmission as a function of wavelength.	138
7.15	PDL measurement.	139
7.16	Coupling efficiency of 2-D grating.	140
7.17	Future perspectives.	141

Bibliography

- [1] T. Shibata, M. Okuno, T. Goh, T. Watanabe, M. Yasu, M. Itoh, M. Ishii, Y. Hibino, A. Sugita, and A. Himeno, "Silica-based waveguide-type 16x16 optical switch module incorporating driving circuits," *IEEE Photon. Technol. Lett.*, vol. 15, pp. 1300–1302, September 2003.
- [2] M. Heiblum and J. Harris, "Analysis of curved optical waveguides by conformal transformation," *IEEE J. Quantum Electron.*, vol. 11, pp. 75–83, February 1975.
- [3] B. Offrein, D. Wiesmann, G. Salis, M. Sousa, I. Meijer, F. Horst, R. Germann, T. Brunschwiler, D. Webb, and G. Bona, "Advances in silicon oxynitride waveguides," in *Proceedings Integrated Photonics Research (IPR)*, Washington, USA, pp. 20–22, OSA, June 2003.
- [4] H. Haus, L. Kimerling, and M. Romagnoli, "Application of high index contrast technology to integrated optical devices," in *Proceedings European conference on optical communication (ECOC)*, Rimini, Italy, p. We 1.2.1, September 2003.
- [5] J. Den Besten, M. Dessens, C. Herben, X. Leijtens, F. Groen, M. Leys, and M. Smit, "Low-loss, compact, and polarization independent PHASAR demultiplexer fabricated by using a double-etch process," *IEEE Photon. Technol. Lett.*, vol. 14, pp. 62–64, January 2002.
- [6] T. Trupke, J. Zhao, A. Wang, R. Corkish, and M. Green, "Very efficient light emission from bulk crystalline silicon," *Appl. Phys. Lett.*, vol. 82, pp. 2996–2998, May 2003.
- [7] R. Emmons and D. Hall, "Buried-oxide silicon-on-insulator structures II: Waveguide grating couplers," *IEEE J. Quantum Electron.*, vol. 28, pp. 164–175, January 1992.

- [8] S. Pogossian, L. Vescan, and A. Vonsovici, "The single-mode condition for semiconductor rib waveguides with large cross section," *IEEE J. Lightwave Technol.*, vol. 16, pp. 1851–1853, October 1998.
- [9] J. Schmidtchen, A. Splett, B. Schuppert, K. Petermann, and G. Burbach, "Low loss single-mode optical waveguides with large cross-section in silicon-on-insulator," *Electron. Lett.*, vol. 27, pp. 1486–1488, August 1991.
- [10] W. Bogaerts, *Nanophotonic waveguides and photonic crystals in silicon-on-insulator*. Ghent University, Phd. thesis, 2004. <http://photonics.intec.ugent.be/publications/phd.asp?ID=135>.
- [11] P. Dumon, W. Bogaerts, V. Wiaux, J. Wouters, S. Beckx, J. Van Campenhout, D. Taillaert, B. Luyssaert, D. Van Thourhout, and R. Baets, "Low-loss SOI photonic wires and ring resonators fabricated with deep UV lithography," *IEEE Photon. Technol. Lett.*, vol. 16, pp. 1328–1330, May 2004.
- [12] M. Notomi, A. Shinya, K. Yamada, J. Takahashi, C. Takahashi, and I. Yokohama, "Structural tuning of guided modes of line-defect waveguides of silicon-on-insulator photonic crystal slabs," *IEEE J. Quantum Electron.*, vol. 38, pp. 736–742, July 2002.
- [13] K. De Mesel, *Spot-size converters for photonic integrated circuits*. Ghent University, Phd. thesis, 2002. <http://photonics.intec.ugent.be/publications/phd.asp?ID=120>.
- [14] M. Galarza, *Leaky-Waveguide-Based Integrated Spot-Size Converters for Alignment-Tolerant Optical Fiber Coupling*. Ghent University - Universidad Publica de Navarra, Phd. thesis, 2003. <http://photonics.intec.ugent.be/publications/phd.asp?ID=131>.
- [15] A. Sure, T. Dillon, J. Murakowski, C. Lin, D. Pustai, and D. Prather, "Fabrication and characterization of three-dimensional silicon tapers," *Opt. Express*, vol. 11, pp. 3555–3561, December 2003. <http://www.opticsexpress.org/abstract.cfm?URI=OPEX-11-26-3555>.
- [16] M. Frish, J. Fijol, E. Fike, A. Jacobson, P. Keating, W. Kessler, J. Leblanc, C. Bozler, M. Fritze, C. Keast, J. Knecht, R. Williamson,

- and C. Manolatou, "Coupling of single-mode fibers to planar Si waveguides using vertically tapered mode converters," in *Proceedings Integrated Photonics Research*, Vancouver, Canada, pp. IFB2–1, OSA, July 2002.
- [17] L. Vivien, S. Laval, E. Cassan, L. Roux, and D. Pascal, "2-D taper for low-loss coupling between polarization-insensitive microwaveguides and single-mode optical fibers," *IEEE J. Lightwave Technol.*, vol. 21, pp. 2429–2433, October 2003.
- [18] T. Shoji, T. Tsuchizawa, T. Wanatabe, K. Yamada, and H. Morita, "Low loss mode size converter from $0.3\mu\text{m}$ square Si wire waveguides to single-mode fibres," *Electron. Lett.*, vol. 38, pp. 1669–1670, December 2002.
- [19] S. McNab, N. Moll, and Y. Vlasov, "Ultra-low loss photonic integrated circuits with membrane-type photonic crystal waveguides," *Opt. Express*, vol. 11, pp. 2927–2938, November 2003. <http://www.opticsexpress.org/abstract.cfm?URI=OPEX-11-22-2927>.
- [20] V. Almeida, R. Panepucci, and M. Lipson, "Compact mode conversion for highly-confined waveguides," in *Proceedings Integrated Photonics Research (IPR)*, Washington, USA, pp. 230–233, OSA, June 2003.
- [21] G. Masanovic, V. Passaro, and G. Reed, "Dual grating-assisted directional coupling between fibers and thin semiconductor waveguides," *IEEE Photon. Technol. Lett.*, vol. 15, pp. 1395–1397, October 2003.
- [22] W. Kuang, C. Kim, A. Stapleton, and J. O'Brien, "Grating-assisted coupling of optical fibers and photonic crystal waveguides," *Opt. Lett.*, vol. 27, pp. 1604–1606, September 2002.
- [23] P. Barclay, K. Srinivasan, M. Borselli, and O. Painter, "Experimental demonstration of evanescent coupling from optical fibre tapers to photonic crystal waveguides," *Electron. Lett.*, vol. 39, pp. 842–844, May 2003.
- [24] T. Ang, G. Reed, A. Vonsovici, A. Evans, P. Routley, and M. Josey, "Effects of grating heights on highly efficient unibond SOI waveguide grating couplers," *IEEE Photon. Technol. Lett.*, vol. 12, pp. 59–61, January 2000.

- [25] R. Orobctchouk, A. Layadi, H. Gualous, D. Pascal, A. Koster, and S. Laval, "High efficiency light coupling in a submicrometric silicon-on-insulator waveguide," *Appl. Opt.*, vol. 39, pp. 5773–5777, 2000.
- [26] S. Lardenois, D. Pascal, L. Vivien, E. Cassan, S. Laval, R. Orobctchouk, M. Heitzmann, N. Bouzaida, and L. Mollard, "Low-loss submicrometre SOI rib waveguides and corner mirrors," *Opt. Lett.*, vol. 28, pp. 1150–1152, July 2003.
- [27] D. Pascal, S. Lardenois, E. Cassan, A. Koster, S. Laval, M. Heitzmann, L. Mollard, N. Bouzaida, B. Dal'Zotto, and R. Orobctchouk, "Efficient light coupling into sub-micrometer rib and strip SOI waveguides," in *Proceedings Integrated Photonics Research (IPR)*, Vancouver, Canada, pp. IThI7–1, July 2002.
- [28] B. Luyssaert, P. Vandersteegen, W. Bogaerts, V. Wiaux, J. Wouters, S. Beckx, and R. Baets, "Compact photonic spot-size converter," in *presented at the fifth Photonic and Electromagnetic Crystal Structures Conference (PECS-V)*, Kyoto, Japan, 7–11 March 2004.
- [29] E. G. Neumann, *Single-mode fibers - fundamentals*. Springer-Verlag, Berlin, 1988. ISBN 3-540-18745-6.
- [30] Oz-Optics, *Polarization maintaining fiber patchcords and connectors*. May 2003. <http://www.ozoptics.com>.
- [31] J. Van der Tol, J. Pedersen, E. Metaal, J. Van Gaalen, Y. Oei, and F. Groen, "A short polarization splitter without metal overlays on InGaAsP-InP," *IEEE Photon. Technol. Lett.*, vol. 9, pp. 209–211, February 1997.
- [32] E. Simova and I. Golub, "Polarization splitter/combiner in high index contrast Bragg reflector waveguides," *Opt. Express*, vol. 11, pp. 3425–3430, December 2003.
- [33] S. Kim, G. Nordin, and J. Jiang, "Ultracompact high-efficiency polarizing beam splitter with a hybrid photonic crystal and conventional waveguide structure," *Opt. Lett.*, vol. 28, pp. 2384–2386, December 2003.
- [34] M. R. Watts, G. Gorni., M. Cherchi, and H. A. Haus, "Polarization splitting and rotating through adiabatic transitions," in *Proceedings*

- Integrated Photonics Research (IPR)*, Washington, USA, pp. 26–28, June 2003.
- [35] D. Taillaert, H. Chong, P. Borel, L. Frandsen, R. De La Rue, and R. Baets, “A compact two-dimensional grating coupler used as a polarization splitter,” *IEEE Photon. Technol. Lett.*, vol. 15, pp. 1249–1251, September 2003.
 - [36] ISI Web of knowledge. <http://newisiknowledge.com>.
 - [37] K. Ogawa, W. Chang, B. Sopori, and F. Rosenbaum, “A theoretical analysis of etched grating couplers for integrated optics,” *IEEE J. Quantum Electron.*, vol. 9, pp. 29–43, January 1973.
 - [38] C. Ghizoni, B. Chen, and C. Tang, “Theory and experiments on grating couplers for thin -film waveguides,” *IEEE J. Quantum Electron.*, vol. 12, pp. 69–73, February 1976.
 - [39] K. Handa, S. Peng, and T. Tamir, “Improved perturbation analysis of dielectric gratings,” *Appl. Phys.*, vol. 5, pp. 325–328, 1975.
 - [40] V. Sychugov, A. Tishchenko, B. Usievich, and O. Parriaux, “Optimization and control of grating coupling to or from silicon based optical waveguide,” *Opt. Eng.*, vol. 35, pp. 3092–3100, November 1996.
 - [41] F. Bloch *Z. Physik*, vol. 52, pp. 555–560, 1928.
 - [42] R. Petit, *Electromagnetic theory of gratings*. Springer-Verlag, 1980. ISBN 3-540-10193-4.
 - [43] S. Peng, T. Tamir, and H. Bertoni, “Theory of periodic dielectric waveguides,” *IEEE Trans. Microwave Theory Tech.*, vol. 23, pp. 123–133, January 1975.
 - [44] D. Marcuse, “Thick dielectric grating on asymmetric slab waveguide,” *Bell System Tech. Journ.*, vol. 56, pp. 329–338, March 1977.
 - [45] D. Rosenblatt, A. Sharon, and A. Friesem, “Resonant grating waveguide structures,” *IEEE J. Quantum Electron.*, vol. 33, pp. 2038–2059, November 1997.
 - [46] M. Salik and P. Chavel, “Resonant excitation analysis of waveguide grating couplers,” *Opt. Commun.*, vol. 193, pp. 127–131, June 2001.

- [47] S. Norton, T. Erdogan, and G. Morris, "Coupled-mode theory of resonant grating filters," *J. Opt. Soc. Am. A*, vol. 14, pp. 629–639, March 1997.
- [48] D. Delbeke, *Design and fabrication of a highly efficient light-emitting diode : the grating-assisted resonant cavity light-emitting diode*. Ghent University, Phd. thesis, 2002. <http://photonics.intec.ugent.be/publications/phd.asp?ID=132>.
- [49] B. Dhoedt, *Theoretical and experimental study of free space optical interconnections based on diffractive lens arrays*. Ghent University, Phd. thesis, 1995.
- [50] D. Lee, *Electromagnetic principles of integrated optics*. John Wiley & Sons, New York, 1986. ISBN 0-471-87978-9.
- [51] W. Streifer, D. Scifres, and R. Burnham, "Coupled wave analysis of DFB and DBR lasers," *IEEE J. Quantum Electron.*, vol. 13, pp. 134–141, April 1977.
- [52] A. Hardy, D. Welch, and W. Streifer, "Analysis of second order gratings," *IEEE J. Quantum Electron.*, vol. 25, pp. 2096–2105, October 1989.
- [53] A. Yariv and A. Gover, "Equivalence of the coupled-mode and Floquet-Bloch formalisms in periodic optical waveguide," *Appl. Phys. Lett.*, vol. 26, pp. 537–539, May 1975.
- [54] M. Matsumoto, "Analysis of the blazing effect in second-order gratings," *IEEE J. Quantum Electron.*, vol. 28, pp. 2016–2023, October 1992.
- [55] H. Hoekstra, "Coupled mode theory for resonant excitation of waveguiding structures," *Opt. Quantum Electron.*, vol. 32, pp. 735–757, 2000.
- [56] P. Bienstman, *Rigorous and efficient modelling of wavelength scale photonic components*. Ghent University, Phd. thesis, 2001. <http://photonics.intec.ugent.be/publications/phd.asp?ID=104>.
- [57] J.-P. Berenger, "A perfectly matched layer for the absorption of electromagnetic waves," *Journ. Comput. Phys.*, vol. 114, pp. 185–200, January 1994.

- [58] P. Bienstman and R. Baets, "Advanced boundary conditions for eigenmode expansion models," *Opt. Quantum Electron.*, vol. 34, pp. 523–540, May 2002.
- [59] M. Hammer, "Quadrilateral eigenmode expansion scheme for 2-D modelling of wave propagation in integrated optics," *Opt. Commun.*, vol. 235, pp. 285–303, March 2004.
- [60] P. Bienstman, *CAMFR 1.2, CAvity Modelling FRamework*. June 2004.
<http://camfr.sourceforge.net>.
- [61] S. Van den Berghe, *Object-oriented electromagnetic simulations with the finite-difference time-domain method*. Ghent University, Phd. thesis, 2000.
- [62] Q. Cao, P. Lalanne, and J. Hugonin, "Stable and efficient Bloch-mode computational method for one-dimensional grating waveguides," *J. Opt. Soc. Am. A*, vol. 19, pp. 335–338, February 2002.
- [63] E. Silberstein, P. Lalanne, J. Hugonin, and Q. Cao, "Use of grating theories in integrated optics," *J. Opt. Soc. Am. A*, vol. 18, pp. 2865–2875, November 2001.
- [64] B. Saleh and M. Teich, *Fundamentals of Photonics*, vol. ISBN 0-471-83965-5. John Wiley & Sons, New York, 1991.
- [65] N. Landru, D. Pascal, and A. Koster, "Modelling of 2-D grating couplers on silicon-on-insulator waveguides using beam propagation method," *Opt. Commun.*, vol. 196, pp. 139–147, September 2001.
- [66] A. Tishchenko, M. Hamdoun, and O. Parriaux, "2-D coupled mode equation for grating waveguide excitation by a focused beam," *Opt. Quantum Electron.*, vol. 35, pp. 475–491, 2003.
- [67] R. Harrington, *Time-harmonic electromagnetic fields*. McGraw-Hill : New York, 1961.
- [68] F. Olyslager, *Electromagnetic waveguides and transmission lines*. Oxford univ. press, 1999.
- [69] D. Taillaert, W. Bogaerts, P. Bienstman, T. Krauss, P. Van Daele, I. Moerman, S. Verstuyft, K. De Mesel, and R. Baets, "An out-of-plane grating coupler for efficient butt-coupling between compact

- planar waveguides and single-mode fibers," *IEEE J. Quantum Electron.*, vol. 38, pp. 949–955, July 2002.
- [70] T. Suhara and H. Nishihara, "Integrated optics components and devices using periodic structures," *IEEE J. Quantum Electron.*, vol. 22, pp. 845–867, June 1986.
- [71] A. Narashima and E. Yablonovitch, "Efficient optical coupling into single-mode silicon-on-insulator thin films using a planar grating coupler embedded in a high index contrast dielectric stack," in *Proceedings Conference on Lasers and Electro-Optics (CLEO)*, Baltimore, USA, pp. CWA–46, OSA, June 2003.
- [72] R. Bockstaele, *Resonant cavity light emitting diode based parallel optical interconnections*. Ghent University, Phd. thesis, 2001.
<http://photonics.intec.ugent.be/publications/phd.asp?ID=106>.
- [73] K. A. Bates, L. Li, R. Roncone, and J. Burke, "Gaussian beams from variable groove depth grating couplers in planar waveguides," *Appl. Opt.*, vol. 20, pp. 2112–2116, 1993.
- [74] R. Waldhausl, B. Schnabel, P. Dannberg, E. Kley, A. Brauer, and W. Karthe, "Efficient coupling into polymer waveguides by gratings," *Appl. Opt.*, vol. 36, pp. 9383–9390, 1997.
- [75] J. Johnson and Y. Rahmat-Samii, *An introduction to genetic algorithms*, pp. 1–27. Electromagnetic optimization by genetic algorithms, Wiley, New York, 1999.
- [76] P. Dinesen and J. Hesthaven, "Fast and accurate modeling of waveguide grating couplers : 3-D vectorial case," *J. Opt. Soc. Am. A*, vol. 18, pp. 2876–2885, November 2001.
- [77] P. Lalanne, S. Astilean, P. Chavel, E. Cambril, and H. Launois, "Blazed binary subwavelength gratings with efficiencies larger than those of conventional echelle gratings," *Opt. Lett.*, vol. 23, pp. 1081–1083, July 1998.
- [78] M. Li and S. Sheard, "Experimental study of waveguide grating couplers with parallelogramic tooth profiles," *Opt. Eng.*, vol. 35, pp. 3101–3105, November 1996.

- [79] M. Hagberg, N. Eriksson, and A. Larsson, "High efficiency surface emitting lasers using blazed grating outcouplers," *Appl. Phys. Lett.*, vol. 67, pp. 3685–3687, December 1995.
- [80] SOITEC. <http://www.soitec.com>.
- [81] M. Emsley, O. Dosunmu, and M. Unlu, "Silicon substrates with buried distributed Bragg reflectors for resonant cavity-enhanced optoelectronics," *IEEE J. Select. Topics Quantum Electron.*, vol. 8, pp. 948–955, July/August 2002.
- [82] H. Levinson, *Principles of lithography*. SPIE PRESS, Bellingham, Washington, USA, 2001. ISBN 0-8194-4045-0.
- [83] JEOL, *A guide to scanning microscope observation*. May 2004. <http://www.jeol.com>.
- [84] Oz-Optics, *V-groove assemblies*. May 2004. <http://www.ozoptics.com>.
- [85] H. Lefevre, "Single-mode fiber fractional wave devices and polarization controllers," *Electron. Lett.*, vol. 16, pp. 778–780, 1980.
- [86] H. Ono, A. Emoto, F. Takahashi, N. Kawatsuki, and T. Hasegawa, "Highly stable polarization gratings in photocrosslinkable polymer liquid crystals," *J. Appl. Phys.*, vol. 94, pp. 1298–1303, August 2003.
- [87] S. Peng and G. Morris, "Experimental demonstration of resonant anomalies in diffraction from two-dimensional gratings," *Opt. Lett.*, vol. 21, pp. 549–551, April 1996.
- [88] S. Peng and G. Morris, "Resonant scattering from two-dimensional gratings," *J. Opt. Soc. Am. A*, vol. 13, pp. 993–1005, May 1996.
- [89] A. Cowan, P. Paddon, V. Pacradouni, and J. Young, "Resonant scattering and mode coupling in two-dimensional textured planar waveguides," *J. Opt. Soc. Am. A*, vol. 18, pp. 1160–1170, May 2001.
- [90] P. Paddon and J. Young, "Two-dimensional vector-coupled-mode theory for textured planar waveguides," *Phys. Rev. B*, vol. 61, pp. 2090–2101, January 2000.